CRACK GROWTH IN ALLOY 709 AT HIGH TEMPERATURES UNDER FATIGUE, CREEP AND DWELL-FATIGUE LOADS

Volume 1

JIN YAN

A thesis submitted to University of

Birmingham for the degree of

Doctor of Philosophy

School of Metallurgy and

Materials College of Engineering and

Physical Science

University of Birmingham

May 2021

Synopsis

Alloy 709 is a new generation austenitic stainless steel under consideration for structural materials of Sodium-cooled Fast Reactors (SFR) at the highest operating temperature up to 550°C. Compared with conventional austenitic stainless steels, this advanced austenitic stainless steel has superior creep resistance. Safe operation of nuclear power plants requires comprehensive understanding of material performance under prolonged stressing in complex operating cycles and environments. One essential element is the capability to predict remaining service life and determine safe inspection intervals of components containing flaws. This relies on understanding of crack growth resistance. Due to the temperature and loading change at start-up and shutdown, understanding crack growth resistance under dwell-fatigue conditions is also an important aspect and in addition to that under pure creep (static) loading. As a relatively new alloy, such databases and detailed mechanistic understanding have not been established to date. This study aims to characterise crack growth resistance in Alloy 709 under creep and dwell-fatigue loading conditions at three temperatures, 550, 650 and 750°C. Fatigue crack growth behaviour was also studied. Furthermore, a small number of tests were carried out on a conventional austenitic stainless steel, 316H, to compare with results obtained on Alloy 709.

To aid the research on crack growth resistance, the microstructure of Alloy 709 has been characterised in both as-received and overaged conditions, using optical microscopy

(OM), scanning electron microscopy (SEM) and transmission electron microscopy (TEM). A series of ageing conditions were selected: 500, 1000 and 2000 hours, at 550, 650 and 750°C respectively. The alloy is shown to be strengthened by fine Nb(CN) precipitates and nano-sized Z phases which form on dislocations. The coarsening of those precipitates during long term thermal exposure and formation of different new phases are studied.

In addition to crack growth testing, tensile and creep testing were also investigated. An increase in yield stress was observed after ageing at 650°C for 2000 hours. Excellent strain hardening behaviour and creep strength are measured, especially at 550°C, which is nearly service temperature of the Sodium-cooled Faster Reactors. This temperature also is close to a transition of fracture mode and/or fracture strain from a relatively brittle (intergranular) to completely ductile (microvoid coalescence) in creep tests.

Crack growth tests were conducted under fatigue (0.25 Hz), dwell-fatigue (1 hour hold time at maximum load) and creep (static) loading using compact tension specimens. Both a linear elastic fracture mechanics (LEFM) parameter, ΔK, and an elastic-plastic time dependent fracture mechanics parameter (the C*-integral) was adopted to characterise crack growth behaviour. Tests were performed at 550, 650 and 750°C in air. A small number of tests were also conducted in vacuum to clarify the effects of air environment on transgranular and intergranular crack growth. A maximum load of 8 kN was applied for most tests to allow comparisons of crack growth resistance to be made

for very similar testpiece geometries. Under fatigue loading (0.25 Hz) only small changes in fatigue crack growth resistance have been confirmed over the temperatures investigated, with largest differences seen at lower growth rates within the Paris regime. In contrast, crack growth resistance varies significantly for intergranular crack growth under creep and dwell-fatigue loading. As shown in plane-sided creep tests, excellent creep crack growth resistance is observed at 550°C. It is at this temperature alone that interaction of fatigue and creep (where the fracture is a mixed mode of transgranular and intergranular crack growth) is confirmed with dwell-fatigue loading and this increases crack growth rates compared to those obtained under (static) creep loading. At a temperature of 650°C, it is found that overageing does not degrade creep crack growth resistance. Also, a significant improvement in creep crack growth behaviour is confirmed in Alloy 709, compared with 316H. When using the C*-integral to characterise creep crack growth resistance which involves signification deformation ahead of the crack tip, all crack growth data collected from various temperatures and different alloys have fallen into a narrow scatter band for all tests suggesting that it is a parameter that can characterise crack growth rates uniquely for a given testpiece geometry.

List of Publications:

Journal articles:

1. Ding, R., J. Yan, H. Li, S. Yu, A. Rabiei, and P. Bowen, *Deformation microstructure and tensile properties of Alloy 709 at different temperatures.* Materials & Design, 2019. **176**: p. 107843.

2. Ding, R., J. Yan, H. Li, S. Yu, A. Rabiei, and P. Bowen, *Microstructural evolution of Alloy 709 during aging.* Materials Characterization, 2019. **154**: p. 400-423.

3. Yu, S., J. Yan, H. Li, R. Ding, A. Lall, A. Rabiei, and P. Bowen, *Fatigue crack growth resistance of the austenitic stainless steel Alloy 709 at elevated temperatures.* Journal of Materials Research and Technology, 2020. 9(6): p. 12955-12969.

4. Yan, J., H. Li, S. Yu, A. Rabiei, and P. Bowen, *A study on dwell-fatigue crack growth behaviour on an advanced austenitic stainless steel.* To be submitted.

5. Yu, S., J. Yan, R. Ding, H. Li, A. Rabiei, and P. Bowen. "*Creep crack growth of an advanced austenitic stainless steel for nuclear application*" To be submitted.

Conference:

Fatigue and Dwell-Fatigue Crack Growth in an Advanced Austenitic Stainless Steel, 14th International Conference on Fracture (ICF 14), Rhodes, Greece, June 18-23, 2017.

Acknowledgements

From the bottom of my heat, sincere gratitude is due to my supervisors, Professor Paul Bowen and Dr. H.Y. Li, without their mentoring, inspiring and endless support, it would be far more challenging to finish my PhD study.

I also greatfully acknowledge the Research Council of The United Kingdom (RCUK) and the United States of America's Department of Energy (DOE) for providing funding and the research materials for this project.

Deepest thanks are due to the help and care from the members of Professor Paul Bowen's research group. Assistance from Dr. S. Yu, Dr. R. Ding, Dr. T. Doel and Mr. D. Price is highly appreciated.

Last but not least, the acknowledgement is due to my loving failmily for their contant help, love and surpport.

Table of Contents

CHAPTER 1 Introduction

The service life for the next generation fast neutron reactors (Gen IV) is designed to be at least 60 years. To meet the increasing demand for clean energy, safe and economic structural materials need to be designed. Austenitic stainless steels are conventionally applied to structural components in the nuclear reactors owing to extraordinary resistance to corrosion environment, high temperature mechanical properties and competitive pricing. The structural materials are subjected to high temperature and high stress service conditions are required to have remarkable mechanical properties, especially creep crack growth resistance. To make sure the safety and performance of the Gen IV nuclear reactors, the investigation of creep crack growth mechanisms is critical both for design and construction. Alloy 709 (Fe-20Cr-25Ni) is an austenitic stainless steel that is being designed for use as a key structural material for Gen IV Sodium-cooled Fast Reactors (SFR). However, experimental data on the creep crack growth behaviour in Alloy 709 is still lacking.

The scheme of this project is mainly to investigate the fatigue, creep and dwell-fatigue crack growth mechanisms in Alloy 709. The evaluation of high temperature crack growth behaviours under fatigue, creep and dwell-fatigue loadings are investigated and both intrinsic (i.e. thermal ageing effects) and extrinsic factors (i.e. temperatures, load ratios, side-groove depth, environmental effects) are considered. To better investigate the creep and dwell-fatigue crack growth behaviours in Alloy 709, the creep and creep-fatigue

crack growth of the conventional 316H (Fe-17Cr-10Ni) is introduced for comparison. Linear elastic fracture mechanics (LEFM) and elastic plastic fracture mechanics (EPFM) techniques have been adopted to characterise the crack growth under fatigue, creep and dwell-fatigue interactions.

The scope of the project can be summarised as follows:

- To evaluate the microstructure variation during ageing (i.e. the precipitation formation with different ageing temperatures and durations) and its effect on subsequent mechanical properties of Alloy 709 (i.e. tensile properties, creep and dwell-fatigue crack growth behaviour);
- To clarify the high temperature crack growth behaviour and understand the mechanisms under different test conditions (especially temperature and environment);
- To obtain the crack growth data and ‘‘master’’ curves for fatigue, creep and dwell-fatigue interaction fracture modes for life prediction and material design.

CHAPTER 2 Literature Review

2.1 Sodium-cooled Fast Reactor and Structural Materials

The world's population has continued to grow rapidly during the past 20 years and the demand for clean, safe and sustainable energy has become more urgent, especially since the year 2000 [1]. In 2013, the total global natural uranium resources that could be extracted for a cost of less than 130 USD/ton was ~5 million tons. Based on the rate of average consumption in 2014, these reserves are sufficient for 135 years [2]. Currently, the most widely used nuclear reactors are Light Water Reactors (LWR) [3], which are thermal neutron reactors that use light water as the coolant with the highest service temperature of 350°C. Regardless of the large amounts of nuclear power that the LWR generates, various issues arise such as low utilization efficiency of nuclear energy, the problem of nuclear waste disposal and the possibility of radiation leakage. Many nuclear accidents have occurred in previous [4]. For example, in 1979, the nuclear leak caused by the Three Mile Island accident in the U.S; in 1986, the radioactive explosion triggered by the Chernobyl disaster in Russia and in 2011, the explosion at the Fukushima nuclear plant in Japan. Advanced nuclear reactor designs are required to have a higher level of safety than the current designs. The next generation of fast neutron reactors (Gen IV) not only easy to achieve sustainable development for future nuclear power plants but also have advantages in safety design. Several possible concepts are being considered such as Sodium-cooled Fast Reactors (SFR), Gas-cooled Fast Reactors (GFR), Lead-cooled Fast Reactors (LFR), Molten Salt Reactors (MSR), Very High Temperature Reactors (VHTR)

and Supercritical-Water-cooled Reactors (SCWR). At the Generation IV International Forum (GIF), it was announced that the SFRs were the closest to commercialisation among all the possible Gen IV nuclear power plants [5].

An SFR is a fast neutron reactor that uses liquid sodium as the coolant. Sodium is selected as a coolant due to its high specific heat capacity, low melting point (98°C), high boiling point (883°C) and is less corrosive to the structural materials [6]. Owing to these properties, a reactor pressure vessel can be produced with high power density without pressurization. However, since the liquid sodium reacts chemically with air and water, a sealed coolant system is needed.

Figure 2.1 illustrates the main components of the pool-type SFR [7]. In this system, fast neutrons sustain the fission chain reaction that generates the heat. This heats the reactor coolant which in turn is used to generate steam. The stream is converted to mechanical energy to rotate turbines.

To achieve higher thermal efficiency and improve safety, this system contains a primary system, an intermediate circuit and a steam generator. In the primary system, the primary sodium temperatures at the inlet and outlet of the reactor vessel are ~380 and 550°C [8]. The coolant is covered by an inert gas and does not exchange its heat with the water. In the steam generator, the secondary sodium temperatures at the inlet and outlet of the steam generator are ~530 and 340°C [8]. The secondary sodium can exchange its heat with water to generate steam. To reduce the possibility of a nuclear accident, i.e. the sodium-water reaction, an intermediate circuit (the secondary cooling system) with non-radioactive

sodium is adopted in the SFR system. This sealed power plant system of an SFR can produce more sustainable energy and reduce nuclear waste compared to thermal neutron reactors [6].

However, in recent years, SFR construction has been limited for some countries, such as the USA, France, United Kingdom, Russian Federation, Kazakhstan, Republic of Korea, Japan, India, China and Germany [9]. The most severe limitation is caused by the failure of the structural material used for the fuel container, which could leak the fuel and/or fission products into the coolant. Also, since sodium is highly reactive with air and water, a sodium leak could cause an explosion and the production of toxic sodium-oxide aerosols [6]. This kind of failure is mainly associated with in-service degradation of crack growth behaviour of the structural components when soaking in the liquid sodium at the prolonged high service temperatures of 500 - 550°C and steam pressure of ~14 MPa [8]. Also, the neutron flux is higher and the coolant is more aggressive than in the LWR. The design criteria of the system and components are required to avoid the chemical reaction between sodium and water in the steam generator. The structural materials for an SFR not only need to have excellent corrosion resistance and irradiation tolerance but are also required to have high temperature capability. Therefore, to enable a design life of 60 years or more [10], outstanding mechanical properties, especially creep resistance, are needed for materials design. Furthermore, during operation, the service temperature and mechanical stress may change, therefore, the structural materials will sustain cyclic loading during power up and down due to the variation in temperature and pressure. Thus,

good resistance against fatigue and dwell-fatigue loads are also important for the components to operate at high temperatures. Also, workability, cost, etc. are all important requirements for the material design. Among the candidate materials, austenitic stainless steels are proposed for use in SFR components owing to their extraordinary mechanical properties, superior resistance to corrosion environment, high temperature formability and cost-effectiveness.

2.2 Microstructures of Austenitic Stainless Steels

2.2.1 A Brief Introduction to Austenitic Stainless Steels

Since the 1950s, austenitic stainless steels have been widely used as the structural material in the SFR to serve under cyclic and static stresses at elevated temperatures. Austenitic stainless steels are normally Fe-Cr-Ni alloys, where 16 to 28 wt% chromium and between 2 and 20 wt% nickel are added. The FCC austenite structure not only enables the austenitic stainless steels to have excellent physical and mechanical properties, such as high durability and toughness but also provides superior thermophysical properties (especially at 550°C and above). In addition, they show better stability than other Fe-based structures. Thus, austenitic stainless steels are advised as significant structural materials where high fatigue, creep and creep-fatigue properties are needed at 550°C and above [11].

2.2.2 Effects of Alloying Elements on Microstructures

Apart from the major alloying elements, Cr and Ni, several alloying elements such as C, N, Mo, Si and Mn are required to obtain desired properties.

Chromium

Chromium is essential to all stainless steels. When the chromium content is above the minimum composition content required in the stainless steel, which is 10.5 wt%, an insoluble film will form on the surface to protect the steel from oxidation. The higher the Cr content, the thicker the protective layer on the material. However, when the Cr content is above a certain level, it causes the formation of brittle phases, which may have detrimental influences on the crack growth behaviour. For example, 25 wt% Cr content in austenitic stainless steel can form intermetallic sigma phase (σ phase), which can lead to embrittlement [12]. When 20Cr 25Ni Nb-stabilised austenitic stainless steels serve at 500°C for ~10^4 hours (Figure 2.2) [13], Cr-rich brittle secondary phases, such as $M_{23}C_6$ carbides, formed on grain boundaries. The secondary phases formed adjacent to grain boundaries can lead to depletion of Cr at grain boundaries. The content of Cr around the grain boundaries may even become lower than the minimum Cr content for stainless steel (10.5 wt%). These brittle grain boundary secondary phases cannot sustain plastic deformation and therefore grain boundary cracking occurs. This could cause the degradation of the material, especially decreasing the creep resistance and corrosion resistance.

Nickel

Nickel is an important stabilising element for austenite, especially for 300 series austenitic stainless steels. It provides excellent high temperature properties for the material, such as high strength, ductility, weldability, toughness and corrosion resistance

[14].

Manganese

Manganese is added to stabilise the austenite, sometimes used as a substitute for Ni. Mn can also increase the solubility of N in austenitic stainless steel without forming nitrides. In the low-nickel austenitic stainless steel (e.g. 200 series stainless steel), Mn is added in higher content (4 - 15 wt%) to replace Ni [12].

Molybdenum

Molybdenum is a ferrite former. The typical Mo content in the austenitic stainless steel is ~3 - 7 wt%. Mo is added to the austenitic stainless steel mainly for obstruction localised pitting corrosion. It helps against the harmful effect of chlorides. Mo improves creep properties by solid solution hardening and promotes the formation of the carbides [4]. In contrast, Mo also promotes the nucleation of the brittle intermetallic σ phase, which can initiate intergranular cracking. Due to the low melting point for the MoO_3 (795°C), when the temperature is higher than 700 - 750°C, this molten molybdenum oxide may degrade the mechanical properties of the material [15].

Silicon

Silicon is a ferrite stabiliser, thus it is important to control the silicon content in the austenitic stainless steel (typically <0.5 wt%). In austenitic stainless steel, a small amount of Si can form a silicon oxide film to protect the iron-based alloy from oxidation [16]. Also, Si can protect the alloy from corrosion by oxidising acids [11]. The material with higher silicon content increases corrosion resistance, such as in 309 and 310 austenitic

stainless steels [17]. However, a high Si level in austenitic stainless steel can form the brittle intermetallic θ phase, once more initiating intergranular cracking.

Niobium

Niobium is a ferrite former. A typical Nb content in austenitic stainless steel is ~ 0.2 - 0.6 wt%. It is added mainly to prevent intergranular cracking by avoiding the formation of continuous globular grain boundary $M_{23}C_6$ carbides. Due to stronger affinity of Nb to C than Cr, the Cr depletion at grain boundaries can be inhibited [11].

Titanium

Similar to niobium, titanium is added to stabilise the ferrite. A typical Ti content in the austenitic stainless steel is below 0.05 wt%. Due to the low carbon levels in the stainless steel (e.g. the maximum C content in 304 is 0.08 wt %), Ti is a strong formation element of carbide, thus preventing the precipitation of continuous globular grain boundary $M_{23}C_6$ carbides [11].

Nitrogen

Nitrogen is not only an austenite stabiliser but also a solid solution strengthener. A typical N content in the creep austenitic stainless steel is ~0.1 - 0.5 wt%. N helps to increase strength and hardly reduces the ductility and weldability of the austenitic stainless steel. The solid strengthening effect of N is even more obvious than C [11]. In creep resistant materials, N can precipitate as secondary phases, such as nitrides and carbonitrides, which can increase the creep resistance for the austenitic stainless steel at high temperatures. However, when the N content is above 0.2 wt%, it possibly has a detrimental effect on

steel manufacturing, especially for steel machining and cold working.

Carbon

Carbon is the solid solution former, which is squeezed in between the iron atoms as an interstitial solute in the FCC structure. Also, carbon is a common austenite stabiliser, but its low solubility limits the stabilisation of the austenitic structure. The typical C content in the austenitic stainless steel is between 0.02 to 0.03 wt%. At elevated temperature, the formation of grain boundary $M_{23}C_6$ carbides causes chromium depletion at grain boundaries. The cracking of grain boundary carbides leads to intergranular failure and thus they have a detrimental influence on the high temperature properties of the material.

2.2.3 Phases in 20Cr-25Ni Nb-stabilised Austenitic Stainless Steels

The basic phase for 20Cr-25Ni Nb-stabilised austenitic stainless steel is γ-austenite. Secondary phases are formed from the alloying elements (e.g. Mn, Mo, Si, Nb and Ti). The Time, Temperature, Precipitation (TTP) diagram for 20Cr-25Ni Nb-stabilised austenitic stainless steel (Figure 2.2) was summarised by Powell [13], in which the time and temperature for each phase were first observed can be noted.

2.2.3.1. Austenite (γ) Matrix

The allotropes for iron can be classified into three groups: the α-ferrite, γ-austenite and ε-steel [18]. The most fundamental structure of the austenitic stainless steel is the γ-austenite phase, which has a face-centred cubic (FCC) structure, see Figure 2.3 [19]. Due to its high modulus and multiple slip systems, the FCC γ-austenite phase enables the austenitic stainless steels to have outstanding mechanical properties, e.g. tensile, creep

and fatigue resistance. Owing to the high content of alloy elements, especially the austenite stabilisers, the austenite matrix is also relatively stable at elevated temperatures (up to 1394°C). These provide austenitic stainless steels with superior high temperature performance.

2.2.3.2. $M_{23}C_6$

$M_{23}C_6$ precipitates are the Cr rich carbides with alloying elements such as Mo, Ni and Fe substituting for Cr element [11, 12]. High temperature (>550°C) helps the precipitation of $M_{23}C_6$ carbides. They are found in most grades of austenitic stainless steels but with different morphologies. $M_{23}C_6$ initially forms at grain boundaries globularly, and then at incoherent twin boundaries. It can also form at coherent twin boundaries with a plate-like shape. With prolonged ageing time cuboidal $M_{23}C_6$ can precipitate on dislocations or around other particles such as niobium carbonitrides [12, 20, 21]. Fine discontinuous intergranular $M_{23}C_6$ carbides can resist grain sliding and promote creep resistance. With higher temperatures and longer ageing time, $M_{23}C_6$ coarsen faster than other carbides or nitrides [22] and become continuous at the grain boundaries, which can degrade the high temperature properties by initiating intergranular cracking. $M_{23}C_6$ distributed on twin boundaries is not susceptible to cracking due to its low boundary energy [23]. The precipitation of $M_{23}C_6$ carbides can be affected by other elements. Normally, the addition of Mo and Ni decreases the solubility of carbon and therefore promote the precipitation of nano-sized $M_{23}C_6$ carbides. N additions prevent the precipitation of detrimental $M_{23}C_6$ by increasing the solubility of C [11].

2.2.3.3. Z-Phase (CrNbN)

Z-phase, with a tetragonal crystal structure and a general formula of CrNbN. It is a relatively complex phase [24]. It favours precipitating in the Nb-stabilised austenitic stainless steels. Higher N levels (>0.4 wt%) in the stainless steel promote the formation of Z-phase [25]. Z-phase is stable at temperatures between 600 to 1200°C with different morphologies. It normally can be found on the grain boundaries and dislocations with a rod-like structure [21] and on incoherent twins and twin boundaries with a plate-like shape [26]. The Z-phase has been observed during ageing with a size of 5 - 50 nm. Nano-sized Z-phase was found to precipitate in TEMPALOY A-3 alloy (22Cr-16Ni stainless steel) and helps to prevent dislocation movement after ageing at 750°C for 18 kh [27]. Due to the high Cr levels in NF709 and Alloy 709, intragranular rod-like Z-phase is present as residual particles in the as-received material [21, 26].

2.2.3.4. Nb(CN)

Niobium carbonitride is a short term precipitate observed in 20Cr-25Ni niobium stabilised austenitic stainless steels with an average ageing time below 1000 hours (e.g. ageing at 550°C for 500 hours) [12, 28-30]. It distributes at grain boundaries and grain interior with different sizes and morphologies. Precipitates with sizes between 1 - 10 μm are primary Nb(CN) which may be formed during the casting process. Nano-sized Nb(CN) is secondary Nb(CN), which possibly forms during the cooling stage of annealing and solidification [31]. Precipitation of fine Nb(CN) (~120 nm) pin grain growth, thus facilitating high temperature mechanical strength [32-34]. Common morphologies are

rectangular and globular. Also, Nb(CN) performs as a nucleation site for $M_{23}C_6$ carbides in material aged between 650 and 750°C even for 500 hours [21]. At high temperatures, Nb(CN) particles broken during deformation can initiate microvoids and thus can degrade the high temperature performance of the material.

2.2.3.5. Intermetallic Phases

Theta Phase (θ Phase)

Theta phase (θ phases) is an intermetallic phase found in the 20Cr-25Ni Nb-stabilised austenitic stainless steels [35]. It has a tetragonal structure, the general formula is $Cr_{23}Ni_2SiN$ [26]. θ phases have different structures and locations. Globular θ phases are normally formed at grain boundaries, plate-like θ phases are preferentially formed on the dislocations and cuboidal θ phases form around the $M_{23}C_6$ carbides [12]. The grain boundary θ phases can crack during high deformation causing ductile failure. The fine θ phases dispersed inside grains increases the creep resistance.

G Phase and Sigma Phase (σ Phase)

G phase and σ phase are intermetallic phases in 20Cr-25Ni steels. The general formula for G-phase is $Ni_{16}Nb_6Si_7$ [12]. The G phase normally precipitates after ageing between 750 and 850°C [36] and is observed to participate from residual intergranular Nb(CN) at 550°C and above [37]. σ phase has been found in 20Cr-25Ni stainless steel with a Mo content of 4.5 to 6.0 wt% [37], in which the composition of σ phase close to 44Cr 40Fe 10Ni 6Mo (wt%) [26]. The existence of σ phase to a great extent can decrease the ductility of the material, in consequence, reduce the creep ductility.

2.2.4 Hardening Mechanisms

Obstruction of the movement of dislocations in austenitic stainless steel will decrease plastic deformation and improve strength. Generally, austenitic stainless steels that operate at high temperatures are hardened through four hardening mechanisms: work hardening, solid solution hardening, precipitation hardening and grain boundary hardening.

2.2.4.1. Work Hardening

Work hardening, also named strain hardening, is due to interactions between dislocations. It is known that the dislocation movement can lead to plastic deformation, and at the same time the new dislocations are formed. As a consequence, the dislocation density increases, thus pinning dislocation movement. By decreasing the dislocation movement, the strength of the material is increased. Work hardening is more effective at lower temperatures. At high temperatures, the dislocations are more mobile, dynamic recovery is more likely and the dislocation density does not increase in the same way. Higher strain rate contributes to the formation of increased dislocation density thus promoting the cold working effect. Lower temperature and higher strain rates promote the work hardening effect.

2.2.4.2. Solid Solution Hardening

Solid solution hardening occurs by applying alloying atoms to improve the strength of the matrix material. These alloying atoms such as Cr, Ni, Mn, Mo, Si, Nb, Ti and N are distributed randomly. Depending on the different sizes of the solute atoms, they locate

either in interstitial or substitutional sites. The sizes for solute atoms are different to base iron atoms, thus they provide strain fields in the crystal lattice. These strain fields around the solute atoms hinder dislocation movement therefore increasing the strength. The larger the difference between the solute atoms and the base atoms the larger the lattice distortion and the better the obstruction to dislocation movement [38]. Solute atoms with a higher melting point can increase the hardening effect due to higher lattice cohesion and lower diffusion, especially at high temperatures [39]. The effective solid solution hardening effects contribute to the creep behaviour of austenitic stainless steels. Furthermore, due to dislocation movement being harder in base materials with lower stacking fault energy (SFE), solute atoms can harden the materials by decreasing the stacking fault energy (SFE) in the crystal lattice. The quantity of solute that can be added is limited and beyond this limit secondary phases may be formed.

2.2.4.3. Precipitation Hardening

Precipitation hardening requires a uniform dispersion of small particles throughout the matrix which hinder dislocation movement. However, some intermetallic phases, i.e. θ phase, G phase and σ phase, with larger sizes have a detrimental effect on strength. They supply an appropriate place for stress concentration, thus the formation and propagation of voids, which degrade the mechanical properties of material. Also, they can decrease the solid solution hardening influence by removing the solute atoms from the matrix thus reducing the creep strength of the material. In austenitic stainless steel, the solute atom depletion can also decrease the corrosion resistance. For 20Cr-25Ni niobium stabilised

austenitic stainless steel, nano-sized Z-phase can pin the movement of dislocations. However, higher temperature and longer ageing duration promote the coarsening of Z-phase thus decrease the pinning effect of dislocation movement.

2.2.4.4. Grain Boundary Hardening

In austenitic stainless steels, a strengthening effect also can be achieved by pinning grain boundary sliding. The grain boundary strengthening effect affected by the structure of grain boundary and the misorientation between each grain. The dislocation should change its direction when it meets the grain boundary due to the mismatch in the lattice orientation at grain boundaries [40]. Discontinuous globular grain boundary carbides and carbonitrides are the most effective grain boundary precipitates for obstructing grain boundary sliding. However, continuous film-like particles can have a detrimental effect on the ductility and creep resistance of the material. Also, the grain size variation can influence the grain boundary sliding at different temperatures. At low temperature, smaller grain size promotes the pinning effect for the grain boundary sliding because of the higher yield stress for the material. On the contrary, materials with smaller grain sizes become softer at higher temperatures, consequently the creep resistance for the material decreases.

2.2.4.5. Microstructure/ Property Relationship of Austenitic stainless steel

The effects of alloying elements and secondary phases on mechanical properties have been given in section 2.2. It is known that even small variations in chemical composition can change the properties of the material. A Schaeffler diagram is mainly applied to

predict microstructure and properties in weld metals over a larger compositional range, especially in predicting the amount of delta ferrite in steel welds [41]. It is possible to use the Schaeffler diagram to predict which phase is stable in a certain composition of stainless steel. As shown in Figure 2.4, the components in austenitic stainless steel are shown in the modified Schaeffler diagram [42]. This diagram is developed by establishing the stable phases (at room temperature) for different compositions of stainless steel after heating an alloy to 1050°C for 30 minutes and then quenching in water. The coordinates were given as an indication of the austenite formers (Ni, Mn, C, etc.) and ferrite formers (Cr, Mo, Si, Nb, Ti, etc) on the vertical and the horizontal axes respectively. The effects of alloying elements can be expressed mathematically by the nickel and chromium equivalent expressions, which, using compositions in weight percent, are given as follows:

$Ni_{eq} = Ni + Co + 30C + 25N + 0.5Mn + 0.3Cu,$

and the chromium equivalent is given by:

$Cr_{eq} = Cr + 2Si + 1.5Mo + 5V + 5.5Al + 1.75Nb + 1.5Ti + 0.75W.$

In this diagram, four types of stainless steels: austenitic, ferritic, martensitic and duplex, can be produced by varying the chemical composition.

2.3 Engineering Fracture Mechanics

2.3.1 Linear Elastic Fracture Mechanics

The linear elastic fracture mechanics is mostly used for investigation of fracture in brittle and high-strength alloys under small-scale yielding.

Generally, brittle failure in the material is particularly initiated by transgranular cleavage

fracture and fatigue failure. The first model related to the energy balance theory was proposed by Griffith in the 1920s when studying crack propagation in a brittle glass. It was found that if the total energy is reduced because of crack growth, then a crack in a component will propagate. Later, the model was extended and applied to metal materials by Irwin [43] and Orowan [44]. Their theories are regarded as fundamental to modern fracture mechanics [45].

2.3.1.1. Griffith's Energy Balance Theory

Griffith proposed the energy balance theory to predict crack propagation [46]. For crack propagation in an elastic material, if the total energy adjacent the crack tip is released by crack growth, then a crack will propagate. Under plane stress, the stress required for crack propagation can be calculated according to the following equation:

$$\sigma_F = \sqrt{\frac{2E\gamma_s}{\pi a}} \qquad \text{(Equation 2.1)}$$

where σ_F is the failure stress, E is the Young's modulus, γ_s is the free surface energy per unit area and 2a is the crack length.

2.3.1.2. The Stress Intensity Approach

To characterise the stress of any point adjacent the crack tip, the stress intensity approach was proposed by Irwin in the 1920s [47]. There are three crack displacement modes classified by deformation types and loading types, as shown in Figure 2.5 [47]. Mode I is the tensile mode (or opening mode). Mode II is the sliding mode. Mode III is the tearing mode.

Motivated by Williams [48], Irwin proposed that for a through-thickness crack of length

2a in a biaxially loaded infinite plate, the Mode I stresses at the crack tip are shown below:

$$\sigma_x = \frac{\sigma\sqrt{\pi a}}{\sqrt{2\pi r}}\cos\frac{\theta}{2}\left(1 - \sin\frac{\theta}{2}\sin\frac{3\theta}{2}\right)$$

$$\sigma_y = \frac{\sigma\sqrt{\pi a}}{\sqrt{2\pi r}}\cos\frac{\theta}{2}\left(1 + \sin\frac{\theta}{2}\sin\frac{3\theta}{2}\right) \qquad \text{(Equation 2.2)}$$

Where σ is applied stress, σ_x and σ_y is the stress at point (r, θ), r is the distance between the crack tip to the point and θ is the elevation from the crack plane, see Figure 2.6 [47]. The stresses are functions of the geometric position ($\frac{f(\theta)}{\sqrt{2\pi r}}$), the applied stress and the square root of the crack length. The Mode I stress intensity factor K_I can be calculated according to the following equation:

$$K_I = \sigma\sqrt{\pi a} \qquad \text{(Equation 2.3)}$$

Where σ is the nominal applied stress and a is the crack length.

The testpieces geometry used for this work is compact tension (CT) testpiece. The stress intensity factor for the compact tension (CT) specimen is shown below:

$$K_I = \frac{YP}{B\sqrt{W}} \qquad \text{(Equation 2.4)}$$

Where P is the load applied, B and W are the thickness and width of the specimen, Y is the compliance [49].

2.3.2 Elastic-plastic (Ductile) Fracture Mechanics

The local plasticity must be limited for LEFM to be used. The mechanics appropriate to evaluate the stress and deformation field near the crack front in low strength materials have been investigated. Low strength ductile alloys, especially under plane stress exhibit large-scale yielding and a large plastic zone exists at the crack front compared with the crack length and the dimensions of the specimen. In this case, elastic-plastic fracture

mechanics is appropriate for characterisation of crack initiation and growth.

One application for EPFM is to characterise creep crack growth at high temperature in low strength ductile materials. Under these conditions, crack tip opening displacement (CTOD), the J-integral and C*-integral are common approaches to correlate crack growth during extensive creep [50].

2.3.2.1. Crack Tip Opening Displacement

The crack tip opening displacement (CTOD) parameter was originally suggested by Wells [51] in 1961 to illustrate the fracture behaviour at the crack tip (Figure 2.7) . Since strain accumulated at the sharp crack tip under loading in tension, the crack tip will blunt because of the formation of plastic zone at the crack tip [50, 52], the CTOD will reach a critical value before fracture.

Under large-scale yielding condition, where $\sigma \gg \sigma_{ys}$, the CTOD can be calculated according to:

$$\mathrm{CTOD} = \frac{\mathrm{K}^2}{\mathrm{E}\sigma_{\mathrm{ys}}} \qquad \text{(Equation 2.5)}$$

This equation is appropriate for large-scale yielding and it is limited for an infinite plate and plane stress conditions. A more general expression for the CTOD under LEFM conditions can be shown below:

$$\mathrm{CTOD} = \alpha\left(\frac{\mathrm{K}^2}{\mathrm{E}\sigma_{\mathrm{ys}}}\right) \qquad \text{(Equation 2.6)}$$

where α is a constant, which is influenced by flow stress, geometry as well as work hardening exponent. Under plane strain and plane stress conditions, the value of α is 1.0

and 0.49 individually [53, 54].

2.3.2.2. J-integral Approach

The J-integral is an approach to correlate the stresses and strains field ahead of a crack, first proposed by Rice in 1968 [55]. The J-integral was proposed as a line integral along a contour which encircles a tip of a crack, which begin with the lower surface and ends at the upper surface (Figure 2.8) [56]. The J-integral is independent of path and it is defined as follows:

$$J = \int_{\Gamma} \left(wdy - T \cdot \frac{\partial u}{\partial x} ds\right) \qquad \text{(Equation 2.7)}$$

where w is the strain energy per unit volume, Γ is the path of the integral, T is the normal stress acting on the contour Γ, u is the displacement vector and ds is an increment of the contour path, x and y are the rectangular coordinates and $T \cdot (\frac{\partial u}{\partial x})\, ds$ is the rate of work input from the stress into the area enclosed by Γ.

The J-integral can be applied to linear or non-linear elastic material, where the parameter is related to the change of potential energy rate release with crack growth. However, in elastic-plastic materials, J is only valid for prediction of ductile crack extension under monotonic loading with no unloading [57]. Thus, the physical meaning for J is more linked with the energy flow into the crack tip. It is worth mentioning that the J-integral is only appropriate to this case under small-scale yielding conditions [58].

2.3.2.3. C*-integral

The C*-integral was originally proposed by Landes and Begley [59] and Nikbin et al. [60]

in 1976. It is an elastic-plastic fracture mechanics analogous to the J-integral. The C*-integral can be interpreted as the energy difference between two identical loaded bodies having different crack lengths:

$$C^* = \int_\Gamma (\dot{w}dy - T \cdot \frac{\partial \dot{u}}{\partial x} ds) \quad \text{(Equation 2.8)}$$

where $\dot{w}$ is the strain energy rate per unit volume, $\dot{u}$ is the displacement vector rate. C* was proposed to characterise the stresses and strain-rate fields at a crack tip [61] under extensive creep deformation. Moreover, C* is also linked with the variations of potential energy release rate with crack extension [59]. Similar to the J-integral, C* was also found to be path-independent [62], which indicates any contour surrounding the crack tip will result in the same C* value.

In 1988, Hyde [63] calculated C* using compact tension (CT) and thumbnail testpieces. It was noted that CT specimens were the simplest and most accurate geometry for C* calculation.

For the CT specimen, according to ASTM E 1457-15 [64], C* can be calculated according to the equation below:

$$C^* = \frac{P\dot{V}}{B_N(W-a)} \frac{n}{n+1} [2 + 0.522(1 - \frac{a}{W})] \quad \text{(Equation 2.9)}$$

where P is the load, $\dot{V}$ is the load-line displacement rate, B_N is the net thickness of the side-grooved testpieces, W and a are the width of the specimen and the crack length, and n is the creep exponent. According to standard ASTM E 1457-15 [64], the displacement rate can be measured from load-line or crack tip opening (CTOD) positions.

Creep crack growth rates can be calculated from the C*-integral and the relationship is shown below,

$$\frac{da}{dt} = DC^{*q} \qquad \text{(Equation 2.10)}$$

where D and q are the constants related to the material properties.

To validate the creep crack growth test results, according to ASTM E 1457-15 [64], data points for the first 0.2 mm crack extension are excluded. Time to 0.2 mm crack extension is defined as the crack incubation time.

2.3.2.4. C(t)

For small-scale creep, the stress fields at crack tip were characterised by Ohji [65], Riedel and Rice [66] and Bassani and McClintock [67], C(t)-integral was discribed similar as C^*-integral, but to characterise the crack tip stress field at the crack tip and during the transition creep region. C(t) is given by:

$$C(t) = \frac{K^2(1-\nu^2)}{E(n+1)t} \qquad \text{(Equation 2.11)}$$

where K is the applied stress intensity parameter, ν is the Poisson's ratio, E is Young's modulus, n is the creep exponent, t is the creep time.

The creep zone expands until the whole cracked body creeps during the transition time, t_T. The relationship is given by [66]:

$$t_T = \frac{K^2(1-\nu^2)}{E(n+1)C^*} \qquad \text{(Equation 2.12)}$$

In the creep crack growth tests on X20CrMoV121 steel and its weld joint by Park [68], it was observed that the transition time takes up 0.3 - 0.8% of the total creep time.

2.4 Fatigue

Metals often fail under cyclic loading, where the maximum loading is lower than the 0.2% proof stress. This failure mode is named 'fatigue' [69]. The applied stress range in the cyclic loading can be express as below:

$$\Delta\sigma = \sigma_{max} - \sigma_{min} \quad \text{(Equation 2.13)}$$

The stress ratio, R, can be expressed as:

$$R = \frac{\sigma_{min}}{\sigma_{max}} \quad \text{(Equation 2.14)}$$

The stress intensity factor range ΔK is defined as:

$$\Delta K = K_{max} - K_{min} = Y\sigma_{max}\sqrt{\pi a} - Y\sigma_{min}\sqrt{\pi a} = Y\Delta\sigma\sqrt{\pi a} \quad \text{(Equation 2.15)}$$

where Y is the compliance coefficient for the specimen related with the ratio of crack length to the specimen width, W, $\Delta\sigma$ is the stress range.

Fatigue life was first evaluated using the S-N curve in the early 1860s by August Wohler [70]. The S-N curve shows the correlation of applied load and the number of cycles to failure. However, information on the two primary separate stages of fatigue failure (crack initiation and propagation), cannot be distinguished on the S-N curve.

2.4.1 Fatigue Crack Initiation

Stress concentrations at the free surface area or internal flaws (i.e. particles, grain boundaries or notches and holes due to manufacturing processing) can initiate a fatigue crack [71]. Under cyclic loading, 'persistent slip bands (PSB)' form on the surface, stress then concentrates on PSBs, thus they act as initiation points for the microcracks [72]. Once a microcrack has initiated, the crack grows along the PBS. After accumulating with

time, crack deviation may occur.

2.4.2 Fatigue Crack Propagation

When plotted fatigue crack growth rates against ΔK (Figure 2.9) [73], a sigmoidal curve is seen. It contains three regions.

Region I: The crack growth rate is slow, and the crack propagation is not continuous. When the ΔK value is below the threshold value, ΔK_{th}, the crack growth rate is generally lower than 10^{-8} mm/cycle and thus it cannot be detected. The crack growth rate is affected largely by several factors, i.e. microstructure, stress ratio, test temperature and environment. During Region I, the plastic zone diameter is within or have the same size as one grain.

Region II: Paris et al. proposed that fatigue crack growth rate, da/dN is related to ΔK [74]. The Paris law equation is shown below:

$$\frac{da}{dN} = A(\Delta K)^m \qquad \text{(Equation 2.16)}$$

where A and m are constants, which can be influenced by the microstructure, the applied frequency and waveform, stress ratio, R, test temperature as well as environment.

The crack growth is continuous. In this region, the plastic zone size is larger than the grain size. The fracture surface is marked with fatigue striations. Among several models relate to the mechanisms for striation formation, the first and most prominent one is the plastic blunting model proposed by Laird [75] (Figure 2.10). He suggested that the crack tip is influenced by plastic slip during cyclic loading. When tensile stress applied, the crack tip gets blunted due to the plastic shearing. The plastic slip concentrates at the crack tip and

at 45° to the direction of maximum stress. During the unloading, the plastic slip directions are reversed and then a new sharp crack tip formed, which leads to the formation of a striation.

Hence the observation of fatigue striations has a relationship with fatigue loading. A large amount of research has been confirmed that the local fatigue crack growth rate can be estimated from the width of striations and it has been documented that the fatigue crack growth rate can be determined from striation spacings [76]. However, some research has concluded that the width of striations does not always link to the crack growth rate [77]. In research carried out by Davidson, [78] it was suggested that at low ΔK regions, the striation spacing is larger than the crack growth rate. At high ΔK regions, Knott [50] found that the spacing of a striation is normally smaller than the fatigue crack growth rate found using the d.c.p.d. technique.

Region III: the crack growth rates speed up dramatically. The final fracture happens when the maximum K value is the same as the fracture toughness, K_{IC}. Microvoid coalescence in ductile materials is the final fracture mechanism.

2.4.3 Crack Tip Plasticity

As shown in equation 2.2, the crack tip stress value tends to infinity when r approaches zero. The near infinity stress can lead to a catastrophic fracture. However, for most metals, the material would have deformed when the stress is beyond the 0.2% proof stress. At this time, a plastic zone will form at the crack tip. Thus, it is crucial to evaluate the plastic zone size.

For plane stress conditions, if it is assumed that the plastic zone is near-circular. σ_{ys} can be substituted for σ_y in equation 2.2 and the theoretical plastic zone diameter, r_y, can be calculated according to the equation [79]:

$$r_y = \frac{1}{2\pi}\left(\frac{K_I}{\sigma_{ys}}\right)^2 \qquad \text{(Equation 2.17)}$$

The plastic zone diameter under plane strain determined by [80]

$$r_y \approx \frac{1}{6\pi}\left(\frac{K_I}{\sigma_{ys}}\right)^2 \qquad \text{(Equation 2.18)}$$

The plastic zone for a finite plate is shown in Figure 2.11 [81], where the plastic zone diameter varies along the crack tip.

2.4.4 Crack Closure

The fatigue crack growth can be affected by the crack tip plasticity and the crack closure between crack faces. The crack closure is incomplete contact between the two crack surfaces during tensile cyclic loading. It results from the residual plastic deformation in the vicinity of crack tip and the decrease in displacement at crack tip. The effective K value, ΔK_{eff}, can be calculated according to the equation 2.19:

$$\Delta K_{eff} = K_{max} - K_{cl} \qquad \text{(Equation 2.19)}$$

where K_{cl} is the stress intensity at which the crack surfaces firstly contacting during the unloading or start to fully open during the reloading.

There are numerous factors that induce the crack closure behaviour, such as residual plasticity (known as plasticity-induced crack closure), oxidation near crack tip (Oxide-induced crack closure) [81] and roughness of the fracture surfaces (roughness-induced

crack closure), et al.

2.5 Creep

2.5.1 Creep Curves

Creep is time and temperature dependent inelastic deformation under long-term exposure at constant stress or constant load for both single and polycrystalline solids. Unlike conventional plastic deformation, creep can happen when the load or stress is below the 0.2% proof stress.

For a material that sustains static loading at elevated temperatures, generally, there are three regions of plastic deformation in the creep curves [82] (Figure 2.12):

Primary creep region showing a rapid acceleration and then deceleration of creep rate with time;

Secondary creep region showing a constant creep rate, $\dot{\varepsilon}_{min}$, where the longest creep period occurs;

Tertiary creep region showing an accelerating creep rate until creep rupture.

In most materials, three stages of creep can be observed at a wide temperature and stress range. However, scientific works put emphases on the secondary creep region due to its stable characteristics.

2.5.2 Creep Mechanisms

2.5.2.1. Creep failure mechanisms

When a material is subjected to a tensile stress for a long time, time-dependent deformation and necking occurs, which may lead to ultimate failure. In a metallic material,

intergranular and transgranular failure modes can be observed. Intergranular creep deformation may happen on the grain boundaries in polycrystals, while transgranular mechanisms can occur within individual grains of polycrystalline material. When creep deformation occurs, one or both of these failure modes can be observed. The intergranular failure mechanism often occurs when stress levels are relatively low at high temperatures (above 0.3 - 0.5 of the melting point [83]). Whereas the transgranular creep mechanism is often observed under high stress levels and low temperatures. Previous observations of the fracture surface for 316H stainless steel show that the intergranular failure mode is the dominant mechanism in creep and creep crack growth tests at 550°C [84, 85].

2.5.2.2. Theoretical Creep Mechanisms Model

Since temperature and stress are important to creep deformation, the creep mechanisms can be classified according to temperature and stress conditions. So far, there is no generally accepted theoretical model that explains all creep mechanisms. Diffusional creep and dislocation creep are two generally accepted creep mechanisms that contribute to creep deformation at different stages [86].

Diffusional creep occurs under low stress levels. There are two types of diffusional creep depending on the applied temperature: Coble creep occurs under low stress and medium to high temperatures, where vacancies can move along grain boundaries; Nabarro-Herring creep occurs under low stress and higher temperatures, where vacancies can move through a crystal. Dislocation creep occurs when dislocations move. Due to the high sensitivity to differential stress on the material, dislocation creep is the dominant

creep mechanism under high stress levels.

Several works have reviewed the creep mechanisms in austenitic stainless steels [87-93]. According to the published work, the diffusional creep and dislocation creep contain in the primary and the secondary creep regions [94]. In the tertiary creep region, the dominant creep mechanism is grain boundary sliding [95-97].

In the steady creep region, the state of the material is dependent on the applied load and temperature. The deformation-mechanism map for 316 stainless steels is seen in Figure 2.13 [86]. Two mechanisms are shown in the secondary creep region: diffusional flow in the lower stress region, and power-law/dislocation creep in the higher stress region and higher temperature.

Figure 2.14 shows the creep zone changes during creep crack growth [98]. Figure 2.14a shows the small-scale creep condition, where the creep zone size is relatively smaller than the crack size and the remaining ligament. As the creep strains accumulate faster compared with the secondary creep, in this condition, the primary creep zone becomes dominant in the specimen. With the increase of creep time, the secondary creep zone expands in the primary creep zone (Figure 2.14b). Figure 2.14c shows the primary creep zone has extended to cover all the uncracked ligament and the secondary creep zone size is larger with creep time elapses. Figure 2.14d shows the secondary creep zone has reached the whole ligament and the extensive secondary creep condition is attained.

2.5.3 Minimum Creep Strain Rate

For the creep curves, the creep strain rates are the most fundamental features. Normally,

the minimum creep strain rate ($\dot{\varepsilon}_{min}$) is used to characterise the creep strain rate in the secondary creep region and it related to the applied stress, σ. The relationship can be expressed according to Norton's relationship, as shown below:

$$\dot{\varepsilon}_{min} = A\sigma^{n} \qquad \text{(Equation 2.20)}$$

where A and n are constants related to the material.

2.5.4 Application of Fracture Mechanics to Creep

The stress intensity factor, K is valid to describe crack growth in 'creep-brittle' conditions, where only small-scale yielding occurs at crack tip. However, if the creep zone dominates the elastic zone and there is a large amount of creep deformation leading to the stress redistribution at the crack tip, K is not applicable. In this state, the material becomes 'creep-ductile'. The C*-integral then is an appropriate approach for describing the stress and strain in the steady-state creep region. To identify whether K or C* is appropriate, the standard ASTM E 1457-15 [64] requires that C* should be used if:

$$\dot{V}_C/\dot{V} \geq 0.5 \qquad \text{(Equation 2.21)}$$

where $\dot{V}_C$ is the load-line displacement rate due to creep and $\dot{V}$ is the total load-line displacement rate showing the summation of creep, plastic and elastic components. When plane stress applied, the $\dot{V}_C$ can be defined as:

$$\dot{V}_C = \dot{V} - \frac{\dot{a}B_N}{P}\left(\frac{2K^2}{E}\right) \qquad \text{(Equation 2.19)}$$

where $\dot{a}$ is the creep crack growth rate, B_N is net section thickness for CT specimens, P is the load, K is the stress intensity factor and E is Young's modulus.

In order to use C* to correlate creep crack growth behaviour, the steady-state creep

damage and steady creep stress distribution should be attained ahead of a crack tip [99, 100]. A 'tail' part of the curve with a nose-like shape can be observed on C* versus da/dt curves. This tail part is defined as the incubation period [99-102] (Figure 2.15).

In 1980, Riedel and Rice proposed that austenitic stainless steels become creep ductile at 550 to 650°C [66]. Their tests results indicated that the creep crack growth rate is related to the C*-integral and the crack growth rate can be calculated from load-line displacement rate.

During steady-state creep, the data is found to fall on one narrow band for austenitic stainless steels in the creep crack growth resistance curve. This is the case even if there are variations in test conditions, such as temperature, material thermal history, minor differences in composition and specimen geometry [98, 103-106]. For example, in the creep crack growth tests of 316L stainless steel [107] using CT testpieces, circumferentially cracked round bars and double-edged notched tension specimens, the C* versus da/dt curves obtained at temperatures of 550, 575, 600 and 650°C all fall on one line, which can be applied as a creep crack growth resistance master curve for the material. Shibli and Le Mat Hamata [108] carried out creep crack growth tests on P22 low alloy steel cross weld CT testpieces at 550°C, and observed that the curves for testpieces with different microstructures almost overlapped.

In previous work conducted on the creep crack growth on 316 stainless steels, the crack tip morphology was observed in detail. It was suggested that the crack tip blunted after a very long incubation time without crack extension. However, it becomes sharper during

secondary creep [109]. In the incubation period, damage gradually formed at the crack tip, very small crack growth was detected [110], then a deceleration in creep crack growth rate with lower C* value. When steady creep is obtained, where $t > t_T$, a constant creep stress distribution is produced.

Numerous previous creep crack growth resistance curves of da/dt versus C* have shown a scattered behaviour in the early stage of crack growth [110-112]. It has been suggested the creep crack growth prior to the establishment of steady-state creep region is mainly influenced by the applied initial K value and the properties of the material. In ductile material, the creep crack growth rate during the primary and transition creep regions was found much lower than the extensive/steady-state creep region. This is mainly due to the cavities nucleated by the secondary phases in these regions [112]. During the incubation period, the creep damage extends throughout the remaining ligament. Therefore, Riedel and Rice suggested that C* is a valid driving force parameter in the whole creep crack growth region [66].

2.6 Dwell-fatigue

In engineering components operating at high temperatures, failure can not only happen under pure fatigue and pure creep conditions but can also occur due to creep and fatigue interactions. Creep-fatigue interactions can occur when dwells (hold periods) usually at maximum load are introduced into the cyclic loading.

A trapezoidal waveform is normally applied to the fatigue crack growth with dwell time in the peak load. During the dwell period of the fatigue cycle, plastic and creep

deformation can accumulate in front of the crack tip. Consequently, under one dwell-fatigue cycle, the material may sustain both fatigue and creep mechanisms. Dwell-fatigue loading can lead to the following changes in mechanisms:

i. The application of linear elastic fracture mechanisms may be limited;

ii. The fracture mode can change from transgranular to intergranular.

The insertion of hold periods either at constant strain or constant stress can result in creep damage. In austenitic stainless steels, severe damage is more likely to happen when a tensile dwell rather than a compressive dwell is applied. For example, in creep-fatigue crack growth tests conducted in cast Type 316 stainless steel at temperatures between 570 to 625°C under low cycle fatigue tests, when cavities were found at grain boundaries due to longer hold time in tension which reduced the cyclic life [113], Hale classified three possible failure mode for high temperature dwell-fatigue: transgranular, intergranular and inter/transgranular mixed modes (Figure 2.16) [114]. These indicate three failure modes: fatigue-induced failure, creep-induced failure and creep-fatigue mixed failure mode. Among these, the fracture mode owing to the mixture of creep and fatigue is the most severe fracture mode.

2.7 Mechanical Properties of Austenitic Stainless Steels

Owing to the excellent metallurgical stability and creep strength at high temperatures, a series of austenitic stainless steels have been selected as the candidate structural materials for the components in the nuclear power plant, i.e. Alloy 709, N709, high-temperature ultrafine-precipitation strengthened (HT-UPS) austenitic stainless steels, HR3C, alloy

800, type 310 stainless steel, type 347 stainless steel and 316H. Among these heat-resistant austenitic stainless steels, Alloy 709, HT-UPS and 316H have been selected as the prime candidates for SFR structural materials.

The type 347 stainless steel (17Cr-11Ni-2Mn-Nb-C) and type 310 stainless steel (25Cr-20Ni-1.6Mn-C) have been used as the structural material for the Gen II pressurized water reactors (PWRs) and boiling water reactors (BWRs) at ~350°C, owing to their high corrosion resistance, oxidation resistance and weldability. 316H stainless steel (Fe-10Ni-17Cr-1.5Mn-2Mo-Nb-C-N) is considered as a candidate for SFR structural materials, not only because of its outstanding oxidation resistance, weldability and low material cost but also owing to its better corrosion resistance to liquid sodium than type 310 and 347 stainless steel [115]. However, the creep strength for 316H is lower than NF709 and HT-UPS (Figure 2.17) [116].

The Alloy 800 (21Cr-32Ni-Mn-C) has been used for steam generator tubes in the PWRs and BWRs for its excellent corrosion resistance. However, the ultimate tensile strength and yield stress are lower than the other alloys [117].

The HR3C steel (25Cr-20Ni-1.2Mn-Nb-C-N) was developed as a modification of type 310 stainless steel, by adding Nb and N, to have better creep properties and oxidation resistance. These advantages make HR3C steel a promising candidate material for components in supercritical power plants with a steam temperature of greater than 650°C [118].

The HT-UPS alloys (14Cr-16Ni-2Mn-2.5Mo-V-Ti-Nb-C-B-P) were selected as the prime

candidates for the SFR structural applications due to their better creep properties and lower cost than NF709. However, a previous study reported that lower weldability compared to NF709 is a critical problem for HR3C and HT-UPS. This potential weldability issue is mainly related to hot cracking and heat-affected-zone (HAZ) liquation cracking at high temperatures [119].

The NF709 (20Cr-25Ni-Mn-1.5Mo-Nb-C-B-N) alloy was developed by Nippon Steel during the late 1980s and 1990s especially as a structural material in ultra-supercritical reactors [120] owing to its outstanding creep properties, oxidation resistance and good weldability.

The advanced austenitic stainless steel Alloy 709 is a derivative of NF709, but mainly designed for components in SFRs, such as, but not limited to, the reactor vessel, tubing and core support structures. The evaluation has been made according to the following criteria: creep properties, creep-fatigue resistance, sodium capability, weldability, tensile properties and thermal stability. The preliminary data shows that Alloy 709 is superior to HT-UPS and 316H austenitic stainless steel not only owing to its excellent tensile strength (TS) and weldability, but also the excellent resistance to high operating temperatures, creep-fatigue loading and corrosion environment (Figure 2.17) [116]. This is predominately due to precipitation hardening from the formation of fine $M_{23}C_6$ carbides and fine Z-phase at high temperatures, which hinder dislocation movement. The previous studies on mechanical properties and crack growth behaviour of alloy 709 and other candidates austenitic stainless steels are summarised in the following sections:

2.7.1 Tensile Properties of Alloy 709

Recently, a study of tensile property of Alloy 709 from room temperature to 800°C was conducted by Alomari et al. [121] The results indicate that serrated stress-strain curves were observed between 350 to 600°C at strain rates of 10^{-4}/s. This behaviour is known as dynamic strain ageing (DSA), which is due to the interactions between solute atoms and dislocations. Furthermore, in contrast to the detrimental effect of DSA, a clear increase in ductility was found, which was attributed to an increase in uniform elongation and work hardening rate in dynamic strain ageing. In-situ tensile tests carried out in Alloy 709 from RT to 950°C at a strain rate of 2.61×10^{-4}/min also reported a serrated stress-strain curve between 550 to 800°C [122].

2.7.2 Fatigue Crack Growth

The fatigue life of NF709 and 316H stainless steel at 700°C is shown in Figure 2.18 [123]. The NF709 has a similar fatigue performance to 316 stainless steel.

Several factors can affect the crack growth behaviour under cyclic loading, such as testing temperature and environment. Temperature influences the fatigue crack growth resistance mainly by affecting other factors, such as the mechanical properties (yield stress and elastic modulus) and environmental parameters (oxidation). Numerous studies on different materials have found that the fatigue crack growth rates accelerate with higher temperature in air. For example, it was reported that higher temperatures accelerate the fatigue crack growth rate in the mid-range of growth rates in SS 316LN at 27 to 559°C. This was attributed to a decrease of elastic modulus with higher temperature. [124].

However, in fatigue crack growth studies conducted by Sandananda [125] on Type 316 stainless steel tested in vacuum at 427 and 593°C, it was suggested that temperature had a negligible effect on fatigue crack growth. The effect of temperature was minimised in vacuum environment, due to the absence of the extrinsic factors in inert environments. Similar environmental attack on fatigue crack growth resistance at high temperatures was found in Type 316 stainless steel tested at 316, 427, 538 and 649°C by James et al [126] and crack growth in 18% Cr ferritic stainless steel at 500, 600 and 700°C [127].

Floreen and Raj [128] have listed some mechanisms which possibly clarify the environmental influences on high temperature fatigue crack growth. The formation of oxides has a detrimental effect on high temperature fatigue crack growth behaviour at intermediate ΔK levels in austenitic stainless steels. Under cyclic loading, the brittle oxide layer at the crack tip is easily broken. This allows oxygen penetration into the material. Oxygen can then react with the precipitates in the material, such as carbides, which leads to the decohesion of carbides from the matrix and results in the formation of brittle or weakly bonded metal oxides, which can initiate microvoids or microcracks and thus degrade the material leading to high temperature fatigue failure.

Fatigue crack growth tests carried out in Alloy 709 using CT testpieces have shown higher fatigue crack growth rates at 700 than at 600°C under 15 Hz sinusoidal waveform loading in air [129]. Deeper secondary cracks and more voids were seen in the high ΔK region at 700 than 600°C, which indicates more plastic deformation at higher temperature in air.

2.7.3 High Temperature Creep Crack Growth

It has been reported that the creep strength of Alloy 709 is superior to 316H at 700°C (Figure 2.19) [116]. The creep strength for Alloy 709 at 10,000 hours is ~100 MPa, but is only ~50 MPa for 316H.

In previous work, da/dt versus K curves were reported to show a worse correlation compared with C* in assessing creep crack growth behaviour in austenitic stainless steels [109, 130]. The changes in crack growth rate with K values under different test conditions indicate that K is not the exclusive crack tip parameter controlling the creep crack growth of austenitic stainless steel. As seen in Figure 2.20, for creep crack growth tests in 316 stainless steel with different sample sizes at 649°C, the da/dt versus K curve shows different geometries provide different correlations [109]. This is presumably because the K parameter is invalid for use in characterising the stress/strain field ahead of a crack tip in the presence of an extensive creep region. C* is a more appropriate parameter to correlate with creep crack growth resistance. Creep crack growth rates for many materials can be correlated to C* under different conditions of temperature, sample size, geometry, load and minor changes in microstructure. All fall on one narrow band, which can be used as a da/dt versus C* ‘‘master’’ curve for prediction of remaining creep life. For example, Figure 2.21 illustrates the creep crack growth rates correlation with C* on one line in a 1Cr-1/2 Mo steel despite different test temperatures (450, 550 and 600°C) [103].

equation 2.9 shows that for a constant load, geometry and crack length, any changes in load-line displacement rate will lead to a different C* value, thus corresponding to a different creep crack growth rate.

The load-line displacement rate also can be affected by changes in yield stress and Young's modulus (equation 2.5). Therefore, variations in the microstructure of material and other external tests conditions, such as temperature, can shift C* values on the master curve, thus giving different da/dt values.

2.7.3.1. Effects of Temperature

The crack opening displacement rates will be higher with higher test temperatures. Therefore, the C* will move to a higher point on the master curve. In 316 stainless steel higher C* values were found at 649 than 593°C to give higher crack growth values [109]. Fractography indicated that higher temperatures promote larger creep deformation under the same test conditions.

2.7.3.2. Effects of Microstructure

It has been found that the creep crack growth resistance curve for the material with minor changes in microstructure all fall on one narrow band [104]. This indicates that the crack growth rate correlation with C* is insensitive to minor changes in microstructure. However, materials with different creep resistance will give a different crack tip opening displacement rate under the same test condition, thus changing C* values.

For austenitic stainless steels with the same composition but different heat treatments, the formation of strengthening phases during ageing may increases the yield stress compared with the as-received material, thus promoting creep resistance. Therefore, the C* value may be lower than the as-received samples on the master curve.

For austenitic stainless steels, the most common strengthening secondary phases formed

during thermal ageing is fine discontinues $M_{23}C_6$ carbides, which normally nucleate at grain boundaries and nano-sized Z-phase, which are found on dislocations. These strengthening phases are able to obstruct the grain boundary sliding and dislocation movement, thus restraining the crack propagation [21, 131]. It was found that the creep mechanisms for testpieces with the as-received and thermally aged microstructures are all intergranular at the same test temperature under steady-state creep [132].

2.7.4 High Temperature Dwell-fatigue Crack Growth

2.7.4.1. Effect of Temperature

At low temperatures, dwell-fatigue crack growth is cycle-dependent which is controlled by the linear stress intensity factor range. With increasing test temperature, creep becomes more dominant and crack growth behaviour is more time dependent. Creep damage near the crack tip may cause accelerated crack growth rates. This is attributed to competition between faster creep strain accumulation and stress relaxation near the crack tip under a given stress. The creep-fatigue crack growth tests in Type 316 stainless steel after 20% cold work with both 1 min and 0.1 min tensile load at 427 and 593°C [133] indicated that at a given dwell time and ΔK, higher testing temperature promotes the acceleration in creep-fatigue crack growth rate.

2.7.4.2. Effect of Environment

Numerous studies have been carried out to study the influence of different environments on the dwell-fatigue crack growth behaviour of austenitic stainless steels at elevated temperatures. The environments included air, liquid sodium and water [134].

In cold-worked Type 316 stainless steels, it has been reported that dwell-fatigue crack growth rates in air and vacuum are almost the same at 593°C with a dwell period of 1 minute, in low and medium stress intensity factor range regions [125]. This implies almost all of the time dependent contribution during hold loading is from creep rather than environment. At high stress intensity factor region, the change in creep resistance influences dwell-fatigue crack growth rate.

The crack growth rates in vacuum were found slower compared with it in air, and the difference in crack growth rate becomes smaller at larger ΔK levels in dwell-fatigue crack growth in both annealed and cold-worked Type 316 austenitic stainless steel [125]. This is because at high ΔK regions, the crack behaviour is mainly influenced by dwell time rather than the environment.

2.7.4.3. Effect of Hold Time

Dwell-fatigue crack growth tests were carried out in Alloy 709 with 60 and 600 s tensile holding at 600 and 700°C in air [129]. There was a negligible effect of 60 s holding on pure fatigue crack growth resistance at the temperature investigated. However, there were clear changes in fatigue crack growth rates when increasing the dwell time to 600 s. However, under these hold times, the fracture failure modes were all transgranular. Recently, the creep-fatigue behaviour of Alloy 709 was reported by Porter et al. [135, 136]. They proposed that for 30 minutes of tensile hold, the failure mechanisms at 550 and 650°C were intergranular.

The creep-fatigue crack growth tests for annealed 304 and 316 stainless steels were

conducted at 593°C. It was found 6 and 60s tensile hold can accelerate the fatigue crack growth rate (Figure 2.22) [137]. However, for Alloy 709 tested at the same condition, the 6 and 60 s tensile hold have no influence on baseline cyclic loading.

A similar observation was found in the creep-fatigue crack growth test in casts of Type 316 stainless steel at temperatures between 570 to 625°C under low cycle fatigue [113]. Their results showed that the intergranular cracking is more obvious when the tensile hold increases. Consequently, the fatigue life is reduced.

2.7.4.4. Effect of Dwell-fatigue Interactions

It has been documented that tensile holding increases the crack growth rate at elevated temperature in 316 stainless steel [138] by promoting voids to nucleate at grain boundaries. The failure mechanism changes from transgranular to intergranular failure. Results also show lower fatigue crack growth rates in subsequent pure fatigue crack growth. Gao, et al. [139] conducted creep-fatigue crack growth tests on Type 316 stainless steel at 550°C. They proposed that tensile holding dramatically decreases creep-fatigue crack growth resistance of the material. This reduction was due to the early crack growth and intergranular damage caused by local creep strains, oxidation, precipitation and the coalescence of surface microcracks.

2.8 Previous Work on Alloy 709

Microstructural evolution has been investigated for the as-received and aged NF709 (Fe-20Cr-25Ni) by Sourmail [26]. Static ageing treatment was conducted at 750 and 800°C for 200, 2500, 5000 and 10000 hours. After exposure for 200 hours at 750°C, $M_{23}C_6$ was

found on grain boundaries and Z-phase was observed on dislocations. As the ageing time increased, Cr_3Ni_2SiN was observed. Also, more rod-like Z-phase were found on dislocations at both temperatures.

Alloy 709 has a similar composition to NF709, although the thermo-mechanical processing parameters for these two materials are not exactly the same. For Alloy 709, a detailed microstructure evolution during ageing was reported in a parallel programme [21]. TEM characterisation was performed on both as-received and aged samples to study ageing influences of microstructure and mechanical properties. In this study, Alloy 709 was aged at 550, 650 and 750°C for 500, 1000 and 2000 hours. In as-received material, the predominant secondary phase is Nb(CN), with only a few Z-phase particles observed. Ageing at 550°C for up to 2000 hours did not promote the precipitation of new phases. After ageing at 650°C, $M_{23}C_6$ were found precipitated on grain boundaries, twin boundaries, in the grain interior and on Nb(CN). Nano-sized Z-phase particles were observed on dislocations after ageing at 650°C for 500 hours. After ageing at 650°C for 1000 hours, θ phase $(Cr, Mo)_3(Ni, Fe)_2SiN$ was formed at grain boundaries. More and denser secondary phases were observed at 750°C. Also, θ phase is more stable than $M_{23}C_6$, since some $M_{23}C_6$ phases were found transfer to θ phase at 750°C. The results indicate that Alloy 709 is relatively stable at 550°C even after exposure for a long time, which is a desirable characteristic for the structural material for an SFR. However, long term exposure at higher temperatures promotes the precipitation of grain boundary carbides ($M_{23}C_6$), which may have a detrimental effect on creep resistance. The brittle

$M_{23}C_6$ may not accommodate deformation under fatigue, creep and dwell-fatigue loads. Hence fractured grain boundary $M_{23}C_6$ can promote crack initiation and propagation. Nano-sized Z-phase formed on dislocations can impede the dislocation movement, which has a beneficial effect on the creep properties of Alloy 709.

Porter et al. [140] reported their work on the precipitation evolution of Alloy 709 during static ageing, low cycle fatigue and creep-fatigue testing. The as-received Alloy 709 was aged at 550, 650 and 750°C for 1 to 2500 hours at 650°C. Also, low cycle fatigue and creep-fatigue tests (with 30 minutes hold) were conducted at 550 and 650°C using as-received testpieces. After the tests, microstructure analysis was carried out on the static aged sample, fractured fatigue testpieces, fractured creep-fatigue testpieces, as well as interrupted creep-fatigue testpieces. They found that the precipitate formation under static ageing is different to that under fatigue and creep-fatigue testing. Finer and denser precipitates formed under fatigue loading than static ageing conditions under similar times and temperatures. Fine cuboidal carbides were observed on dislocations during cyclic loading, which have an obvious strengthening effect on Alloy 709. They also concluded that a lower strain-hardening rate is associate with the formation of carbides and nitrides, which decreases creep-fatigue resistance by reducing the solution strengthening effect.

After comparing the low cycle fatigue life, creep-fatigue life and deformation mechanisms of Alloy 709 at 550 and 650°C [136], Porter's group concluded that a reduction in creep-fatigue life was observed compared to low cycle fatigue life at both

temperatures. A more obvious reduction was found at 550 than 650°C. This is owing to more continuous grain boundary phases formed under 30 minutes of tensile holding at 550°C, which act as void nucleation sites and promote intergranular cracking.

For the tensile properties and deformation mechanisms of Alloy 709 at different temperatures, Rabiei's group [122] conducted tensile tests in both in-situ SEM and air. The in-situ SEM tensile tests were carried out at temperatures ranging from room temperature up to 950°C, and tensile tests were conducted in air at 550, 650 and 750°C. They reported that the results in air agree well with the results in the in-situ SEM at the same testing temperatures. Moreover, the stress-strain curves show serrations at temperatures between 550 to 800 °C. These serrations are formed because of the interaction between the moving dislocations and solute atoms. The grain boundary void formation and coalescence were observed at all high temperatures. Also, plastic deformation accommodated by slip band formation was found at 550 and 650°C.

Rabiei's group also conducted creep-fatigue crack growth tests of Alloy 709 in an in-situ SEM under 1 second, 1 minute and 1 hour dwell times at 750°C [141]. They found that short dwell times (1 second and 1 minute at peak load) promote transgranular cracking, while intergranular cracking and cavitation formation dominate with longer dwell times (1 hour at peak load). Fracture surface analysis confirmed that slip bands promote transgranular cracking, whereas microvoid coalescence assists the intergranular crack propagation.

CHAPTER 3 Experimental Techniques and Methodology

3.1 Material Characteristics

3.1.1 Chemical Composition

Alloy 709 material used in the current study was supplied by Oak Ridge National Laboratory, US and produced by Carpenter Technology Corporation in the form of a rolled plate. The material was firstly manufactured by vacuum-induction melting (VIM) and electro-slag remelting (ESR) processes. Subsequently, the material was hot forged and rolled into plates. Finally, the rolled plates were water quenched after annealing at 1100°C in the air. Three batches of material were supplied. The microstructure for one batch of the material plate numbered 011593-1-B is outside specification microstructure. This was used for machining some of the fatigue crack growth testpieces. The other batches of material numbered 011502-H6 and 011594-1, consist of a uniform, equiaxed grain structure, they were mainly used for the rest of the mechanical tests.

As the conventional 316H has similar tensile properties and grain structure with Alloy 709, hence it was selected for such purpose. The 316H (UNS S31609) stainless steel studied was acquired from SIJ Acroni Steel. The Alloy was solution annealed at a minimum of 1052°C and water quenched. Nominal chemical compositions of Alloy 709 and 316H are listed in Table 3.1.

3.1.2 Thermal Ageing

To examine the microstructure of Alloy 709 and 316H used in the current research, small blocks of materials were cut from the plates provided before machining into testpieces.

In order to characterise the microstructure of Alloy 709 under different heat exposure conditions, the material was cut into $5 \times 5 \times 5$ mm cubic pieces, then they were encapsulated in glass filled with argon and thermal aged at 550, 650 and 750°C for 500, 1000 and 2000 hours. 550°C is the operating temperature, which is the most important. Due to 2000 hours being a relatively short time for use in practice, 650 and 750°C, which are higher than the working temperature were used to evaluate the microstructure changes under harsher conditions.

To study the influences of thermal ageing on mechanical properties and crack growth behaviours of Alloy 709, the as-received material was aged at 650°C for 2000 hours. The overaged material was machined into compact tension and cylindrical testpieces for crack growth tests and tensile tests. The specifics of the experimental methods used are listed below.

3.1.3 Metallographic Examination

Metallographic samples for both Alloy 709 and 316H were prepared according to the following steps:

i. Cutting and mounting: the specimens were cut with an Al_2O_3 cutting disc, and they were mounted into conductive Bakelite at elevated temperature;

ii. Polishing: Firstly, the wet SiC grinding papers of grit size 120, 240, 400, 800, 1200, 2500 and 4000 were applied in sequence for grounding. Then the sectioned sample was transferred to cloth polishing discs, and polished using diamond suspensions in the order of 6, 3, and 0.04 μm;

iii. Electrochemical etching: the polished samples were electrochemically etched with 10% oxalic acid (10 g oxalic acid crystals dissolved in 90 ml deionized water) at ~6 volts at room temperature;

iv. Metallographic examination: A Keyence VHX-6000 optical microscope was applied to image the grain structures. The average grain size for Alloy 709 was characterised and quantified using an Oxford Instruments Nordlys EBSD detector with step size of 1 μm. To investigate the precipitates, both a high-resolution scanning electron microscope (SEM) and a transmission electron microscope (TEM) were used. Energy dispersive X-ray spectroscopy (EDX) and diffraction patterns were used to identify the types of precipitates. Thin foils, 3 mm in diameter for TEM examination were electropolished using a solution of 10% perchloric acid + 30% 2n-ethoxy-butanol + 60% ethanol, using a twin-jet electro-polisher at 25 volts. TEM characterisation was performed on a Talos 2000F microscope, 200 kV was applied, which is equipped with a Silicon Drift Detector (SDD) for EDX study.

It should be noted here that the as-received material was cut from three directions, L: Longitudinal; T: Long transverse; ST: short transverse.

3.2 Mechanical Testing

3.2.1 Tensile Tests

To have a better understanding of tensile properties of both the as-received and overaged Alloy 709, tensile testpieces were machined according to the drawing shown in Figure

3.1. All tensile tests were carried out in air. The testpieces were loaded onto a Zwick screw driven tensile testing machine equipped with an electric furnace, see Figure 3.2. Test temperatures of room temperature, 550, 650 to 750°C were used. Temperature was controlled by an N-type thermocouple touching the central part of the sample. The nominal initial strain rate was 1×10^{-4}/s, which was applied using a constant ramp rate. The temperature was kept within the range of $\pm$ 2°C and the sample was soaked at the test temperature for 30 minutes before testing. The extension of the gauge length was monitored by a linear variable displacement transducer (LVDT). Loads cell in the range of 0~10 kN. Real-time load-displacement signals were monitored by a computer-controlled data acquisition system. According to the standard [142], the engineering stress-strain curves were achieved.

To understand fracture mechanisms, longitudinal metallographic sections were analysed using SEM.

3.2.2 Creep Tests

In this project, all creep tests were performed by Swansea Materials Research & Testing Ltd. Creep tests were conducted to investigate the creep exponent value required for C* calculations in the creep crack growth tests. Creep tests were carried out at elevated temperature with cylindrical samples, see Figure 3.3. An extensometer was applied to measure the strain, which was mounted on the shoulders of the testpiece. The creep data provided by the Oak Ridge National Lab were for 650 and 750°C, but not for 550°C. Thus, only one test was conducted at 650 and 750°C to validate the existing results for

Alloy 709. Three tests were carried out at 550°C. Due to the periods required for creep tests of Alloy 709, some long tests were interrupted after the minimum creep rate had been reached but before the test piece ruptured. Table 3.2 summarises the conditions for creep tests of Alloy 709.

3.2.3 Fatigue Crack Growth Tests

Fatigue crack growth tests were conducted in both air and vacuum on compact tension CT specimens, see Figures 3.4a - c. The specimens were machined from two batches of materials as described in section 3.1.1. The orientations for the testpieces were in the L-T and ST-L direction, see Figure 3.4d. For some testpieces, 0.5 and 1 mm depth side grooves were machined on both sides of the testpiece in order to regulate the crack shape and study the influence of depth of side-groove on fatigue crack growth resistance (Table 3.3).

CT specimens were first fatigue precracked at RT using an Amsler vibrophore machine with a frequency ~50 Hz and an R ratio of 0.1. After precracking, the crack length was normally ~1 mm and the final ΔK value was ~15 MPa$\sqrt{m}$. For air tests, the CT specimens were transferred to an Intron 8501 screw driven machine (Figures 3.5a and b) with a load cell of 100 kN, which is suitable for the load in this study (8 kN). The testing temperatures used were 550, 650 and 750°C. An ESH servo-hydraulic mechanical test machine equipped with a vacuum chamber was used for the vacuum tests, see Figures 3.5c and d. The heat was provided by four quartz-halogen lamps which are fitted inside the chamber. During the vacuum tests, the vacuum level of ~1.5×10^{-5} mbar was achieved in the

chamber. An N-type thermocouple was attached to the sample for monitoring the testing temperature. All tests followed ASTM E 647-15e1 [143]. The test matrix is listed in Table 3.3. Stress ratios used in the tests were 0.1 and 0.5. A 0.25 Hz sinusoidal load waveform was applied to all the tests. A direct current potential drop (d.c.p.d.) measurement method was adopted to detect crack extension. This study mainly focuses on stress intensity ranges from ~20 to ~40 MPa√m, which is within the Paris regime. After the tests, the furnace was switched off and the testpieces were cooled down to room temperature then taken out from the furnace and broken open. A Keyence VHX-6000 optical microscope was used for the measurement of the initial and final crack lengths. Those measured crack lengths were used for calibrating the d.c.p.d data, using an in-house calibration equation. ΔK and ΔK_n (for the side-grooved testpieces) values, were calculated by equations shown below [143]:

$$\Delta K = \frac{\Delta P}{B\sqrt{W}} \frac{2+\alpha}{(1-\alpha)^{1.5}} (0.886 + 4.64\alpha - 13.32\alpha^2 + 14.72\alpha^3 - 5.6\alpha^4)$$

(Equation 3.1)

$$\Delta K_n = \Delta K \sqrt{\frac{B}{B_n}}$$

(Equation 3.2)

where α = a/W (a is the crack length, W is the width of the test piece), ΔP is the load range, B and B_n are the thickness and net specimen thickness of the testpiece.

Fractography was conducted under SEM to identify fatigue crack growth mechanisms.

3.2.4 Creep Crack Growth Tests

To investigate the creep crack growth behaviour of the as-received, aged Alloy 709 and

316H at high temperatures, the methodology of crack extension with the increase of K under static load was applied to this study. Tests were carried out according to standard ASTM E 1457-15 [64]. The test matrix is listed in Table 3.4. A standard compact tension geometry of compact tension CT was used: width (W) is 26 mm and the thickness (B) is 13 mm. On both sides of the specimen, 1 mm depth side-grooves were machined to regulate the crack shape, see Figures 3.6a and b. Along the load line, two knife edges were machines to mount an extensometer, see Figure 3.6c. Note the orientation for the testpieces are all L-T and they are all machined from optimised microstructure material. For all the standard CT testpieces, the initial notch depth is 9.1 mm which corresponds to a/W ~0.35. Before the high temperature creep crack growth test, the testpiece was precracked using an Amsler Vibrophore machine at room temperature with a ~50 Hz fatigue to generate a ~1 mm crack length to eliminate the influence of the notch. After precracking, the a/W value reached ~0.4. Creep crack growth tests were conducted on a Zwick screw-driving servo-electric testing machine, with a load cell of 10 kN, which is suitable for the 8 kN static load used in this study, see Figure 3.7. Similar to fatigue crack growth tests, a direct current potential drop (d.c.p.d) technique was applied to monitor the crack length. A high temperature resistant clip-on gauge was mounted onto the two knife edges of the CT sample to record the load-line displacement rate for C* calculation.

Note that one creep crack growth test was also conducted on the testpiece with W is 50 mm, B is 20 mm and B_n is 18 mm (referred to as '2-inch', numbered 'A2-1') at 650°C to study the geometry influences on crack growth resistance of the material.

After the test, the sample was cross-sectioned by EDM perpendicular to the fracture surface. To clarify the failure mechanisms, one part which was not fully opened was polished for microstructural characterisation around the crack tip; the other part was fatigued open at room temperature for crack length measurement and fracture surface characterisation. As only one half of the fracture surface was used, the crack length measurement may not be quite as accurate compared with the complete fracture surface. However, the crack shapes were found to be symmetrical, therefore the crack length measurements seem to be consistent with those measured on complete fracture surfaces. The fracture surfaces were analysed under a Keyence VHX-6000 optical microscope for crack length measurement. An in-house polynomial calibration equation was used to convert d.c.p.d readings to crack lengths. Then the corresponding K and its C* can be calculated. ΔK, ΔK_n and C* value can be calculated using equations 3.1, 3.2 and 2.9.

After creep crack growth testing, fracture surfaces were characterised using SEM to give a detailed understanding of crack growth mechanisms.

3.2.5 Dwell-fatigue Crack Growth Tests

Dwell-fatigue crack growth tests were performed on CT testpieces of the as-received Alloy 709 and 316H, all machined from the desired uniform microstructure. Tests were carried out according to standard ASTM E 2760-10 [144].The test matrix is listed in Table 3.5. All testpieces have an L-T direction. The geometry for the CT samples was similar to what used in fatigue crack growth tests. The width and thickness of the test pieces are ~26 and 13 mm (Figures 3.4a and b). A d.c.p.d method was applied to monitor the real-

time crack length.

The testing procedure for dwell-fatigue crack growth tests is shown in Figure 3.8. Before the high temperature dwell-fatigue crack growth test, the sample was precracked with the same conditions as fatigue crack growth testpieces, as described in section 3.2.3. After precracking, the testpiece was transferred to a Zwick screw-driven servo-electric machine for crack growth testing, see Figure 3.7.

A trapezoidal dwell-fatigue waveform, see Figure 3.9, was applied to dwell-fatigue crack growth rests. The loading and unloading times were kept the same, all 1 second, the hold time at peak load of 60 minutes. After the unloading to the minimum load, there was a one-second hold at minimum load. '1-3600-1-1' is used to represent this kind of dwell-fatigue waveform in this thesis. Due to the long period of time required for the tests, the waveform was changed to 0.25 Hz sinusoidal to prolong the crack length. The dwell form was introduced again afterwards. This was repeated 3 to 4 times in every test. A stress ratio of 0.1 was used for all the dwell-fatigue loading. Note that the maximum load during both 1-3600-1-1 dwell-fatigue loading and 0.25 Hz fatigue loading was kept constant at 8 kN throughout the test.

After a given amount of crack extension under 0.25 Hz cyclic loading, 1-3600-1-1 dwell-fatigue loading was reapplied again. Since the applied load was kept constant, the ΔK value in the 2^{nd} dwell - fatigue crack growth becomes higher. Such a switch between 1-3600-1-1 dwell fatigue loading block and 0.25Hz fatigue loading block were repeated 2 to 3 times in each testpiece to cover a large range of crack driving force. The 0.25 Hz

sinusoidal cyclic loading segments in between the 1-3600-1-1 dwell cycles can also act as baseline therefore comparisons can be made with pure fatigue crack growth behaviour. The final loading section is all 0.25 Hz fatigue loading at high temperature, until the crack depth reached an a/W ~0.7. After the final high temperature fatigue crack growth, the furnace was switched off, after cooling down to room temperature, the testpiece was broken into two halves using a fatigue loading. The actual crack lengths were measured under an optical microscope for calibration. The stress intensity factor range, ΔK, is calculated using equation 3.1.

In order to investigate the temperature influences on dwell-fatigue crack growth behaviour, tests were conducted in air at 550, 650 and 750°C. To investigate the environmental influences on dwell-fatigue crack growth behaviour, a test was conducted in vacuum, but only at 650°C. The testing conditions were kept the same as with what applied in air.

A Keyence VHX-6000 optical microscope and an SEM was applied for fracture surface analysation to understand the crack growth mechanisms. To further verify mechanisms, one half of the fractured testpiece was cross-sectioned perpendicular to the fracture surface for the observation of subsurface damages along the path of crack propagation using both SEM and Electron Backscatter Diffraction (EBSD).

CHAPTER 4 Results

4.1 Microstructure of Alloy 709

4.1.1 As-received Alloy 709 and Its Comparison with 316H

Three metallographic sections on different orientations of the Alloy 709 plate with optimised microstructure are shown in Figure 4.1a. Out of three sections, i.e. with their normal axis of longitudinal (L), long transverse (T) and short transverse (ST), two sections show a banding appearance. Samples for metallographic and texture analysis were conducted on the section normal to the rolling direction, later referred to as 'ST-L'. Figures 4.1b - c show higher magnification optical images. At higher magnifications, banding is less visible and it can be seen that it consists of equiaxed grains. Hence the banding is associated with the distributions of both coarse and fine particles. The microstructure of the out of specification Alloy 709 plate shows more severe banding, as shown in Figures 4.1d - e. For this plate, the bands of coarse and fine grains are also observed. Testpieces machined from this plate are primarily used to explore the influence of extreme microstructure and orientation (L-T and ST-L) on fatigue crack growth behaviour.

Figures 4.2a and b show optical micrographs of 316H. Similar equiaxed austenite grains were also observed as well as a comparable grain size with optimised Alloy 709. However, cleaner micrographs indicate fewer strengthening precipitates possibly formed in 316H than as-received Alloy 709.

In order to evaluate the grain size and confirm the nature of banding in the as-received

Alloy 709 with an optimised microstructure, EBSD mapping was conducted. A grain orientation map of single γ phase (matrix) is shown in Figure 4.3. Note that the grains were detected using grain detection angle of 5°. Overall around 1000 grains are detected with an average grain size of 45 μm. Figure 4.3 suggests that the grains are in random colour, implying insignificant texture. Also, it confirms that the grains are equiaxed.

In order to have a better understanding of the banded structures within optimised as-received Alloy 709, more detailed characterisations have been conducted. As shown in Figures 4.4a - b, strings of particles parallel to the rolling surface, typically of size from 1 to 10 μm, are the most apparent feature of the bands (Figure 4.4a). They appear as white blocky precipitates in the SEM images taken under the backscattered mode. EDX analysis of those particles confirmed that they are Nb-rich carbonitrides, i.e. Nb(CN), see Figure 4.4c. They probably formed during the casting process, and are referred to as primary Nb(CN).

As can be seen in Figures 4.1b - c, Alloy 709 appears to have dispersed fine precipitates within the matrix. TEM characterisation of various size scales of precipitates was completed in a parallel programme [21]. The results are summarised here. It was observed that the fine secondary phases are also Nb carbonitrides but with a size varying from 50 to 400 nm. They are distributed reasonably uniformly within the austenite grains. Unlike the larger primary Nb carbonitrides, they formed during cooling after annealing. A small number of rod-shaped Z-phases (CrNbN) are also found in the as-received Alloy 709 (see Figure 4.5). In addition, few dislocations were observed. A summary of all phases

observed is given in Table 4.1.

4.1.2 Microstructure of the Aged Alloy 709

The microstructural characterisation was conducted for the Alloy 709 after ageing at 550, 650 and 750°C for 500, 1000 and 2000 hours respectively. Table 4.1 summarises the secondary phases observed for the individual ageing conditions. The following sections report the observations in detail.

4.1.2.1. Ageing at 550°C

SEM images for samples after ageing at 550°C for 500, 1000 and 2000 hours are shown with two magnifications (800× and 1500×) in Figure 4.6. After checking the grain boundaries and grain interiors for samples aged for all three durations at 550°C, there is no visible change on precipitate formation even after the longest ageing time (2000 hours). According to the published TEM results, 550°C thermal exposure only encourages the segregation of Cr and Mo at grain boundaries [21]. This indicates that Alloy 709 is considerably stable around 550°C, which is the aimed service temperature.

4.1.2.2. Ageing at 650°C

SEM images for samples after ageing at 650°C for 500, 1000 and 2000 hours are shown with two magnifications (800× and 1500×) in Figure 4.7. It can now be seen from SEM images in Figures 4.7a and d that precipitates begin to form at both grain boundaries and in the grain interior after 500 hours. TEM observations confirmed most precipitates are $M_{23}C_6$ carbides (Figures 4.8a - c) [21]. They have different morphologies, globular at grain boundaries and plate-like in the grain interior, some cuboidal $M_{23}C_6$ carbides were

formed around Nb(CN) precipitates. Meanwhile, nano-sized Z-phases were found on dislocations very occasionally [21], see Figures 4.8d and e.

After ageing for 1000 hours, with increased ageing time, denser and coarser precipitates were confirmed both inside grain and on the grain boundaries compared with those aged for 500 hours (compared Figures 4.7b and e with Figures 4.7a and d). In addition, TEM analysis confirmed that Si-rich θ phases start to form on grain boundaries [21]. Furthermore, more Z-phases are promoted on grain dislocations [21].

As shown in Figures 4.7c and f, after the material aged for 2000 hours, even more perfused precipitates on grain boundaries and in the grain interior were found without form new phases [21]. Note that this overaged condition was selected to conduct further mechanical testing, i.e. tensile and crack growth resistances under fatigue and creep conditions.

4.1.2.3. Ageing at 750°C

Figures 4.9a and d show the coarsening of particles on grain boundaries (arrowed in Figure 4.9d) after aged at 750°C for 500 hours. TEM results also confirmed the existence of coarse $M_{23}C_6$ and Si-containing phases [21]. Furthermore, Z-phases were also found on dislocations [21].

When increased the ageing time to 1000 hours, more and coarser secondary phases were formed (compared Figures 4.9b and e with Figures 4.9a and d). TEM analysis revealed $M_{23}C_6$ carbides can transfer to θ phases [21]. This suggests that θ phases are more stable than $M_{23}C_6$ at 750°C [21].

Figures 4.9c and f show no obvious changes in microstructure characterisations after further ageing for 2000 hours which is also confirmed by TEM [21].

4.2 Mechanical Testing Results

4.2.1 Tensile Tests in the As-received and Aged Alloy 709

4.2.1.1. Tensile Properties

The measured values of 0.2% proof stress (PS), tensile strength (TS), fracture strain (ε_f) and area reduction (A.R.) and engineering stress-strain curves for the as-received and aged material are shown in Table 4.2 and Figure 4.10.

From the above results, true stress and true strain within the uniform deformation region (up to reaching a plateau in an engineering stress-strain curve) can be obtained by:

$$\sigma_T = \sigma(1 + \varepsilon) \quad \text{(Equation 4.1)}$$

$$\varepsilon_T = \ln(1 + \varepsilon) \quad \text{(Equation 4.2)}$$

where σ_T is the true stress, ε_T is the true strain.

For many alloys and metal, the relationship between true stress-strain curve within the uniform plastic deformation (from ε_T =0.2% to tensile strength) can be expressed according to Hollomon's law:

$$\sigma_T = K\varepsilon_T^n \quad \text{(Equation 4.3)}$$

where n is the strain hardening exponent, K is the strength coefficient. In order to determine the value of n, the true stress-strain curves were plotted in log-log axes up to maximum tensile strength:

$$\log(\sigma_T)=\log(k) + n \log(\varepsilon_T) \quad \text{(Equation 4.4)}$$

Strain hardening exponent, n, which represents how the material behaves when it been formed. The material with a higher n value has better formability than the one with a low n value [145]. The n value is the slope of linear part of $\log(\varepsilon_T)$ - $\log(\sigma_T)$ curve. Table 4.3 listed the average of the strain hardening exponent (n) values for all testpieces.

The fracture stress, σ_f, was also calculated at the point of fracture according to the following relationship:

$$\sigma_f = \frac{F_f}{A_f} = \frac{\sigma_{failure}}{1 - A.R} \qquad \text{(Equation 4.5)}$$

Where $\sigma_{failure}$, F_f and A_f are the stress, force and area at the failure point in the engineering stress-strain curve, A.R is area reduction. Further values of true tensile strength and strain, fracture stress, strain hardening exponent, and the corresponding strain interval are listed in Table 4.3.

From these results the influences of temperature and ageing on tensile properties of the investigated material can be clarified, and are described below:

- **0.2% proof stress**

The 0.2% proof stress for the as-received Alloy 709 is ~300 MPa at RT. With test temperature increased to 550°C, it was measured to reduce to ~170 MPa, it then remained relatively unchanged with further increase of temperature to 750°C. When testing under similar conditions (temperature and strain rate), the 0.2% proof stress for the aged sample is always higher than the as-received material, see Figure 4.11.

- **Tensile strength**

As shown in Figure 4.11, in the as-received condition, the tensile strength reduces with

higher temperature. As a result, the tensile strength at 750°C has roughly halved the value at RT. When tested at high temperatures, the tensile strength of the aged material is generally lower than that of the as-received material, however, it demonstrates the same trend with temperature.

- **Fracture stress**

It is also clear that the fracture stress decreases with higher temperature for both the as-received and aged Alloy 709 (Table 4.3). After ageing, there is a clear reduction in fracture stress at RT and 550°C, the higher fracture stresses were observed at 650 and 750°C compared with the as-received material.

- **Ductility**

As listed in Table 4.2, excellent ductility is observed at all temperatures. The lowest elongation was measured to be 38 and 31% for the as-received and overaged conditions respectively (both at 650°C). The highest elongation was measured to be 49 and 42% for the as-received and overaged conditions, respectively, at 750°C. There is a general reduction in ductility for the overaged material, however, the trend is similar, see Figure 4.11.

- **Strain-hardening exponent**

The strain-hardening exponent, n, was also influenced by temperature and ageing. According to Table 4.3, the strain hardening n values decrease with higher temperatures for both the as-received and aged conditions, except the n value for the as-received condition at 550°C (0.40), which is the highest n value among all the test conditions (even

higher than RT). This indicates the highest strain hardening ability after elastic-plastic transition was found in the as-received material at 550°C. This may result from the dynamic strain ageing effect. This average n value at 550°C is ~1.57 times higher than the average n value at 750°C (0.26), which shows the lowest work hardening. Thermal ageing decreases the strain hardening ability compared with the as-received material at all temperature range from RT to 750°C. According to the published work on the deformation microstructure and tensile properties of Alloy 709 [131], this decreasing in n values after ageing is mainly due to the formation of brittle grain boundary $M_{23}C_6$ precipitates, which cannot accommodate the high stress leads to the cracking of particles and the formation of microcracks in-between the precipitates and matrix, therefore, decrease the strain hardening ability.

4.2.1.2. Fractography and Failure Mechanism

The optical images of the fractured as-received and aged tensile testpieces are shown in Figure 4.12. To further investigate the failure mechanisms in Alloy 709, the fracture surfaces, as well as their metallographic sections (along sample longitudinal axis) were carefully examined under SEM for testpieces in both conditions. A summary of fractographic and metallographic results of the as-received testpieces tested at different elevated temperatures is shown in Figure 4.13. In general, two zones were observed, the inner zone, where the crack initiated and an outer shear-lip zone which fails last. Such inner and outer fracture zone can be clearly seen for the samples tested at RT and 750°C, giving a typical ‘cup and cone’ appearance (Figures 4.13a and d), also accompanied with

obvious necking (Figure 4.13a). The inner fracture zone becomes less obvious for the samples tested at 550 and 650°C, especially the 550°C one. Note that insignificant necking occurred at these two temperatures. These results are coincident with BSE images of the metallographic-sectioned testpieces (Figures 4.13i - l). All the fracture surfaces show a ductile failure mode with coarse and fine dimples. It is noted that dimples become bigger and deeper with high temperatures of 650 and 750°C. It appears that the dimples are the finest at 550°C. A close-up of the arrowed region in Figure 4.13f is shown in Figure 4.14a. At this magnification numerous clearly defined dimples were observed on the fracture surface. They are deduced to have nucleated at the primary Nb(CN) (arrowed in Figure 4.14a, and as shown in Figure 4.14b), whereas fine dimples nucleate at fine Nb(CN). These are also to be the case with samples tested at all other temperatures. The metallographic sections (Figures 4.13i-l) show the formation of voids close to the fracture location, associated with the ones nucleated from the primary carbides. There appear to be more voids in testpieces at higher temperatures, except the testpiece at 550°C, in which the least of void formation is seen.

To gain a better understanding of ageing effects on ductility and fracture mode of Alloy 709, the fracture surface and metallographic sections for the aged tensile samples were also characterised in detail, see Figure 4.15. Unlike the as-received testpieces, numerous secondary cracks were found in the aged testpieces at room temperature, see Figure 4.15e. After checking the longitudinal metallographic section of the fractured sample at room temperature, see Figure 4.16a, it can be confirmed that those secondary cracks are likely

to associate with intergranular cracking. As shown in Figure 4.16b, this intergranular failure is mainly due to the linkage of grain boundary carbides formed during thermal exposure at 650°C for 2000 hours. It can be seen from Figure 4.16c that voids were still found on the fracture surface, but shallower compared with the as-received testpieces at room temperature, compared with Figure 4.13e. This leads to a ~11 % reduction of elongation after ageing (37 %) compared with the as-received sample at 550°C (48 %), see Figure 4.10. With an increase of testing temperature, more deformation occurred around carbides, which leads to fewer secondary cracks, see Figure 4.15f. As shown in Figures 4.15c and d, more 'necking' was found on the aged sample tested at 650 and 750°C.

4.2.2 High Temperature Fatigue Crack Growth in the As-received Alloy 709

4.2.2.1. Fatigue Crack Growth Resistance

A complete test matrix for this part of the work is listed in Table 4.4. In Figures 4.17 - 4.24, fatigue crack growth resistance, da/dN versus ΔK, curves are plotted with different sets of data in order to better demonstrate the influences of various factors, i.e. side-grooves, orientation, R ratio, temperature and environment.

- **Effect of Side-groove Depth**

Figure 4.17 shows the fatigue crack growth resistance curves for testpieces with 0, 0.5 and 1 mm side-groove. Note that an empirical function shown below was used to account for the influence of side-groove on stress intensity factor.

$$\Delta K_n = \Delta K \sqrt{\frac{B}{B_n}} \qquad \text{(Equation 4.6)}$$

where ΔK_n is the stress intensity factor range for the side-grooved testpieces, B and B_n are the thickness and net specimen thickness of the testpiece.

The three curves almost completely overlap with each other within the Paris region. This indicates that side-groove depth has no influences on fatigue crack growth behaviour within the Paris regime, within ΔK value of 14 to 28 MPa√m. However, the differences can be seen in the static fracture region, where ΔK >28 (K_{max} >56) MPa√m. These imply that equation 4.6 can be successfully used for the calculation of stress intensity factor of the side-grooved testpieces for studying fatigue crack growth behaviour. However, it might lead to scatters in creep crack growth, dwell-fatigue crack growth tests, when presenting crack growth data using K as the driving force.

- **Effect of Crack Plane Orientation**

Figure 4.18 shows a comparison of fatigue crack growth resistance curves for testpieces with different orientations (L-T and ST-L) tested in air at 650°C. L-T orientation in a rolled plate (crack plane is normal to the rolling direction, and crack growth direction is parallel to the transverse direction, see Figure 3.4d) is usually the 'strongest' orientation, while the ST-L (with crack plane normal to the short transverse direction, and crack growth direction parallel to the longitudinal direction, see Figure 3.4d) is the 'weakest' orientation. Figure 4.18 shows the fatigue crack growth resistance curve of the two orientations overlaps throughout the entire ΔK range tested. This suggests that microstructure differences in distributions of large and/or fine carbides have no influence

on fatigue crack growth resistance of the as-received Alloy 709.

- **Effect of Stress Ratio (R Ratio)**

The fatigue crack growth resistance curves with different R ratios (0.1 and 0.5) tested in air at 650°C are plotted in Figure 4.19. Faster crack growth rates are seen for the R ratio of 0.5 at both lower and higher ΔK regions, with similar crack growth rates measured at intermediate ΔK regions. When compared under a given ΔK value, the faster crack growth rates with R ratio of 0.5 at ΔK values (>30 MPa√m) is associated with high K_{max} values, which promote static fracture mode, whereas the faster fatigue crack growth rates observed at low ΔK region are likely to be associated with lesser amount of crack closure hence larger effective mechanical driving forces at higher R ratio of 0.5. These observations are common for fatigue crack growth in ductile materials [146, 147].

- **Effect of Environment**

Figures 4.20 - 4.22 show comparisons of the fatigue crack growth resistance curves (L-T orientation, R=0.1) tested in air and vacuum at three different temperatures (550, 650 and 750°C respectively). It can be observed that the crack growth rates in air are generally consistently larger than those in vacuum at all three temperatures at any given ΔK values. The differences in da/dN are more pronounced in the lower ΔK region, and the differences in da/dN are reduced gradually with the increase of ΔK, and diminish when ΔK >50 MPa√m. These lead to larger A and smaller m value in the Paris equation compared to those of the vacuum tests, see Table 4.4.

It is noticeable that the gap between the air and vacuum tests becomes larger with the

increase of temperature. For example, at ΔK ~20 MPa√m, the crack growth rate in air is roughly twice that in vacuum at 550°C, while this difference increases to four times at 750°C.

In order to understand the effects of environment on fatigue crack growth behaviour, the curves in Figures 4.20 - 4.22 were rearranged in Figures 4.23 and 4.24 to show vacuum and air data separately. It can be seen from Figure 4.23 that there are small variations in fatigue crack growth resistance in vacuum among three testing temperatures. Again, these differences become diminished when ΔK >30 MPa√m. For the tests carried out in air, as shown in Figure 4.24, there is a clear dependence on test temperature with the highest temperature (750°C) demonstrating the poorest crack growth resistance. Again, the largest variations in fatigue crack growth rate occur at lower ΔK values. These indicate that the faster crack growth rates seen at higher test temperatures are largely related to air environment.

4.2.2.2. Fractography

Optical images of the representative broken testpieces after testing are shown in Figure 4.25. As can be seen from these images, the high temperature fatigue section (the region between room temperature precracking and final fracture broken, as shown between the dotted line in Figure 4.25) is rather flat and smooth. The fracture surface becomes rougher towards the end of the fatigue crack growth region and the roughness increases with higher test temperature. It is clearly seen, for the 750°C test, that there is a severe matrix deformation (reduction in thickness) towards the end of crack growth region, compared

with 650°C (compared Figure 4.25h with Figures 4.25c - f).

SEM fractographs were taken at mid-thickness of each fractured testpiece at different stress intensity factor, ΔK, values of ~ 22, 30, 45 and above 50 MPa√m. The SEM images are presented at both low (500×) and high (1500×) magnifications in Figures 4.26 - 4.33. Low magnification fractographs give an overview of the fracture surfaces, high magnifications show the details of fracture surface morphology. As shown in Figures 4.26 to 4.31, the striated crack growth mechanism dominates the fatigue crack growth tests at low and medium ΔK regimes (ΔK of ~20 to 45 MPa√m), regardless of the difference in testing temperature, side-groove depth and orientation. The striations on the fracture surfaces for air testpieces are more distinct than those tested in vacuum, compared in Figures 4.29a and b. When it comes to a high ΔK region (ΔK $>$50 MPa√m), for testpieces tested in air and vacuum at 550°C, as shown in Figures 4.33a and b, striated transgranular crack growth still dominates the fracture mechanism. However, for the testpieces tested at 650 and 750°C, as shown in Figures 4.32c - d and e - f, the ductile microvoid coalescence is the main failure mechanism.

As shown in Figures 4.27d and 4.31d, it is interesting to note that in tests carried out in vacuum at 650°C, where ΔK of ~20 and 45 MPa√m, there are two kinds of parallel spacing that can be observed. The average spacing of the coarse lines in Figure 4.27d is about 1 μm, which is approximately eight times the measured crack growth rate (1.2×10^{-4} mm/cycle). The fine lines (0.48 μm) in Figure 4.27d seem to be closer to the crack growth rates in the test. As shown in Figure 4.31d, when crack driving force value

increases to ~ 45 MPa√m, the average spacing of the coarse lines is 2.2 μm. This agrees with the measured crack growth rate (1.7×10^{-3} mm/cycle).

4.2.3 High Temperature Creep in the As-received Alloy 709

The representative creep strain versus elapse time curves at temperatures of 550, 650 and 750°C are shown in Figure 4.34. The stress used in the test carried out at 750°C was only 120 MPa, but this led to very fast strain accumulation after creep loading and a rupture life of 505 hours. In contrast, the stress for the 650°C creep test is more than twice the stress used at 750°C, i.e. ~250 MPa, but the creep rupture life is much longer (886 hours). For creep test at 550°C, when under a stress of 450 MPa, which is more than two times of the yield stress at this temperature (173 MPa), a rupture life of 1266 hours was obtained, which is ~2.5 times of the rupture time measured at 750°C under a stress of 120 MPa. Clearly creep occurs faster at higher temperatures and higher applied loads. The dependence of steady-state creep rate (minimum creep rate), $\dot{\varepsilon}$, on stress, σ, at a given temperature was described by Norton creep law:

$$\dot{\varepsilon} = A\sigma^n \qquad \text{(Equation 4.7)}$$

In order to obtain the power law exponent, n, creep tests were conducted at various stresses to measure the associated minimum creep rates. The test results are provided in Table 4.5. Note that most of the test results were provided by Oak Ridge National Laboratory, a small number of tests were organised within the current project and conducted at Swansea University. In Figure 4.35, the applied stress versus minimum creep rate are replotted under log-log scale, the creep exponent, n, is determined as the

slope of linear regression of the individual curves at the individual temperatures:

$$\log(\dot{\varepsilon}_{min}) = \log(A) + n\log(\sigma) \qquad \text{(Equation 4.8)}$$

The creep exponent values (n) are measured to be 8.4, 6.0 and 5.3 for 550°C, 650°C and 750°C respectively. Those values are later used for calculating, C* values, the creep crack growth driving force parameter.

Figure 4.36 shows optical macrographs of the side view and fracture surface for creep testpieces that had been tested to failure at 550, 650 and 750°C. Figure 4.36c and d show the creep testpieces at 650 and 750°C have a 'cup-and-corn' shape (also demonstrating 'necking' on the side view). Almost no necking was found in the testpiece tested at 550°C, all the plastic deformation occurred in a uniform form at this temperature.

SEM micrographs for the creep testpieces tested to failure are given in Figures 4.37 - 4.39. Figure 4.37 shows that dominated ductile fracture mode with numerous microvoids at 550°C, although isolated areas of intergranular cracking were observed in Figure 4.37c. It should be noted that this sample was tested at a stress ~2.6 times of the yield stress and the total fracture strain is 25 % (~10 % creep strain), which is significantly smaller than the fracture strain obtained in the tensile test under the same temperature, i.e. 45 %. Compared to the tensile test, the material appears more "brittle" under creep condition. As shown in Figures 4.38b - c and 4.39b - c, the failure mode in the centre of both the 650 and 750°C samples was ductile microvoid coalescence. At the edge, for both the 650 and 750°C, see Figure 4.38d - e and Figures 4.39d - e, the fracture surface is relatively flat, with shallower and smaller voids compared with the area in the middle. Clearer shear

lips are now observed on the testpieces at 650 and 750°C. The failure modes observed here are generally similar to those of the tensile tests, perhaps appear more “ductile” than those of the tensile tests. The total fracture strain of those two creep tests are 55 and 67% (predominantly creep strain), which are significantly higher than the fracture strain of the tensile tests, i.e. 38 and 49% respectively (Table 4.2).

To investigate the fracture modes for testpieces tested at 650 and 750°C, metallographic sections cut perpendicular to the loading direction were analysed under SEM and the BSE images are provided in Figures 4.40 and 4.41. It should be noted here that the narrower area for the cross-section sample at 750°C is due to the cut not being in the middle of the testpiece. Areas close and away to the fracture surface were analysed. As can be seen from Figures 4.40c and 4.41c that the voids near the fracture surface can be seen to be due to particle cracking. These particles are similar in appearance to the Nb(CN) particles, seen in the microstructure of this material, see Figure 4.4b. However, some microvoids were found at grain boundaries in the area away from the fracture surface, see Figures 4.40e and g and Figures 4.41e, g and h. This indicates that intergranular cracking occurred at the early stage of creep damage. It is also interesting to note that even in the area near the fracture surface, see Figure 4.41b, there are still some grain boundary microvoids formed. This indicates that intergranular cracking formed when ‘necking’ occurred.

4.2.4 High Temperature Creep Crack Growth in Alloy 709 and 316H

In this study, crack growth results are represented by crack growth rate versus C* relationships. After removing the data during the first 0.2 mm crack extension, the results

of all tests, including that of a 316H (high carbon content) austenitic stainless steel, are shown in Figure 4.42. An elastic-plastic fracture mechanic, the C*-integral, is applied to characterise crack growth rates under the static load. As the applied load was kept constant at all temperatures for most of the tests, i.e. 8 kN, and the testpiece geometry was also kept the same, the creep crack growth resistance curves are also plotted against stress intensity factor, K, for the convenience of comparison (Figure 4.43).

Under the fixed applied loading, the influence of temperature on crack growth rate can be easily recognised in the da/dt vs. K plot (Figure 4.43), faster crack growth rates are seen at higher temperatures for the as-received Alloy 709, compared under any given K values. It can also be seen that creep crack growth resistance of the aged Alloy 709 is similar to that of as-received Alloy 709, and 316H has poor resistance compared to Alloy 709, compared at a single temperature of 650°C and under any given K values. All the crack growth resistance curves, however, seem to follow the same straight line (under log-log scale axes) in the da/dt vs C* plot.

The creep crack growth results including the crack extension, the duration and transition time of creep crack growth of Alloy 709 tested at 550, 650 and 750°C and 316H tested at 650°C are listed in Table 4.6. Note that the initial crack length after fatigue precracking for each testpiece was similar.

4.2.4.1. Creep Crack Growth at 550°C in the As-received Alloy 709

The optical image in Figure 4.44a shows the testpiece at 550°C (sample numbered ‘CS1’), the crack growth under static load can be seen as darker bands, labelled ‘CCG’. The test

was interrupted by cyclic fatigue loading (lighter and flatter regions, labelled 'FCG') and divided into four individual creep crack growth regions, labelled as 1st, 2nd, 3rd and 4th CCG. The crack growth regions with a fatigue loading were labelled as 1st to 5th FCG accordingly. Such a segmental testing procedure was applied to define the criteria for crack growth, as well as saving the test time. As listed in Table 4.6, for sample numbered 'CS1', no more than 100 μm crack extension was found during the 1st and 2nd CCG testing which lasted for ~40 days, then 0.25 Hz sine waveform fatigue were applied to propagate the crack further, after a certain crack extension under cyclic loading, 8 kN static loading was switched back. With a longer crack, the net section stresses increased. Continuous crack growth had only been obtained within the 4th CCG region. In order to understand the relationship between creep crack growth and load-line displacement, records of crack length, crack extension (Δa) and load-line displacement, load-line displacement rate and associated crack growth rate and are plotted against time, see Figure 4.45.

Note that the crack extension during the first three creep crack growth segments are limited (Figure 4.45a), crack extension was found primarily at the onset of each static holding period, after the initial growth, the crack growth become arrested with continuous static holding for the 1st and 2nd CCG, but growing at an extremely slow rate in the 3rd CCG region. Only in the 4th CCG region, an increase in crack extension and load-line displacement were detected (Figures 4.45b - c)

The trend of load-line displacement rate versus time curves (Figure 4.45d) is similar at the initial parts of all four crack growth regions: relatively high load-line displacement

rates which is followed by deceleration and reaching a plateau after ~100 hours. Different behaviours are seen after reaching a plateau, the load-line displacement rate was found to maintain or even reduce for the 1st to 3rd CCG, only found to increase for the 4th CCG, which associated with an observation of continuous acceleration of crack growth (Figure 4.45e).

4.2.4.2. Creep Crack Growth at 650°C in the As-received Alloy 709

To have a better prediction of the creep crack growth behaviour at operating temperature (550°C) for longer service time, creep crack growth tests were also conducted at 650 and 750°C to accelerate the crack growth.

Optical fractographs of the tests conducted at 650°C are shown in Figures 4.44b - c (sample numbered 'CS4' and 'A1-3'). Different to the fracture surface at 550°C, there was only one creep crack growth segment introduced for 650°C testpieces, the same 8 kN static load was applied. The curves for crack length, crack growth resistance, load-line displacement and displacement rate with time of sample CS4 are shown in Figure 4.46. As can be seen clearly in Figure 4.46b that again load-line displacement rate shows three phases of an initial deceleration, plateau at ~600 hours and then eventually acceleration. Interestingly, this trend corresponding to three phases of crack growth of slight deceleration, reaching a minimum and turning to acceleration (Figure 4.46c).

4.2.4.3. Creep Crack Growth at 650°C in the Aged Alloy 709

Optical fractography of the creep crack growth tested on an aged Alloy 709, 'HT1' (tested at 650°C), is seen in Figure 4.44d. The plots of crack length, crack growth rate, load-line

displacement and load-line displacement rate versus time for this sample are shown in Figure 4.47. Note that the sudden change at around ~4000 hours corresponds to increasing the applied load from 8 kN to 10 kN. Due to the limited amount of crack growth under 8 kN over long period of time ~170 days, 10 kN was applied mainly to accelerate the creep crack growth rate. Figures 4.47c - d show a similar trend between crack growth rate and load-line displacement rate plotted against time was found compared with the as-received testpieces (compared Figures 4.47c-d with Figures 4.46b - c). As shown in Figure 4.47d, there is a first deceleration and then acceleration behaviour found in load-line displacement rate versus time curve under both 8 and 10 kN condition, which correspond to deceleration and acceleration of crack growth in Figure 4.47c.

4.2.4.4. Creep Crack Growth at 750°C in the As-received Alloy 709

Optical fractography of the test conducted at 750°C is shown in Figure 4.44f. Similar to 650°C, only one creep crack growth segment was applied. Similar trends were found in the plots of crack length, da/dt, load-line displacement and load-line displacement rate, see Figure 4.48, with a minimum load-line displacement rate corresponding to a minimum crack growth rate. It is noticed that the initial deceleration is rather insignificant and quicker at 750°C, ~27 hours. The overall crack growth rate is significantly faster with a 4.13 mm of crack growth occurred in ~6 days (under the same applied load as those used for tests at 550 and 650°C, i.e. 8 kN).

4.2.4.5. Fractography

An overview of the fracture surface for the as-received Alloy 709 (numbered ‘CS1’)

tested at 550°C is shown with an optical image and a low magnification SEM image in Figure 4.49, detailed SEM fractographs for the four individual crack growth segments are shown in Figure 4.50. The red arrows in Figures 4.49a and b, indicate the four creep crack growth areas described above in section 4.2.4.1. In the first CCG region (Figures 4.50a and b), there is almost no crack growth occurring, apart from some isolated intergranular areas and secondary cracks. Between the transgranular fracture surfaces (result from fast cycling) there is a small band of intergranular failure for the second CCG, the crack extension now is a slightly deeper and appeared more continuous than the first CCG (Figures 4.50c and d, note the difference in magnification between Figures 4.50a and 4.50c). Also, secondary cracking is more pronounced. There is even more crack extension found in the third CCG (Figure 4.50e and f). An almost continuous severe secondary crack and a larger region of intergranular failure can be seen. It is believed that bifurcation of crack has occurred, with the intergranular surface showing one branch of bifurcated crack, the other appears as secondary crack.

The fourth CCG is shown in Figures 4.50g and h, the largest and accelerating crack growth, also in intergranular mode, is seen in this region. Two segments of deep secondary cracks were again found at the beginning of CCG after fatigue resharpening (Figure 4.49a), which is similar to that found in the third CCG region.

The fracture mechanisms at 550°C (numbered 'CS1') were confirmed on the side view of the 2nd CCG (K value of ~40 MPa√m), see Figure 4.51. The areas near crack surface were analysed, see Figure 4.51b. Figure 4.51c showing the intergranular damage in the

2nd CCG at 550°C is mainly associated with linkage of grain boundary microvoids (red arrow in Figure 4.51c) and wedge cracking formed at triple junctions (white arrow in Figure 4.51c).

Fractography for the as-received Alloy 709 tested at 650°C (numbered 'CS4') is shown in Figures 4.52 - 4.53. There is only one creep crack growth segment on the fracture surface, see Figures 4.52a and b. Figure 4.53 illustrates the fracture surface morphology at the beginning, middle and end of the crack growth region (pointed out in Figure 4.52b). At the beginning of the creep crack growth, the deformation appears directional at the fatigue crack front, becoming more homogenous with the extension of the crack. The intergranular grains are sharper at the beginning, turning to round shape with the increase of the crack length, see Figures 4.53a and d. The failure mechanism becomes more ductile with increasing crack length and K, the intergranular mode is replaced with microvoids, see Figures 4.53e and f.

Different to that observed at 550°C, the secondary cracks seen here are shorter and more evenly distributed, indicating less severe bifurcation occurred at 650°C for the as-received Alloy 709 (compare Figure 4.52a with 4.49a).

Optical and SEM fractography for the aged Alloy 709 tested at 650°C are shown in Figures 4.54 - 4.55 (sample ID: HT1). Despite similar crack growth resistance indicated by Figure 4.43, the fracture surface morphology appears different. On the aged Alloy 709, it appears in a ductile fracture mode throughout without a clear sign of intergranular cracking, see Figure 4.55. It should be noted here that there is load change during this one

segment of crack extension. There is 0.61 mm crack extension within 8 kN applied load, followed by the subsequent 0.53 mm crack extension under 10 kN, which is applied to force crack growth. Similar ductile fracture is seen as in the earlier crack growth, compare Figures 4.55b, c and d. Although not showing here, similar ductile failure mode was found for another test on the aged Alloy 709 (numbered 'HT2').

Optical and SEM fractography for the as-received Alloy 709 tested at 750°C is shown in Figures 4.56 and 4.57, a complete ductile fracture mode was seen throughout together with narrowing of the sample thickness. There is no clear sign of intergranular fracture (Figure 4.57).

4.2.4.6. Creep Crack Growth in 316H Stainless Steel at 650°C

Optical images for 316H numbered 'S2 and S3' are shown in Figure 4.58. The representative optical image and SEM fractographs for testpiece '316H S2' are shown in Figures 4.59 and 4.60. As can be seen clearly in Figure 4.60 that the fracture surface for 316H is markedly different to Alloy 709, intergranular failure with a clear definition now dominates the majority of the area, secondary cracking can still be seen but not as significant as those seen in Alloy 709 at the same temperature, compare Figure 4.59b with Figure 4.52b.

4.2.5 High Temperature Dwell-fatigue Crack Growth in Alloy 709

As adopt in creep crack growth resistance tests, dwell-fatigue waveform was introduced as several discontinuous blocks with baseline fatigue loading applied in-between. The total number of dwell cycles, the crack increment and ΔK range for each dwell-fatigue

block can be found in Table 4.7. Note that the maximum load used here was kept constant for all tests at three temperatures at 8 kN, which was the case for the fatigue crack growth tests, and most of creep crack growth tests mentioned earlier. The stress ratio used is 0.1 which is the same as in the fatigue crack growth resistance tests. The dwell-fatigue crack growth resistance versus stress intensity factor range curves obtained at 550, 650 and 750°C in air are shown in Figures 4.61 - 4.63. Note that one tests were conducted in vacuum, the result (sample 'A1-10') is also included in Figure 4.62.

It can be seen that at all three temperatures, 1-3600-1-1 dwell loading increases fatigue crack growth rates and this effect is greater at higher temperatures. To elaborate, at 550°C (Figure 4.61) and at a ΔK value of ~35 MPa$\sqrt{m}$, the dwell fatigue crack growth rate is 2.1×10^{-3} mm/cycle, which is ~2 times larger than the baseline fatigue crack growth rate (1.1×10^{-3} mm/cycle). With the increase of test temperature to 650°C (Figure 4.62), at the same ΔK value of ~35 MPa$\sqrt{m}$, the dwell-fatigue crack growth rate is ~2.0×10^{-3} mm/cycle for 'A1-1' and 2.0×10^{-2} mm/cycle for 'A1-8', which are ~2 - 10 times faster than the crack growth rate under pure cyclic loading (1.3×10^{-3} mm/cycle). Figure 4.63 shows the dwell-fatigue crack growth resistance curve measured at 750°C (sample numbered 'S5'), at a ΔK value of ~35 MPa$\sqrt{m}$, the dwell-fatigue crack growth rate is 8.0×10^{-2} mm/cycle, which is over one order of magnitude above the baseline fatigue crack growth rate (1.5×10^{-3} mm/cycle).

Despite the trend of increased crack growth rate seen at higher temperatures, it should be emphasised that the crack growth behaviour is different at different temperatures.

An immediate acceleration followed by deceleration then steady acceleration with the increase of ΔK is generally found after switching from fatigue loading to dwell fatigue loading. However, no acceleration after initial deceleration was found in the 1st and the 2nd dwell-fatigue crack growth regions for both tests carried out at 550°C, where ΔK <40 MPa√m, see Figure 4.61. This was also the case for the 1st dwell-fatigue loading at 650°C (sample 'A1-1' and 'A1-8'), with ΔK <30 MPa√m, see Figures 4.62. Another extreme is insignificant deceleration (almost only acceleration) found at 750°C in all dwell-fatigue loading blocks, ΔK >20 MPa√m, see Figure 4.63.

After each dwell-fatigue period when the waveform was changed back to baseline 0.25 Hz, fatigue crack growth rates were found to be below the baseline values expected. With higher ΔK, the crack growth rates gradually returned to the expected baseline levels. As can be seen from Figure 4.62, in vacuum (sample 'A1-10'), dwell-fatigue loading also increases the crack growth rate above baseline fatigue crack growth rates and the increase appears to be even greater than that seen in air at higher ΔK levels.

4.2.5.1. Fractography

Optical fractographs of the as-received Alloy 709 testpieces after dwell-fatigue crack growth testing at 550, 650 and 750°C are shown in Figure 4.64. The dark bands on the fracture surfaces are the 1-hour dwell-fatigue crack growth regions, also indicated on the images. It is obvious that the fracture surfaces under dwell-fatigue loading appear rougher and contain secondary cracks. It should be noted that in the case of the 1st dwell-fatigue loading block in testpieces 'A1-1' and 'A1-10', which were tested in air and vacuum at

650°C, the colour contrast of the bands to the surrounding fatigue crack growth regions, as well as the total crack extension are small, see Figures 4.64c and e. Compared with testpieces tested at 650 and 750°C, testpieces tested at 550°C show less lateral deformation and less non-uniform crack growth through thickness (crack tunnelling). The amount of lateral deformation and tunnelling effect was found to be more severe at higher test temperatures.

SEM Fractography

Under 0.25 Hz fatigue loading, a similar flat and smooth striated transgranular failure mode was found for all temperatures in Alloy 709 which are provided in section 4.2.2.2 and will not be mentioned here.

Tests at 550°C

Representative SEM fractographs for the as-received Alloy 709 tested in air at 550°C (sample 'A1-11') are shown in Figures 4.65 - 4.67. Figure 4.65 was taken at a ΔK value of ~20 MPa√m. The dwell-fatigue region shows a transgranular morphology, see Figure 4.65a. Under higher magnifications, fatigue striations can be clearly observed, examples of striations from the beginning and end of the dwell region are shown in Figures 4.65b and c, from which a spacing of 0.42 and 0.16 μm can be measured. Those values agree well with the test result obtained d.c.p.d. method which yielded crack growth rate of 4.0×10^{-4} and 1.4×10^{-4} mm/cycle at the initial and towards the end of the dwell-fatigue region. Both suggest a deceleration in crack growth in this dwell-fatigue region (ΔK value of ~20 MPa√m).

Figure 4.66 shows the fractographs taken within the second dwell-fatigue region of sample A1-11 With a starting ΔK >35 MPa √ m. Figure 4.66a shows an overview of the region which appears to be intergranular, some secondary cracks are present. Figures 4.66b - d illustrate the fracture surface morphology at the beginning, central and end area of dwell-fatigue crack growth regions (outlined in Figure 4.66a). Figure 4.66b shows that at the onset of the dwell-fatigue region, the fracture surface shows some transgranular crack growth with almost continuous fatigue striations (roughly parallel to the fatigue crack front). There is a stretch zone, which separates the baseline fatigue crack growth and dwell-fatigue crack growth region, the spacing in the dwell-fatigue region is similar but slightly larger than the baseline region. Figures 4.66c and d were taken from the middle and end regions of dwell-fatigue, showing both intergranular crack growth and striations. No obvious microvoids were found on the fracture surface, see Figure 4.66a.

With further increase of ΔK >50 MPa√m (third dwell-fatigue region), the surface appears to contain a mixture of striated transgranular crack growing, intergranular, secondary cracking and some signs of ductile fracture, see Figures 4.67b and c.

To confirm the amount of matrix deformation occurred at 550°C, an EBSD mapping was conducted on the metallographic sections perpendicular to the fracture surface, the results are shown in Figure 4.68. The EBSD mapping located in the second dwell-fatigue region of sample 'A1-11', where ΔK value of ~35 MPa√m. The inverse pole figure map shows no subgrain formation (Figure 4.68c). The misorientation map suggests that no obvious matrix deformation occurred in the 2nd CCG region and high misorientation is observed

near grain boundaries, see Figure 4.68d.

Tests at 650°C

The representative SEM fractography for dwell-fatigue crack growth of the as-received Alloy 709 tested in air at 650°C (sample 'A1-1') is seen in Figures 4.69 - 4.71. The fracture surface shows transgranular failure mode within the first dwell-fatigue region (ΔK ~20 MPa√m), which is similar to what found at this low ΔK value at 550°C (sample 'A1-11'), compare Figure 4.69a with Figure 4.65a.

Figure 4.70 was taken within the 2nd dwell fatigue region at a starting ΔK >35 MPa√m, the whole region appears to be intergranular with presence of many secondary cracks. Figures 4.70b - g illustrate detailed fracture surface morphology at higher magnifications for the beginning, middle and end of the crack growth region. Similar intergranular morphology is observed for the three areas although the grain edges are getting smoothened towards the end of the region, suggesting increased amount of local and matrix deformation.

A region of ductile failure was observed at ΔK value >50 MPa√m (the 3rd dwell fatigue region), as shown in Figure 4.71. The fracture surface shows deeper secondary cracks. Ductile fracture dominates with the observation of coarse and fine microvoids within the entire region of crack growth, as shown in Figure 4.71a.

An EBSD mapping was conducted in the 2nd and 3rd dwell-fatigue regions of sample 'A 1-1', where ΔK ~35 and 50 MPa√m, see Figures 4.72 and 4.73. In the second dwell-fatigue region, the EBSD banding contrast map shows the existence of grain boundary

voids (Figure 4.72b). The inverse pole figure map indicates no subgrain formation (Figure 4.72c). High misorientation is observed near grain boundaries implies the matrix deformation occurred in the 2nd CCG at 650°C, see Figure 4.72d. In the third dwell-fatigue region, Figure 4.73d shows higher misorientation concentrates near grain boundaries, which indicate severe matrix deformation and subgrain formation when ΔK value of ~50 MPa√m.

SEM fractographs for the as-received Alloy 709 tested in vacuum at 650°C ('A1-10') are shown in Figures 4.74 - 4.76. Figure 4.74 was taken at a ΔK value of ~20 MPa√m. The dwell-fatigue region shows isolated intergranular facets, arrowed in Figure 4.74b, which is different to the tests at 550 and 650°C in air at this ΔK value (compare with Figures 4.65a and 4.69a).

More substantial intergranular failure appeared with ΔK >30 MPa√m (2nd dwell), this is accompanied by a deep secondary crack at the beginning of the region (Figure 4.75a). No grain boundary voids were found, see Figure 4.75b.

Figures 4.76 was fractographs taken at a starting ΔK >50 MPa√m (3rd dwell). The region appears to contain both intergranular, ductile failure modes and some secondary cracks. At the beginning of the dwell-fatigue region, the fracture surface shows predominantly intergranular failure. A deep secondary crack and some regions of striated transgranular cracking were also found. Figure 4.76c, which is from the middle of this dwell-fatigue region, clearly shows that the failure mode is intergranular with microvoids decorating the grain boundaries. As can be seen in Figure 4.76d, at the end of dwell-fatigue region,

the fracture surface shows a ductile failure mode. Some microvoids and the grain structure deformation were found.

Test at 750°C

Figures 4.77 - 4.79 show the SEM fractographs from dwell-fatigue crack growth of the as-received Alloy 709 tested in air at 750°C (sample 'S5'). A ductile failure and severe deformations are observed throughout, the severity of deformation increases with the increase of ΔK. Note that secondary cracks are spread across all three regions of dwell-fatigue growth.

4.2.5.2. Dwell-fatigue Crack Growth in 316H at 650°C

In Figure 4.80, the dwell-fatigue crack growth resistance curve obtained for 316H at 650°C in air is compared with that of Alloy 709 obtained at 650 and 750°C. It is obvious that the dwell-fatigue crack growth resistance is poorer in 316H as equivalent resistance is found in Alloy 709 within an increase of 100°C, i.e.750°C. Similar observation is also made from creep crack growth tests, see Figure 4.43. This suggests the difference between 316H and Alloy 709 come from creep crack growth resistance, rather than fatigue crack growth resistance which is confirmed from the comparison of the crack growth resistance curves segments in the baseline fatigue crack growth regions.

An optical macrograph of the fracture surface of 316H tested at 650°C ('316H S4') is shown in Figure 4.81. Similar to Alloy 709 testpieces, the dwell-fatigue regions appear rougher and darker. There is a more severe lateral deformation occurred in 316H compared to that of Alloy 709 at the same temperature, compare with Figure 4.64c

(sample ‘A1-1’). A tunnelling effect can be observed in every dwell segment in 316H. For Alloy 709 testpieces tested in air at 650°C, the tunnelling effect was seen only when $\Delta K > 45$ MPa$\sqrt{m}$ (Figure 4.64c).

SEM fractographs of 316H testpiece are shown in Figures 4.82 - 4.84. Figure 4.82 was taken at a starting $\Delta K > 20$ MPa$\sqrt{m}$. The fracture surface shows intergranular failure mode with some secondary cracking.

When $\Delta K > 35$ MPa$\sqrt{m}$, as can be seen in Figure 4.83, the fracture surface shows a ductile failure mode with numerous secondary cracks and microvoids. More and fuller developed microvoids were observed with the increase of crack length, see Figures 4.83b and c.

Figure 4.84 shows a ductile failure mode when $\Delta K > 50$ MPa$\sqrt{m}$, shear fracture and dimples can be observed, which is similar to Alloy 709 at 750°C (sample ‘S5’), compare with Figure 4.79.

In order to have a better comparison between 316H and Alloy 709 under dwell-fatigue loading at similar test conditions. A montage of BSE images and an EBSD mapping was conducted in the second dwell-fatigue region of ‘316H S4’ testpiece (where $\Delta K \sim 35$ MPa$\sqrt{m}$, tested at 650°C), see Figure 4.85. The inset in Figure 4.85a shows the formation of grain boundary voids and the formation of subgrains, which can be proved by the results in the inverse pole figure map (Figure 4.85b) and the misorientation profile shown in Figure 4.85c.

CHAPTER 5 Discussion

5.1 Fatigue Crack Growth of the As-received Alloy 709

5.1.1 The Validity of ΔK

It is known that stress intensity factor range (ΔK) is a unique fracture mechanics parameter to correlate crack growth under cyclic loading conditions when small-scale yielding condition is fulfilled. For Alloy 709, as shown in Table 4.2, the 0.2% proof stress is ~170 MPa at high temperatures, therefore, even at low ΔK levels (ΔK ~20 MPa√m) a large plastic zone, which exceeds 1 mm in radius, exists (calculated according to equation 2.17). It is therefore questionable, whether ΔK is still a ‘‘valid’’ parameter to investigate the fatigue crack growth behaviour in Alloy 709. Published works have already applied ΔK in describing the fatigue crack growth mechanisms and correlating the data from small - scale yielding to large-scale yielding in 316L stainless steel [148]. It has been suggested ΔK remains an appropriate parameter as long as the isotropic hardening of the material is large. Therefore, in this work, ΔK is used to characterise the fatigue crack growth resistance of Alloy 709.

As described in Chapter 2, for austenitic stainless steels, both intrinsic (i.e. yield stress, Young’s modulus) and extrinsic factors (i.e. test temperature, oxygen and corrosive environment) may influence the high temperature fatigue crack growth behaviour. This section concentrates on discussing the effects of side-groove depth, crack plane orientation, R ratio, test temperature and environments on high temperature fatigue crack growth resistance of Alloy 709.

5.1.2 Effects of Side-groove, Orientation and R ratio

Side-groove

Optical fractographs in Figures 4.25 clearly indicate that side-groove depth influences the overall crack shape. Figure 4.25h shows that the only sample (numbered 'B1-6') without side-grooves has a thumbnail shaped crack and more lateral deformation compared with side-grooved specimens (compared with Figure 4.25i) when tested at the same temperature. For the samples with side-grooves, the crack front was found in general to be straighter (Figures 4.25c and d). On the fatigue crack growth curves obtained, tests with different side-groove depths (0, 0.5, 1 mm) overlap in the Paris regime, see Figure 4.17. This suggests the empirical treatment (equation 4.6) of evaluating stress intensity factor range of side-grooved testpieces, in which both B and B_n were taken into account, is appropriate. It should be mentioned that adaptation of side-grooves is not important for fatigue loading but essential with a static loading such as in creep crack growth tests, in which case only B_n (net-section) is taken into account in evaluating C* values.

Orientation

Figure 4.18 shows a comparison between the fatigue crack growth resistance curves obtained from the testpieces with L-T and ST-L orientations, which is believed to be the strongest and the weakest orientations if there were any impact of sample extraction orientation. Similar fatigue crack growth rates have been measured over the entire applied ΔK range (in the Paris regime). This indicates that high temperature fatigue crack growth behaviour of Alloy 709 is not sensitive to crack plane orientation. The homogeneousness

of fatigue crack growth behaviour is likely to be linked with the ductile nature of the material as well as a flat transgranular crack growth path. Similar observation has been made in the study of fatigue crack growth rate of 304 stainless steel and austenitic metastable stainless steel AISI 301LN with orientations of L-T and ST-L [149].

R ratio

Figure 4.19 shows that higher R ratio leads to greater fatigue crack growth rates at low and high ΔK levels, while the relatively little effect of R ratio was found at intermediate ΔK levels (ΔK between ~25 to 33 MPa√m). This trend has been commonly acknowledged in the effect of R ratio on fatigue crack growth resistance in steels [150]. It was suggested that at low ΔK levels towards to near threshold regime, higher R ratio leads to less crack closure, give rise to higher effective stress intensity factor range, hence faster crack growth rates. At higher ΔK levels, with the K_{max} approaching K_{IC} of the material, monotonic fracture is introduced at lower ΔK values with higher R ratios, consequently, instability in crack growth starts at lower ΔK values [151].

5.1.3 Effects of Temperature and Environments

In vacuum, the fatigue crack growth resistance curves obtained at different temperatures distribute in a narrow data band. In the Paris regime, very mild influence of temperature is observed over the investigated temperature range, 550 to 750°C (Figure 4.23). However, when compare fatigue crack growth rates obtained in air and vacuum to those obtained in air, a clear difference is seen, with faster crack growth rate are measured in air at a given temperature. This implies the acceleration in crack growth rates come from the influence

of environment rather than temperature. The difference in crack growth resistance curves is most pronounced at 750°C, and with ΔK values below 40 MPa√m (Figure 4.24). Mechanisms presumably associated with the oxidation embrittlement in the vicinity of the crack tip operating at high test temperatures under 0.25 Hz cyclic loading [104]. This effect is elaborated below:

At a given ΔK value, higher oxygen diffusivity is expected at higher temperatures. According to the equation below:

$$D = D_0 \cdot \exp\left(-\frac{E_A}{RT}\right) \qquad \text{(Equation 5.1)}$$

where D is the diffusivity, D_0 is the diffusion coefficient, E_A is the activation energy for diffusion, T is the absolute temperature, R is the universal gas constant (8.31 J/mol·K). If D_0 is a temperature-independent constant, the activation energy for oxidation of Alloy 709 at 550 to 750°C is found to be 229 kJ/mol [152]. Take a ΔK values of ~20 MPa√m for example, the fatigue crack growth rate at 750°C is about ~4 times higher than 550°C. This corresponds to ~1123 times increasing in diffusivity of oxygen from 550 to 750°C.

It is well acknowledged that the environmental influences on fatigue crack growth resistance may vary with different ΔK levels [128]. At near threshold regime, the slower crack growth rates may due to the oxides induced crack closure [153, 154]. At the ΔK values in the Paris regime, detrimental effect of air environment is often found. Due to slower crack growth rates at lower ΔK values, the oxygen damage within each cycle would be a more significant proportion of the total growth. Taking the difference in growth rate between air and vacuum as oxidation damage. At a ΔK of 20 MPa√m at 650°C,

the oxidation damage is ~0.1 μm (1×10^4 mm), at a ΔK of 40 MPa√m it is ~0.5 μm (0.5×10^3 mm), see Figure 4.21. The oxidation damage is half of the total growth at 20 MPa√m but reduce to 30% of the growth at a ΔK of 40 MPa√m. The fact that larger absolute oxidation damage (but of smaller percentage of total growth) seen at higher ΔK indicates the oxidation damage can be influenced by either growth rate or stressing state. Similar observations were also reported in fatigue crack growth tests in Type 316 stainless steel at elevated testing temperatures [125, 134].

In order to clarify the fatigue crack growth mechanisms in Alloy 709, the fatigue striations have been carefully analysed on each fracture surface. For ΔK values from 22 to 45 MPa√m, the values of striation width measurements listed in section 4.2.2.2 agree very well with the fatigue crack growth rates at all test temperatures in air and vacuum. Although the appearance of striations in different environments is not quite the same (compare Figure 4.27c with d), it is evident that the mechanism of striated fatigue crack growth occurs under both conditions. Note that the striations observed in vacuum are generally smoother and less distinctive than those observed on the sample tested in air. Some coarsely spaced lines (arrowed in Figure 4.27d under a ΔK of ~22 MPa√m) were observed on the fracture surface of the sample tested in vacuum, they are believed to result from interaction of slip planes and striations. The spacing of these coarse lines does not agree with the crack growth rates measured.

With the increase of ΔK values to 45 and 50 MPa√m, striated crack growth is mixed with some localised microvoids. There are also observations of secondary cracks. Larger

quantity of microvoids and secondary cracks are found at higher ΔK and higher temperatures. SEM fractographs (Figure 4.30e) show that voids occurred in the earlier stage of the crack growth (with shorter crack length) at 750°C compared to those at 550 and 650°C. For example, the voids occurred at a crack length of 16.3 mm (ΔK values ~45 MPa√m) in air at 750°C while at ~16.6 mm at 550 and 650°C (ΔK values ~50 MPa√m). At 750°C and ΔK of 50 MPa√m the fracture surface is dominated by the formation of ductile microvoids (Figures 4.32e and f). The formation of microvoids and secondary cracks indicates severe deformation, presumably results from increased net-section stress with increase of crack length (ΔK). More severe microvoids formation at 750°C, is likely to relate to a lower tensile strength at this temperature (true tensile strength of testpiece tested at 750°C is 394 MPa), compared to those at 550 and 650°C (796 and 633 MPa respectively). This contributes to overall rougher fracture surface and more lateral deformation at higher temperatures, see Figure 4.25h.

5.2 Creep Crack Growth in Alloy 709

5.2.1 Creep Crack Growth Resistance Curves

The $\dot{V}_C/\dot{V}$ value, shows the proportion of load-line displacement rate due to time dependent deformation to the total load-line displacement rate (summation of creep, plastic and elastic components), has been calculated. For creep crack growth behaviour in Alloy 709, the $\dot{V}_C/\dot{V}$ value is above 0.9 under all test conditions. According to ASTM E 1457-15 , Alloy 709 is therefore 'creep-ductile' at all temperatures. Thus, K is no longer ''appropriate'' to characterise crack growth rate. The C* - integral is herein a more

appropriate crack driving force parameter. Despite this, creep crack growth rate data has still been plotted against K as a reference approach to compare crack growth resistance curve obtained at different temperatures (Figure 4.43). Note that the test load was kept constant for most of the tests at 8 kN and the testpiece dimensions are same apart from thickness which is either 10 or 11 mm, however the resulted stress variations at various thickness are relatively small, which can be estimated from Figure 5.1, this makes comparisons between different test temperatures possible using da/dt vs. K plots.

Figure 4.43 implies a dependence of creep crack growth rates with temperature in a da/dt versus K plot. It is clear that creep crack growth rates increase with increase in temperature in the as-received Alloy 709. This is due to creep damage being more severe at higher temperature. However, when crack growth rates are plotted against C*-integral, see Figure 4.42, all the creep crack growth data points obtained for Alloy 709 at 550, 650, 750°C lie around a single line on a da/dt versus C* plot, suggesting there is a unique relationship between creep crack growth rate and C* value. It is therefore confirms that C*-integral is the relevant parameter to correlate steady state creep crack growth behaviour with larger C* values correspond to higher crack growth rates. The C* values can be worked out by experiment or calculated by computational simulations [99]. The experimental approach involves measurements of load-line displacement rate, $\dot{V}$, and Norton creep exponent, n, obtained normally from uniaxial smooth specimens, see equation 2.9. Apparently, C* parameter is closely related to creep resistance of a material, particularly load-line displacement rate.

5.2.2 Normal Creep Test on Smooth Cylindrical Testpieces

When a plain-sided crack-free specimen is subjected to a static load, often three phases can be observed, typically represented by a creep strain versus time plot as shown in Figure 4.34. During primary creep region (also known as transient creep stage), the strain rate increase sharply at the beginning, then gradually decreases with time (Figure 4.34). The decreasing creep rate in this phase reflects domination of work hardening which inhibits dislocation motion. Note that the primary creep stage appears insignificant, and is invisible here under the current horizontal scale. In the secondary creep region, the creep strain increases linearly with time, constant strain rate, see Figure 4.34. This steady-state creep stage corresponds to minimum creep strain rate and represents a balance between work hardening and thermally activated recovery (softening) process [56]. In the tertiary creep region, creep strain accelerates, showing increased strain rate, which leads to final rupture. This phase is the actual damage phase, which could be caused by a number of factors including increase in stress (reduction of net-section) of a constant load test, formation of microvoids and cracks, and overageing [56]. In the primary and secondary phases, the creep deformation is relatively uniform, while more localised deformation occurs in the tertiary creep region. Therefore, by analysing the areas near and away from the fracture surface of the metallographic section for the fractured creep testpieces, different creep phases can be observed. In the area away from the fracture surface, where the stress level and creep strain rate are low, isolated intergranular microvoids were initiated (Figures 4.40e and g and Figures 4.41e, g and h), this

presumably relate to early stage of tertiary creep. In the area near the fracture surface, where the stress and the creep strain rate increase, large deformation of matrix and the formation of numerous voids can be seen (Figure 4.40c and Figure 4.41b). This is related to later stage of tertiary creep.

5.2.3 Temperature Influences on Creep (on Crack-free Cylindrical Samples)

Since the creep process is temperature dependent, creep strains and creep life are exponentially depending on testing temperature [155]. As can be seen in Figure 4.34 the rupture life reduces significantly with the increase of temperature, even at reduced stress levels. However, lower failure strains are associated with low temperatures, especially at 550°C. It is worth pointing out that the failure strain obtained at 650 and 750°C is higher than the elongation measured from tensile tests, but much lower than the tensile elongation at 550°C. (compared to Table 4.5 and Table 4.2). Figure 4.36 shows different failure modes can be also observed on creep testpieces after testing at different temperatures. Less 'necking' and absence of shear lips are observed on the creep testpieces at 550°C, which indicate that more homogenous deformation compared with that at 650 and 750°C. This is perhaps the result of the larger work-hardening (Table 4.3) and serrated plastic deformation at 550°C, which help to pin the dislocation movement. This reduction in creep strain at 550°C is corresponding to the observation of an intergranular dominated fracture surface morphology. Note that ductile microvoids coalescence are seen at both 650 and 750°C.

5.2.4 Creep Zone Ahead of the Crack Tip

It is widely acknowledged that the stress around a crack tip is higher than the net-section nominal stress due to stress concentration. With creep-ductile materials sustain the static loading before fracture, the creep deformation head of the crack tip produces a stress relaxation in the vicinity of the crack tip, leading to blunting of the crack and spreading of plastic zone over time. Eventually, the initiation and nucleation of creep damages can lead to crack growth [156]. Therefore, understanding the crack growth and damage mechanisms is crucial for characterising and predicting life for Alloy 709.

Due to variation of stress at different distance to the crack tip, it is expected that different phases of creep (as in the normal creep tests) could be experienced at different location at the crack tip at any one time. It is reasonable to propose that the development of creep damage at the crack tip is in the same sequence as in the creep damage in the plane-sided specimens, tertiary, secondary and primary creep zone exist in succession moving away from the crack tip, as schematically presented in Figure 5.2. When a “fresh” sharp fatigue precrack is subject to a static load, it is expected the crack tip region experiences primary creep (initial creep deformation, blunting), secondary creep (constantly blunting with accumulation of creep deformation), and tertiary creep (cracking, growth of the crack). As a result, there is an incubation period before the establishment of steady-state crack growth, and damages accumulate at the crack tip. After sufficient damages accumulated, crack growth can be observed. It would be worth clarifying the correlation of crack growth with load-line displacement rate.

After transfer from fatigue loading to static loading, normally, two types of crack growth

can be detected: the deceleration and then acceleration, or acceleration, depending on the magnitude of mechanical driving force (stress, or K) and temperature. It is observed that an acceleration in crack growth rate, presumably taking the form of the linkage of grain boundary voids and wedge cracks (Figure 4.51c), is related to an increase in load-line displacement rate. This is also suggested in the creep-fatigue crack growth tests in Type 316 stainless steel at 625°C [157] and proposed by Neumann in several plasticity models [158].

5.2.5.1 Effect of Temperature and Stress

Figure 5.1 shows the net section stress (includes both tensile and bending stresses) distribution ahead of the crack tip during creep and dwell-fatigue crack growth at 550, 650 and 750˚C with applied K of 20 to 50 MPa√m and different thickness values (11 and 12 mm). It indicates that in the CT testpieces, the net section stress ahead of the crack tip becomes higher with longer crack length. The actual crack tip stresses are very complicating due to both stress concentration and plastic deformation. the values provided a rough estimation from elastic analysis without considering stress concentration. It can be seen that the stress increases exponentially with the increase of crack length and K value. It should be noted that thickness of testpieces has a mild influence on net section stress ahead of the crack tip.

In order to have an obvious crack extension during the 1st, 2nd and 3rd CCG regions, plenty of time (~1000 hours or more than 1 month) has been given to propagate the crack (Table 4.6). However, Figure 4.45d shows that no increases in load-line displacement rates were

found during the 1st, 2nd and 3rd CCG (where K value of ~31, 40 and 45 MPa√m), the crack still cannot grow consistently, only limited crack extensions were found (~0.04, 0.10 and 0.20 mm). In these three regions, the net section stresses ahead of the crack tip are 390, 553 and 669 MPa (Figure 5.1). This may due to the observation of bifurcation leads to the redistribution of stress at crack tip, this 'barrier' leads to insufficient crack tip stress to drive the crack growth, eventually, the crack stopped (Figure 4.49b and Figure 4.50e). It should be noted that in these three regions, the steady-state creep never been established. Despite the limited crack extensions, intergranular fracture modes were still been observed, see Figures 4.50b, d and f.

In the 4th CCG (K values between ~49 to 53.5 MPa√m), continuous increase in load-line displacement rate, different to previous three creep crack growth segments, was detected, which corresponds to an acceleration in crack growth rate (Figure 4.45e), 0.56 mm crack extension was observed during the similar test time to the previous three CCG regions (~1000 hours). According to Figure 5.1, since the corresponding net section stresses now vary from ~757 to 818 MPa, which are around tensile strength at 550°C (796 MPa), The fracture modes change to a mixture of intergranular and ductile microvoids (Figure 4.50g). It is noteworthy that this observation is coincident with the combination of failure modes seen on the creep (intergranular) and tensile (ductile) testpieces, see Figure 4.37c and Figure 4.13f. This remarkable creep crack growth resistance of Alloy 709 is believed owing to the highest strain-hardening ability and creep resistance at 550°C (see Table 4.3). When tested at 650 and 750°C (testpieces 'CS4' and 'CS2'), the load-line displacement

rate becomes steeper with longer testing time (Figure 4.46b and Figure 4.48b). The net section stresses at crack tip at the beginning of creep crack growth (where K value of ~35 and 30 MPa√m) are ~500 and 369 MPa respectively, which are all approach to the tensile strengths (633 and 394 MPa) at the corresponding temperatures, see Figure 5.1. Subsequently, fast crack growth rates were detected (Figure 4.46c and Figure 4.48c).

The fractographs for testpiece at 650°C indicate an intergranular dominated failure mode at the beginning (Figures 4.53b and d), with the higher crack growth rate and net section stress (up to 544 MPa at K of ~40 MPa√m), more ductile microvoids were seen in Figure 4.53f. For the testpiece tested at 750°C, the fully ductile failure mode was established at the onset of creep, with the increase of stress, a large number of microvoids resulting in the final creep fracture, meanwhile, clear literal deformation was seen in this stage (Figure 4.56a).

Furthermore, it can be confirmed from the fracture surfaces that the microvoids formed at lower K values (shorter crack length) with higher temperatures. However, it was found at all temperatures that when the microvoids formed, the corresponding net section stresses exceed the tensile strength. For example, the microvoids formed at K values (crack lengths) of ~49 (14.52), 38 (11.34) and 29 MPa√m (9.94 mm) at 550, 650 and 750°C individually. At those stages, the crack tip net section stresses are 734, 472 and 349 MPa, which are all higher than the tensile strength listed in Table 4.2 (568, 474 and 326 MPa).

5.2.5.2 Effect of Prior Ageing

Since the applied load for the creep crack growth tests on the as-received and aged testpieces are different, it is difficult to identify the effect of ageing on the creep crack growth behaviour. However, as shown in Table 4.6, for the aged testpiece 'HT1', plenty of time (~6 months) has been given to propagate the crack under 8 kN, consequently, no sign of increase in load-line displacement rate was detected (Figure 4.47d) and only 0.61 mm crack propagation was obtained (ΔK value of 30 ~ 32 MPa$\sqrt{m}$). For the as-received testpiece 'CS4', which with a longer initial crack length (initial crack lengths are 10.82 and 10.41 mm for the as-received and aged testpieces), therefore, 3.25 mm crack extension was found during the ~102 days (3.4 months) under 8 kN. Despite the different initial crack lengths for both testpieces, it may be speculated from the testing experiences that the creep crack growth resistance after ageing is better or at least no worse than the as-received condition for Alloy 709.

It is noteworthy that the fracture modes are different for the as-received and aged testpieces, see Figure 4.52b and Figure 4.54b. In the as-received condition, intergranular failure mode was observed at the early stage of creep crack growth (when $K < 38$ MPa$\sqrt{m}$). Afterwards, the ductile fracture mode then established. However, after ageing, fully ductile fracture mode was seen at the onset of creep (Figure 4.55b). These different observations may be linked to the higher yield stress and lower tensile strength after ageing, therefore, the strain-hardening exponent decreases, which lead to two different fracture modes. It should be noted here that larger area of ductile overload fracture surface for the aged sample aged at 650°C (Figures 4.55c) could in part be due to the increased

constant load of 10 kN during this creep crack growth test.

5.3 Dwell-Fatigue Crack Growth in the As-received Alloy 709

5.3.1 Crack Growth Mechanisms and Their Interactions

5.3.1.1. Mechanism Map

Crack growth mechanisms of Alloy 709 under fatigue loading including a fixed hold time of 1-hour at the maximum load at high temperatures can be associated with one or a mixture of cyclic dependent failure mode (fatigue) and time dependent failure mode (creep).

Figure 5.3 summarised the fracture modes and crack growth rate observed at three applied ΔK levels (20, 35, 50 MPa√m) for both fatigue (0.25 Hz) and dwell-fatigue (with 1 - hour tensile hold) loading at three testing temperatures. Note that the "creep" mode here includes both "intergranular" and "ductile" fracture, which will be elaborated later. Since the applied load is fixed for all test, the relationship between ΔK and net-section stress ahead of the crack tip is similar for a given crack length. Figure 5.1 shows the calculated net section elastic stresses at different crack length and/or ΔK values. Note that the stresses in the actual testpieces must be different from the ones presented in Figure 5.1 as there will be stress concentration and stress redistribution due to creep deformation. However, these values still provide an indication of relative magnitude and trend of stress variation with the increase of crack length.

It can be seen from the mechanism map (Figure 5.3) that the failure modes under 1 - hour dwell-fatigue loading changes according to test temperature and applied ΔK levels. They

can be summarised as follows: fatigue mode occurs at low ΔK levels (~ 20 MPa√m) at 550 and 650°C; creep mode was observed at 750°C at all applied ΔK regions, and at 650°C in the intermediate and high ΔK levels; fatigue - creep interactions were predominantly occurred at 550°C at ΔK values from 35 up to 50 MPa√m.

Also, from Figure 5.3, it can be seen that the acceleration in crack growth rate can only result from creep mechanism, but not related to the fatigue mechanism. Also, applied stress (represented here by ΔK) promotes creep damages. In this project, it was observed that creep damage accumulates most rapidly at 750°C, even at low ΔK levels (~ 20 MPa√m).

5.3.1.2. Creep - ductile Fracture

According to Figure 5.1, it can be seen that at ΔK value of 50 MPa√m, the estimated net section stress at the crack tip (879 MPa) is higher than tensile strength at 550, 650 and 750°C and even higher than the fracture stress at 650 and 750°C (741 and 576 MPa). This leads to the ductile failure mode at 650 and 750°C. It is noteworthy that the fracture mode changes to ductile fracture at a ΔK value of ~50 and 27 MPa√m at 650 and 750°C for testpieces 'A1-1' and 'S5' respectively, the stresses ahead of the crack tip are calculated to be 879 and 352 MPa, which is above the fracture stress at 650°C (741 MPa) and approaches to the true tensile strength at 750°C (394 MPa). The ductile fracture mode observed here is similar to monotonic fracture mode seen in the fracture surfaces of tensile tests, reflecting severe plastic deformation (compare Figures 4.71 and 4.78 with Figures 4.13g and h).

5.3.1.3. Creep - intergranular Fracture

Below the ΔK and/or stresses that lead to ductile fracture mode, intergranular fracture mode was seen at ΔK value of ~30 - 40 MPa√m for 650°C and below ~22 MPa√m for 750°C. As shown in Figures 4.62 and 4.63, stable accelerating crack propagation was achieved after the initial deceleration at 650°C, while immediate acceleration in crack growth rate was detected when transferred to 1-3600-1-1 dwell-fatigue loading at 750°C. SEM images proved that an immediate transition from transgranular to intergranular was seen after transfer from baseline fatigue into 1-3600-1-1 dwell-fatigue loading at both temperatures, see Figure 4.70a and Figure 4.77a. This indicates that creep damage accumulation along grain boundaries are relatively fast, which made converting back to transgranular crack growth difficult. Under such intergranular crack growth mechanism, higher test temperature promotes greater crack growth rate, the crack growth rates are only increased two times faster than the baseline fatigue crack growth rates at 650°C. However, ~10 times increasing in crack growth rate was detected at 750°C (at ΔK value of ~32 MPa√m). Note that the initial deceleration at the onset of dwell-fatigue loading at 650°C implies that steady state creep zone and creep damage need time to establish. For example, for testpiece 'A1-1', it needs ~200 hours to establish the steady-state creep crack growth (acceleration in crack growth). However, mild or a complete absence of decelerations in crack growth rate was observed at 750°C indicating fast spreading of creep deformation and creep damages.

It should be noted here that this intergranular fracture surface morphology is completely

the same to that found in creep crack growth samples where fatigue cycles are absent (compared Figures 4.70a and 4.77a with Figures 4.53b and d).

5.3.1.4. Creep-fatigue Interaction

As mentioned in section 4.2.5 of the results chapter, this creep-fatigue interaction is mostly found at 550°C, represented by a mixed-mode of intergranular and transgranular failure mechanisms. At this temperature, creep damage is slow and discontinuous, hence transgranular striated fatigue crack growth was allowed to take place, creep-fatigue interaction occurs. Note that without fatigue cycling crack growth was not sustainable, as found in the creep crack growth tests at the same temperature, see section 4.2.4.1. This confirms that creep alone cannot grow the crack continuously, as seen in the 1st - 3rd CCG in the creep crack growth testpiece (numbered 'CS1'). After ~1000 hours holding at K values between 30 to 50 MPa$\sqrt{m}$), the crack has completely stopped growing, see Figure 4.45e.

By analysing the fracture surface (Figures 4.65 and 4.66), only isolated intergranular islands were seen under 1-hour holding, they can be only linked up when the cyclic loading occurs.

5.3.1.5. Fatigue – negligible Creep Damage

Under the 1st dwell-fatigue region at 550 and 650°C, see Figures 4.65a and 4.69a, only transgranular failure modes were observed during the 1-hour dwell-fatigue loading. This proved the significant influences of the magnitude of stress and/or ΔK on failure mechanism and crack growth rate. The creep deformation and creep damage are

insufficient to affect crack extension at these low mechanical driving forces with ΔK values of ~20 MPa√m at 550 and 650°C.

It is noteworthy that the crack growth behaviour in Figures 4.61 and 4.62 during the 1st dwell-fatigue segments are all showing a sharp acceleration, upon transition into dwell-fatigue loading from baseline fatigue loading, followed by a deceleration in crack growth rate. This behaviour is associated with additional tearing under tensile dwell loading. A stretch zone is always seen at the fatigue crack front, especially at high ΔK levels (Figure 4.66b). With the accumulation of creep deformation under the 1-3600-1-1 dwell-fatigue, the crack tip becomes blunted, which lead to a decrease in crack propagation. Figures 4.65b and c provide a comparison of striation spacing between two locations: the beginning and end of dwell loading segment, which confirms initial acceleration and later retardation of crack growth.

5.3.2 Fatigue Influences on 1-3600-1-1 Dwell-fatigue Crack Growth Rate

Different fracture mechanisms were observed under 1-3600-1-1 dwell-fatigue waveform is deduced to the competitions and interactions of individual mechanism of fatigue and creep. It is worth clarifying how cyclic loading influences creep crack growth resistance. Hence, the data of creep crack growth tests are compared with dwell-fatigue crack growth data interpreted in da/dt versus K_{max}, as shown in Figures 5.4 to 5.6. The largest differences in crack growth rate are found for the creep-fatigue interaction regime at 550°C, at least 10 times increase in crack growth rate is seen in dwell-fatigue case. For the creep dominant regime, at 650°C, ~10 times increase was found in dwell-fatigue tests

with K values in the region of ~35-40 MPa√m, a small increase, <2 times, in crack growth rate is seen for the rest of K values in dwell-fatigue tests. At 750°C, less than two times acceleration in crack growth rate is detected for the entire K range. This suggests that cyclic loading has little influence on crack growth rate when creep mechanism dominates.

5.3.3 Crack Growth Rate Variation Found at 650°C in Air and Vacuum

The tests in air and vacuum at 650°C show some variations when ΔK values >45 MPa√m, below ΔK value of 45 MPa√m, the comparison in crack growth behaviour in air and vacuum is difficult to make as the vacuum test was interrupted without reaching steady-state crack growth (Figure 4.62). The influence of oxidation is considered to be minimal or not existing when excessive creep deformation occurs. It is interesting to observe that the testpiece (numbered 'A1-1' tested in air) which showed lower crack growth rates at ΔK values >45 MPa√m had spent a much longer period of testing before reaching this last period of crack growth, ~1100 hours. The testpieces in vacuum had only ~126 hours. It is suspect that much more on-test ageing had occurred in sample A1-1. Hence it is tentatively suggested that the variation seen in the last dwell-fatigue segment is related to microstructure due to on-test ageing.

According to the microstructure characterisation of Alloy 709 after ageing in section 4.1.2.2, it was found that ageing at 650 °C promotes precipitation of $M_{23}C_6$ phase on grain boundaries, twin boundaries and grain interior. In addition, fine dispersed Z-phase forms on dislocations just after ageing for 500 hours, their quantity increases with ageing time and temperature. 2000 hours ageing at 650°C can lead to a noticeable increase in yield

stress (Figure 4.10). Surely these microstructure changes confirmed in the ageing samples would have already occurred with ~1100 hours prior to testing 'A1-1' (tested in air), but minimal in testpiece 'A1-10' (tested in vacuum).

It can be speculated that a certain degree of long-term ageing during service might improve the creep crack growth resistance of Alloy 709, contrasting to a detrimental effect seen in most of the traditional stainless steels [137].

In the next section, the dwell-fatigue crack growth resistance of Alloy 709 is compared with a baseline austenitic stainless steel, 316H.

5.4 Compare Between Alloy 709 and 316H

Alloy 709 represents a class of advanced austenitic stainless steels with excellent creep resistance. This superior creep resistance is primarily promoted from participates strengthening [131]. In this work, the traditional austenitic stainless steel, Type 316H, is used as a base material to compare the creep and creep-fatigue crack growth behaviour with Alloy 709. 316H is currently used as the structural material for nuclear reactors and it has similar tensile properties and grain structure to Alloy 709.

The results for a dwell-fatigue crack growth test conducted in 316H, using the same conditions and procedure as used in Alloy 709 was plotted in Figure 4.80. The fracture morphology was carefully analysed under optical microscope and SEM, see Figures 4.81 - 4.84. Figure 4.80 shows similar fatigue crack growth resistance is found in 316H and Alloy 709 under a 0.25 Hz sinusoidal waveform at 650°C. But the crack growth rates of 316H under dwell-fatigue loading are about two orders of magnitude higher than those

of Alloy 709 at a given ΔK value. Furthermore, at the same ΔK value, more plastic deformations and microvoids can be observed in 316H than Alloy 709, compare Figure 4.83a to 4.70a. Note that the crack growth rate and mechanisms for 316H at 650°C are similar to those measured at 750°C for Alloy 709. These observations confirm a better dwell-fatigue resistance in Alloy 709.

In order to have a better understanding of such differences in crack growth rate, the metallographic section of 316H (along sample longitudinal axis) were made and carefully examined under SEM (see Figure 4.85). Figure 4.85a reveals the formation of voids on grain boundaries. Figure 4.85c shows a significant increase in low angle grain boundaries in a grain orientation map taken within the 2^{nd} dwell-fatigue region. This confirms the formation of subgrains, which are the results of damages at the crack tip. Further detailed TEM analysis was conducted on 316H and Alloy 709 during the 2^{nd} dwell-fatigue region at 650°C [159]. The results show the formation of dynamic recovery and recrystallization in 316H. However, for Alloy 709, the high density of dislocation was found, no subgrains were observed. The comparison indicates that under the same stress and temperature condition, dynamic recovery is delayed in Alloy 709, which increases its creep growth resistance.

CHAPTER 6 Conclusions and Future Research

6.1 Conclusions

Crack growth in Alloy 709 at high temperatures (550, 650 and 750°C) under fatigue, creep and dwell-fatigue loads have been studied in this project. The conclusions are as follows:

- The as-received Alloy 709 had an equiaxed austenite grain structure. Primary Nb(CN) and nano-sized Z-phase particles were found. The microstructure of Alloy 709 is stable at the working temperature of 550°C. No microstructural changes were found after ageing for 2000 hours at 550°C. However, after ageing at 650°C and 750°C, $M_{23}C_6$ phases were found distributed continuously at grain boundaries and in grain interiors. Z-phase was distributed on dislocations.
- For the as-received Alloy 709, the yield stress was remained unchanged at 550, 650 and 750°C. However, the TS decreases with higher test temperatures. The highest strain-hardening exponent was observed at 550°C, which is accompanied by observation of dynamic strain ageing (serrated plastic stress-strain curve). An excellent ductility is observed at all temperatures, the highest ductility is measured at 750°C due to dynamic recovery and recrystallization;
- After ageing at 650°C for 2000 hours, yield stress was increased compared with the as-received Alloy 709 at 550, 650 and 750°C. This is due to the precipitation of fine $M_{23}C_6$ and Z-phase during ageing. However, the brittle $M_{23}C_6$ also formed during ageing, which decreases the tensile strength, strain-hardening ability and

ductility of Alloy 709;

- In the fatigue and 1-3600-1-1 dwell-fatigue crack growth tests, the linear elastic fracture mechanics, ΔK, was applied to correlate the crack growth behaviour. High temperature fatigue crack growth behaviour of Alloy 709 was found to be influenced primarily by environment, rather than temperature. The higher crack growth rates in air than vacuum is related to both test temperature and ΔK value. Smaller oxidation damages, but larger proportion of total crack extension were found at lower ΔK values. The failure mechanisms in both air and vacuum were all found to be striated transgranular crack growth, when ΔK value was below ~45 MPa√m. However, ductile fracture was found when ΔK value was above ~50 MP√m. The microvoids coalescence was found at lower ΔK values (smaller crack length) when tested at higher temperatures;
- In the creep crack growth tests, a time-dependent fracture mechanics (TDFM) parameter, the C*-integral, was used to characterise the crack crack growth, da/dt versus K plots were also used to interpret the results. All the results were found to fall on one line in da/dt versus C* plots, regardless of test conditions. The acceleration of the crack growth rate is found to associate with the increase of load-line displacement rate. For the as-received Alloy 709, the failure modes are dominated by the "creep" failure mode (includes both "intergranular" and "ductile" fracture). The intergranular failure mode was seen at the early stage of creep crack growth. The fracture surface morphology becomes more ductile with the

formation of microvoids and secondary cracks when higher stresses (and/or high K), and high temperatures were applied.

- Dwell-fatigue crack growth tests were conducted on the as-received Alloy 709 with the fixed dwell time of 1-hour at 550, 650 and 750°C in air. Comparing to the baseline of fatigue crack growth rate obtained from continuous fatigue loading with a frequency of 0.25 Hz, any sustainable acceleration in crack growth rates under 1-3600-1-1 dwell-fatigue loading comes from a creep mechanism. The influence of fatigue cycling, when the dominant failure mechanism is creep, is noticeable but small.
- Alloy 709 shows excellent resistance against creep crack growth and dwell-fatigue crack growth at 550°C. This is attributed to excellent creep resistance and strain hardening capability at this temperature. In addition, this is the only temperature that creep-fatigue interaction is observed under 1-hour dwell-fatigue loading.
- Apart from under low ΔK values of ~17.8 - 18.3 MPa$\sqrt{m}$ at 650°C, creep damage is fast to accelerate crack growth at 650 and 750°C, together with the observation of pure creep failure mechanism (intergranular and ductile failure). When creep mechanism dominates, the contribution of fatigue cycling (1-hour dwell-fatigue) was found to be minimal or complete absent.
- Creep damage is sensitive to stress (and/or ΔK) and temperature. A crack growth mechanism map is given to summarise the combined influence of stressing and

temperature.

- The preliminary results suggest that in-test ageing may enhance creep crack growth resistance of Alloy 709.
- The dwell-fatigue and creep crack growth resistance of Alloy 709 is shown to be significantly better than for 316H stainless steel. When tested at 650°C, the crack growth rate in Alloy 709 is at least 10 times slower than that in 316H under the same crack driving force. This is believed to benefit from a dispersion of fine precipitates, especially Z-phases which form on dislocations and pin their movements.

6.2 Future Research

Due to the long duration of creep crack growth tests and the availability of the materials, some of the research areas worth to be further study:

- In order to understand the dwell-fatigue crack growth mechanisms in Alloy 709 at 550°C, long test times are needed to achieve steadily crack growth.
- In order to clarify the ageing effects on creep crack growth resistance of Alloy 709, identical load and similar initial C* or K value should be applied on the as-received and aged material to compare the crack growth rates.
- It is worth carrying out the crack growth tests in an aggressive environment.
- The microstructure influenced the mechanical properties of Alloy 709. It is worth further research on the composition design, especially for the influence of grain size on crack growth behaviour.

References

1. OECD, N. *GIF R&D Outlook for Generation IV Nuclear Energy Systems*. 2009. OECD Nuclear Energy Agency for the Generation IV International Forum.
2. Liu, Z., *Chapter 1 - Global Energy Development: The Reality and Challenges*, in *Global Energy Interconnection*, Z. Liu, Editor. 2015, Academic Press: Boston. p. 1-64.
3. Kelly, J.E., *Generation IV International Forum: A decade of progress through international cooperation.* Progress in Nuclear Energy, 2014. **77**: p. 240-246.
4. Sourmail, T., *Simultaneous precipitation reactions in creep-resistant austenitic stainless steels*. 2002, University of Cambridge.
5. Baudrand, O., D. Blanc, E. Ivanov, H. Bonneville, B. Clement, M. Kissane, R. Meignen, D. Monhardt, G. Nicaise, and T. Bourgois, *Overview of Generation IV (Gen IV) Reactor Designs-Safety and Radiological Protection Considerations*. 2012, Institut de Radioprotection et de Surete Nucleaire-IRSN.
6. Locatelli, G., M. Mancini, and N. Todeschini, *Generation IV nuclear reactors: Current status and future prospects.* Energy Policy, 2013. **61**: p. 1503-1520.
7. *U.S. DOE, A technology roadmap for generation IV nuclear energy systems.* 2002.
8. *Design Features and Operating Experience of Experimental Fast Reactors*. 2013, Vienna: INTERNATIONAL ATOMIC ENERGY AGENCY.
9. Series, I.N.E., *Structural Materials for Liquid Metal Cooled Fast Reactor Fuel Assemblies—Operational Behaviour.* No. NF, 2012.
10. Asayama, T., *18 - Conventional ferritic and martensitic steels as out-of-core materials for Generation IV nuclear reactors*, in *Structural Materials for Generation IV Nuclear Reactors*, P. Yvon, Editor. 2017, Woodhead Publishing. p. 635-649.
11. McGuire, M.F., *Stainless steels for design engineers*. 2008: Asm International.
12. Sourmail, T., *Precipitation in creep resistant austenitic stainless steels.* Materials science and technology, 2001. **17**(1): p. 1-14.
13. Powell, D., R. Pilkington, and D. Miller, *The precipitation characteristics of 20% Cr/25% Ni-Nb stabilised stainless steel.* Acta Metallurgica, 1988. **36**(3): p. 713-724.
14. Peckner, D. and I.M. Bernstein, *Handbook of stainless steels.* McGraw-Hill Book Co., New York. 1977,(Chapters paged separately), 1977.
15. Chawla, S.L., *Materials selection for corrosion control*. 1993: ASM international.
16. Paúl, A., R. Sánchez, O.M. Montes, and J.A. Odriozola, *The Role of Silicon in the Reactive-Elements Effect on the Oxidation of Conventional Austenitic Stainless Steel.* Oxidation of Metals, 2007. **67**(1): p. 87-105.
17. Cunat, P.-J., *Alloying elements in stainless steel and other chromium-containing alloys.* ICDA, Paris, 2004.

18. Bhadeshia, H. and R. Honeycombe, *Steels: microstructure and properties*. 2017: Butterworth-Heinemann.
19. Brog, J.-P., C.-L. Chanez, A. Crochet, and K.M. Fromm, *Polymorphism, what it is and how to identify it: a systematic review.* Rsc Advances, 2013. **3**(38): p. 16905-16931.
20. Sasmal, B., *Mechanism of the formation of lamellar M 23 C 6 at and near twin boundaries in austenitic stainless steels.* Metallurgical and materials transactions A, 1999. **30**(11): p. 2791-2801.
21. Ding, R., J. Yan, H. Li, S. Yu, A. Rabiei, and P. Bowen, *Microstructural evolution of Alloy 709 during aging.* Materials Characterization, 2019. **154**: p. 400-423.
22. Zhou, Y., Y. Li, Y. Liu, Q. Guo, C. Liu, L. Yu, C. Li, and H. Li, *Precipitation behavior of type 347H heat-resistant austenitic steel during long-term high-temperature aging.* Journal of Materials Research, 2015. **30**(23): p. 3642-3652.
23. Laleh, M. and F. Kargar, *Suppression of chromium depletion and sensitization in austenitic stainless steel by surface mechanical attrition treatment.* Materials Letters, 2011. **65**(12): p. 1935-1937.
24. Jack, D. and K. Jack, *Structure of Z-phase, NbCrN.* J. Iron Steel Inst., 1972. **210**(10): p. 790-792.
25. Vodarek, V., *Morphology and orientation relationship of Z-phase in austenite.* Scripta metallurgica et materialia, 1991. **25**(3): p. 549-552.
26. Sourmail, T. and H. Bhadeshia, *Microstructural evolution in two variants of NF709 at 1023 and 1073 K.* Metallurgical and materials transactions A, 2005. **36**(1): p. 23-34.
27. Caminada, S., G. Cumino, L. Cipolla, D. Venditti, A. Di Gianfrancesco, Y. Minami, and T. Ono, *Creep properties and microstructural evolution of austenitic TEMPALOY steels.* International Journal of Pressure Vessels and Piping, 2010. **87**(6): p. 336-344.
28. Hansen, S.S., J.B.V. Sande, and M. Cohen, *Niobium carbonitride precipitation and austenite recrystallization in hot-rolled microalloyed steels.* Metallurgical Transactions A, 1980. **11**(3): p. 387-402.
29. Sumerling, R. and J. Nutting, *Precipitation in a 20 percent Cr-25 percent Ni steel stablized with niobium.* Journal of the iron and steel institute, 1965. **203**: p. 398.
30. Dewey, M., G. Sumner, and I. Brammar, *Precipitation of carbides in a low-carbon austenitic stainless steel containing 20wt-percent Cr-25wt-percent Ni-0.7wt percent Nb.* Journal of the iron and steel institute, 1965. **203**: p. 938.
31. Erneman, J., M. Schwind, H.-O. Andrén, J.-O. Nilsson, A. Wilson, and J. Ågren, *The evolution of primary and secondary niobium carbonitrides in AISI 347 stainless steel during manufacturing and long-term ageing.* Acta materialia, 2006. **54**(1): p. 67-76.
32. Lee, K.-H., J.-Y. Suh, J.-Y. Huh, D.-B. Park, S.-M. Hong, J.-H. Shim, and W.-S. Jung, *Effect of Nb and Cu on the high temperature creep properties of a high Mn–*

N austenitic stainless steel. Materials Characterization, 2013. **83**: p. 49-57.
33. Jung, W.S. and J.Y. Suh, *Improved creep behavior of a high nitrogen Nb-stabilized 15Cr-15Ni austenitic stainless steel strengthened by multiple nanoprecipitates.* Metallurgical and Materials Transactions A, 2011. **42**(11): p. 3378-3385.
34. Peng, B., H. Zhang, J. Hong, J. Gao, H. Zhang, J. Li, and Q. Wang, *The evolution of precipitates of 22Cr–25Ni–Mo–Nb–N heat-resistant austenitic steel in long-term creep.* Materials Science and Engineering: A, 2010. **527**(16-17): p. 4424-4430.
35. Foct, J. and N. Akdut, *Cleavage-like fracture of austenite in duplex stainless steel.* Scripta Metallurgica et Materialia;(United States), 1993. **29**(2).
36. Ecob, R.C., R.C. Lobb, and V.L. Kohler, *The formation of G-phase in 20/25 Nb stainless steel AGR fuel cladding alloy and its effect on creep properties.* Journal of Materials Science, 1987. **22**(8): p. 2867-2880.
37. Jargelius-Pettersson, R.F., *Precipitation trends in highly alloyed austenitic stainless steels.* Zeitschrift für Metallkunde, 1998. **89**.
38. Bhaduri, A., *Mechanical Properties and Working of Metals and Alloys*. Vol. 264. 2018: Springer.
39. Pekguleryuz, M., *Alloying behavior of magnesium and alloy design*, in *Fundamentals of Magnesium Alloy Metallurgy*. 2013, Woodhead Publishing. p. 152-196.
40. Mouritz, A.P., *Introduction to aerospace materials*. 2012: Elsevier.
41. Schaeffler, A.L., *Constitution diagram for stainless steel weld metal.* Metal progress, 1949. **56**(11): p. 680.
42. Schneider, H., *Investment casting of high-hot strength 12% chrome steel.* Foundry Trade J, 1960. **108**: p. 562-563.
43. Irwin, G., *Fracture dynamics, Fracturing of Metals. American Society of Metals*. 1948, Cleveland.
44. Orowan, E., *Fracture and strength of solids.* Reports on progress in physics, 1949. **12**(1): p. 185.
45. Schütz, W., *A history of fatigue.* Engineering fracture mechanics, 1996. **54**(2): p. 263-300.
46. Griffith, A.J.T.R.S., *The phenomena of rupture and flow in solids, Phil.* 1920: p. 163-198.
47. Irwin, G.R., *Analysis of stresses and strains near the end of a crack traversing a plate.* 1997.
48. Williams, M., *Stress singularities resulting from various boundary conditions in angular corners of plates in extension.* Journal of applied mechanics, 1952. **19**(4): p. 526-528.
49. Walker, E. and M. May, *Compliance functions for various types of test specimen geometry.* 1967.
50. Knott, J.F., *Fundamentals of fracture mechanics*. 1973: Gruppo Italiano Frattura.

51. Wells, A.A. *Unstable crack propagation in metals: cleavage and fast fracture*. in *Proceedings of the crack propagation symposium*. 1961.
52. Green, G., J.J.J.o.E.M. Knott, and Technology, *The initiation and propagation of ductile fracture in low strength steels.* 1976. **98**(1): p. 37-46.
53. Rice, J. and D. Tracey. *Numerical and Computer methods in structural mechanics*. in *Proceedings of ONR Symposium*. 1973. Academic Press New York.
54. Tracey, D., *Finite element solutions for crack-tip behavior in small-scale yielding.* 1976.
55. Rice, J.R., *A path independent integral and the approximate analysis of strain concentration by notches and cracks.* 1968.
56. Zhang, J.-S., *High temperature deformation and fracture of materials*. 2010: Elsevier.
57. Broek, D.J.M., Kluwer, Boston, *The Practical Use of Fracture.* 1989.
58. Kumar, P. and K. Prashant, *Elements of fracture mechanics*. 2009: Tata McGraw-Hill Education.
59. Landes, J. and J. Begley, *A fracture mechanics approach to creep crack growth*, in *Mechanics of crack growth*. 1976, ASTM International.
60. Nikbin, K., G. Webster, and C. Turner, *Relevance of nonlinear fracture mechanics to creep cracking*, in *Cracks and fracture*. 1976, ASTM International.
61. Goldman, N.L. and J.W. Hutchinson, *Fully plastic crack problems: the center-cracked strip under plane strain.* International Journal of Solids and Structures, 1975. **11**(5): p. 575-591.
62. Halighongde, S., *Simulation of high temperature crack growth in welds using finite element analysis.* Mechanical, Materials and Manufacturing Engineering, 2009.
63. Hyde, T.H., *Creep crack growth in 316 stainless steel at 600°C.* High Temperature Technology, 1988. **6**(2): p. 51-61.
64. ASTM, *E1457-15: Standard Test Method for Measurement of Creep Crack Growth Times in Metals*. 2015: ASTM International.
65. Ohji, K., K. Ogura, and S. Kubo, *Stress-strain field and modified J-integral in the vicinity of a crack tip under transient creep conditions.* Japan Society of Mechanical Engineers, 1979. **790**: p. 18-20.
66. Riedel, H. and J. Rice, *Tensile cracks in creeping solids*, in *Fracture Mechanics*. 1980, ASTM International.
67. Bassani, J. and F. McClintock, *Creep relaxation of stress around a crack tip.* International Journal of Solids and Structures, 1981. **17**(5): p. 479-492.
68. Park, Y., K. Kim, Y. Chung, and J. Park, *Creep crack growth in X20CrMoV 12 1 steel and its weld joint.* J. Pressure Vessel Technol., 2001. **123**(2): p. 191-196.
69. Metals, A.S.f., *Metals handbook*. Vol. 4. 1969: The Society.
70. Suresh, S., *Fatigue of materials*. 1998: Cambridge university press.
71. Klesnil, M. and P. Lukác, *Fatigue of metallic materials*. Vol. 71. 1992: Elsevier.

72. Bao-Tong, M. and C. Laird, *Overview of fatigue behavior in copper single crystals—II. Population, size distribution and growth kinetics of Stage I cracks for tests at constant strain amplitude.* Acta Metallurgica, 1989. **37**(2): p. 337-348.
73. Ambriz, R.R. and D. Jaramillo, *Mechanical behavior of precipitation hardened aluminum alloys welds.* Light Metal Alloys Applications, 2014: p. 35-59.
74. Paris, P. and F. Erdogan, *A critical analysis of crack propagation laws.* Journal of basic engineering, 1963. **85**(4): p. 528-533.
75. Laird, C., *The influence of metallurgical structure on the mechanisms of fatigue crack propagation*, in *Fatigue crack propagation*. 1967, ASTM International.
76. McMillan, J.C. and R.M. Pelloux, *Fatigue crack propagation under programmed loads and crack tip opening displacements.* Engineering Fracture Mechanics, 1970. **2**(1): p. 81-84.
77. Bathias, C. and R.M. Pelloux, *Fatigue crack propagation in martensitic and austenitic steels.* Metallurgical Transactions, 1973. **4**(5): p. 1265-1273.
78. Davidson, D. and J. Lankford, *Fatigue crack tip mechanics of a powder metallurgy aluminum alloy in vacuum and humid air.* Fatigue & Fracture of Engineering Materials & Structures, 1984. **7**(1): p. 29-39.
79. Irwin, G., *Plastic zone near a crack and fracture toughness.* 1997.
80. McClintock, F.A. and G. Irwin, *Plasticity aspects of fracture mechanics*, in *Fracture toughness testing and its applications*. 1965, ASTM International.
81. Ewalds, H.L., R.J.H. Wanhill, and Edward Arnold, *Fracture Mechanics.* 1984.
82. Penny, R.K. and D.L. Marriott, *Design for creep*. 2012: Springer Science & Business Media.
83. Evans, R.W. and B. Wilshire, *Creep of metals and alloys.* 1985.
84. Dean, D. and D. Gladwin, *Creep crack growth behaviour of Type 316H steels and proposed modifications to standard testing and analysis methods.* International journal of pressure vessels and piping, 2007. **84**(6): p. 378-395.
85. Wilshire, B. and M. Willis, *Creep and creep fracture of prestrained type 316H stainless steel.* Creep, 2001. **1**: p. 6-15.
86. Frost, H.J. and M.F. Ashby, *Deformation mechanism maps: the plasticity and creep of metals and ceramics*. 1982: Pergamon press.
87. Lagneborg, R., *A Modified Recovery-Creep Model and Its Evaluation.* Metal Science Journal, 1972. **6**(1): p. 127-133.
88. Mukherjee, A.K., J.E. Bird, and J.E. Dorn, *Experimental correlations for high-temperature creep.* 1968.
89. Weertman, J., *High temperature creep produced by dislocation motion.* Rate Processes in Plastic Deformation of Materials, ASM, Metals Park, Ohio. 1975, 315-336, 1975.
90. Sherby, O.D. and P.M. Burke, *Mechanical behavior of crystalline solids at elevated temperature.* Progress in materials science, 1968. **13**: p. 323-390.
91. McLean, D., *The physics of high temperature creep in metals.* Reports on Progress

in Physics, 1966. **29**(1): p. 1-33.
92. Lagneborg, R., *Dislocation mechanisms in creep.* International Metallurgical Reviews, 1972. **17**(1): p. 130-146.
93. Ruano, O.A., J. Wadsworth, and O.D. Sherby, *Deformation mechanisms in an austenitic stainless steel (25Cr-20Ni) at elevated temperature.* Journal of materials science, 1985. **20**(10): p. 3735-3744.
94. Jones, D.R.H., *Engineering materials 1: an introduction to their properties and applications*. 1996: Butterworth-Heinemann.
95. Sordi, V. and L. Bueno. *Tensile strength and creep behaviour of austenitic stainless steel type 18Cr–12Ni with niobium additions at 700 C*. in *Journal of Physics: Conference Series*. 2010. IOP Publishing.
96. Amirkhiz, B.S., S. Xu, J. Liang, and C. Bibby. *Creep Properties and TEM Characterization of 347H Stainless Steel*. in *Proceedings of the 36th Annual Conference Canadian Nuclear Society*. 2015. Canadian Nuclear Society Toronto.
97. Osman, H., A. Borhana, and M. Tamin, *Material parameters for creep rupture of austenitic stainless steel foils.* Journal of materials engineering and performance, 2014. **23**(8): p. 2858-2863.
98. Saxena, A., *Creep crack growth in high temperature ductile materials.* Engineering fracture mechanics, 1991. **40**(4-5): p. 721-736.
99. Webster, G.A. and R.A. Ainsworth, *High temperature component life assessment*. 2013: Springer Science & Business Media.
100. Webster, G., *Lifetime estimates of cracked high temperature components.* International Journal of Pressure Vessels and Piping, 1992. **50**(1-3): p. 133-145.
101. Nikbin, K., *The role of creep damage and initiation in the failure of creep brittle materials.* Creep and Fracture of Engineering Materials and Structures, 1997: p. 405-414.
102. Laiarinandrasana, L., R. Piques, R. Kabiri, and B. Drubay, *Master Curve da/dt vs C* for Creep and Creep-Fatigue Crack Growth on CT Specimens.* 2001.
103. Riedel, H. and W. Wagner, *Creep crack growth in nimonic 80A and in a 1Cr-1/2Mo steel*, in *Fracture 84*. 1984, Elsevier. p. 2199-2206.
104. Saxena, A., *Evaluation of C* for the characterization of creep-crack-growth behavior in 304 stainless steel*, in *Fracture Mechanics*. 1980, ASTM International.
105. Saxena, A., *Creep crack growth in high temperature ductile materials.* Engineering Fracture Mechanics, 1991. **40**(4): p. 721-736.
106. Kumar, Y., S. Venugopal, G. Sasikala, P. Parida, and A. Moitra, *Study of creep crack growth behaviour of a type 316 (N) stainless steel weld and its mechanism.* Materials Science and Engineering: A, 2018. **731**: p. 551-560.
107. Laiarinandrasana, L., M. Kabiri, and M. Reytier, *Effect of specimen geometries on the C∗ versus da/dt master curve for type 316L stainless steel.* Engineering fracture mechanics, 2006. **73**(6): p. 726-737.
108. Shibli, I. and N.L.M. Hamata, *Creep crack growth in P22 and P91 welds—*

overview from SOTA and HIDA projects. International journal of pressure vessels and piping, 2001. **78**(11-12): p. 785-793.
109. Majumdar, B., C. Jaske, and M. Manahan, *Creep crack growth characterization of Type 316 stainless steel using miniature specimens.* International journal of fracture, 1991. **47**(2): p. 127-144.
110. Yokobori Jr, A.T. and Y. Takeo, *The crack initiation and growth under high temperature creep, fatigue and creep-fatigue multiplication.* Engineering fracture mechanics, 1988. **31**(6): p. 931-945.
111. Saxena, A. and B. Giescke, *High Temperature Fracture Mechanisms and Mechanics EGF6. P. Bensussan, Editor*. 1990, Mechanical Engineering Publications, London.
112. Gibbons, T., *Creep crack growth, a state of the art report.* VAMAS (Versailles Project on Advanced Materials, 1989.
113. Wareing, J., *Creep-fatigue behaviour of four casts of type 316 stainless steel.* Fatigue & Fracture of Engineering Materials & Structures, 1981. **4**(2): p. 131-145.
114. Hales, R., *A quantitative metallographic assessment of structural degradation of type 316 stainless steel during creep-fatigue.* Fatigue & Fracture of Engineering Materials & Structures, 1980. **3**(4): p. 339-356.
115. Steels, A., *Stainless Steel Grade Datasheets*. Atlas Steels Technical Department, 2013.
116. Sham, S. *ARC Materials Development - Accomplishments and Plans*. 2013; Available from: https://www.energy.gov/sites/prod/files/2013/09/f2/ARC-Matls-CrossCut-2013.pdf.
117. Ren, W. and R. Swindeman. *A review of Alloy 800H for applications in the Gen IV nuclear energy systems*. in *Pressure Vessels and Piping Conference*. 2010.
118. Golański, G., A. Zieliński, M. Sroka, and J. Słania, *The effect of service on microstructure and mechanical properties of HR3C heat-resistant austenitic stainless steel.* Materials, 2020. **13**(6): p. 1297.
119. Swindeman, R., P. Maziasz, E. Bolling, and J. King, *Evaluation of advanced austenitic alloys relative to alloy design criteria for steam service*. 1990, Oak Ridge National Lab., TN (USA).
120. *NIPPON STEEL & SUMITOMO STEEL, NF709 Material Data Sheet*. Available from: http://www.tubular.nssmc.com/product-services/specialty-tube/product/nf709.
121. Alomari, A.S., N. Kumar, and K. Murty, *Enhanced ductility in dynamic strain aging regime in a Fe-25Ni-20Cr austenitic stainless steel.* Materials Science and Engineering: A, 2018. **729**: p. 157-160.
122. Upadhayay, S., H. Li, P. Bowen, and A. Rabiei, *A study on tensile properties of Alloy 709 at various temperatures.* Materials Science and Engineering: A, 2018. **733**: p. 338-349.
123. *Sodium-cooled Fast Reactor (SFR) Technology and Safety Overview.* 2015.

124. Babu, M.N., G. Sasikala, and S.K. Albert, *High-Temperature Fatigue Crack Growth Behaviour of SS 316LN*, in *Proceedings of Fatigue, Durability and Fracture Mechanics*. 2018, Springer. p. 413-422.
125. Sadananda, K. and P. Shahinian, *Effect of environment on crack growth behavior in austenitic stainless steels under creep and fatigue conditions.* Metallurgical Transactions A, 1980. **11**(2): p. 267-276.
126. James, L. and W. Mills, *Fatigue crack propagation behavior of Type 316 (16-8-2) weldments at elevated temperature.* Welding Journal, 1987. **66**(8): p. 229-234.
127. Makhlouf, K. and J. Jones, *Effects of temperature and frequency on fatigue crack growth in 18% Cr ferritic stainless steel.* International journal of fatigue, 1993. **15**(3): p. 163-171.
128. Raj, R., *Flow and fracture at elevated temperatures.* 1985.
129. Shaber, N.L., *Investigation of Fatigue and Creep-Fatigue Crack Growth in Alloy 709 at Elevated Temperatures*. 2018, University of Idaho.
130. Hyde, T., *Creep crack growth in 316 stainless steel at 600°C.* High Temperature Technology, 1988. **6**(2): p. 51-61.
131. Ding, R., J. Yan, H. Li, S. Yu, A. Rabiei, and P. Bowen, *Deformation microstructure and tensile properties of Alloy 709 at different temperatures.* Materials & Design, 2019. **176**: p. 107843.
132. Saxena, A. and S. Stock, *Mechanisms of time-dependent crack growth at elevated temperature. Final project report, July 1, 1986--August 31, 1989*. 1990, Georgia Inst. of Tech., Atlanta, GA (United States). School of Material ….
133. Shahinian, P., *Creep-fatigue crack propagation in austenitic stainless steel.* 1976.
134. James, L.A., *Fatigue-crack propagation in austenitic stainless steels.* Atomic Energy Review, 1976. **14**(1): p. 37-86.
135. Porter, T.D., K.O. Findley, M.J. Kaufman, and R.N. Wright, *Assessment of creep-fatigue behavior, deformation mechanisms, and microstructural evolution of alloy 709 under accelerated conditions.* International Journal of Fatigue, 2019. **124**: p. 205-216.
136. Porter, T. and K. Findley, *Assessment of Creep-Fatigue Behavior of Alloy 709.* Transactions, 2017. **117**(1): p. 559-562.
137. Michel, D., H. Smith, and H. Watson, *Effect of hold-time on elevated temperature fatigue crack propagation in fast neutron irradiated and unirradiated type 316 stainless steel*, in *Structural materials for service at elevated temperatures in nuclear power generation*. 1975.
138. Raj, R., *Nucleation of cavities at second phase particles in grain boundaries.* Acta Metallurgica, 1978. **26**(6): p. 995-1006.
139. Gao, N., M. Brown, K.J.F. Miller, F.o.E. Materials, and Structures, *Crack growth morphology and microstructural changes in 316 stainless steel under creep - fatigue cycling.* 1995. **18**(12): p. 1407-1422.
140. Porter, T., Z. Wang, E. Gilbert, M. Kaufman, R. Wright, and K. Findley,

Microstructure evolution of alloy 709 during static-aging and creep-fatigue testing. Materials Science and Engineering: A, 2021. **801**: p. 140361.
141. Lall, A., S. Sarkar, R. Ding, P. Bowen, and A. Rabiei, *Performance of Alloy 709 under creep-fatigue at various dwell times.* Materials Science and Engineering: A, 2019. **761**: p. 138028.
142. Choudhary, B.K., E.I. Samuel, K. Bhanu Sankara Rao, and S.L. Mannan, *Tensile stress–strain and work hardening behaviour of 316LN austenitic stainless steel.* Materials Science and Technology, 2001. **17**(2): p. 223-231.
143. ASTM, *E647-15, Standard Test Method for Measurement of Fatigue Crack Growth Rates*. 2015: ASTM International.
144. ASTM, *E2760-10: Standard Test Method for Measurement of Creep-Fatigue Crack Growth*. 2010: ASTM International.
145. Totten, G.E., L. Xie, and K. Funatani, *Handbook of mechanical alloy design*. Vol. 164. 2003: CRC press.
146. Schmidt, R. and P. Paris, *Threshold for fatigue crack propagation and the effects of load ratio and frequency*, in *Progress in flaw growth and fracture toughness testing*. 1973, ASTM International.
147. Ritchie, R. and J. Knott, *Mechanisms of fatigue crack growth in low alloy steel.* Acta Metallurgica, 1973. **21**(5): p. 639-648.
148. Ljustell, P., *Fatigue crack growth experiments on specimens subjected to monotonic large scale yielding.* Engineering Fracture Mechanics, 2013. **110**: p. 138-165.
149. Baek, J.-H., C.-M. Kim, W.-S. Kim, and Y.-T. Kho, *Fatigue crack growth and fracture toughness properties of 304 stainless steel pipe for LNG transmission.* Metals and Materials International, 2001. **7**(6): p. 579-585.
150. James, L., *Fatigue-crack propagation in austenitic stainless steels.* Atomic Energy Review, 1976. **14**(1): p. 37-86.
151. Riedel, H., *Nucleation of Creep Cavities/Basic Theories*, in *Fracture at High Temperatures*. 1987, Springer. p. 67-84.
152. Kim, J., S.-B.J.T. Lee, and A.F. Mechanics, *Fatigue crack opening stress based on the strip-yield model.* 2000. **34**(1): p. 73-84.
153. Ritchie, R., *Mechanisms of fatigue crack propagation in metals, ceramics and composites: role of crack tip shielding.* Materials Science and Engineering: A, 1988. **103**(1): p. 15-28.
154. Davidson, D. and J. Lankford, *Fatigue crack growth in metals and alloys: mechanisms and micromechanics.* International Materials Reviews, 1992. **37**(1): p. 45-76.
155. Hayhurst, D. *Computational Continuum Damaged Mechanics: Its use in the Prediction of Creep in Structures—Past, Present and Future*. in *IUTAM symposium on creep in structures*. 2001. Springer.
156. Davis, J.R., *ASM specialty handbook: heat-resistant materials*. 1997: Asm

International.
157. Chang, C.-S., *Fracture processes in simulated HAZ microstructures of stainless steel*. 2000, University of Birmingham.
158. Neumann, P., *The geometry of slip processes at a propagating fatigue crack—II.* Acta Metallurgica, 1974. **22**(9): p. 1167-1178.
159. Yan, J., H. Li, S. Yu, A. Rabiei, and P. Bowen, *A study on dwell-fatigue crack growth behaviour on an advanced austenitic stainless steel.* To be submitted.
160. Janssen, M., J. Zuidema, and R. Wanhill, *Fracture Mechanics - 2nd Edition.* 2004.
161. Saber, M., *Experimental and finite element studies of creep and creep crack growth in P91 and P92 weldments*. 2011, University of Nottingham Doctoral dissertation.

CRACK GROWTH IN ALLOY 709 AT HIGH TEMPERATURES UNDER FATIGUE, CREEP AND DWELL-FATIGUE LOADS

Volume 2

JIN YAN

A thesis submitted to University of

Birmingham for the degree of

Doctor of Philosophy

School of Metallurgy and

Materials College of Engineering and

Physical Science

University of Birmingham

May 2021

Chapter 2

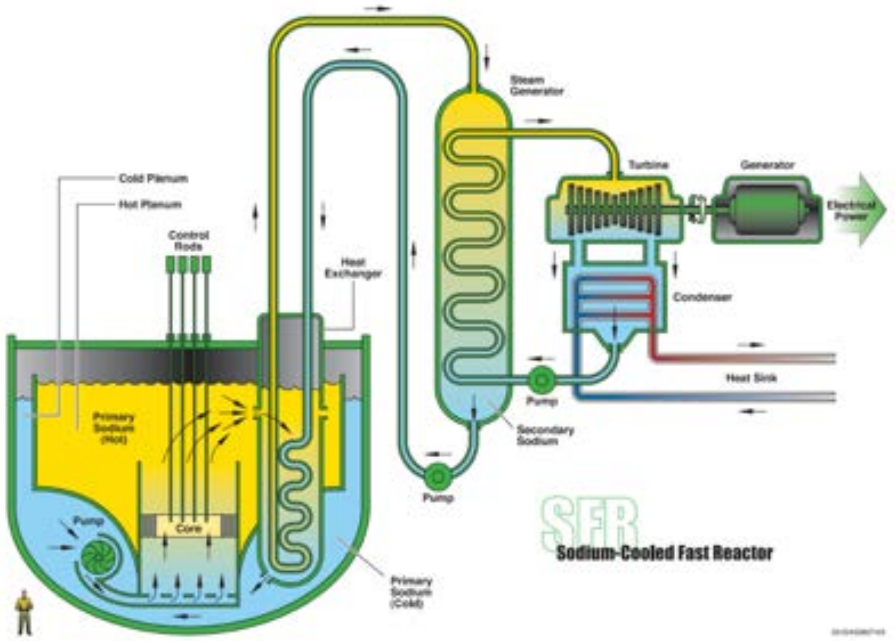

Figure 2.1 The Sodium-cooled Fast Reactor system [7].

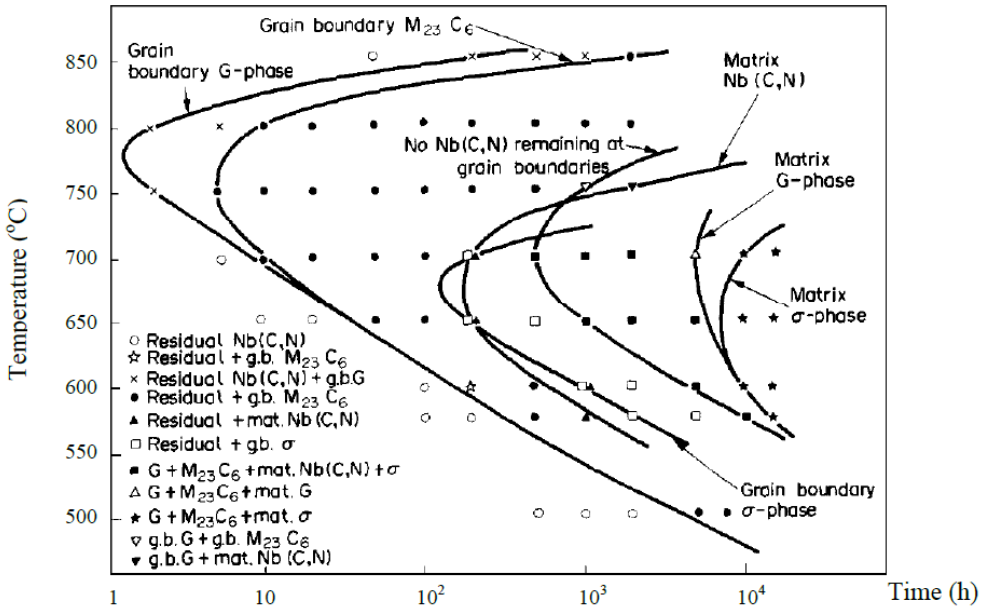

Figure 2.2 Time, Temperature, Precipitation (TTP) diagram for 20Cr-25Ni Nb-stabilised stainless steel [13].

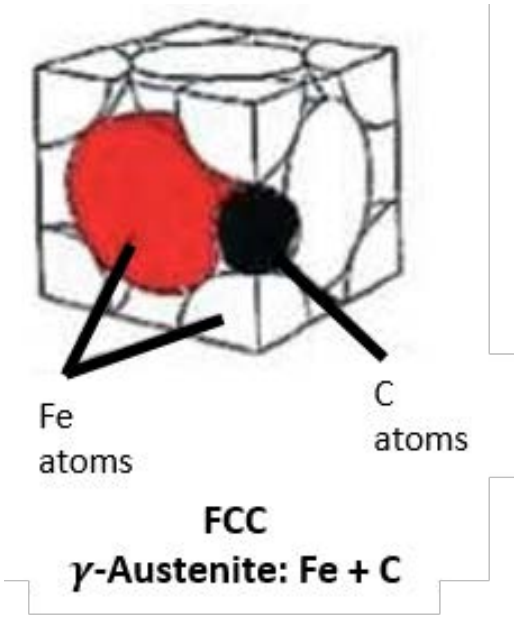

Figure 2.3 Face centred cubic (FCC) structure of austenitic stainless steel [19].

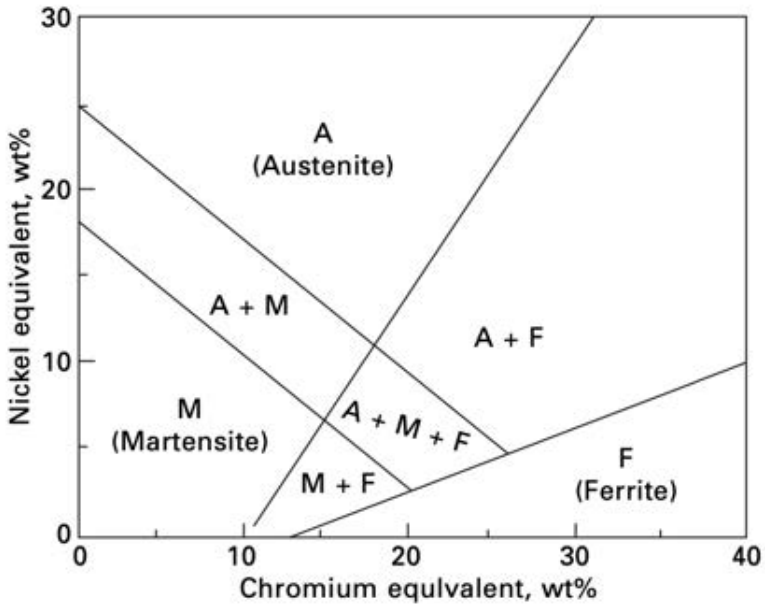

Figure 2.4 A modified Schaeffler diagram showing stable phases for a given alloy after heat treatment for 30 minutes at 1050°C and then quenching in water. The nickel and chromium equivalent expressions, which, using compositions in weight percent, are given as follows: Ni_{eq} = Ni + Co + 30C + 25N + 0.5Mn + 0.3Cu, and the chromium equivalent is given by: Cr_{eq} = Cr + 2Si + 1.5Mo + 5V + 5.5Al + 1.75Nb + 1.5Ti + 0.75W [42].

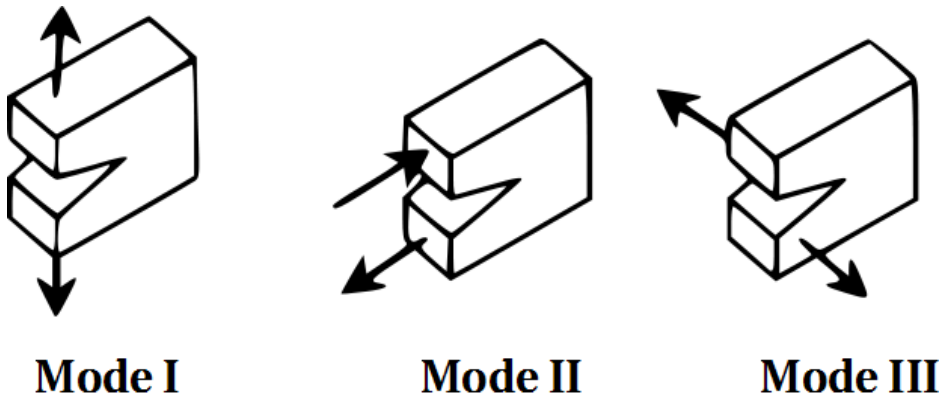

Figure 2.5 Three basic modes of crack loading [47].

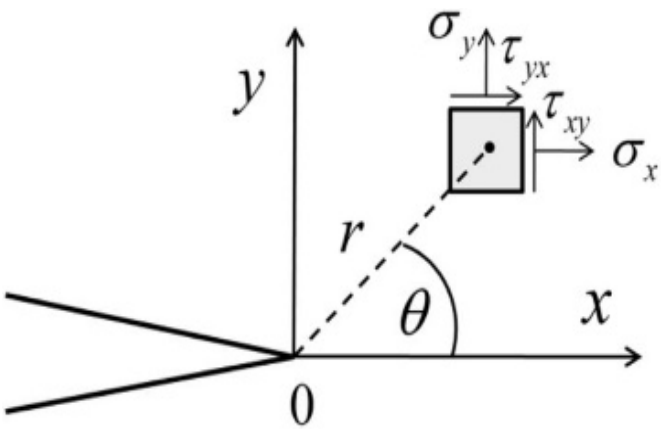

Figure 2.6 The Irwin co-ordinate system presenting the stress around crack tip in the stress plan [47].

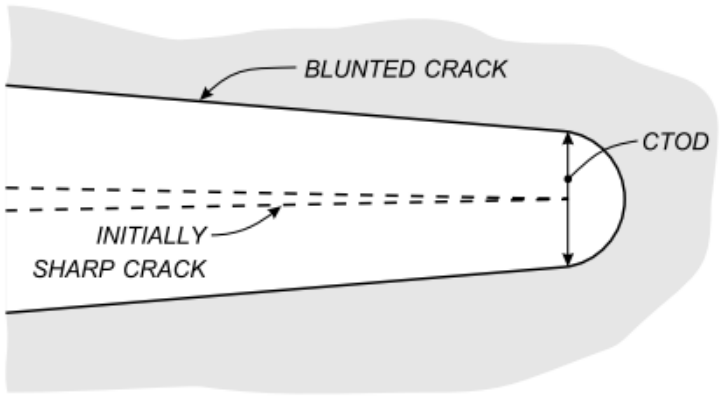

Figure 2.7 Typical displacement at crack tip [160] showing a small increment of crack extension accompanied by a marked amount of crack blunting.

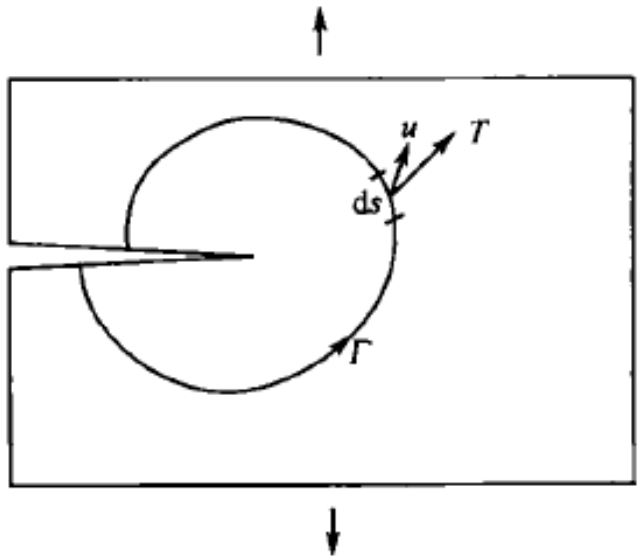

Figure 2.8 J-integral paths and areas [56].

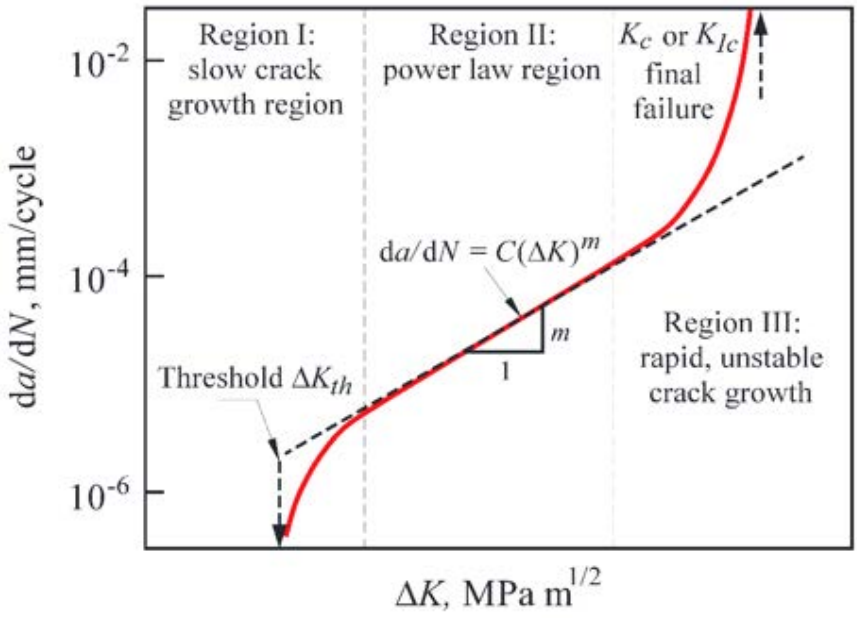

Figure 2.9 Typical fatigue crack growth resistance curve [73].

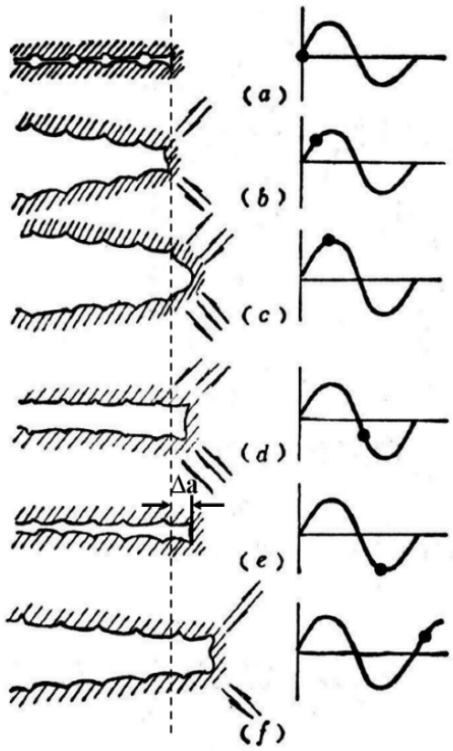

Figure 2.10 Crack tip blunting in fatigue crack growth in stage II showing (a) zero load condition; (b) small tensile load; (c) large tensile load; (d) small unloading; (e) maximum compressive load, and (f) small tensile load [75].

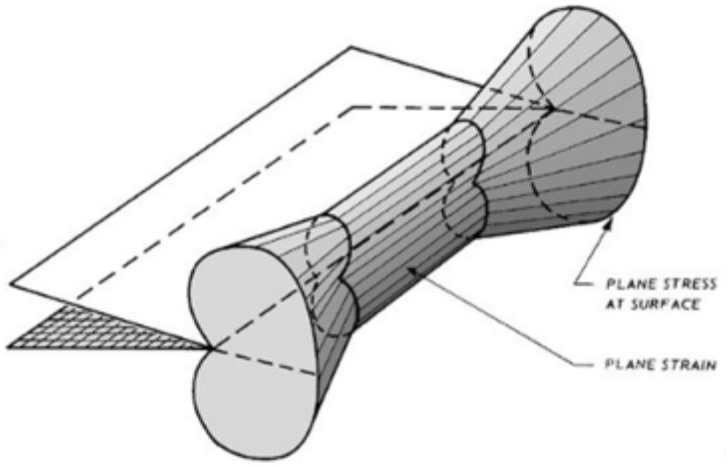

Figure 2.11 Plastic zone in a finite plate [81].

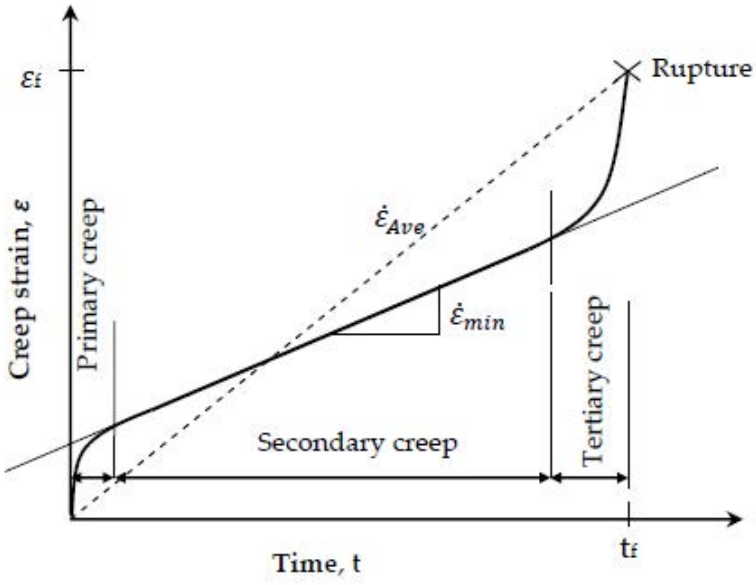

Figure 2.12 Typical creep curve shows three creep regions [161].

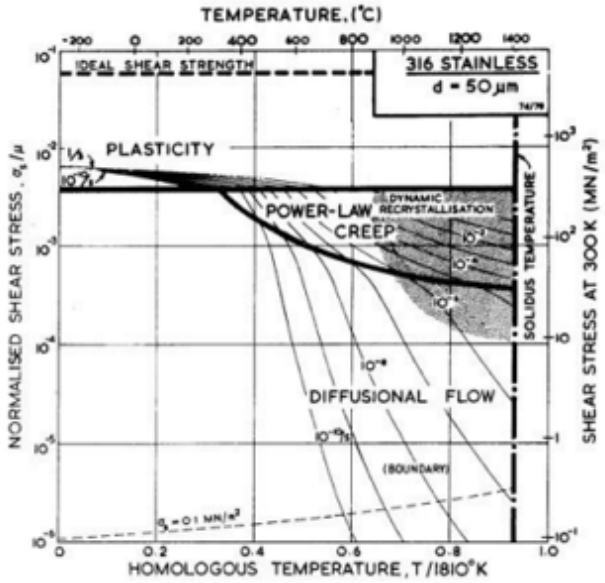

Figure 2.13 Deformation-mechanism map for Type 316 SS with grain size of 50 μm in the secondary creep region [86].

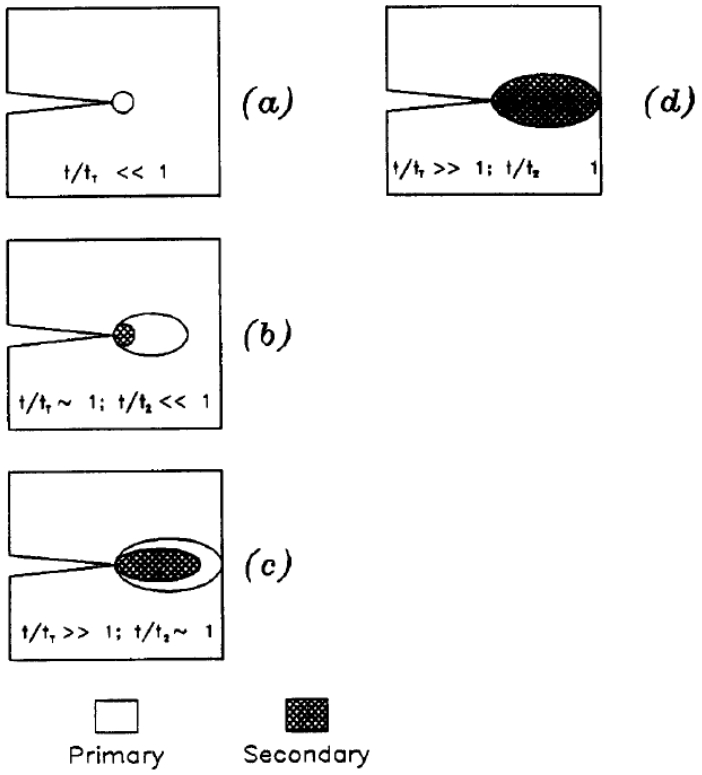

Figure 2.14 Different stages of creep deformation under static loading [98]. (a) small-scale primary creep, (b) transition creep, where a secondary creep zone extends in the primary creep zone, (c) primary creep conditions with a steady secondary creep zone, and (d) extension of secondary creep.

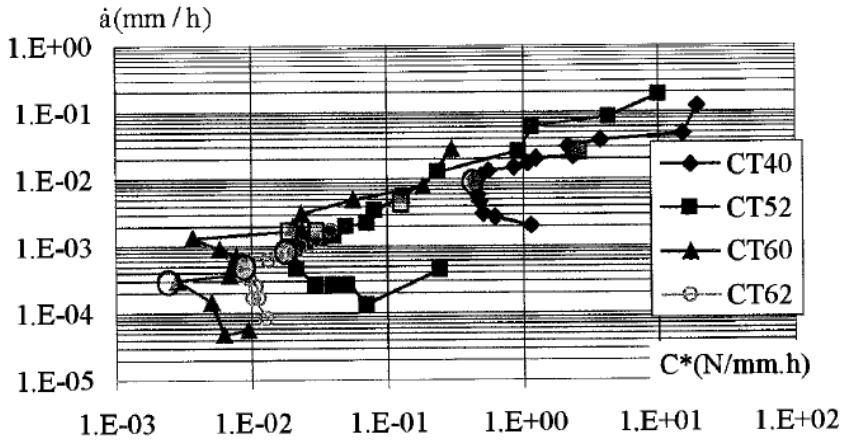

Figure 2.15 Creep crack growth resistance curve for 316L(N) stainless steel showing the 'tail' part [102].

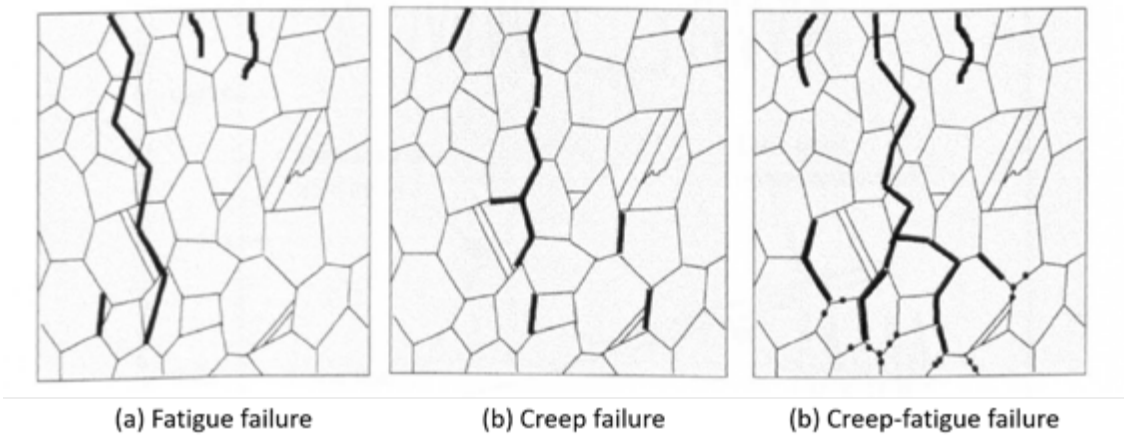

Figure 2.16 Three possible failure modes at high temperatures [157].

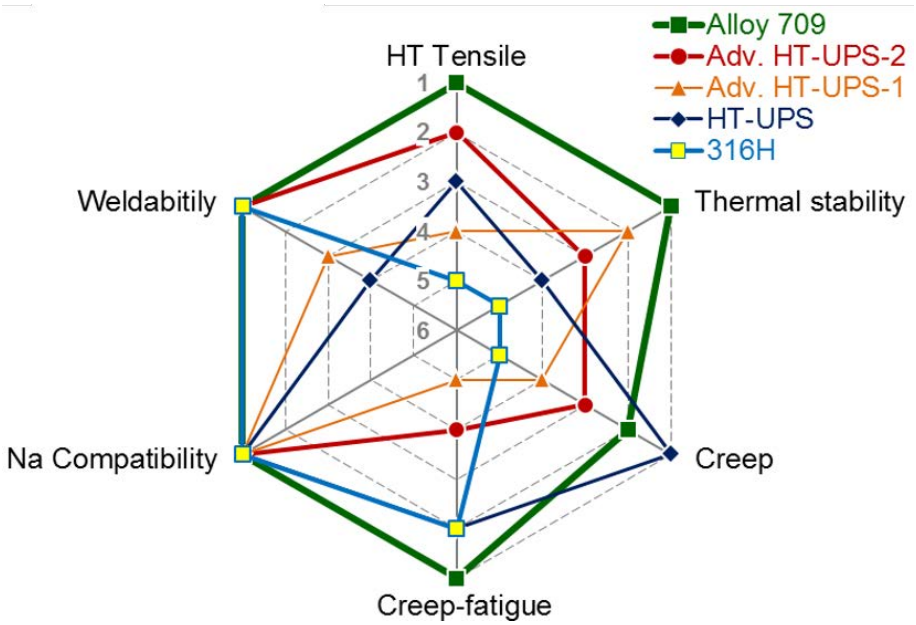

Figure 2.17 Comparison of Alloy 709, HT-UPS alloys and 316H [116].

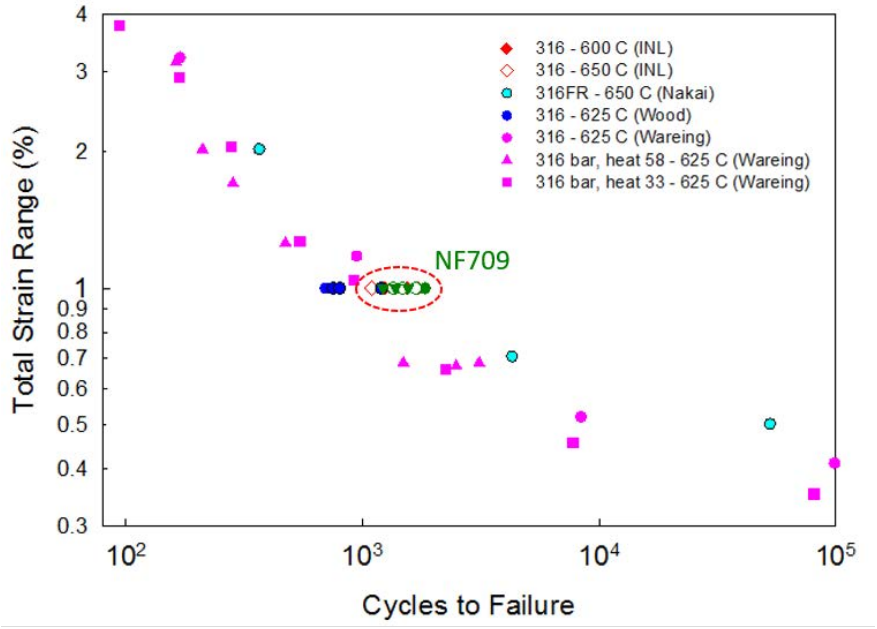

Figure 2.18 Fatigue life compared with NF709 and 316 stainless steel [123].

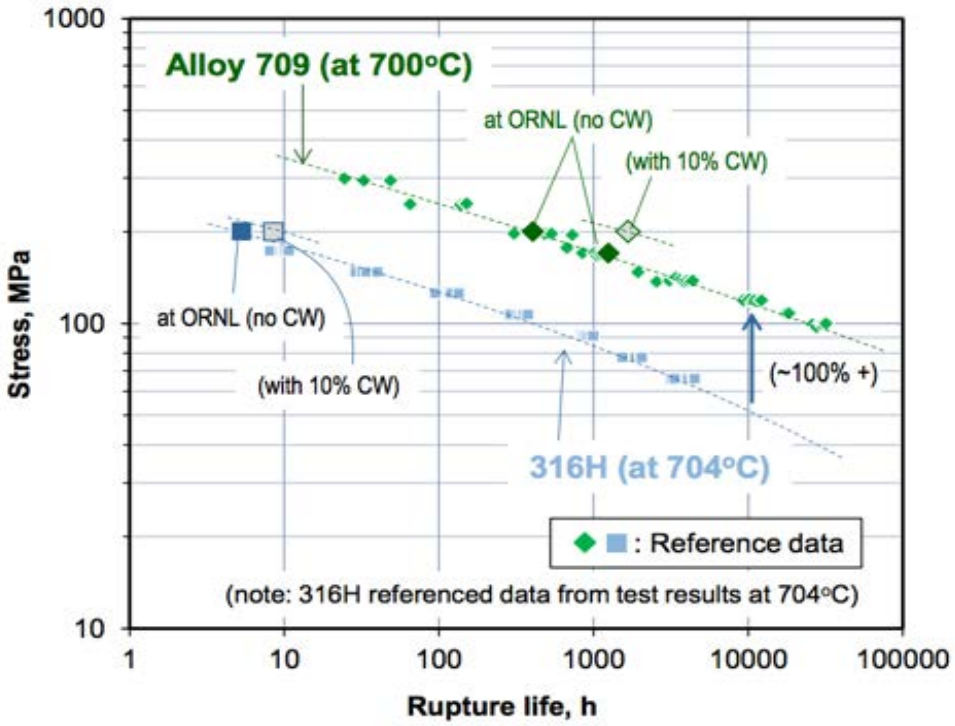

Figure 2.19 Creep rupture properties of Alloy 709 and 316H [116].

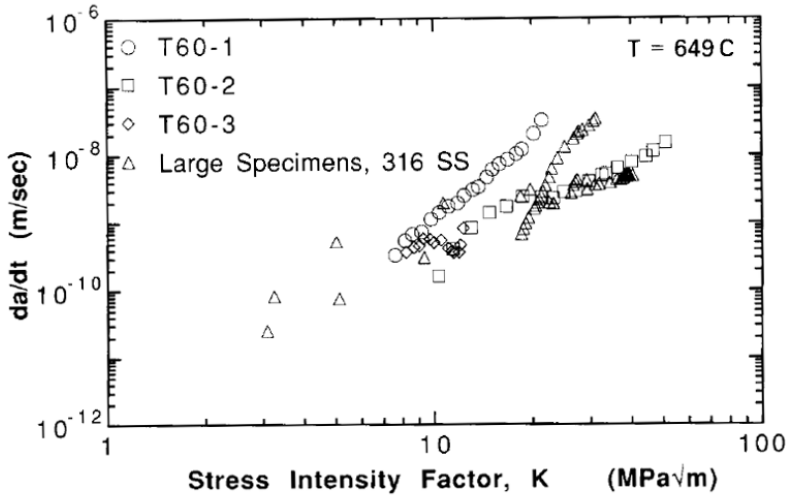

Figure 2.20 Creep crack growth rate, da/dt, in correlation with K in 316 stainless steel tested in large and miniature testpieces under static-state creep conditions at 649°C [109].

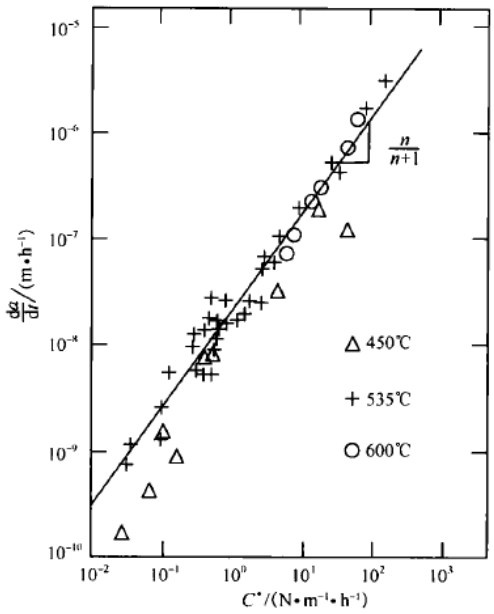

Figure 2.21 Creep crack growth rate, da/dt, versus the C*-integral in a 1Cr-1/2Mo steel under static-state creep conditions at 450, 535 and 600°C under static loading of 52 MPa [103].

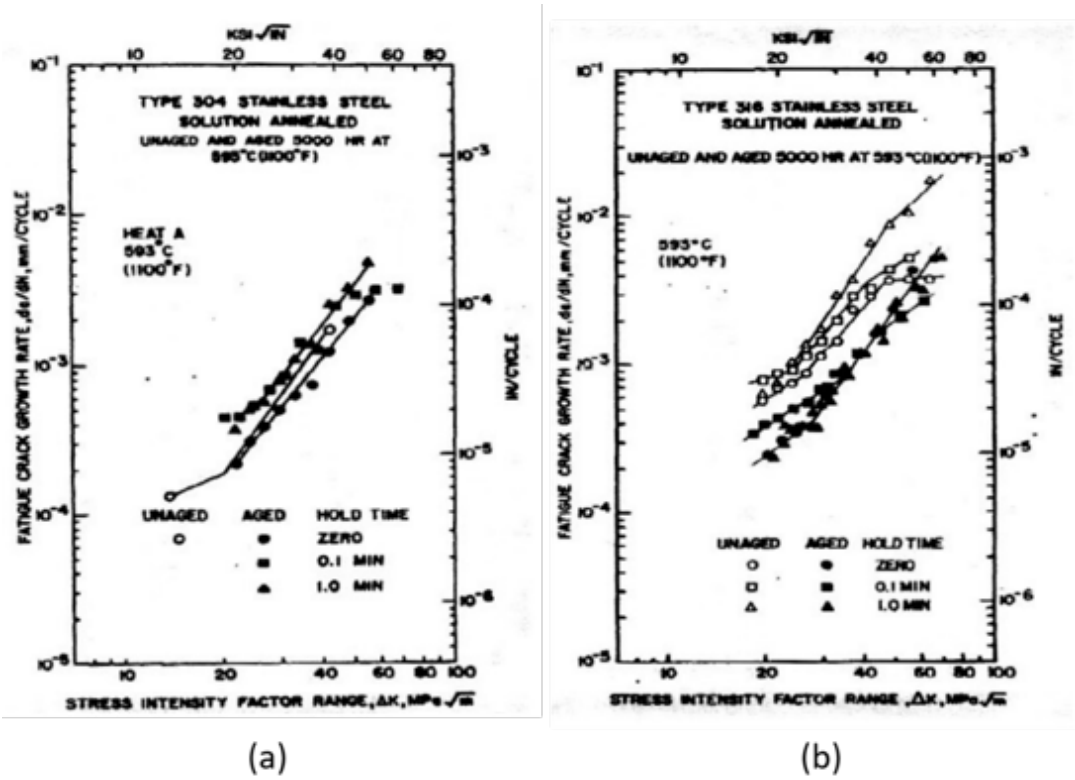

Figure 2.22 Dwell-fatigue crack growth behaviour in as-received and aged solution annealed 304 and 316 SS at 593°C [137].

Chapter 3

Table 3.1 Chemical composition of Alloy 709 and 316H (wt%).

	Cr	Ni	Mo	N	Ti	Nb
Alloy 709	19.69	25.00	1.46	0.14	<0.001	0.23
316H	16.61	10.26	2.006	0.0315	0.005	0.005
	C	Mn	Si	P	S	B
Alloy 709	0.063	0.88	0.28	<0.005	<0.001	0.0022
316H	0.041	1.536	0.329	0.036	0.001	-

Table 3.2 Testing condition and results of creep tests in as-received Alloy 709.

Sample ID	**Temperature (°C)**	**Stress (MPa)**
C1	750	120
C2	650	250
C3	550	450
C4	550	420
C5	550	390

Table 3.3 Test matrix for high temperature fatigue crack growth in Alloy 709.

Sample ID	Plate ID	P_{max} (kN)	Orientation	Temperature (°C)	Environment	Load Ratio	Side-groove (mm)
B1-2	011593-1-B	8	L-T	550	Air	0.1	0.5
S6	011502-H6	8	L-T	550	Vacuum	0.1	0.5
B1-3	011593-1-B	8	L-T	650	Air	0.1	0.5
B1-7	011593-1-B	8	ST-L	650	Air	0.1	1
B1-8	011593-1-B	10	ST-L	650	Air	0.5	1
B1-9	011593-1-B	10	ST-L	650	Air	0.5	0.5
A1-5	011502-H6	8	L-T	650	Vacuum	0.1	1
B1-6	011593-1-B	8	L-T	750	Air	0.1	0
B1-10	011593-1-B	8	ST-L	750	Vacuum	0.1	1

Note: A-from plate 011502-H6.
B-from plate 011593-1-B, outside specification microstructure.

Table 3.4 Test matrix for creep crack growth in Alloy 709.

Sample ID	Material (condition)	Temperature (°C)	Load (kN)
CS1	Alloy 709 (as-received)	550	8
A1-3	Alloy 709 (as-received)	650	8
CS4	Alloy 709 (as-received)	650	8
HT1	Alloy 709 (aged)	650	8 10
HT2	Alloy 709 (aged)	650	10 12
A2-1 (2-inch)	Alloy 709 (as-received)	650	30
CS2	Alloy 709 (as-received)	750	8
316H S2	316H	650	8
316H S3	316H	650	8

Note: Alloy 709 material with uniform, equiaxed grain structure.

Table 3.5 Test matrix for dwell-fatigue crack growth in Alloy 709.

Sample ID	Temperature	Environment
A1-11	550°C	Air
S1	550°C	Air
A1-1	650°C	Air
A1-8	650°C	Air
A1-10	650°C	Vacuum
CT-5	750°C	Air
316H S1	650°C	Air

Note: Alloy 709 material with uniform, equiaxed grain structure.

Figure 3.1 Macrograph of the tensile testpiece.

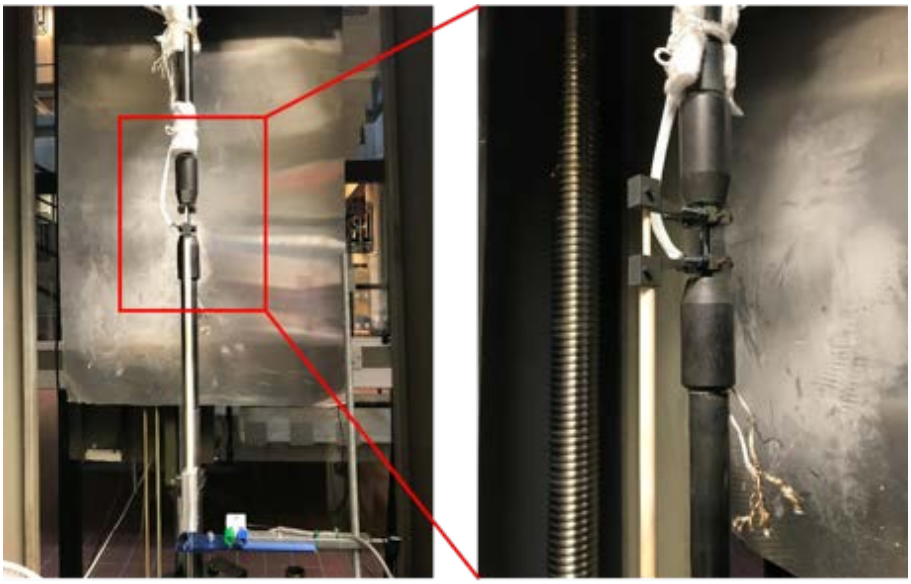

Figure 3.2 Zwick screw driven tensile testing machine with an extensometer.

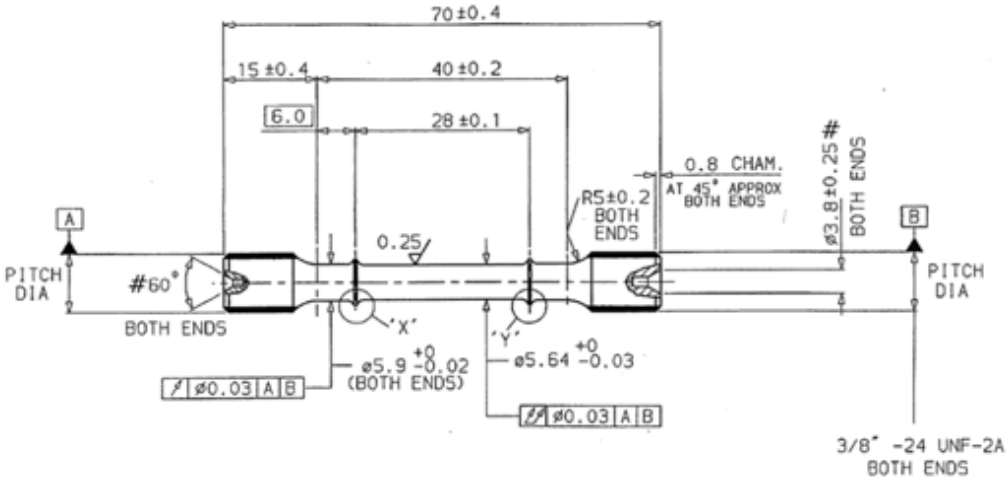

Figure 3.3 Schematic drawing of the cylindrical samples used for creep tests.

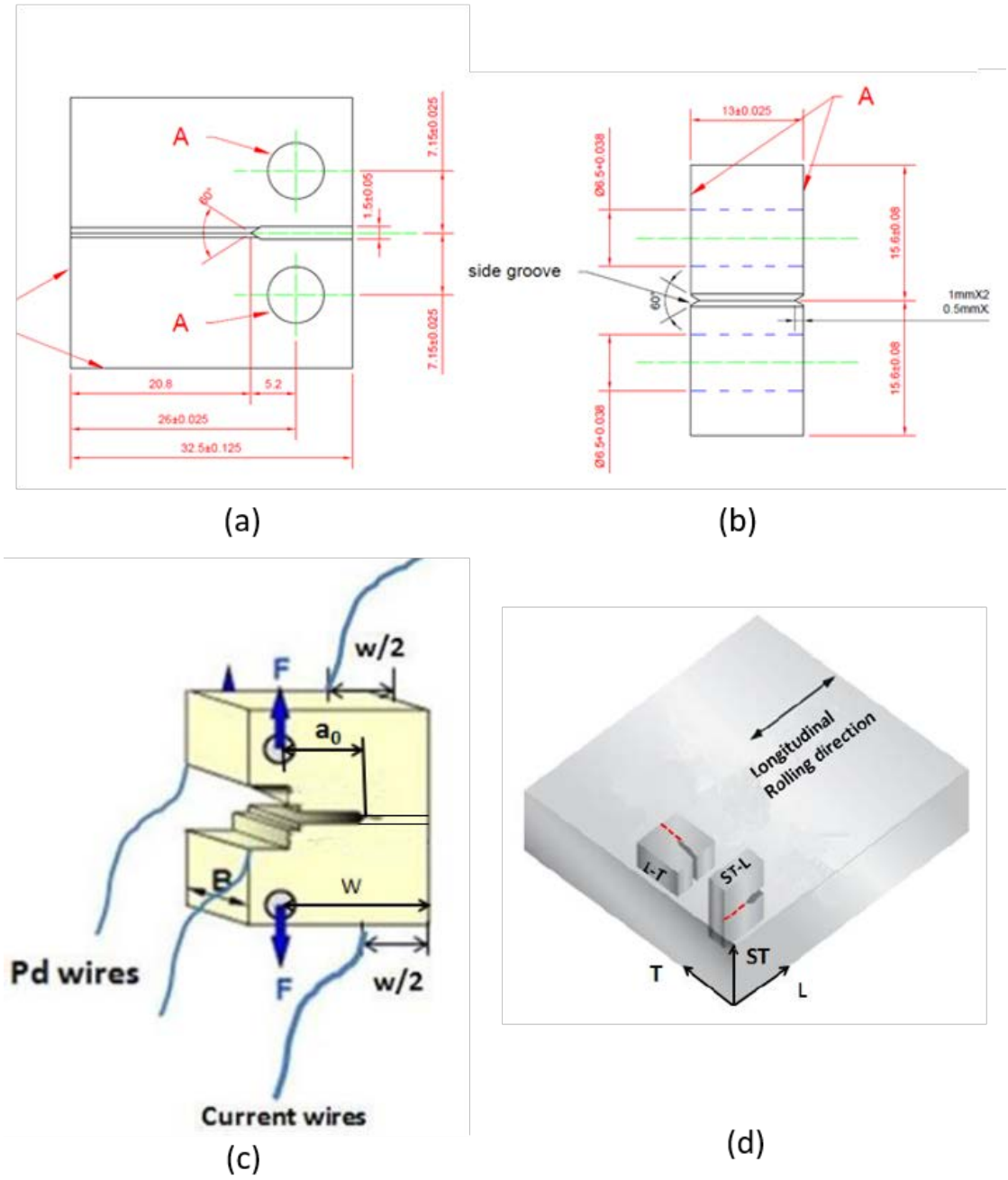

Figure 3.4 (a) and (b) Compact Tension (CT) testpiece for high temperature fatigue and dwell-fatigue crack growth resistance study, (c) wiring method for d.c.p.d method and (d) testpieces with two different orientations: L-T and ST-L.

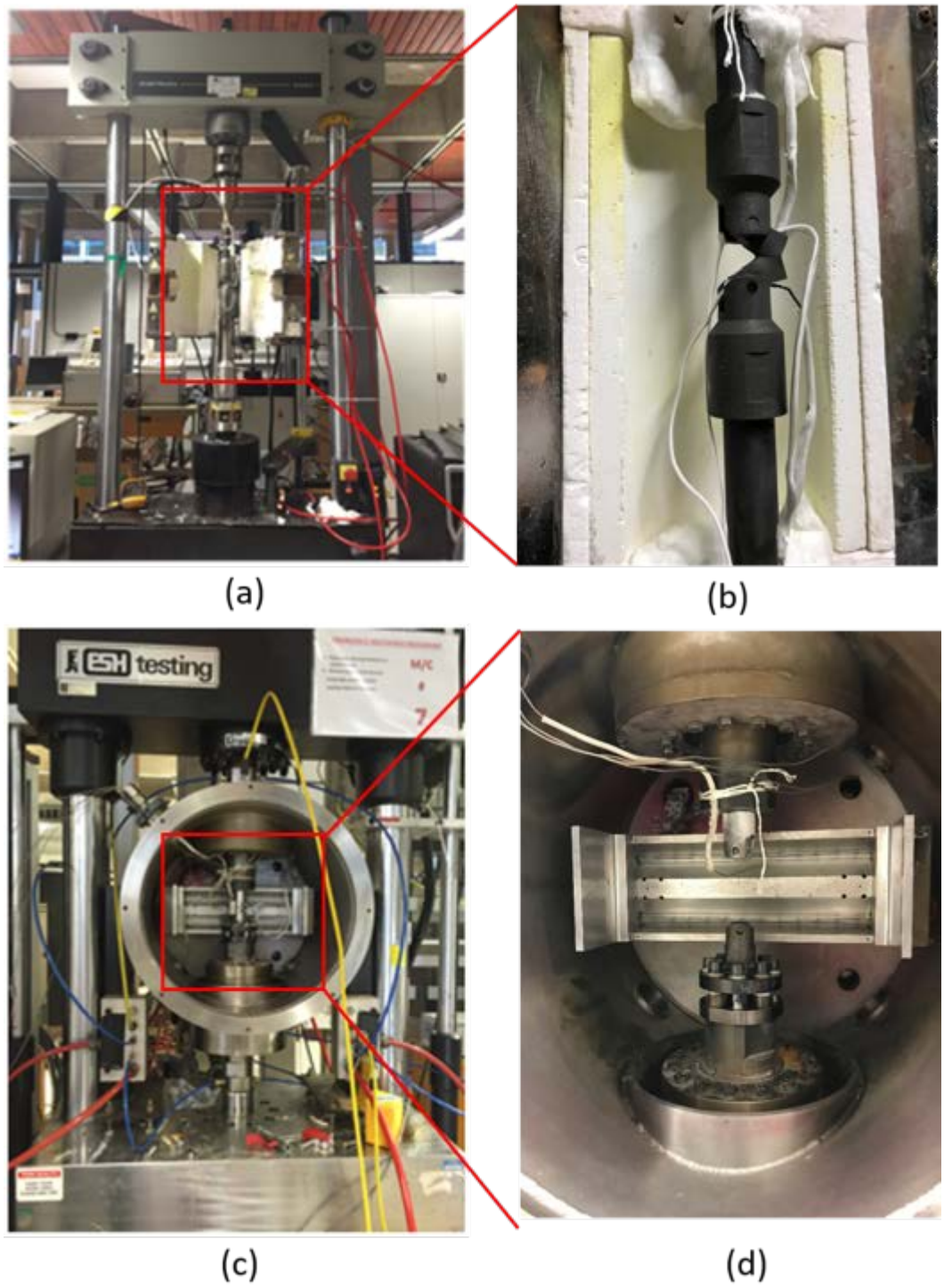

Figure 3.5 (a) and (b) Instron 8501 screw driven testing machine with a ceramic line resistance furnace and d.c.p.d unit; (c) and (d) ESH servo-hydraulic testing machine with a vacuum chamber and d.c.p.d unit.

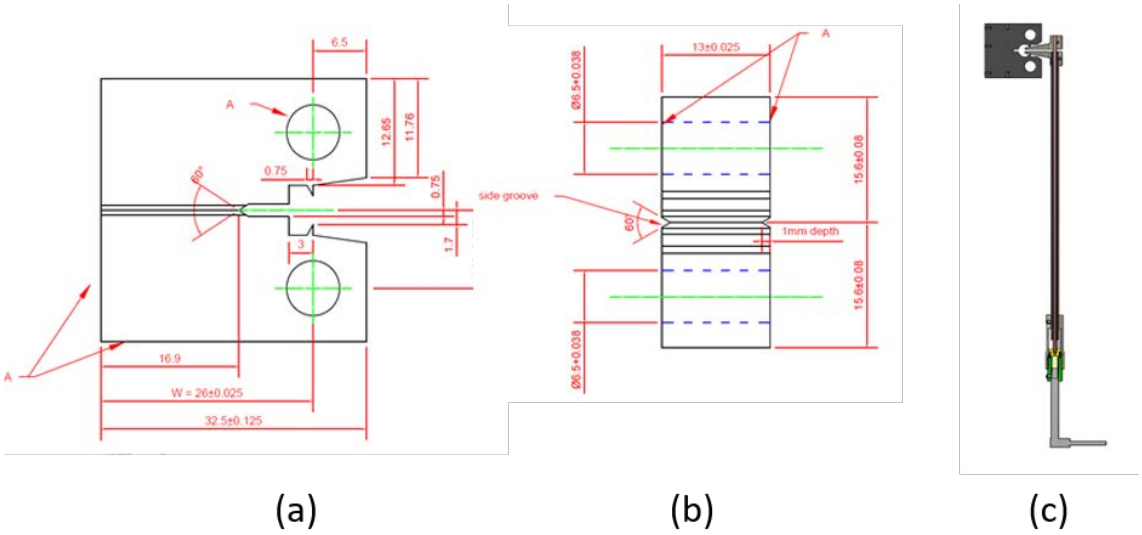

Figure 3.6 (a) and (b) Schematic drawing of CT testpiece for creep crack growth tests and (c) shows how does an extensometer is attached to the testpiece.

Figure 3.7 Zwick screw-driven servo-electric testing machine with a resistance furnace, d.c.p.d unit and extensometer.

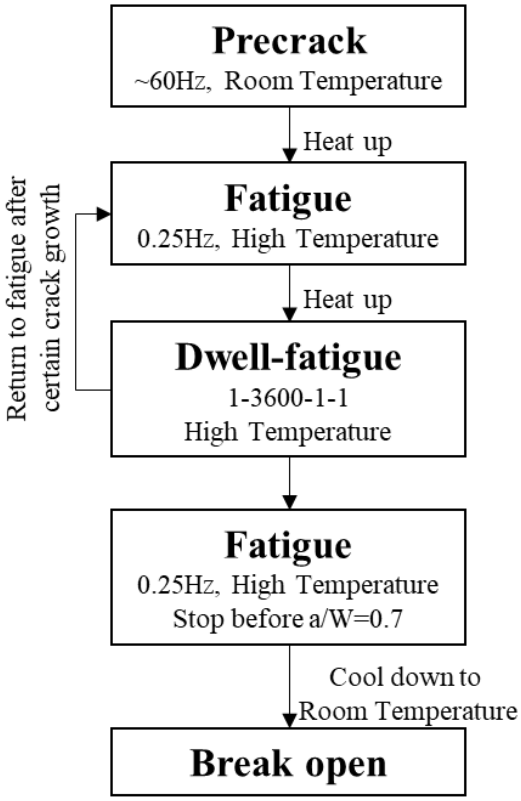

Figure 3.8 Testing procedure of dwell-fatigue crack growth tests.

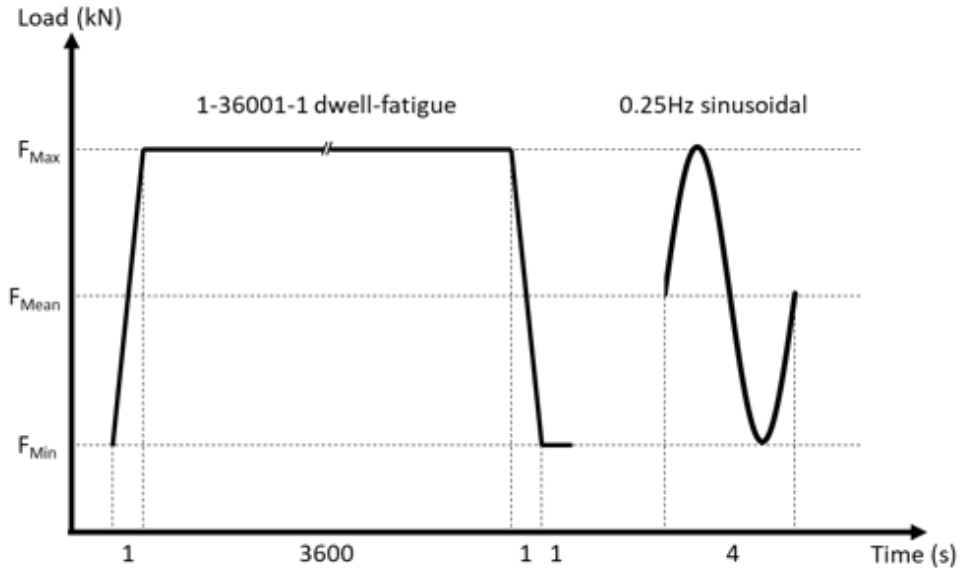

Figure 3.9 1-3600-1-1 dwell fatigue loading waveform and 0.25Hz sinusoidal fatigue waveform.

Chapter 4

Table 4.1 Summary of observations of secondary phases in the as-received and aged Alloy 709.

Phase	Location/Morphology	Typical size	As-received Alloy 709	Aged Alloy 709								
				550°C			650°C			750°C		
				500 h	1000 h	2000 h	500 h	1000 h	2000 h	500 h	1000 h	2000 h
Nb(CN)	Anywhere (rectangular) Anywhere (globular)	1 to 10 μm 50 to 400 nm	√	√	√	√	√	√	√	√	√	√
$M_{23}C_6$	Grain boundary (globular) CTB and ITB (plates) Around Nb(CN) (cuboidal)	100 to 500 nm					√	√	√	√	√	√
θ phases $(Cr,Mo)_3(Ni,Fe)_2SiN$	Grain boundary (globular) CTB and ITB (plates) Around $M_{23}C_6$ (cuboidal)	100 to 500 nm						√	√	√	√	√
Z-phase CrNbN	Dislocation (rods) On $M_{23}C_6$ (rod)	5 to 30 nm	√	√	√	√	√	√	√	√	√	√

Table 4.2 Tensile properties of Alloy 709.

Sample ID	temperature (°C)	0.2% Proof stress (MPa)	Tensile strength (MPa)	Fracture strain (%)	Area reduction (%)
T4	RT	303	678	48	78
T3	550	173	568	45	60
T2	650	172	474	38	46
T1	750	168	326	49	70
HT1	RT	363	702	37	57
HT3	550	230	527	28	67
HT2	650	225	428	31	68
HT4	750	204	275	42	88

Note: T- the as-received microstructure material;
HT- the Aged microstructure material.

Table 4.3. True tensile strength, fracture stress and strain hardening exponent of Alloy 709.

Sample ID	temperature (°C)	True stress at maximum load (MPa)	True strain at maximum load (%)	Fracture stress (MPa)	Strain hardening exponent, n
T4	RT	918	31	1909	0.32
T3	550	796	36	1345	0.40
T2	650	633	31	741	0.35
T1	750	394	22	576	0.26
HT1	RT	864	22	1302	0.23
HT3	550	636	20	1282	0.28
HT2	650	501	17	781	0.23
HT4	750	304	14	742	0.12

Table 4.4 Summary of parameters (A and m) in Paris regime for fatigue crack growth of Alloy 709 for ΔK in MPa$\sqrt{m}$ and da/dN in mm/cycle.

Temperature	Sample ID	P_{max} (kN)	Side-groove depth (mm)	Environment	Orientation	Load Ratio	A (mm/cycle)	m
550°C	B1-2	8	0.5	Air	L-T	0.1	5.91×10^{-9}	3.33
550°C	S6	8	0.5	Vacuum	L-T	0.1	2.79×10^{-10}	4.06
650°C	B1-3	8	0.5	Air	L-T	0.1	1.28×10^{-8}	3.21
650°C	B1-7	8	1.0	Air	ST-L	0.1	7.12×10^{-9}	3.40
650°C	B1-8	10	1.0	Air	ST-L	0.5	6.48×10^{-7}	2.12
650°C	B1-9	10	0.5	Air	ST-L	0.5	3.31×10^{-7}	2.31
650°C	A1-5	8	1.0	Vacuum	L-T	0.1	7.04×10^{-10}	3.86
750°C	B1-6	8	0	Air	L-T	0.1	3.17×10^{-7}	2.43
750°C	B1-10	8	1.0	Vacuum	ST-L	0.1	7.25×10^{-10}	3.94

Table 4.5 Summary of minimum creep rates measured at 550, 650 and 750°C in the as-received Alloy 709.

Temperature (°C)	Stress (MPa)	Minimum creep rate (/h)	Creep exponent, n	Rupture life (h)	Fracture Strain (%)	Source
550	450	2.60E-03	5.3	1266	25	Swansea
	420	1.59E-03		Interrupted when the minimum creep rate is determined		Swansea
	390	1.31E-03				Swansea
650	250	8.50E-03	6.0	886	55	Swansea
	255	4.00E-03		-	-	ORNL
	215.8	2.00E-03		-	-	ORNL
	186.3	4.00E-04		-	-	ORNL
	156.9	3.00E-04		-	-	ORNL
750	120	2.00E-02	8.4	505	67	Swansea
	117.7	1.95E-02		-	-	ORNL
	98.1	3.47E-03		-	-	ORNL
	83.4	6.55E-04		-	-	ORNL
	73.6	1.39E-04		-	-	ORNL

Table 4.6 Summary of creep crack growth results of the as-received Alloy 709, aged Alloy 709 and 316H tested at 550, 650 and 750°C.

Sample ID	Material (condition)	Temperature (°C)	Load (kN)	Crack extension (mm)	Test duration (h)	Transition time (h)
CS1	Alloy 709 (as-received)	550	8	0.04	995	109.60
			8	0.10	884	
			8	0.20	1080	
			8	0.56	1002	
A1-3	Alloy 709 (as-received)	650	8	0.46	24	1.92
			8	2.25	244	
CS4	Alloy 709 (as-received)	650	8	3.24	2452	10.27
HT1	Alloy 709 (aged)	650	8	0.61	4080	12.48
			10	0.53	336	
HT2	Alloy 709 (aged)	650	10	0.26	335	7.80
			12	0.97	339	
A2-1 (2-inch)	Alloy 709 (as-received)	650	30	2.46	288	9.40
CS2	Alloy 709 (as-received)	750	8	4.13	163	0.13
316H S2	316H	650	8	4.77	7.5	0.19
316H S3	316H	650	8	2.38	11	0.04

Table 4.7 Summary of dwell-fatigue crack growth tests conducted on the as-received Alloy 709.

Temperature and Environment	Sample ID	DF loading block	$\Delta K_i \sim \Delta K_f$ (MPa√m)	Crack extension (mm)	Number of cycles	Failure mechanism
550°C Air	A1-11	1^{st}	20.0 ~ 20.1	0.02	90	TG
		2^{nd}	32.9 ~ 33.9	0.28	118	IG+TG
		3^{rd}	41.7 ~ 42.9	0.34	47	IG+TG
		4^{th}	47.3 ~ 51.2	1.1	55	IG+TG
550°C Air	S1	1^{st}	26.2 ~ 26.8	0.21	313	TG
		2^{nd}	34.7 ~ 37.2	0.61	328	IG+TG
		3^{rd}	48.1 ~ 49.0	0.13	22	IG+TG
650°C Air	A1-1	1^{st}	17.8 ~ 18.3	0.25	354	TG
		2^{nd}	31.8 ~ 39.7	1.88	753	IG
		3^{rd}	45.0 ~ 86.2	3.76	93	D
650°C Air	A1-8	1^{st}	27.0 ~ 27.6	0.24	54	TG
		2^{nd}	34.4 ~ 38.3	0.88	72	IG
		3^{rd}	51.8 ~ 69.8	1.72	3	D
650°C Vacuum	A1-10	1^{st}	18.8 ~ 18.9	0.05	15	TG
		2^{nd}	30.5 ~ 31.9	0.41	85	IG
		3^{rd}	43.5 ~ 58.0	1.90	26	IG+D
750°C Air	S-5	1^{st}	18.9 ~ 22.2	1.56	189	IG+D
		2^{nd}	24.1 ~ 29.5	2.02	75	IG+D
		3^{rd}	30.4 ~ 48.9	2.21	33	D
650°C Air	316H S1	1^{st}	21.2 ~ 26.2	2.18	448	IG
		2^{nd}	32.5 ~ 42.9	2.42	53	D
		3^{rd}	52.4 ~ 49.8	0.36	0.5	D

DF: Dwell-fatigue; ΔK_i and ΔK_f: initial and final stress intensity factor range;
TG: Transgranular fatigue; IG: Intergranular; D: Ductile fracture
CCG: Crack growth rate.

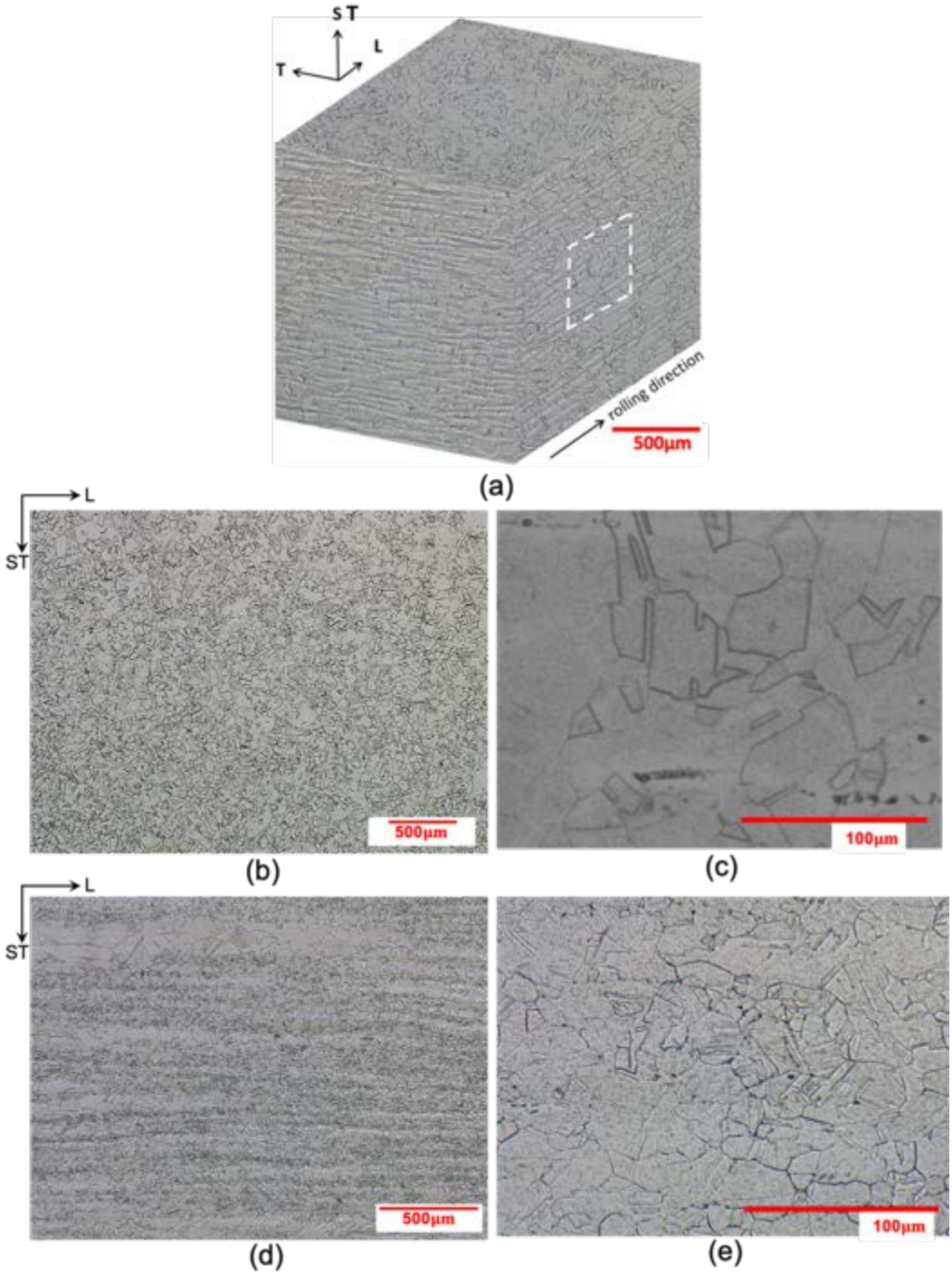

Figure 4.1 (a) Optical micrographs of etched as-received Alloy 709, numbered 011502 - H6, (b) Higher magnification of etched as-received optimised Alloy 709, numbered 011502-H6, (c) close-up of (b). (d) Optical images of etched off-specified as-received Alloy 709, numbered 011593-1-B, (e) close-up of (d). All specimens were electrochemically etched by 10% oxalic acid, ST-L: normal to the rolling direction.

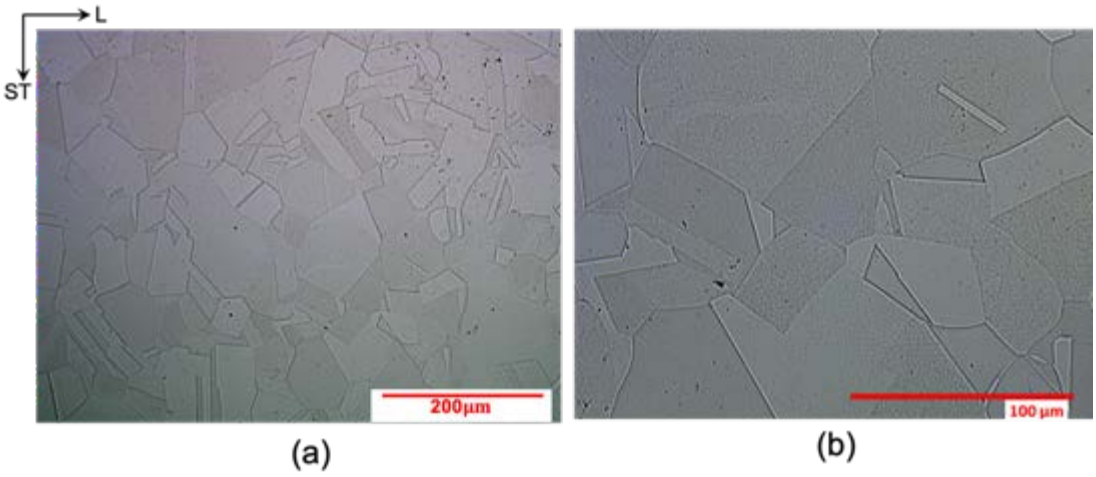

Figure 4.2 (a) Optical images of etched 316H, (b) close-up of (a). All specimens were electrochemically etched by 10% oxalic acid, ST-L: normal to the rolling direction.

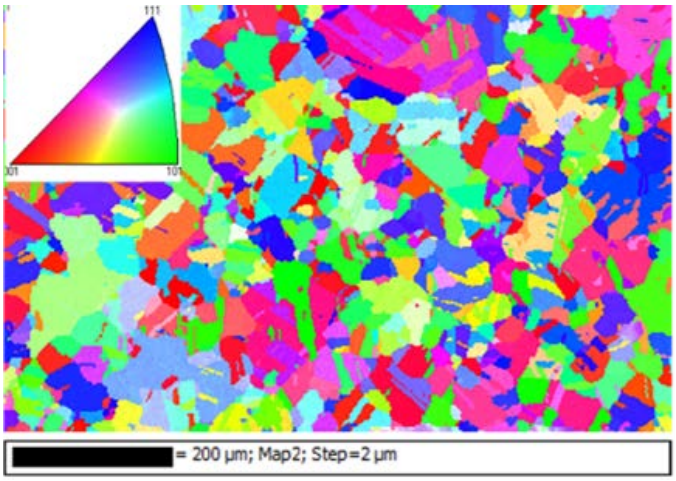

Figure 4.3. Inverse Pole Figure (IPF) mapping of the as-received optimised Alloy 709.

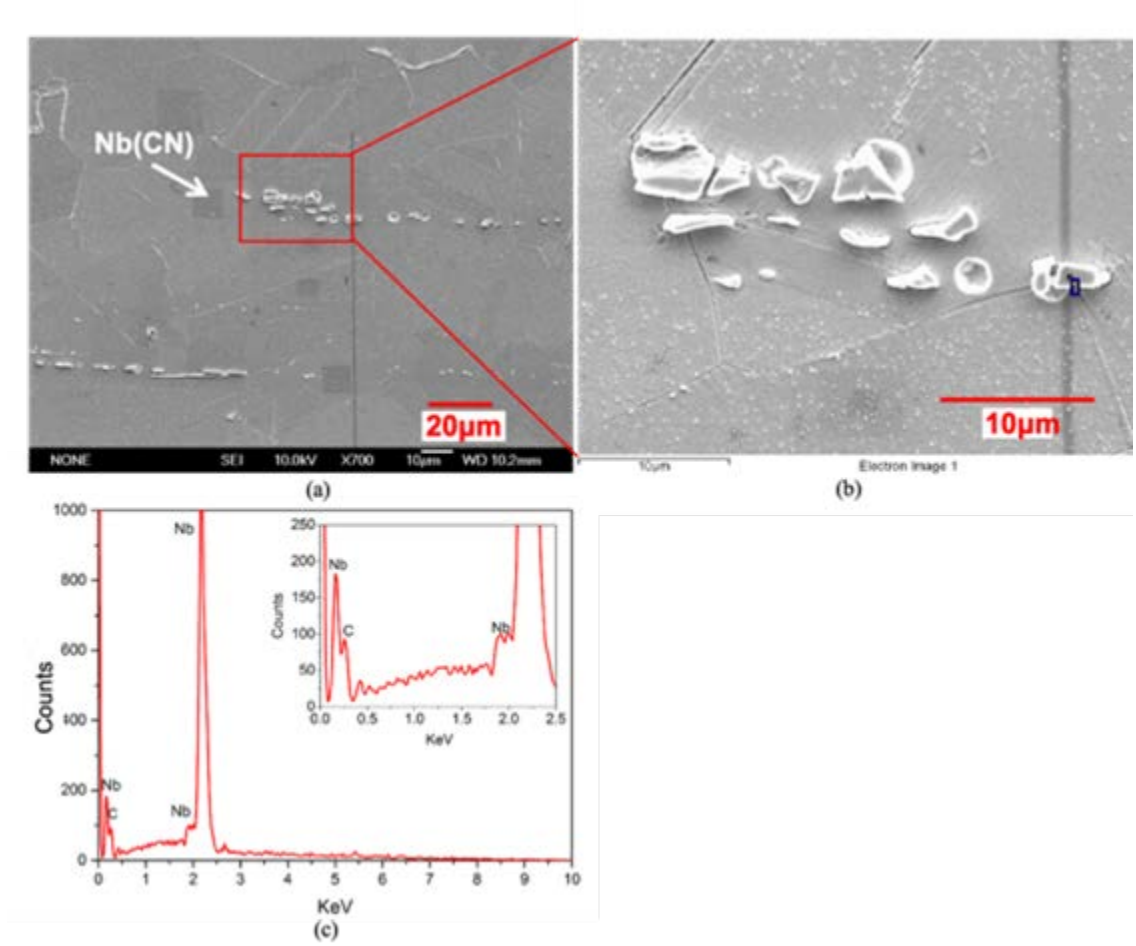

Figure 4.4 (a) BSE image of the as-received Alloy 709 showing a banded white inclusion, (b) close-up of (a) and (c) EDX chemical composition analysation confirmed the white inclusions are primary Nb-rich carbonitrides.

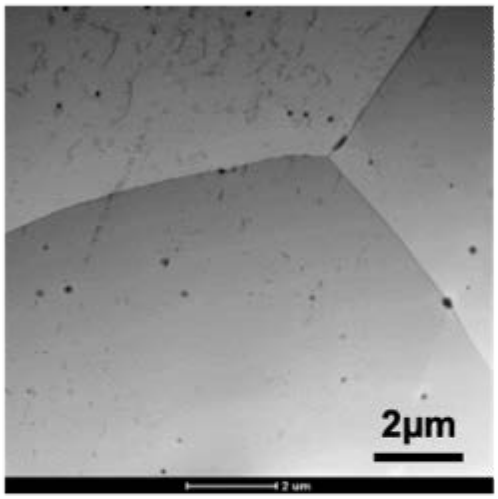

(a)

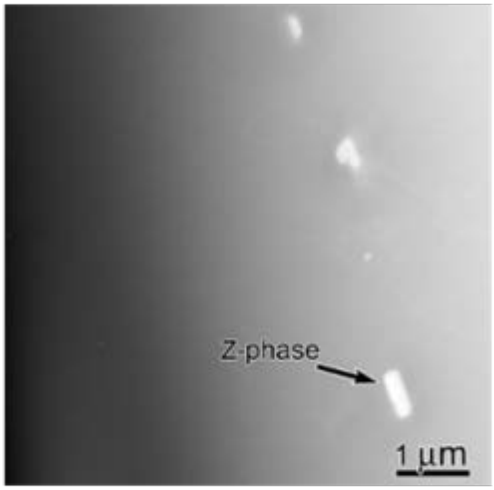

(b)

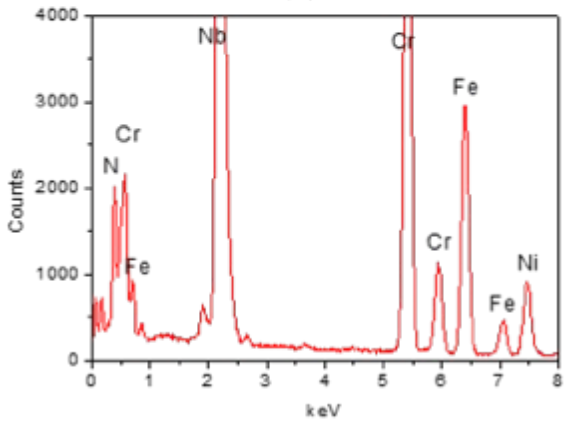

(c)

Figure 4.5 (a) TEM images of as-received Alloy 709, showing the nano-sized precipitates distributed in grain interior, (b) TEM image shows the existence of rod-shaped phases and (c) The EDX spectrum confirmed they are Z-phases.

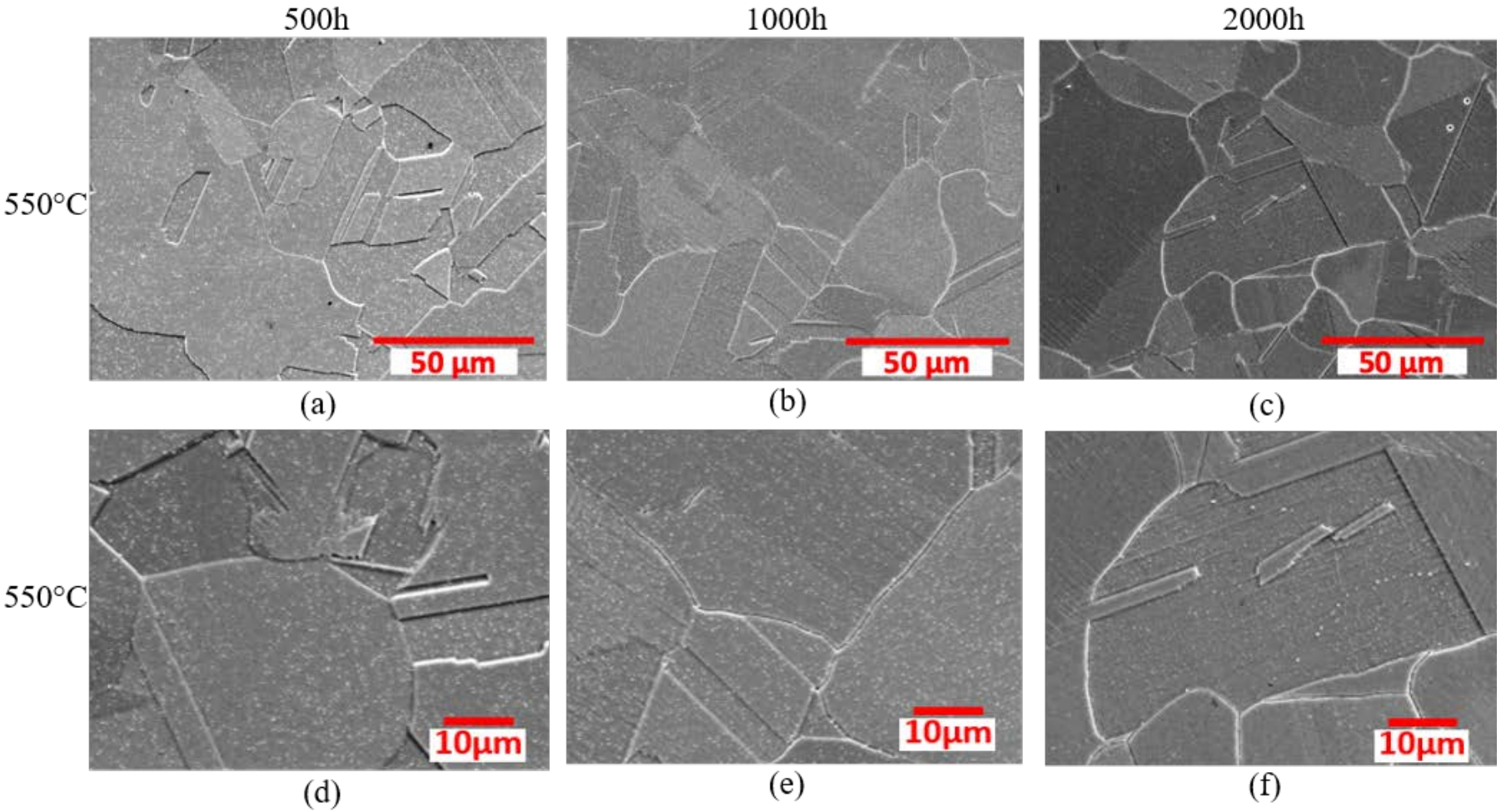

Figure 4.6 SEM images of Alloy 709 aged at 550°C for (a) 500 hours, (b) 1000 hours and (c) 2000 hours (10% oxalic acid electrochemically etched), (d), (e), (f) close-up of (a), (b), (c).

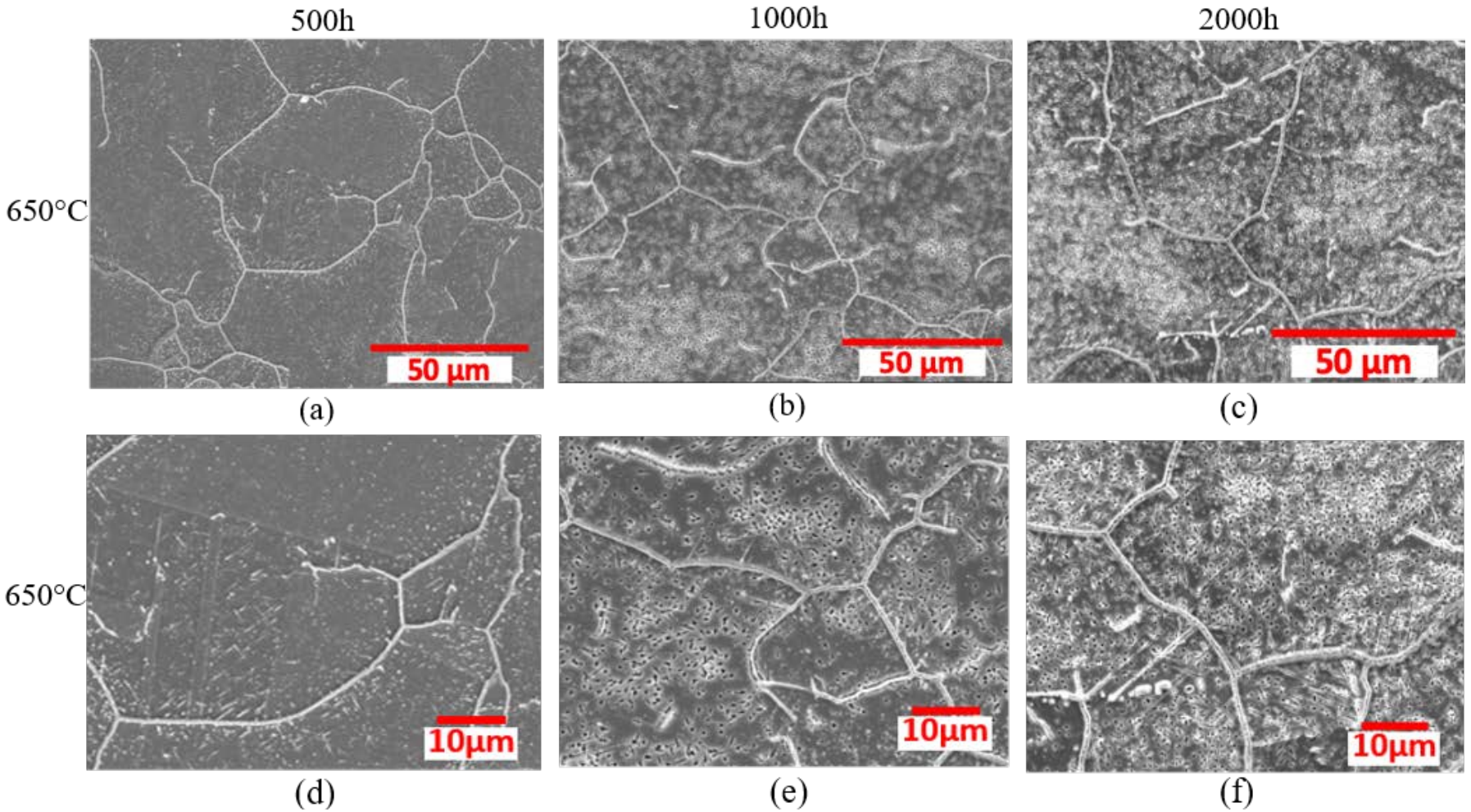

Figure 4.7 SEM images of Alloy 709 aged at 650°C for (a) 500 hours, (b) 1000 hours and (c) 2000 hours (10% oxalic acid electrochemically etched), (d), (e), (f) close-up of (a), (b), (c).

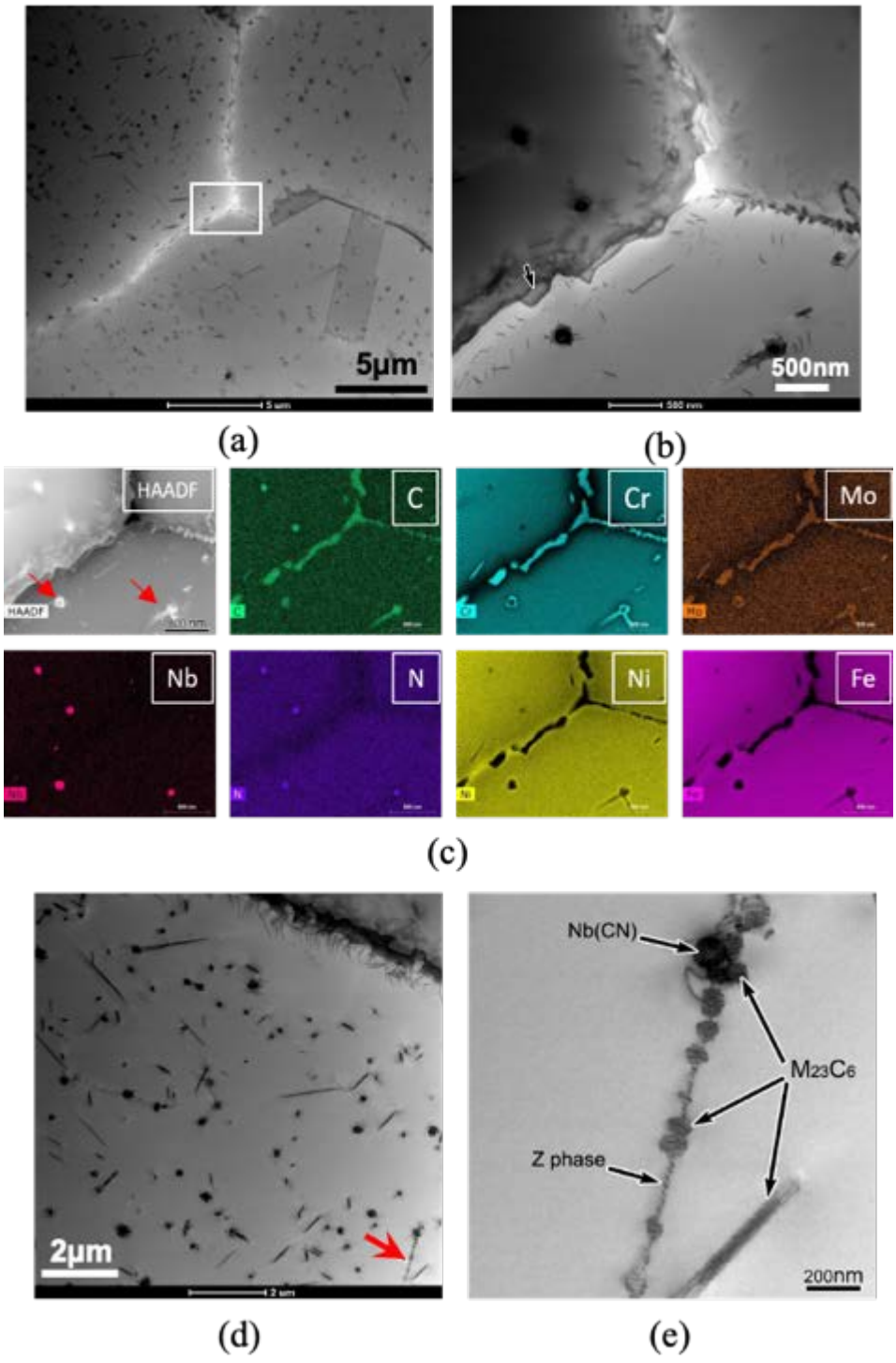

Figure 4.8 TEM images of Alloy 709 aged at 650°C for 500 hours, (a) TEM image showing the nearly continuous globular intergranular participates and a large number of small globular and plate-like intragranular particles. (b) Higher magnification image of grain boundaries in Figure 4.8a, (c) The EDX spectrum confirmed they are $M_{23}C_6$ carbides, (d) TEM micrograph for globular and plate-like intragranular particles in Figure 4.8a and (e) TEM confirmed the existence of Z-phases, Nb(CN) and $(CrMo)_{23}C_6$ on the dislocation (arrowed in Figure 4.8d).

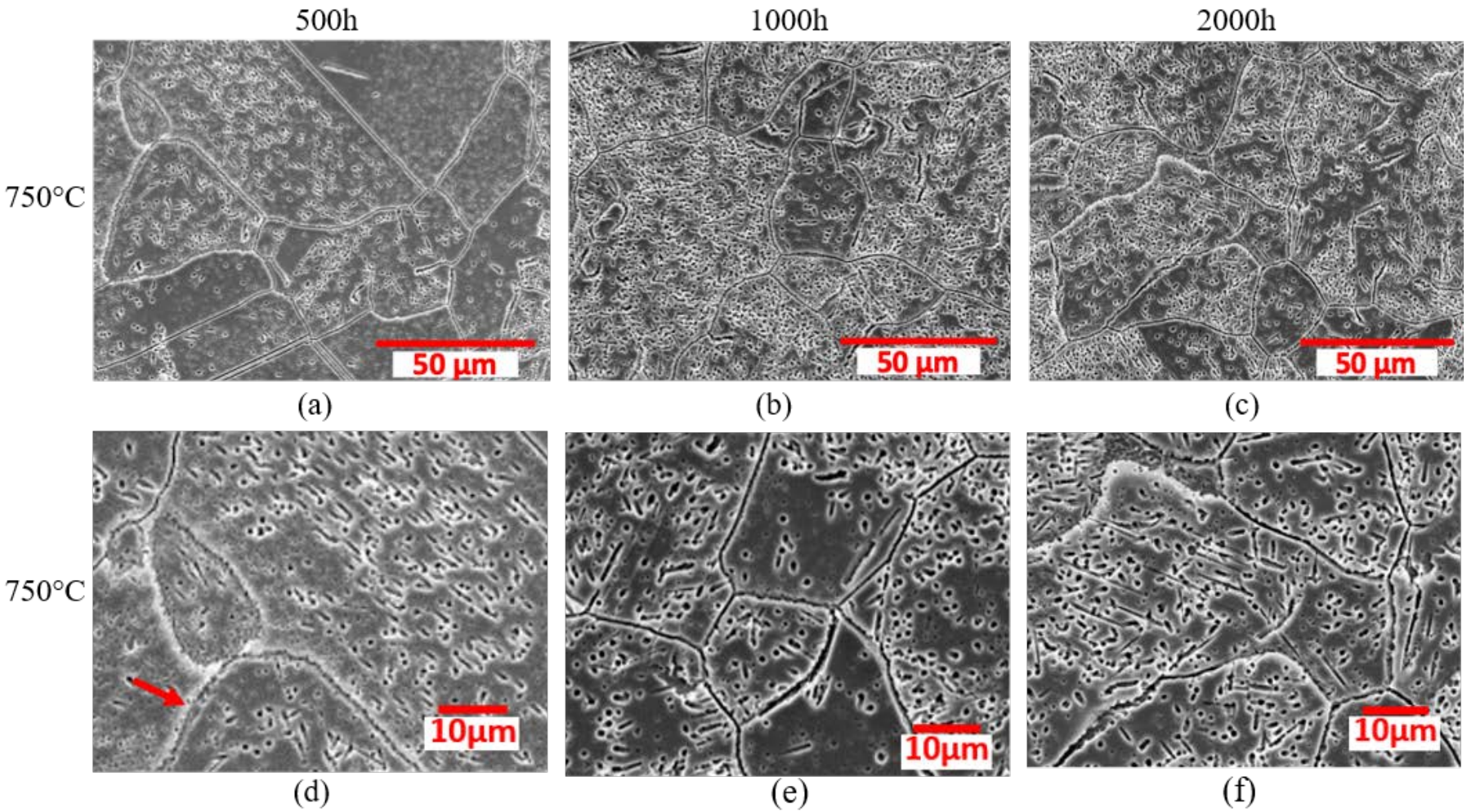

Figure 4.9 SEM images of Alloy 709 aged at 750°C for (a) 500 hours, (b) 1000 hours and (c) 2000 hours (10% oxalic acid electrochemically etched), (d), (e), (f) close-up of (a), (b), (c).

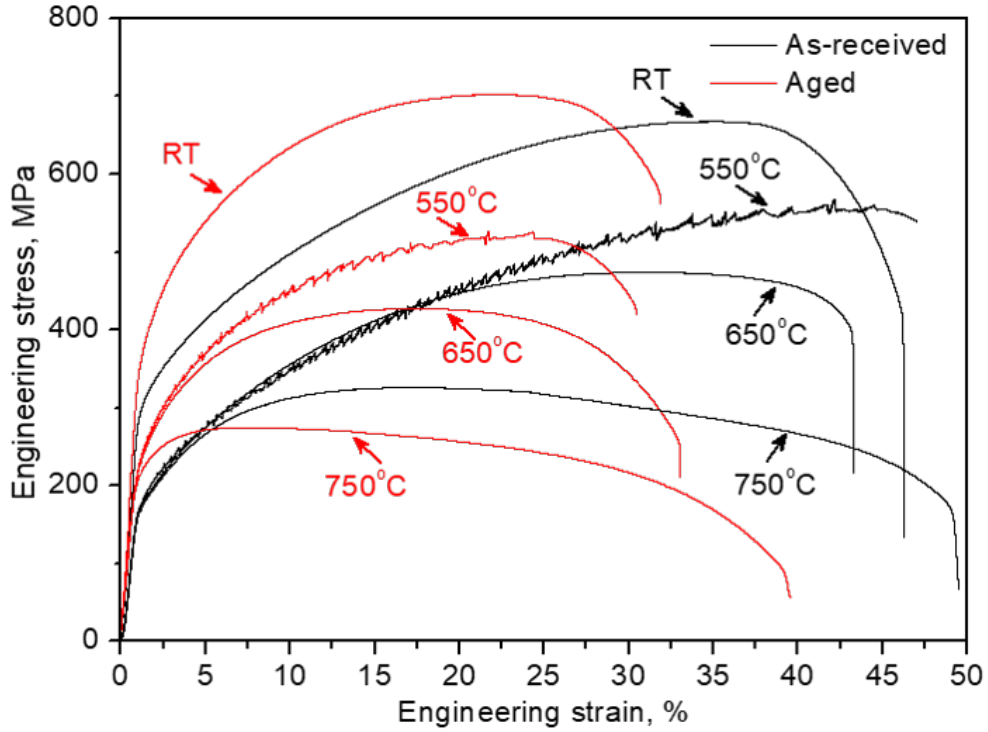

Figure 4.10 Engineering stress-strain curves for the as-received and thermally aged (at 650°C for 2000 hours) Alloy 709 at different temperatures.

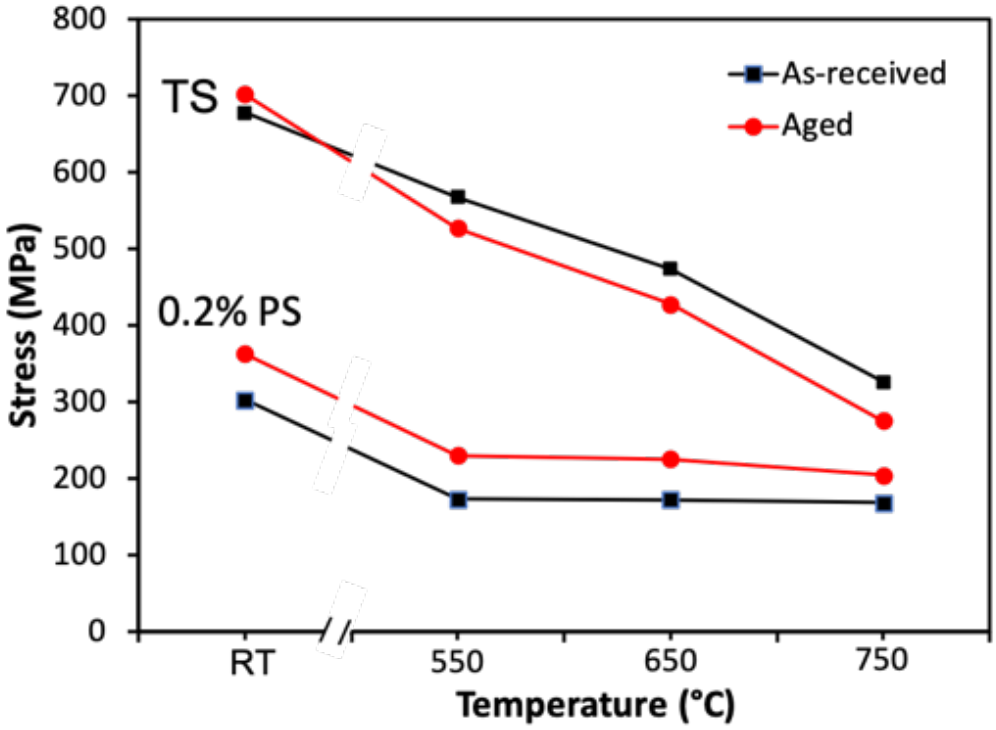

Figure 4.11 Influence of temperature on 0.2% proof stress (PS) and tensile strength (TS).

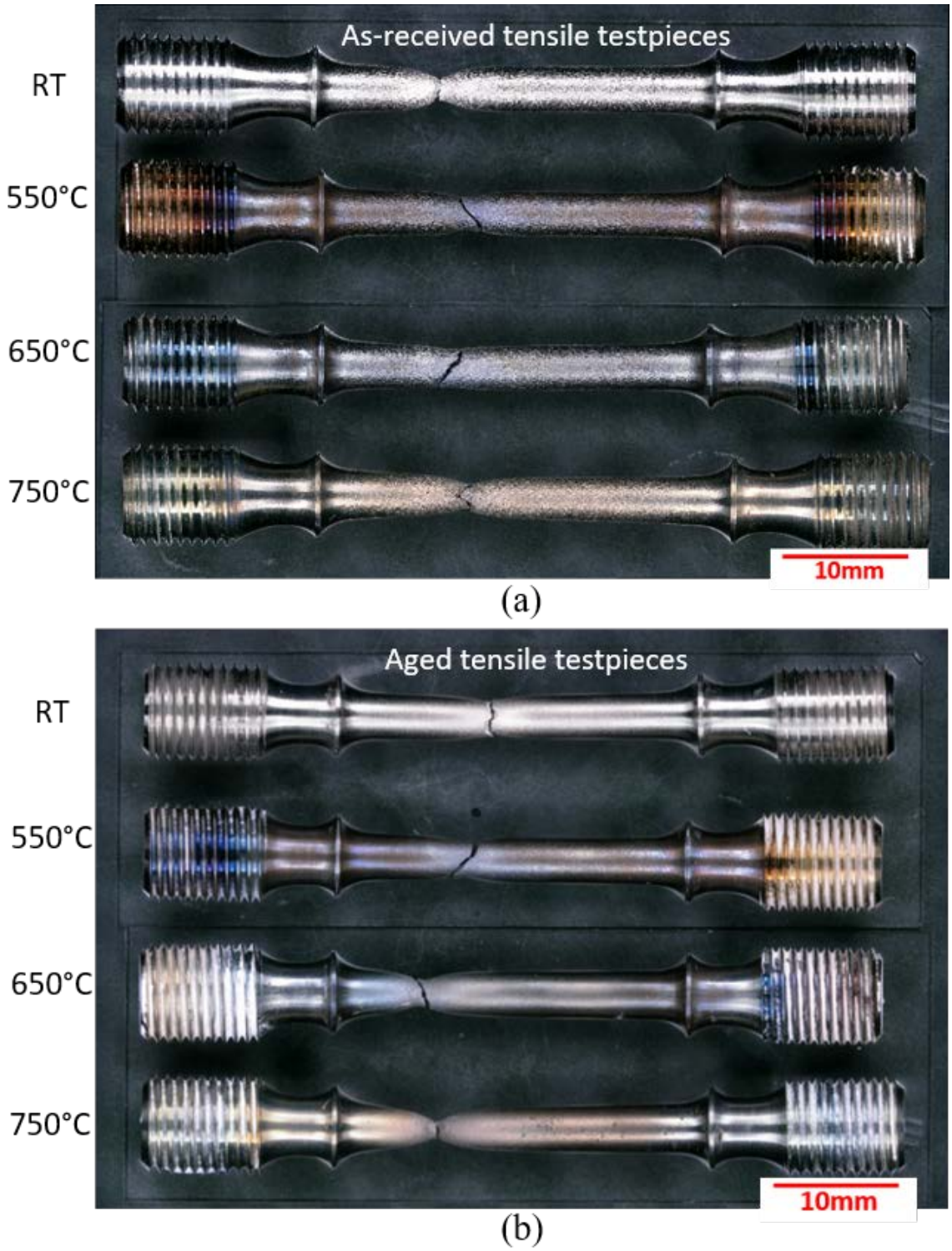

Figure 4.12 Optical images of the fractured tensile testpieces for the (a) as-received Alloy 709, (b) aged Alloy 709 tested at different temperatures, showing the failure mode and necking behaviour.

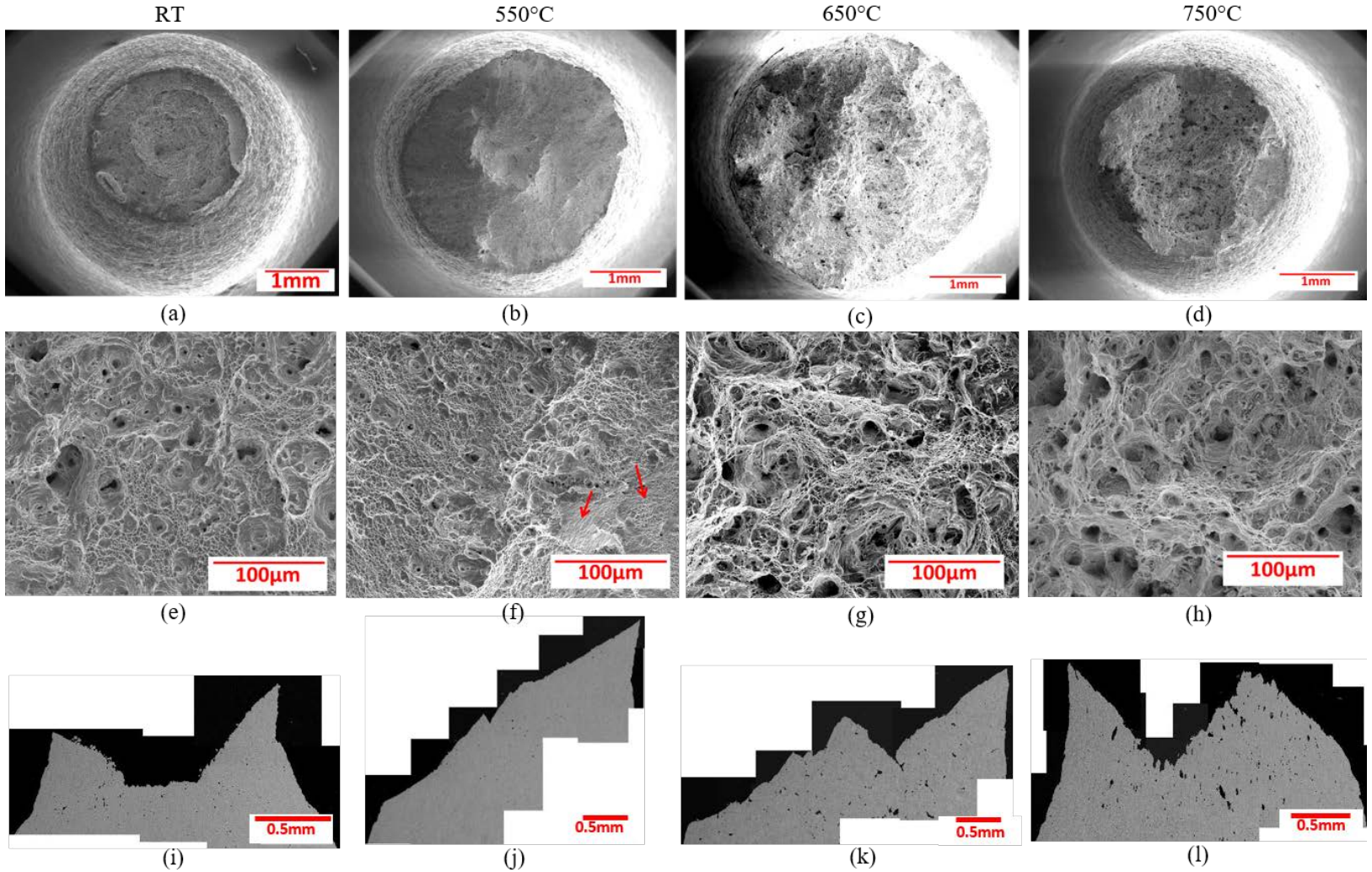

Figure 4.13 Fracture surface analysis of the as-received tensile testpieces in (a - d) low and (e - h) high magnification and (i - l) the longitudinal cross-sectioned specimens tested at (a), (e), (i) RT, (b), (f), (j) 550, (c), (g), (k) 650 and (d), (h), (l) 750°C.

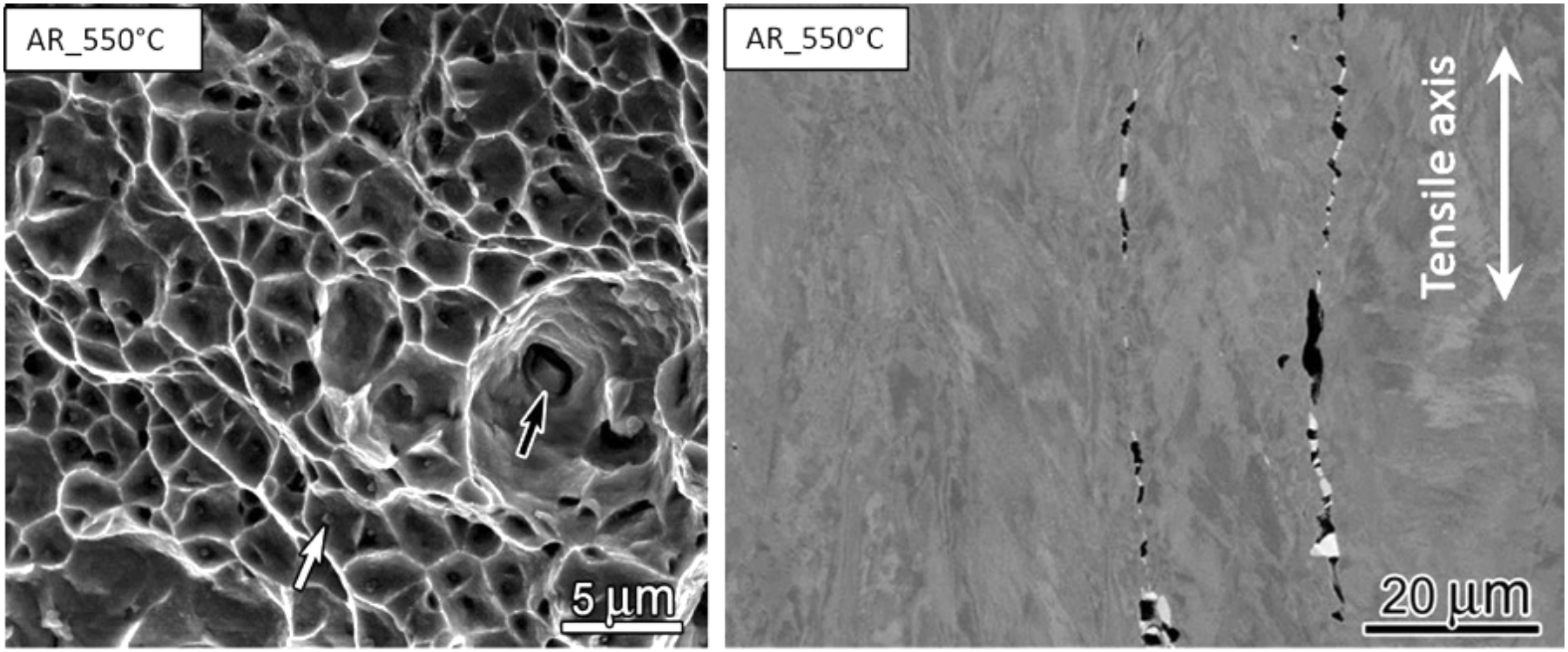

(a) (b)

Figure 4.14 (a) SEM fractographs of the fractured as-received testpieces at 550°C showing the dimples on the fracture surface, primary Nb(CN) (black arrow) leads to coarse dimples, fine Nb(CN) (white arrow) leads to fine dimples, (b) BSE image of corresponding metallographic sections implying that cracks initiate from the primary Nb(CN).

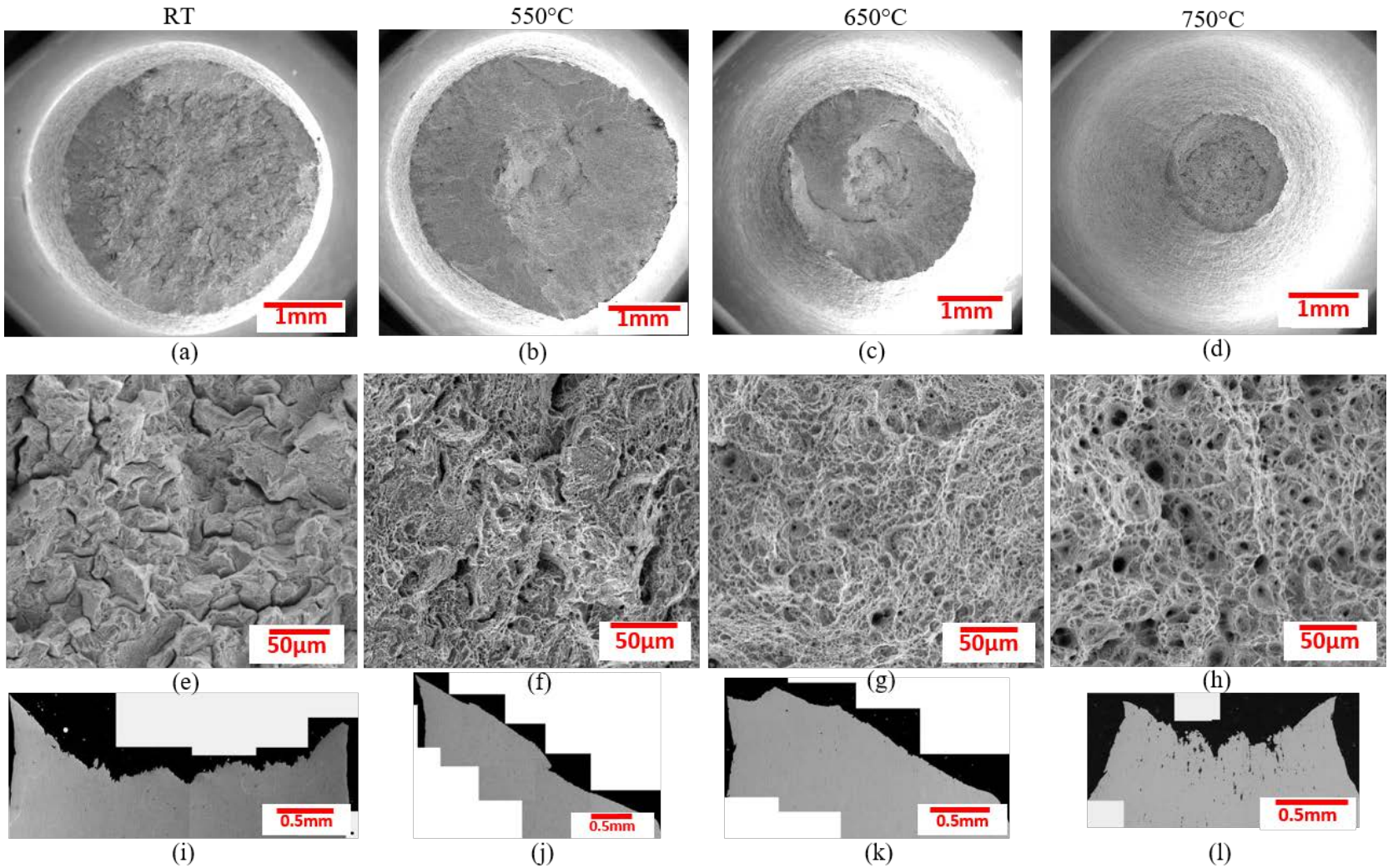

Figure 4.15 Fracture surface analysis of the thermally aged tensile testpieces in (a - d) low and (e - h) high magnification and (i - l) the longitudinal cross-sectioned specimens tested at (a), (e), (i) RT, (b), (f), (j) 550, (c), (g), (k) 650 and (d), (h), (l) 750°C.

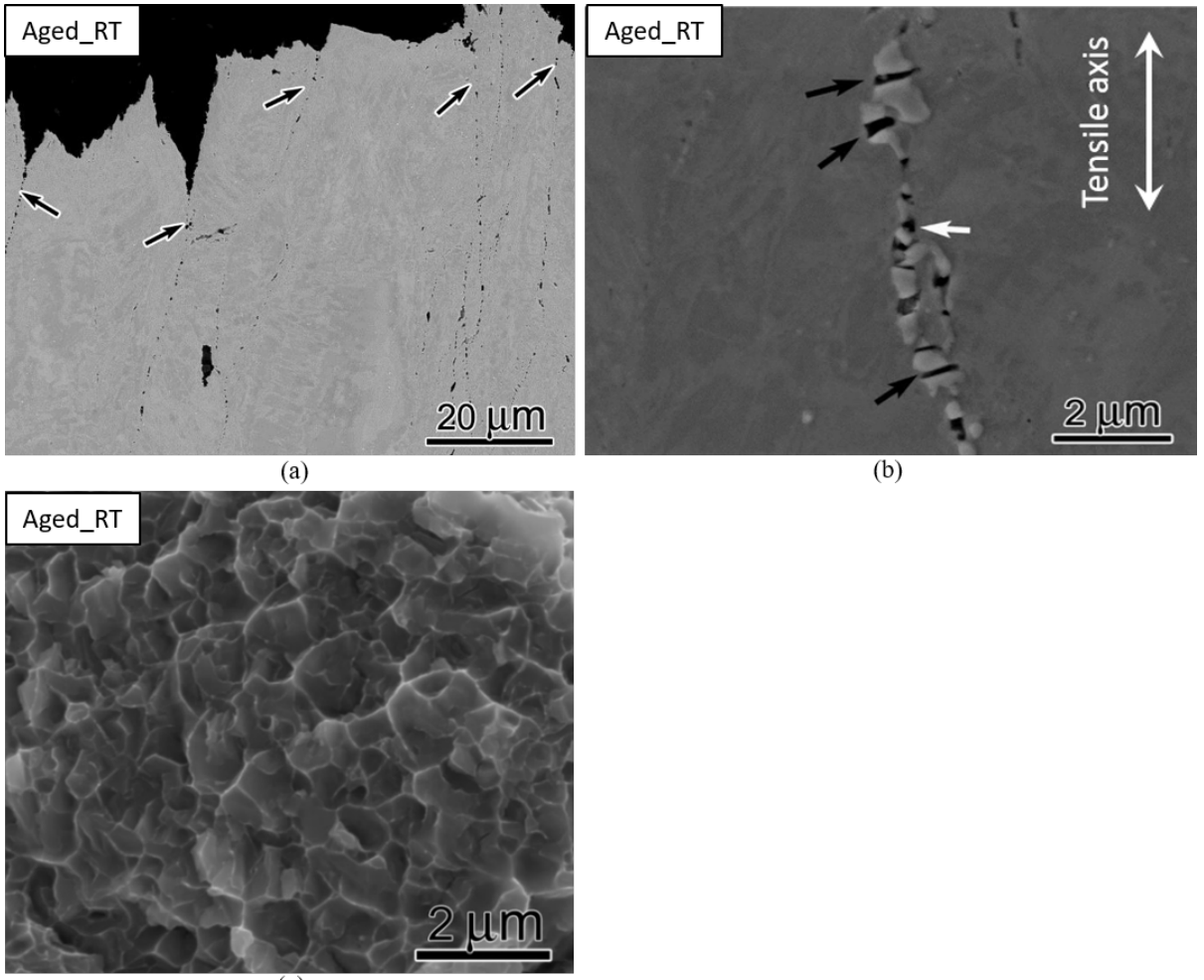

Figure 4.16 (a) BSE image of the cross-section for the fractured aged sample tested at RT showing damage initiated at grain boundaries (arrowed). (b) higher magnification image showing that grain boundary carbides that fracture (black arrow) when the voids formed on the interface of fine grain boundary carbides and base material (white arrow), (c) higher magnification of Figure 4.15e showing fine dimples.

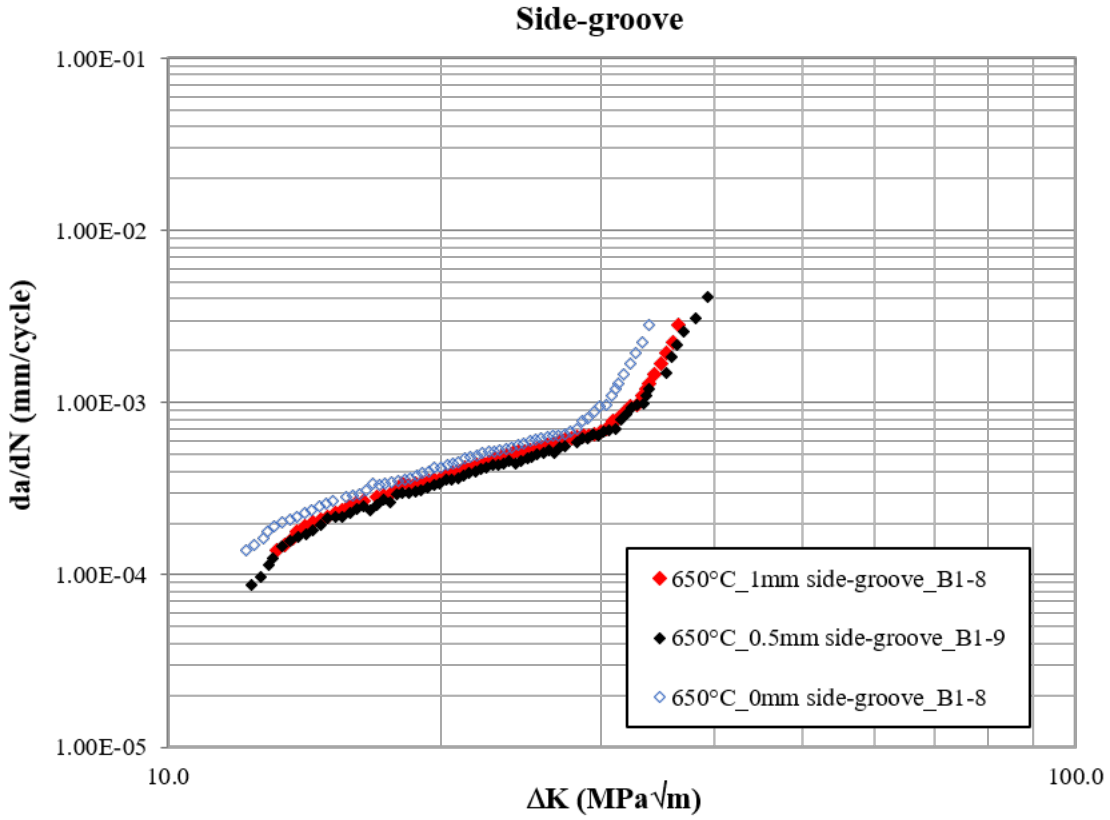

Figure 4.17 The effect of side-groove depth on the fatigue crack growth rate of the as-received Alloy 709.

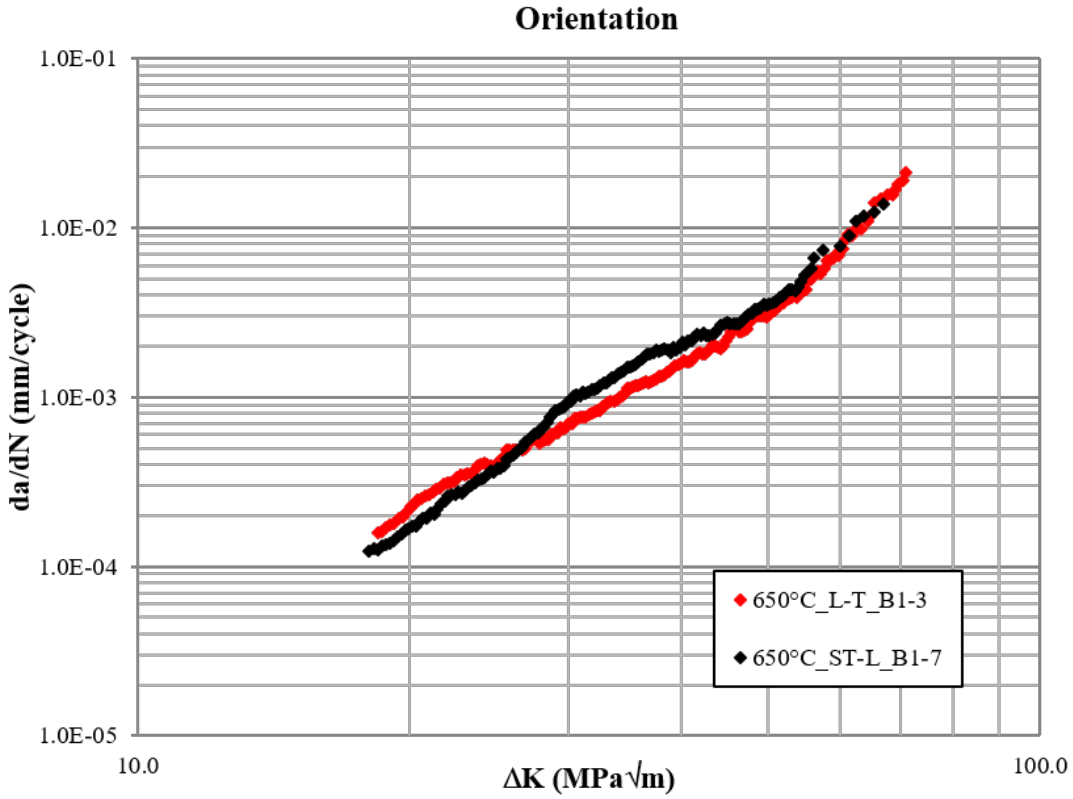

Figure 4.18 The effect of orientation on the fatigue crack growth rate of the as-received Alloy 709.

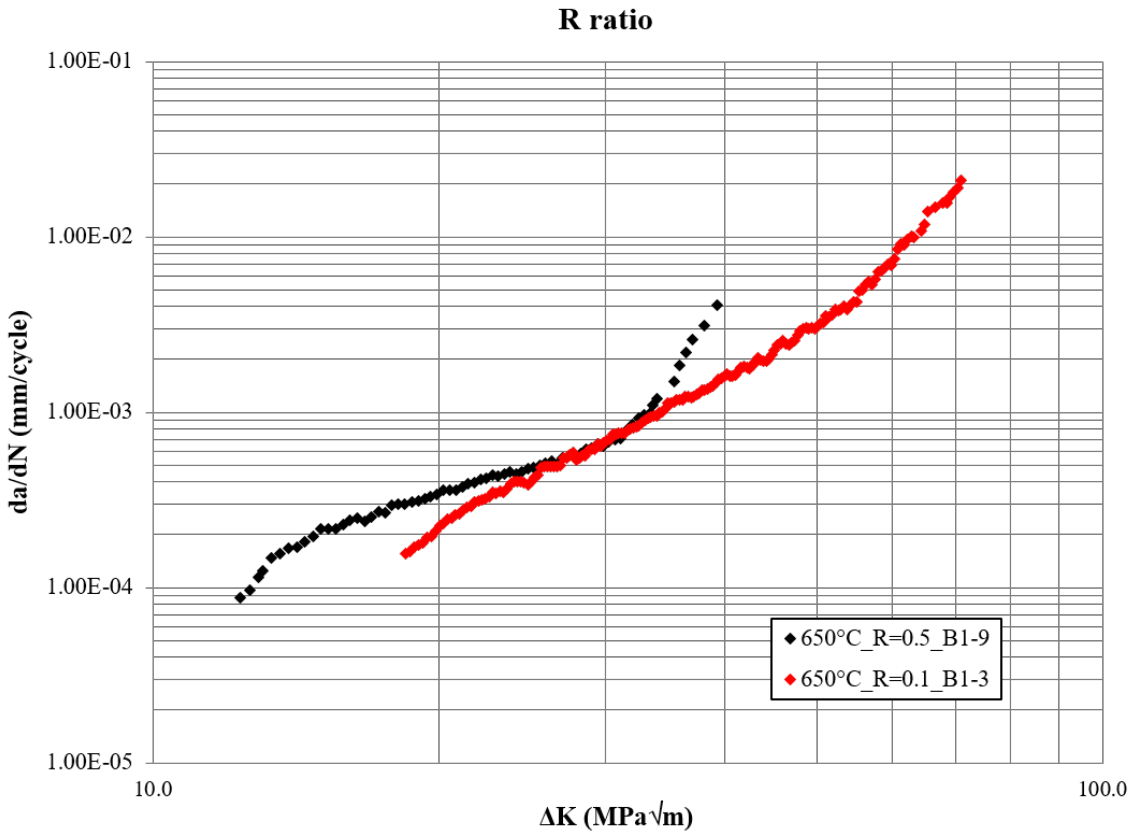

Figure 4.19 The effect of R ratio on the fatigue crack growth rate of the as-received Alloy 709.

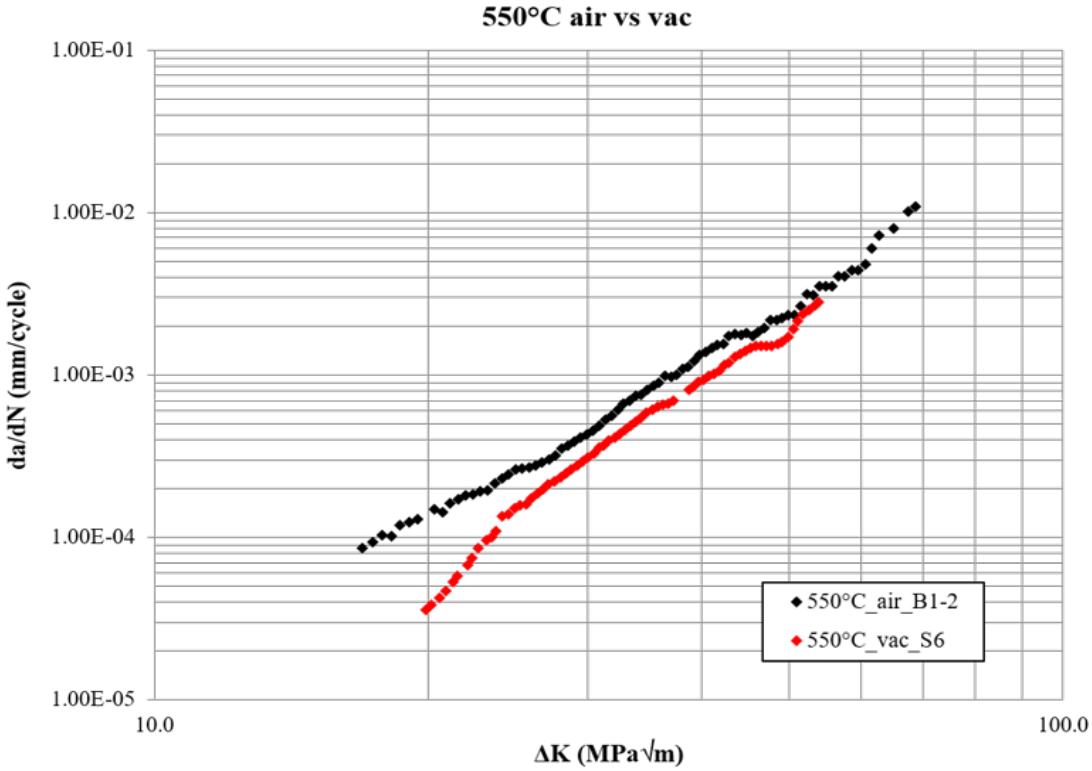

Figure 4.20 Fatigue crack growth resistance curves of the as-received Alloy 709 tested in air and vacuum at 550°C.

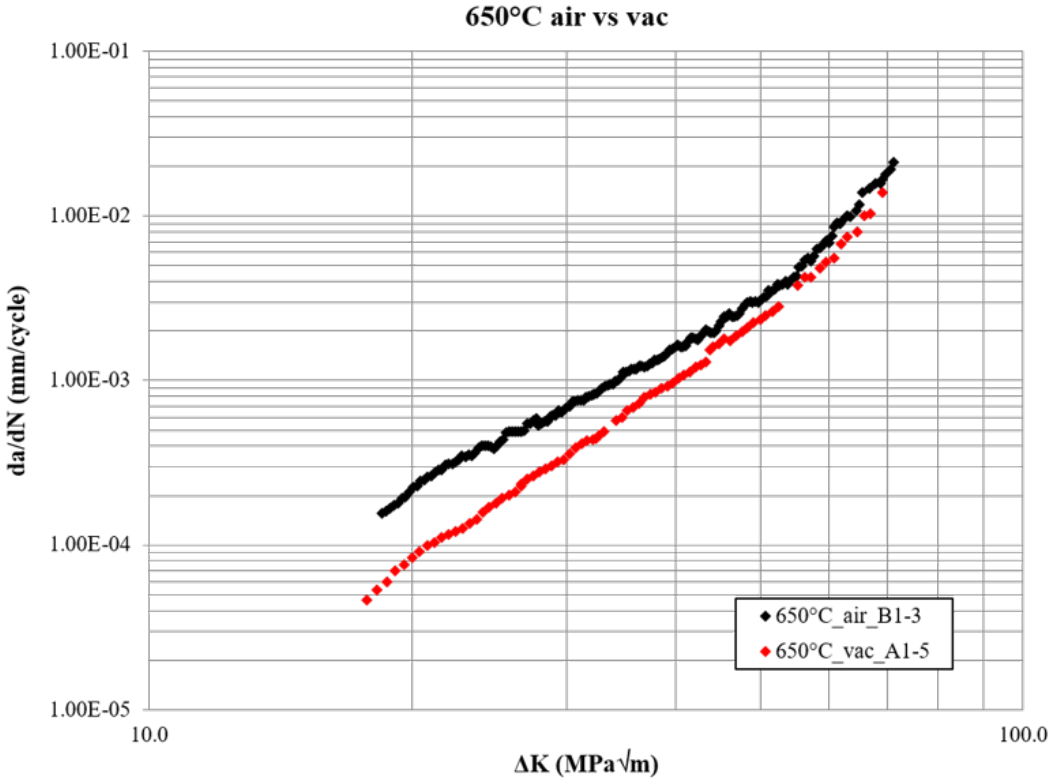

.

Figure 4.21 Fatigue crack growth resistance curves of the as-received Alloy 709 tested in air and vacuum at 650°C.

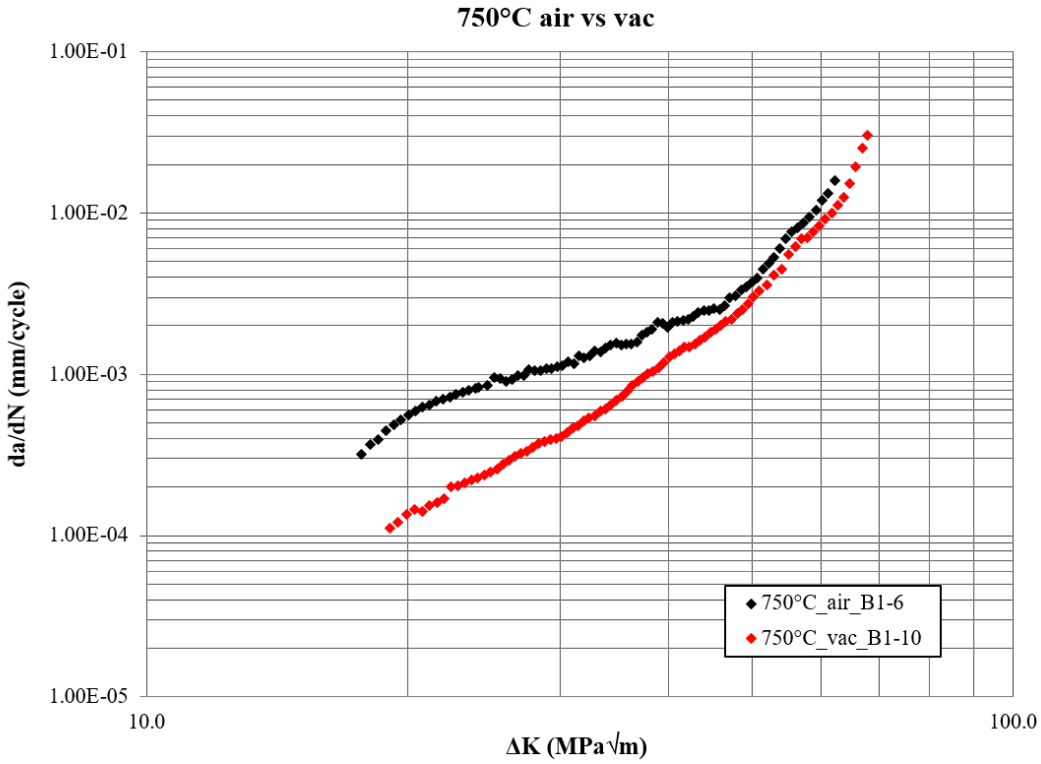

Figure 4.22 Fatigue crack growth resistance curves of the as-received Alloy 709 tested in air and vacuum at 750°C.

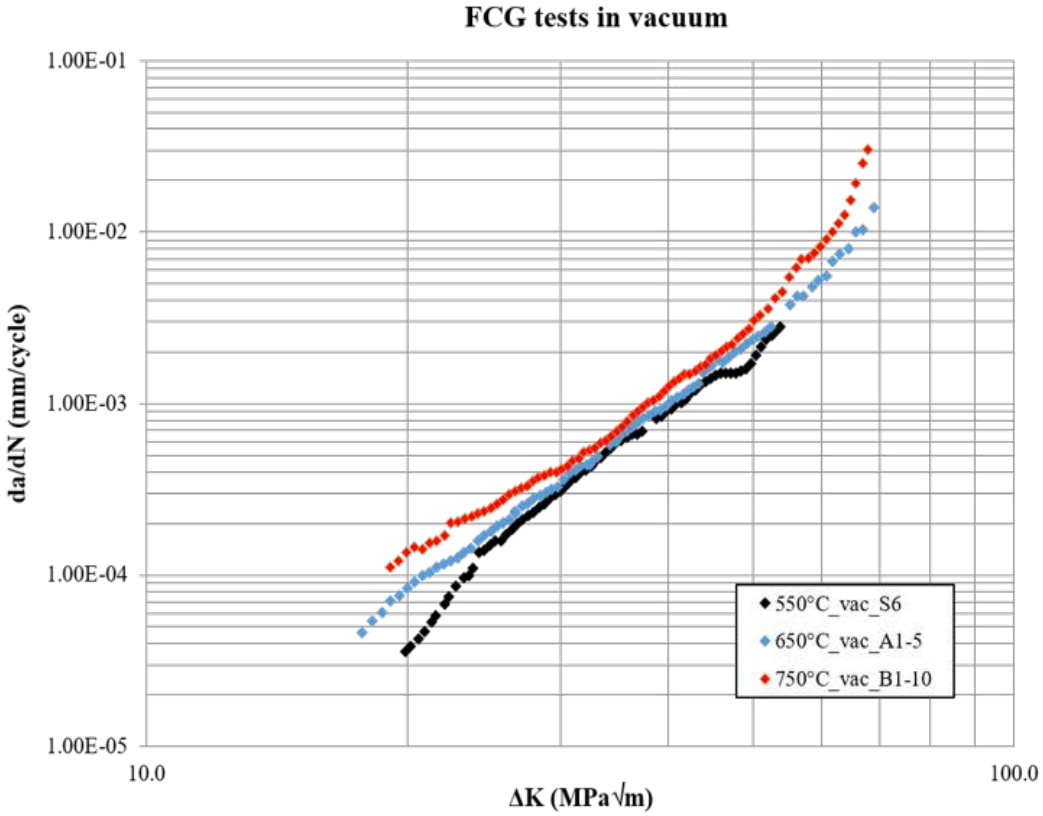

Figure 4.23 Fatigue crack growth resistance curves of the as-received Alloy 709 tested at different temperatures in vacuum.

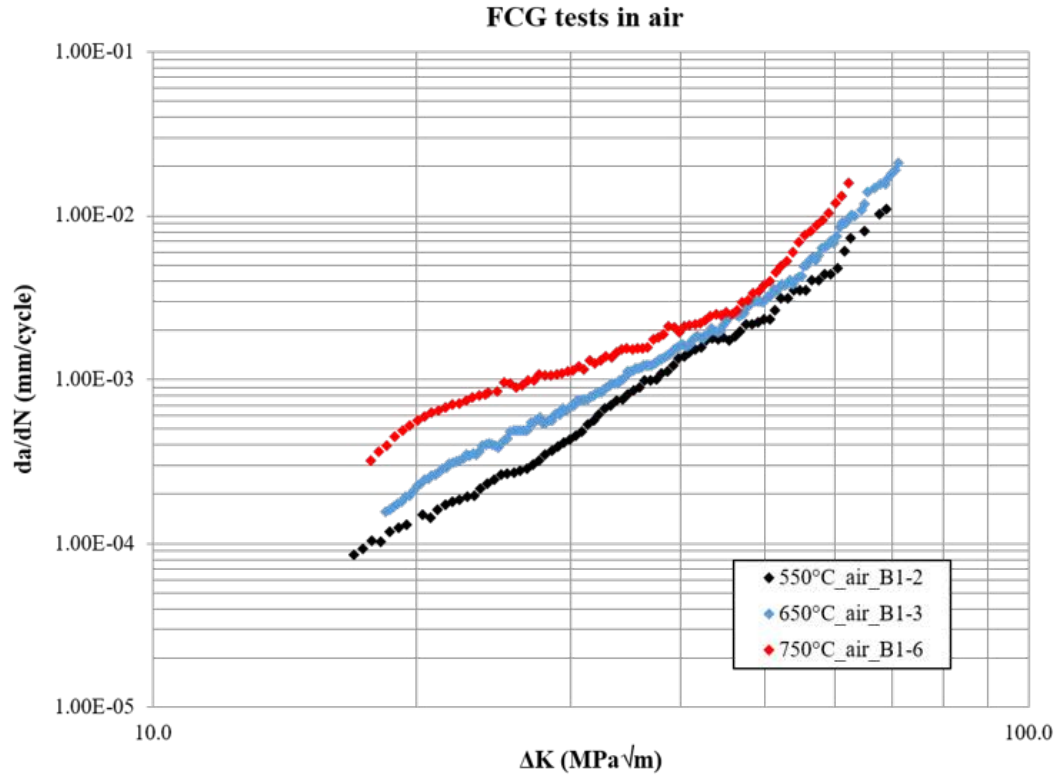

Figure 4.24 Fatigue crack growth resistance curves of the as-received Alloy 709 tested at different temperatures in air.

Figure 4.25 Optical fractographs for fatigue crack growth testpieces of the as-received Alloy 709 tested in air at (a), (b) 550, (c) - (f) 650°C, (g) 650°C in vacuum (h) 750°C in air and (i) 750°C in vacuum. Note: Red arrows indicate the direction of crack growth. A back-face notch was applied using a hand saw to facilitate the breaking open of the testpieces. Continued overleaf.

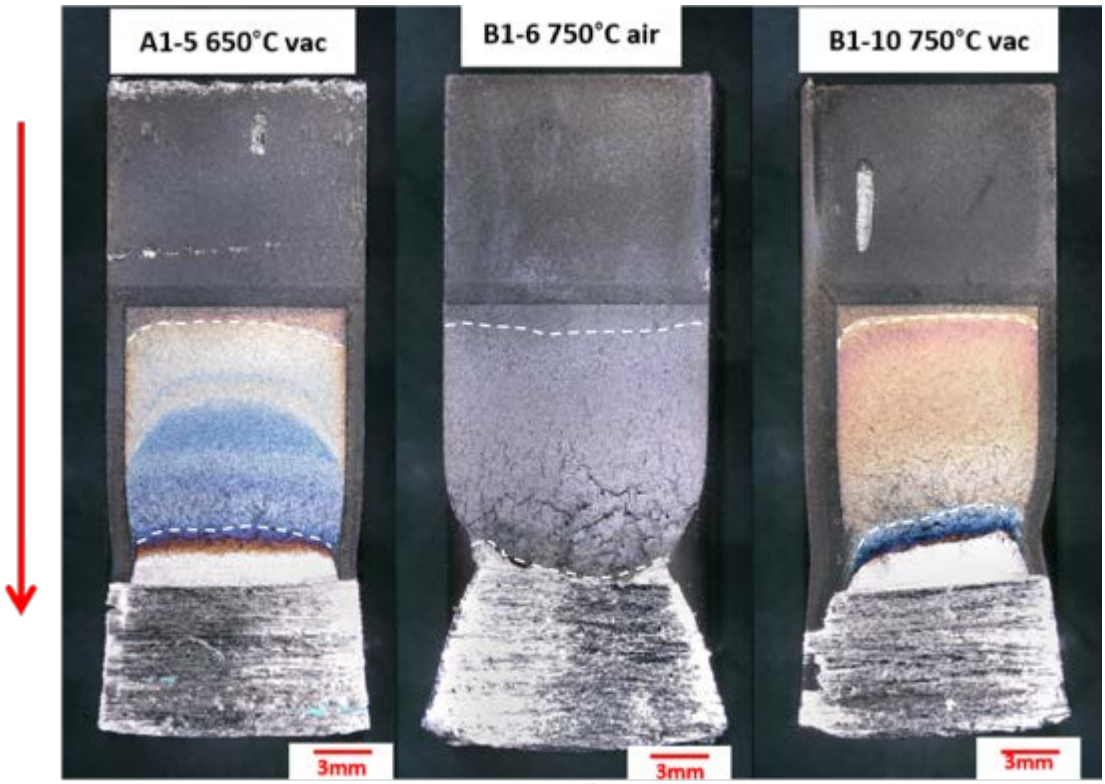

Figure 4.25 Continued. Optical fractographs for fatigue crack growth testpieces of the as-received Alloy 709 tested in air at (a), (b) 550, (c) - (f) 650°C, (g) 650°C in vacuum (h) 750°C in air and (i) 750°C in vacuum. Note: Red arrows indicate the direction of crack growth. A back-face notch was applied using a hand saw to facilitate the breaking open of the testpieces.

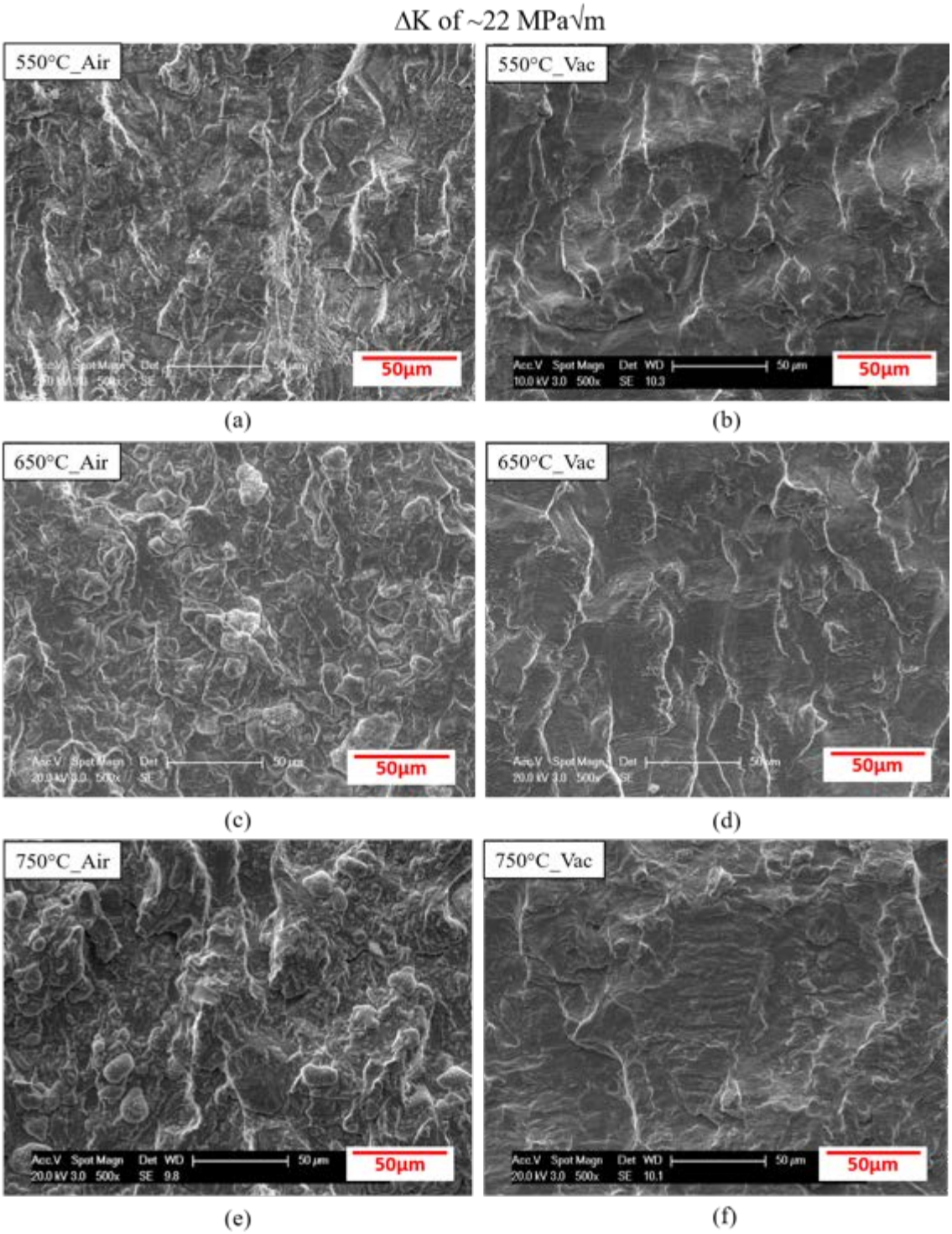

Figure 4.26 SEM fractographs of the as-received Alloy 709 fatigue crack growth specimens taken at ΔK of ~22 MPa√m tested in (a), (c), (e) air and (b), (d), (f) vacuum at (a), (b) 550, (c), (d) 650 and (e), (f) 750°C.

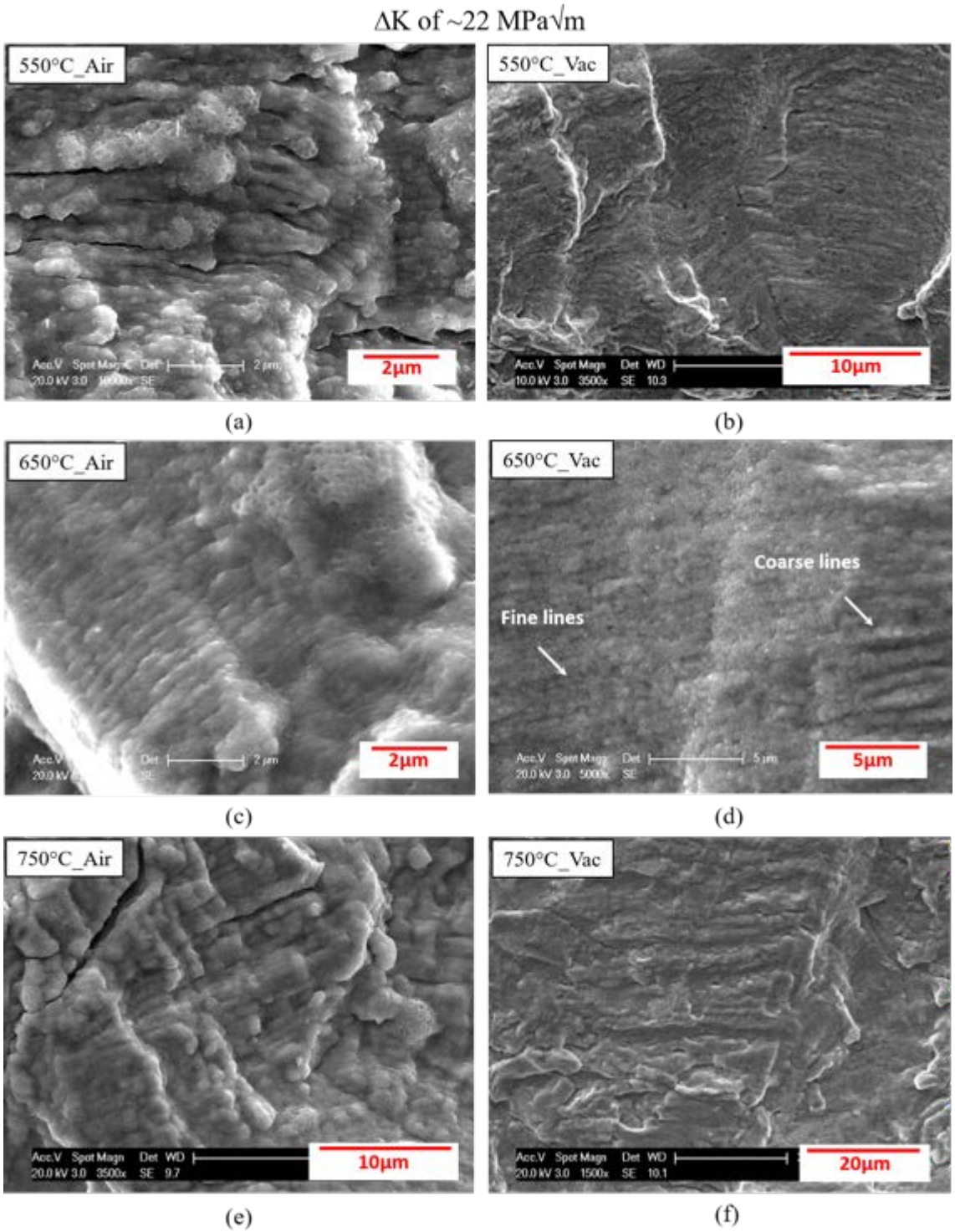

Figure 4.27 The corresponding SEM fractographs with higher magnification of the as-received Alloy 709 specimens revealing the morphology of striations in Figure 4.26 under ΔK of ~22 MPa√m.

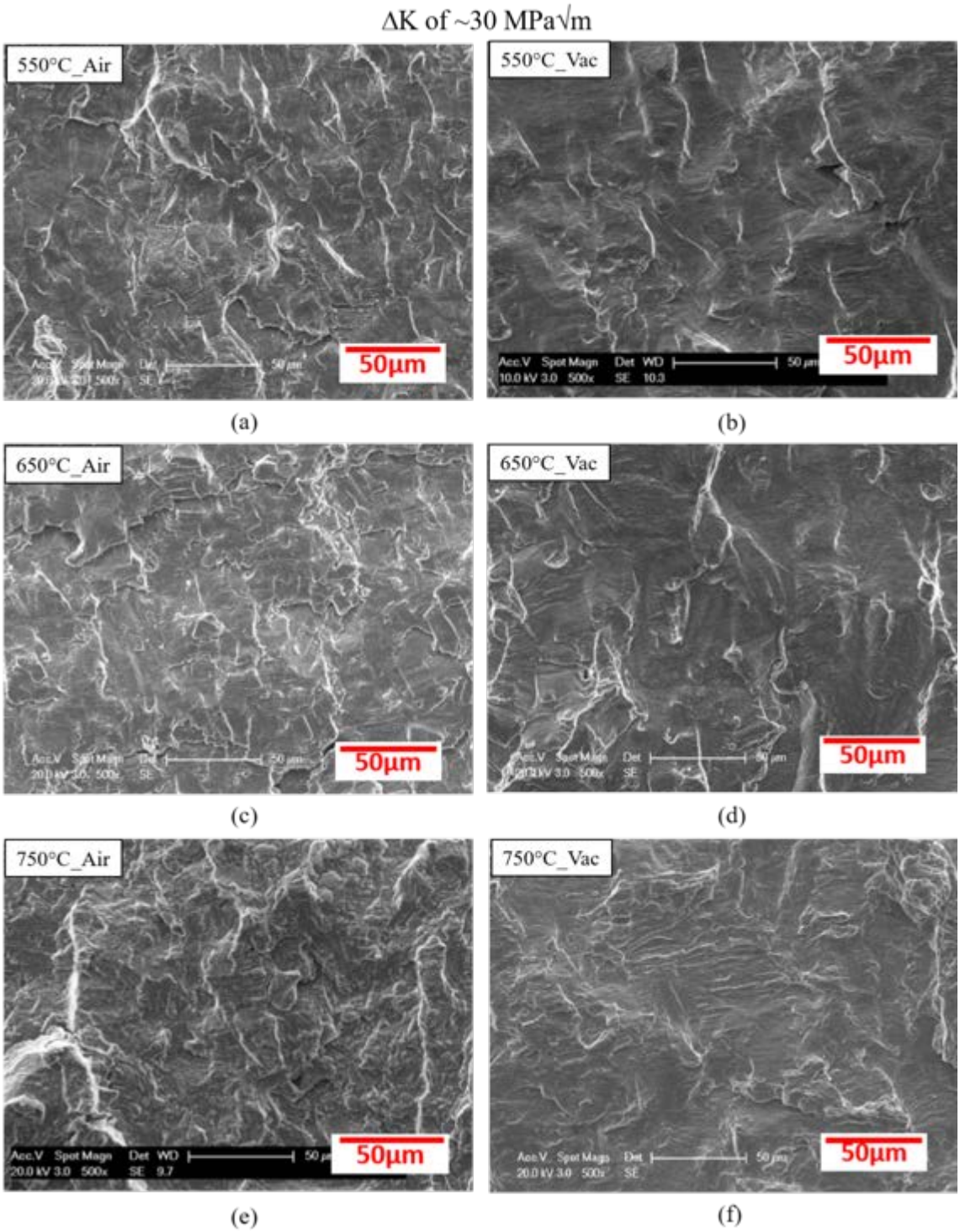

Figure 4.28 SEM fractographs of the as-received Alloy 709 fatigue crack growth specimens taken at ΔK of ~30 MPa√m tested in (a), (c), (e) air and (b), (d), (f) vacuum at (a), (b) 550, (c), (d) 650 and (e), (f) 750°C.

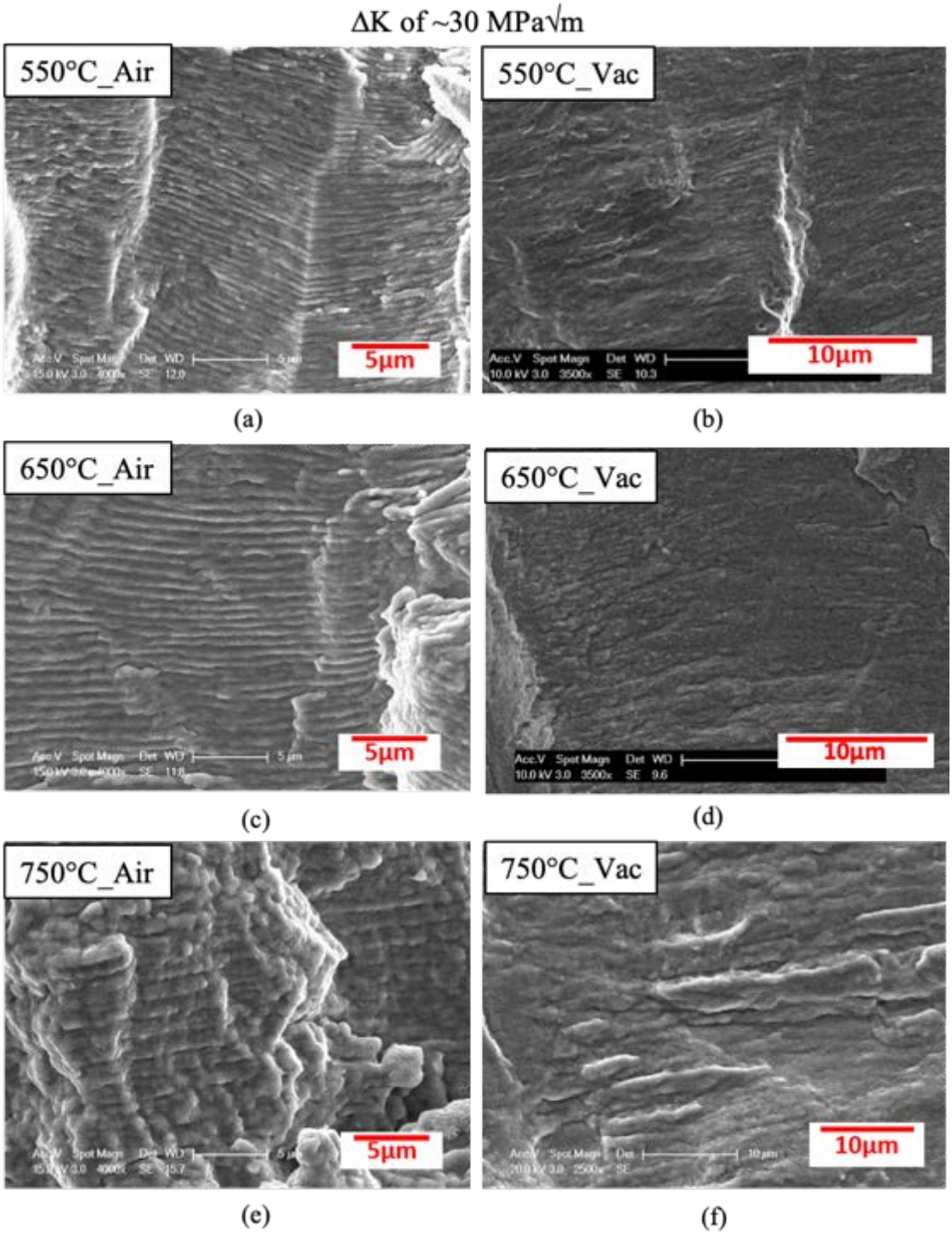

Figure 4.29 The corresponding SEM fractographs with higher magnification of the as-received Alloy 709 specimens revealing the morphology of striations in Figure 4.28 under ΔK of ~30 MPa√m.

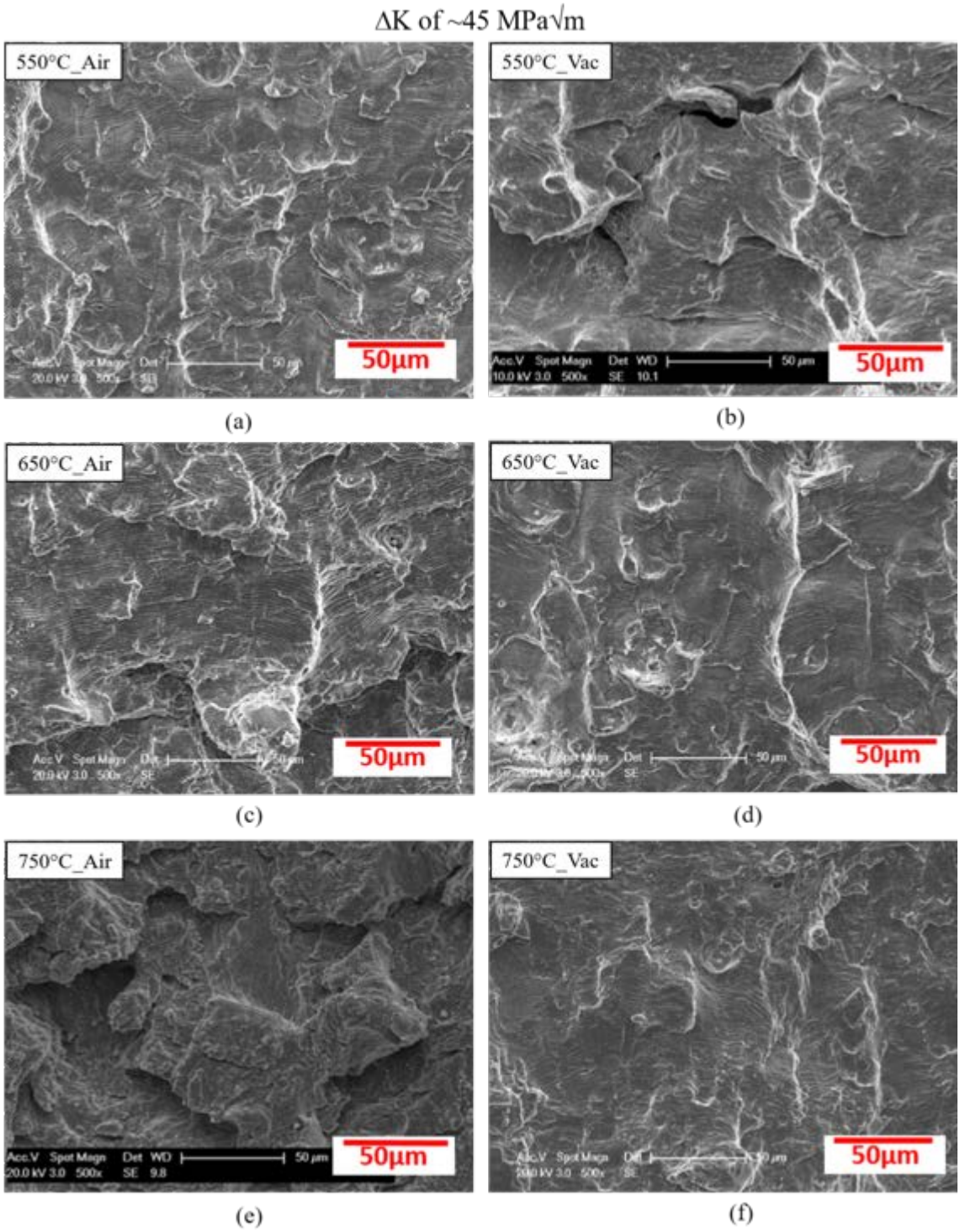

Figure 4.30 SEM fractographs of the as-received Alloy 709 fatigue crack growth specimens taken at ΔK of ~45 MPa√m tested in (a), (c), (e) air and (b), (d), (f) vacuum at (a), (b) 550, (c), (d) 650 and (e), (f) 750°C.

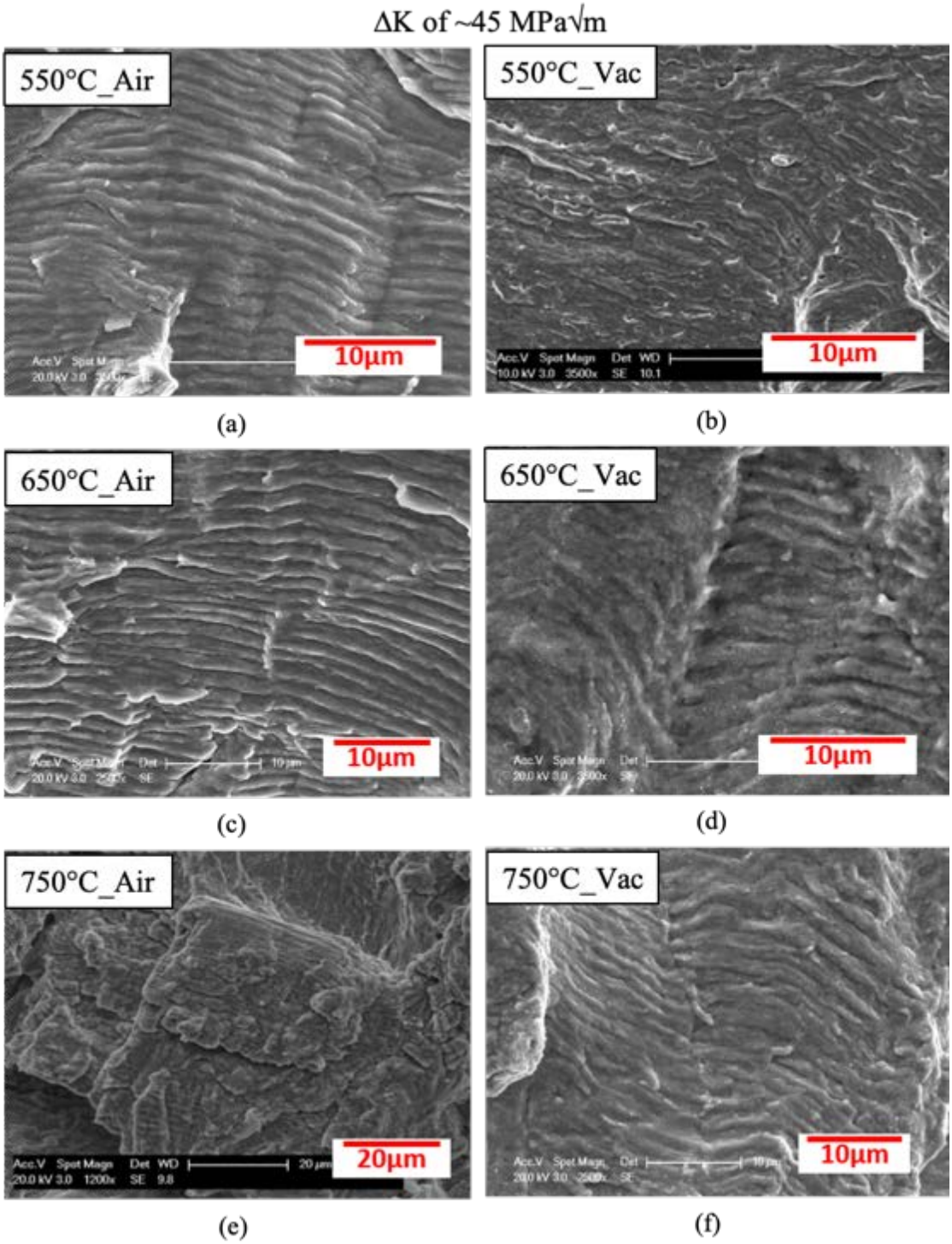

Figure 4.31 The corresponding SEM fractographs with higher magnification of the as-received Alloy 709 specimens revealing the morphology of striations in Figure 4.30 under ΔK of ~45 MPa√m.

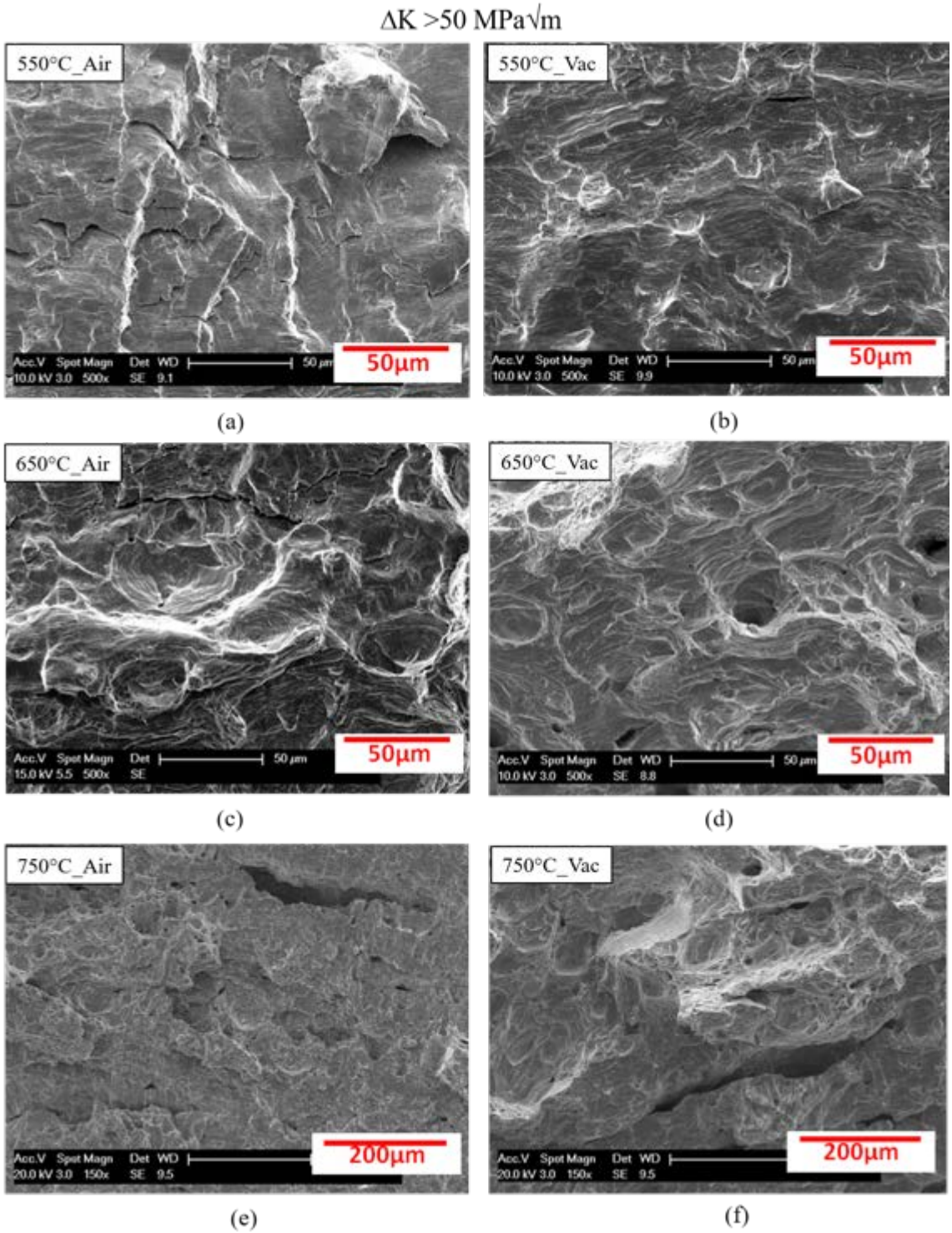

Figure 4.32 SEM fractographs of the as-received Alloy 709 fatigue crack growth specimens taken at ΔK >50 MPa√m tested in (a), (c), (e) air and (b), (d), (f) vacuum at (a), (b) 550, (c), (d) 650 and (e), (f) 750°C.

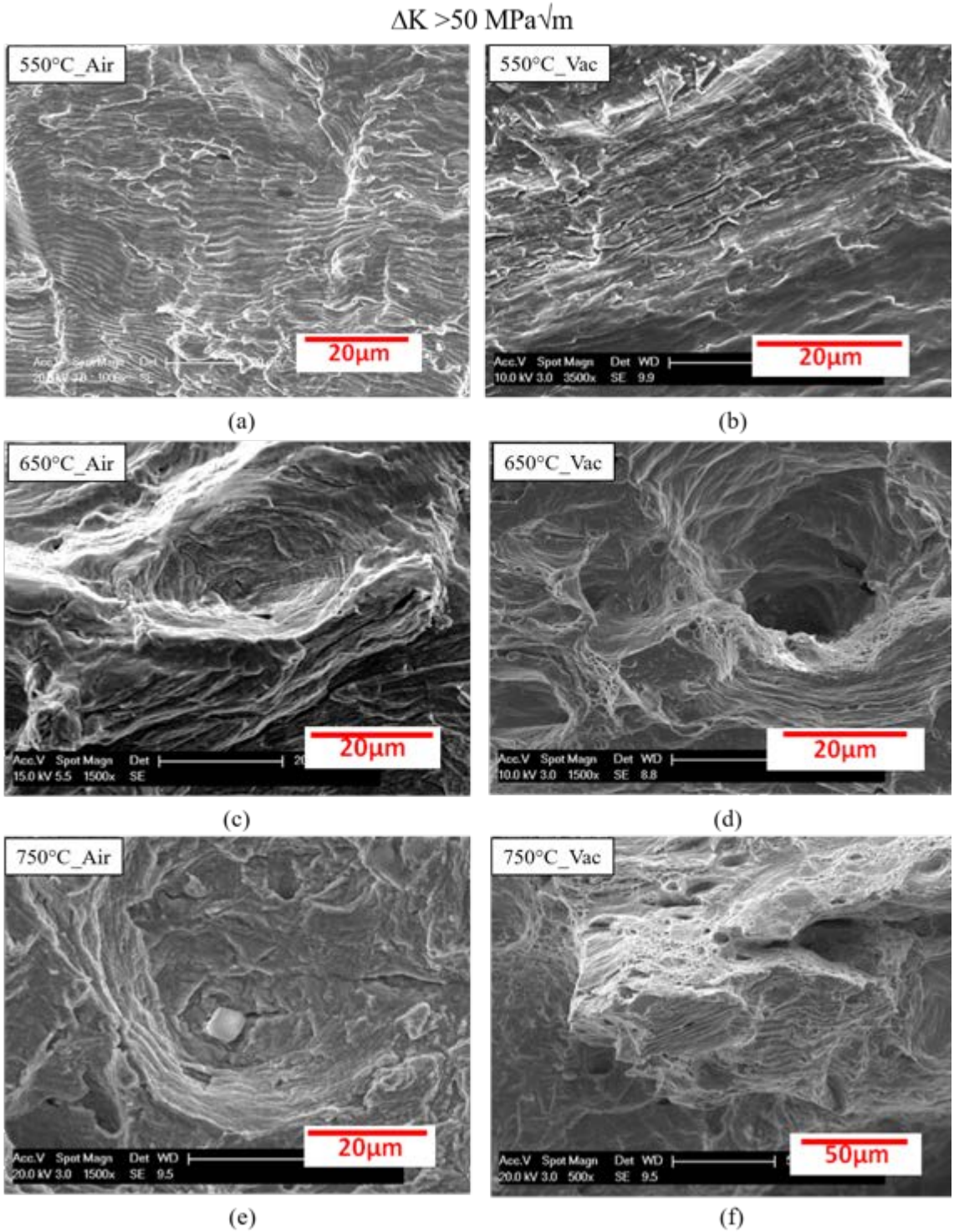

Figure 4.33 The corresponding SEM fractographs with higher magnification of the as-received Alloy 709 specimens revealing the morphology in Figure 4.32 under ΔK >50 MPa√m.

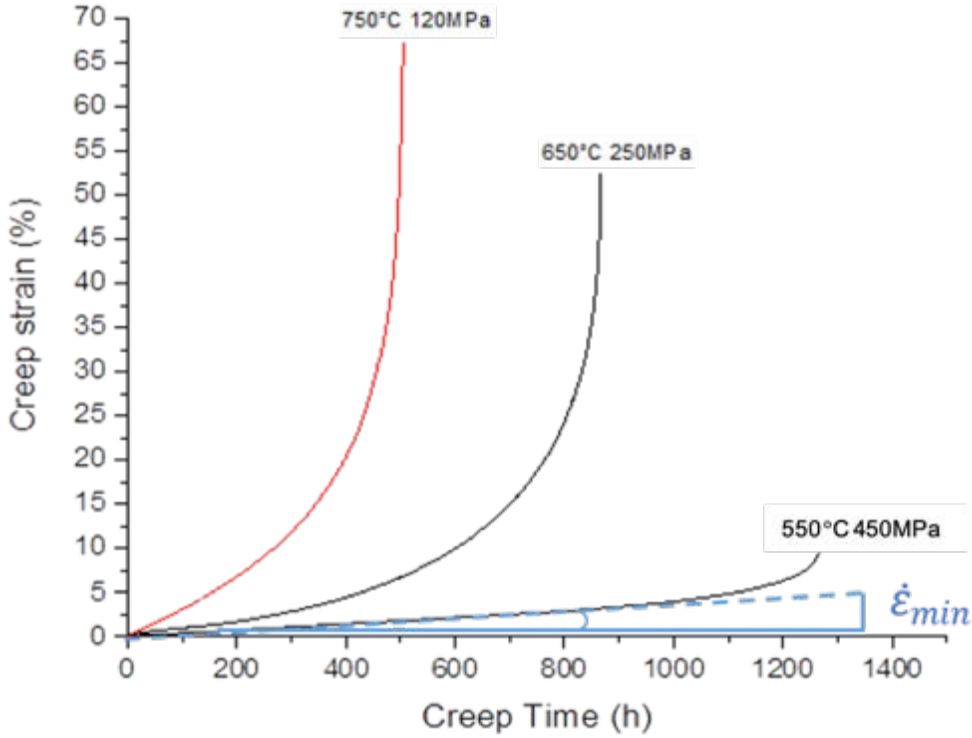

Figure 4.34 Creep curves of Alloy 709 tested at elevated temperatures.

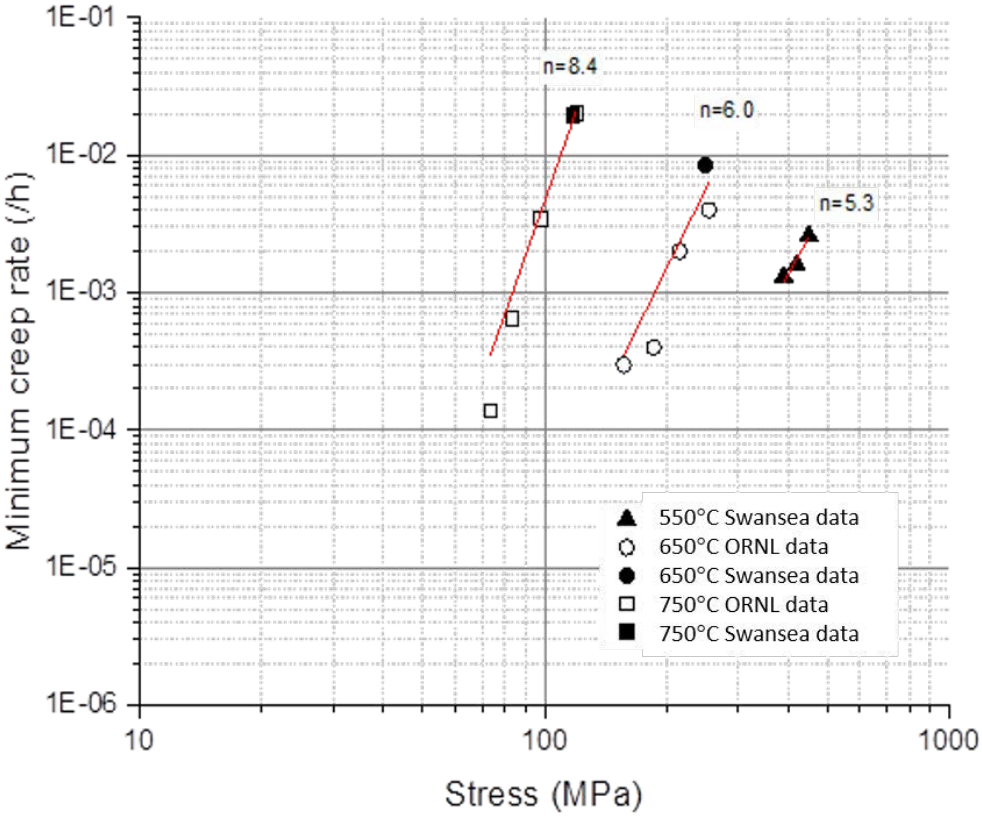

Figure 4.35 Plot of minimum creep rates against stress measured in Alloy 709 at elevated temperatures.

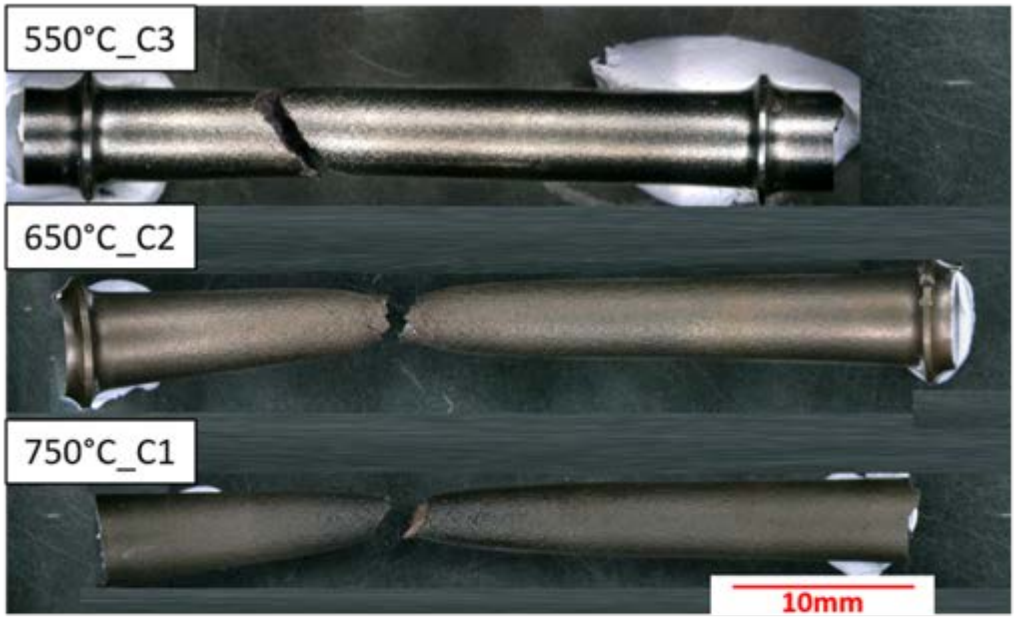

(a)

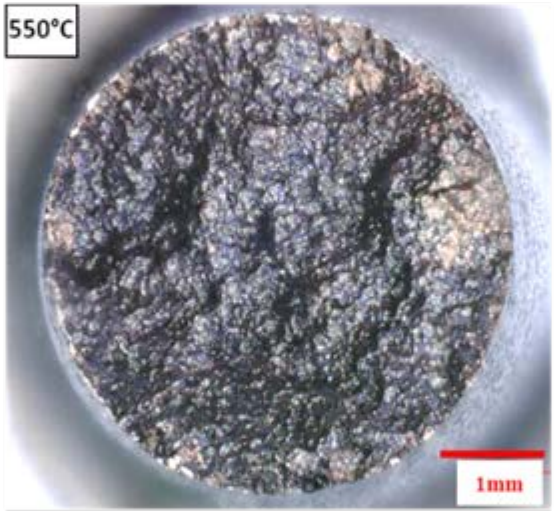

(b)

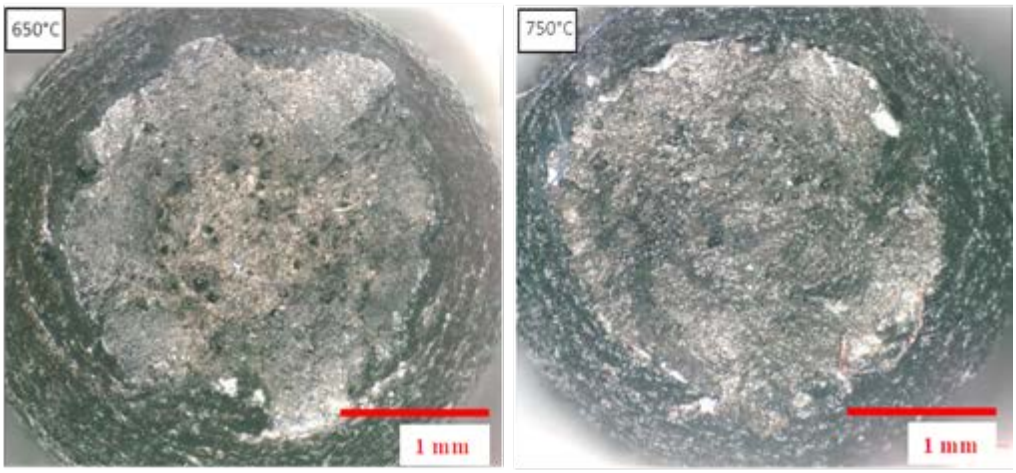

(c) (d)

Figure 4.36 Optical images of creep testpieces tested at (b) 550, (c) 650 and (d) 750°C.

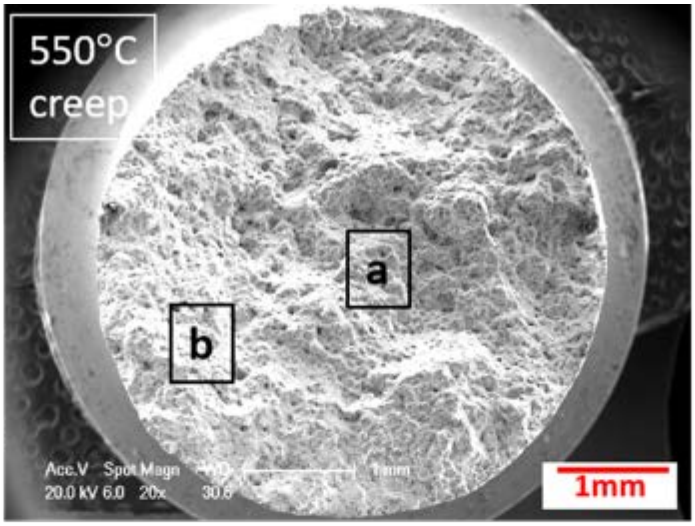

(a)

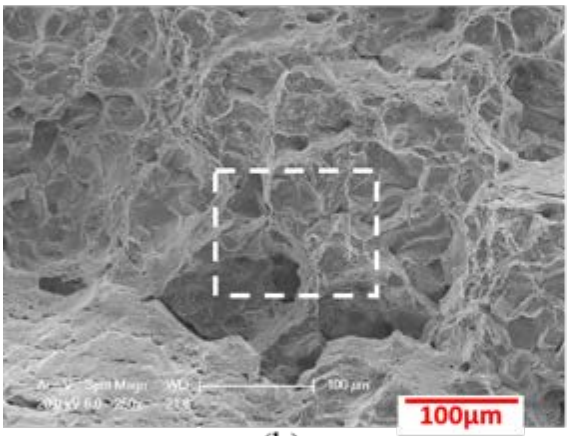

(b)

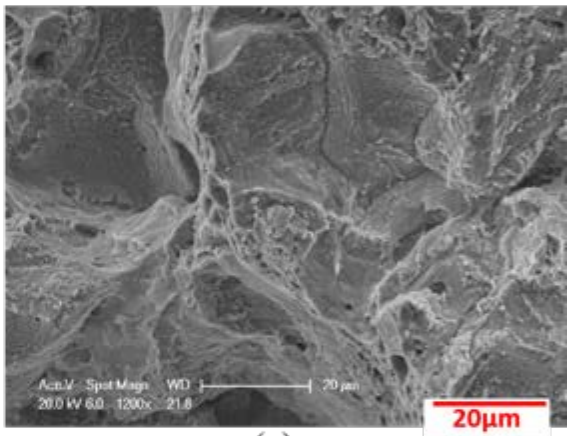

(c)

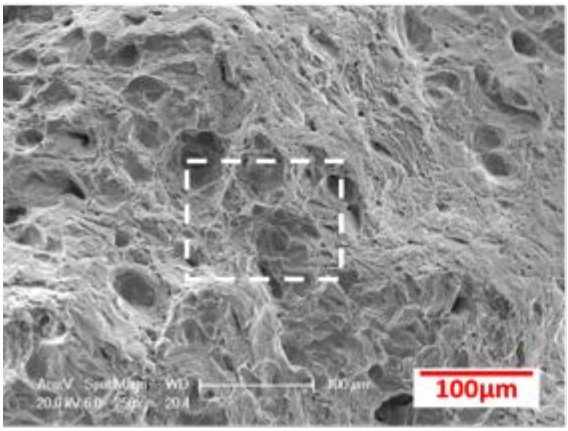

(d)

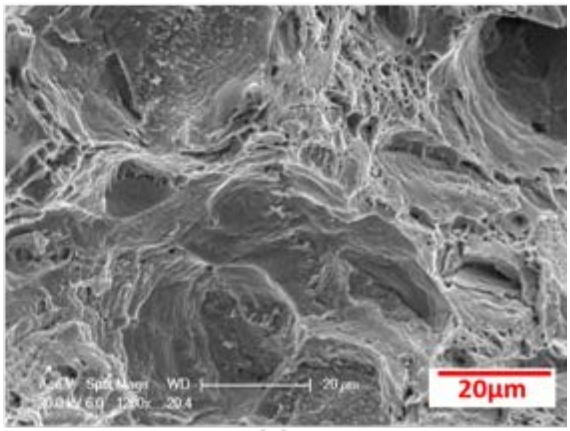

(e)

Figure 4.37 SEM micrographs showing (a) the fracture surface of creep testpieces of Alloy 709 at 550°C, (b) the failure mode in the central area (a in Figure 4.37a), (d) the failure mode in the edge area (b in Figure 4.37a), (c) close-up of (b), (e) close-up of (d).

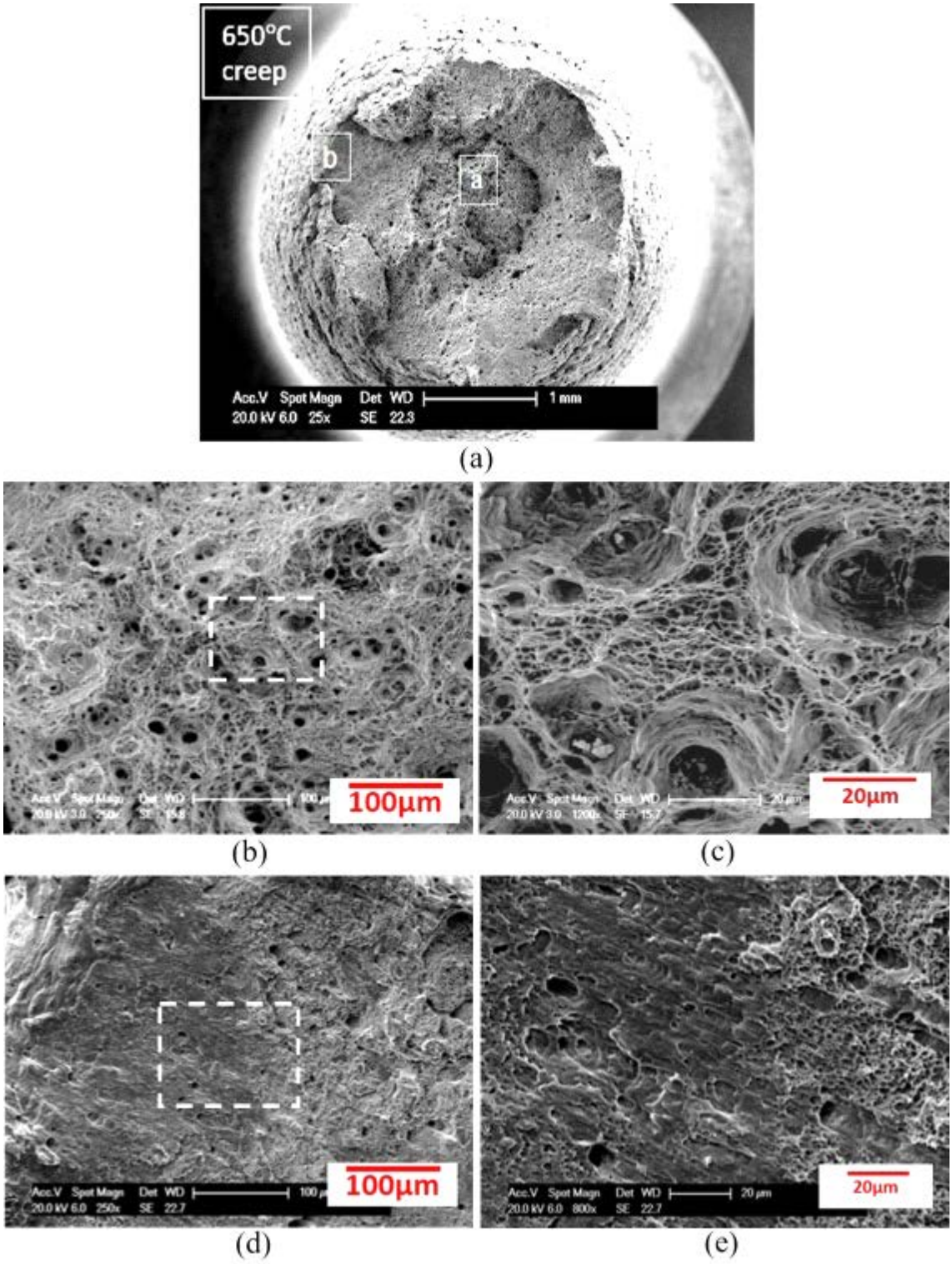

Figure 4.38 SEM micrographs showing (a) the fracture surface of creep testpieces of Alloy 709 at 650°C, (b) the failure mode in the central area (a in Figure 4.38a), (d) the failure mode in the edge area (b in Figure 4.38a), (c) close-up of (b), (e) close-up of (d).

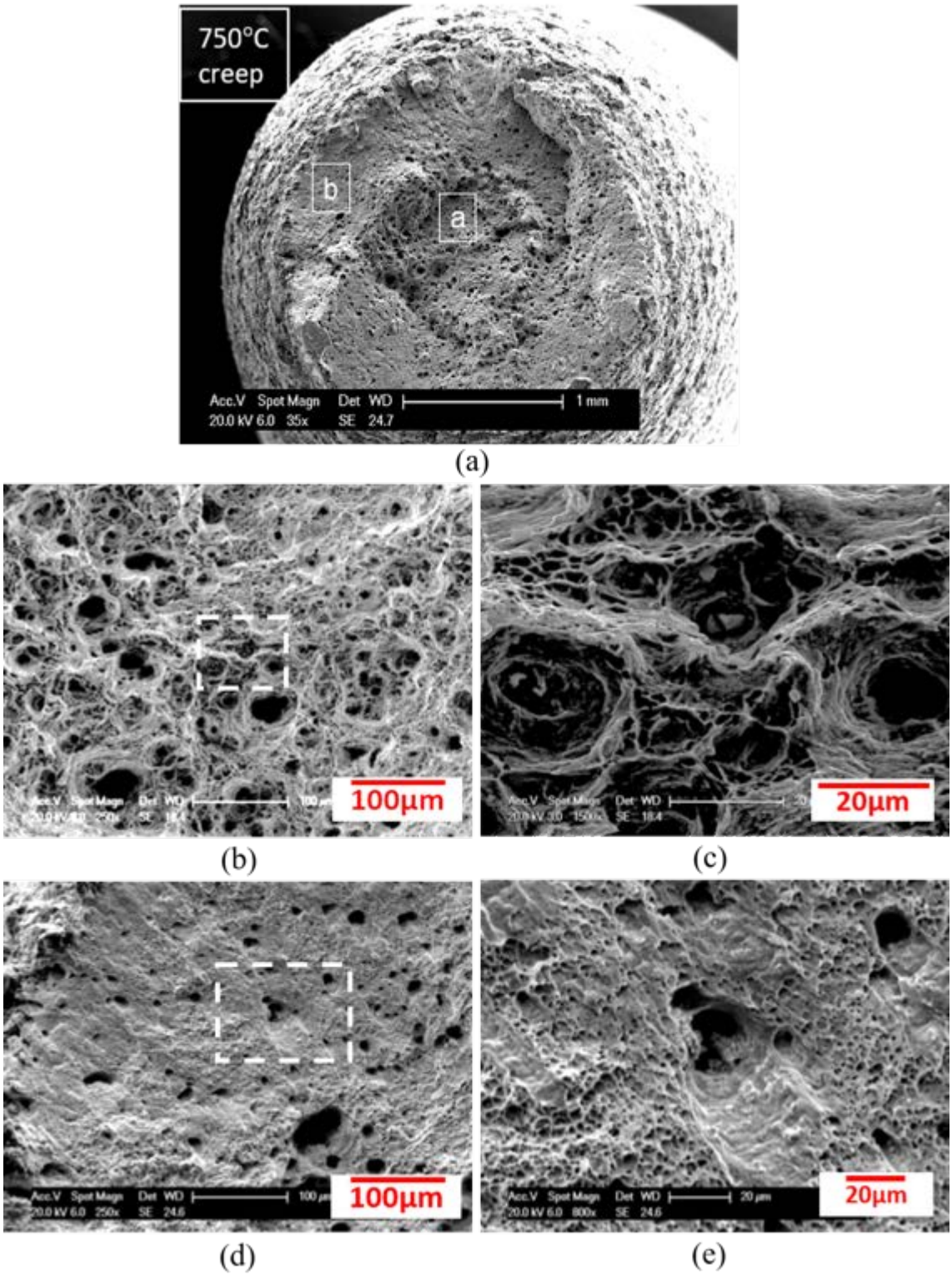

Figure 4.39 SEM micrographs showing (a) the fracture surface of creep testpieces of Alloy 709 at 750°C, (b) the failure mode in the central area (a in Figure 4.39a), (d) the failure mode in the edge area (b in Figure 4.39a), (c) close-up of (b), (e) close-up of (d).

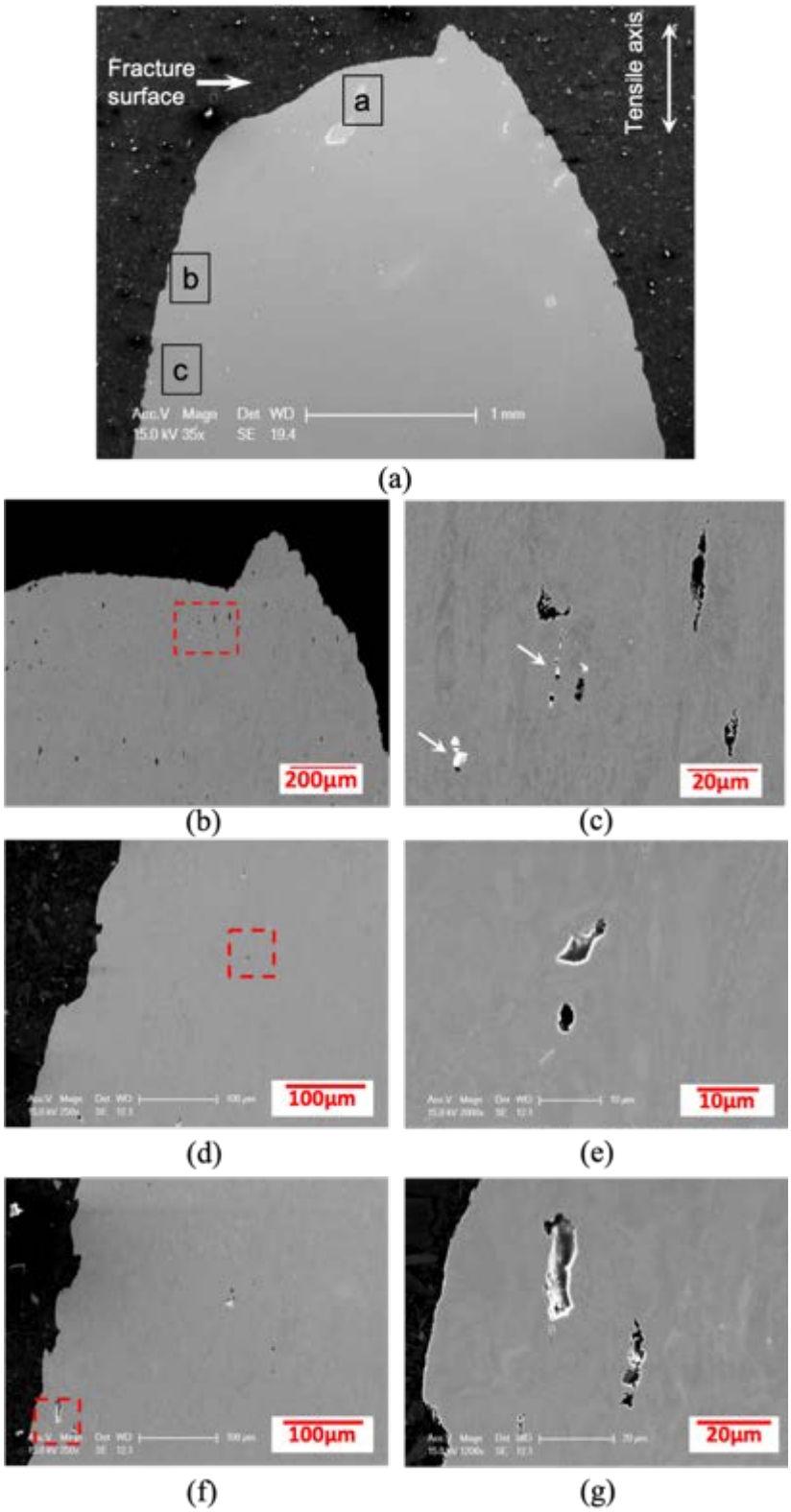

Figure 4.40 (a) BSE images taken from the longitudinal cross-sectioned creep specimens tested at 650°C, (b) microvoids near the fracture surface (a in Figure 4.40a), (c) close-up of Figure 4.40b showing the Nb(CN) particles fractured (white arrow) when the voids formed, (d) and (f) microvoids away from the fracture surface (b and c in Figure 4.40a), (e) and (g) close-up of (d) and (f) showing microvoids formed at grain boundaries.

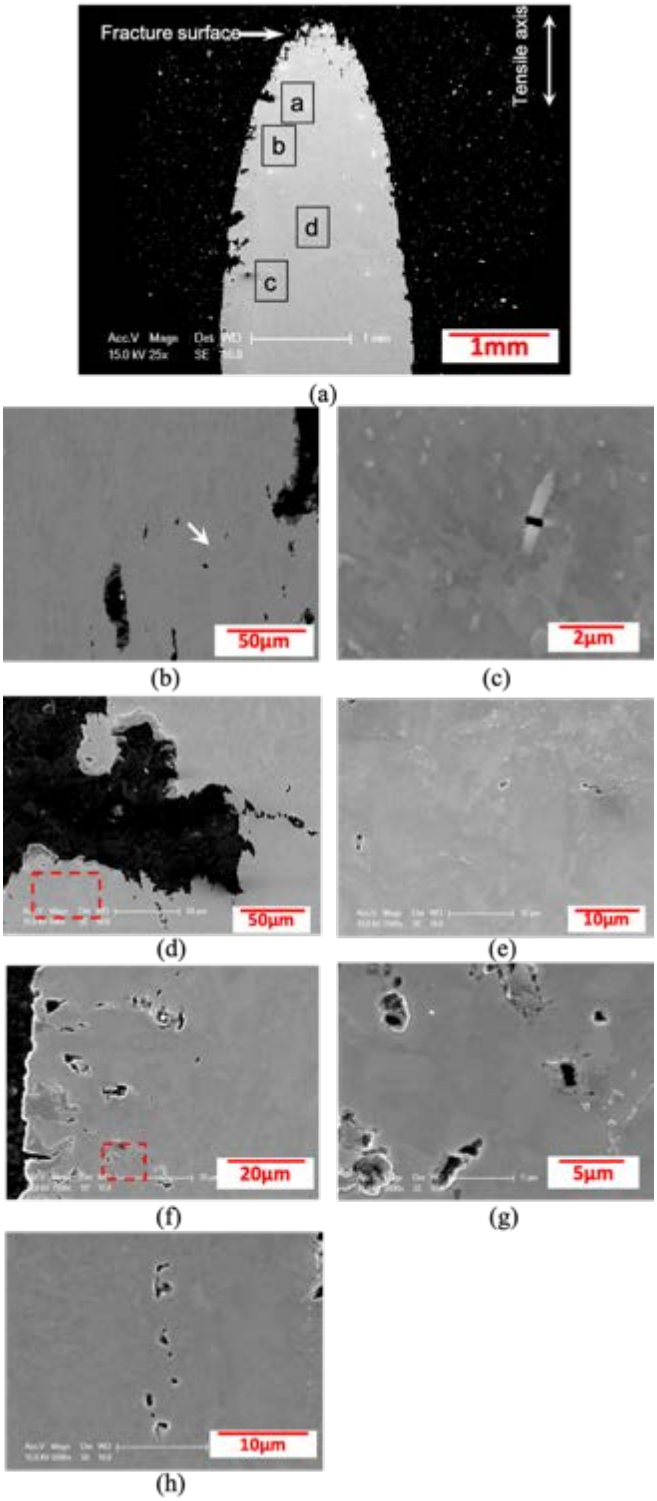

Figure 4.41 BSE images taken from the longitudinal cross-sectioned creep specimens tested at 750°C, (b) area near the fracture surface (a in Figure 4.41a), (c) close-up of Figure 4.41b showing the Nb(CN) particles fractured when the voids formed (white arrow), (d) and (f) microvoids away from the fracture surface (b and c in Figure 4.41a), (e) and (g) close-up of (d) and (f) showing microvoids formed at grain boundaries and (h) grain boundary microvoids formed in the central area of the specimen (d in Figure 4.41a).

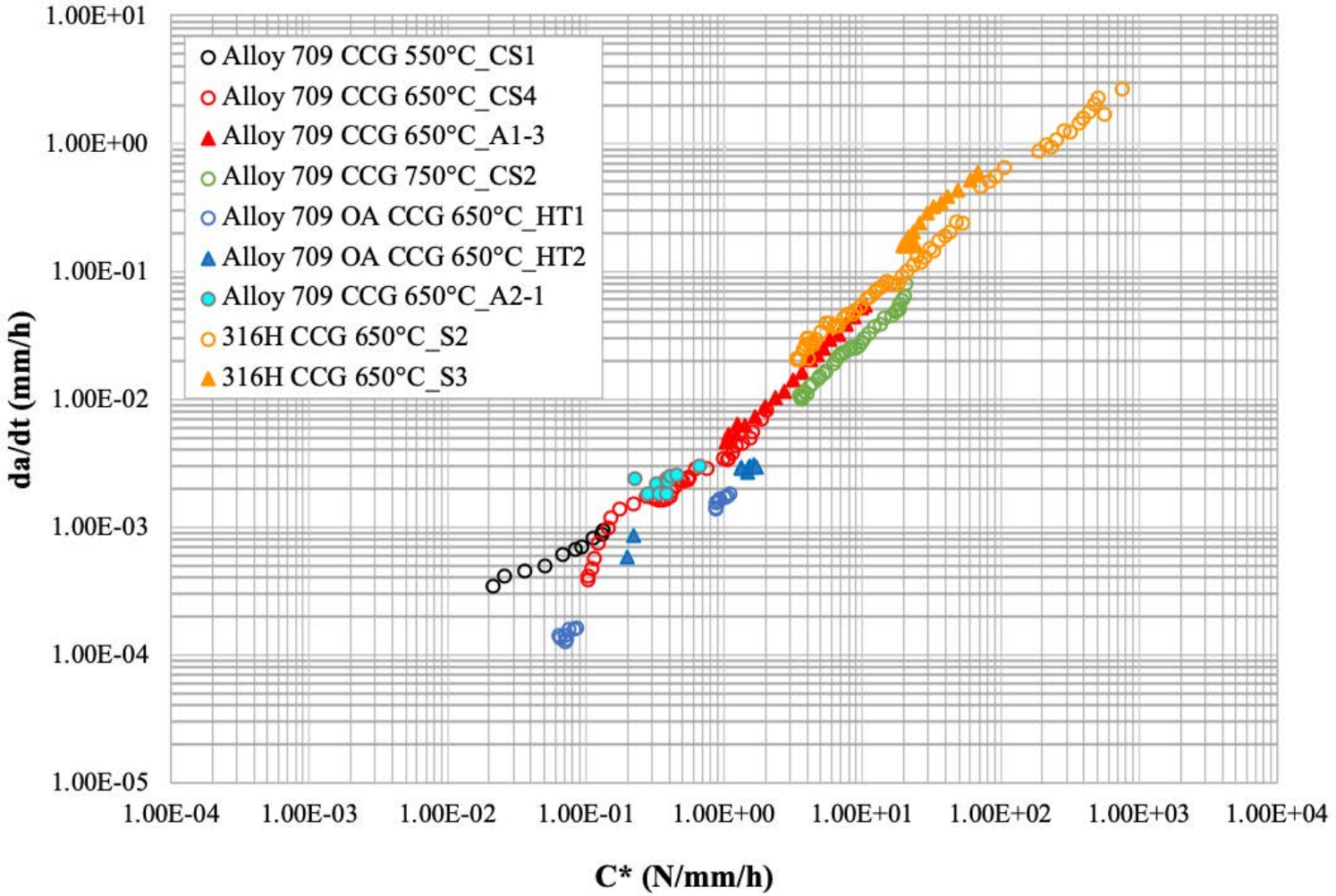

Figure 4.42 Creep crack growth rate plotted against C^* of the as-received Alloy 709 at 550, 650 and 750°C and the aged Alloy 709 and 316H at 650°C. Note that the crack growth data before reaching a steady-state creep status at crack tip are removed.

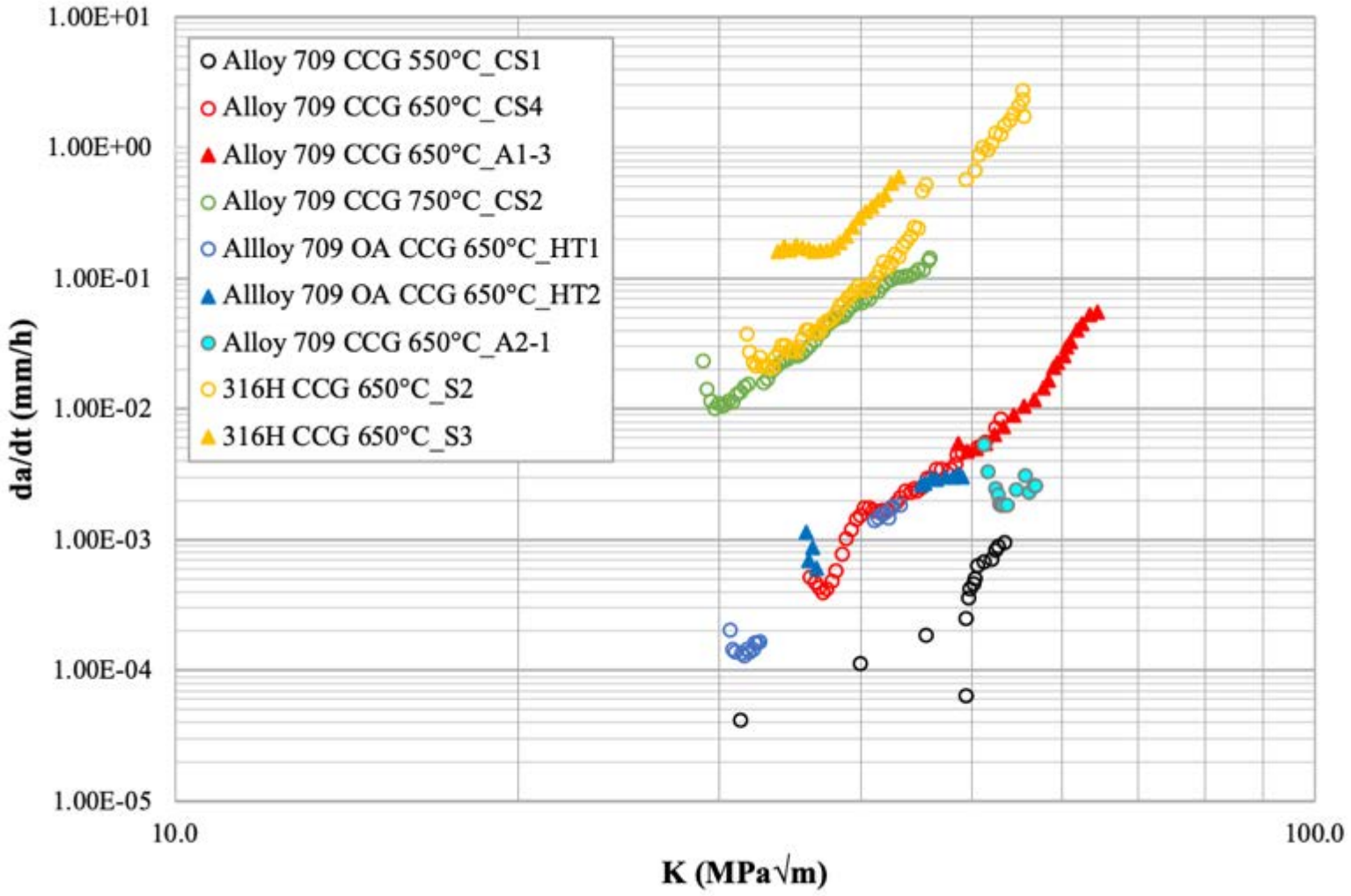

Figure 4.43 Creep crack growth rate plotted against K of the as-received Alloy 709, aged Alloy 709 and 316H at 550, 650 and 750°C.

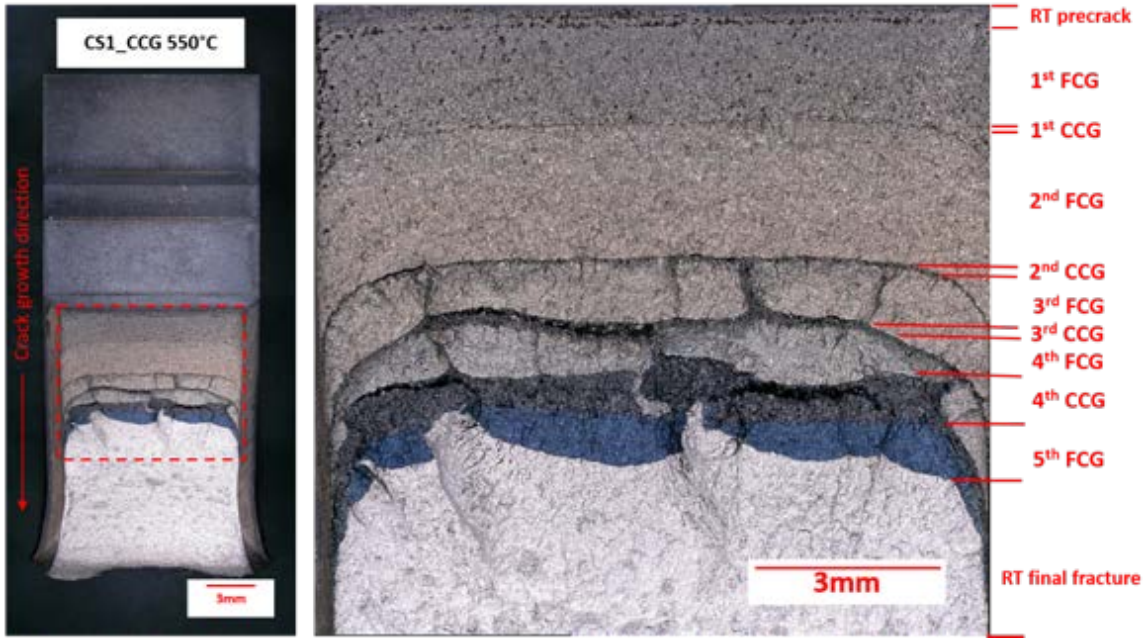

(a)

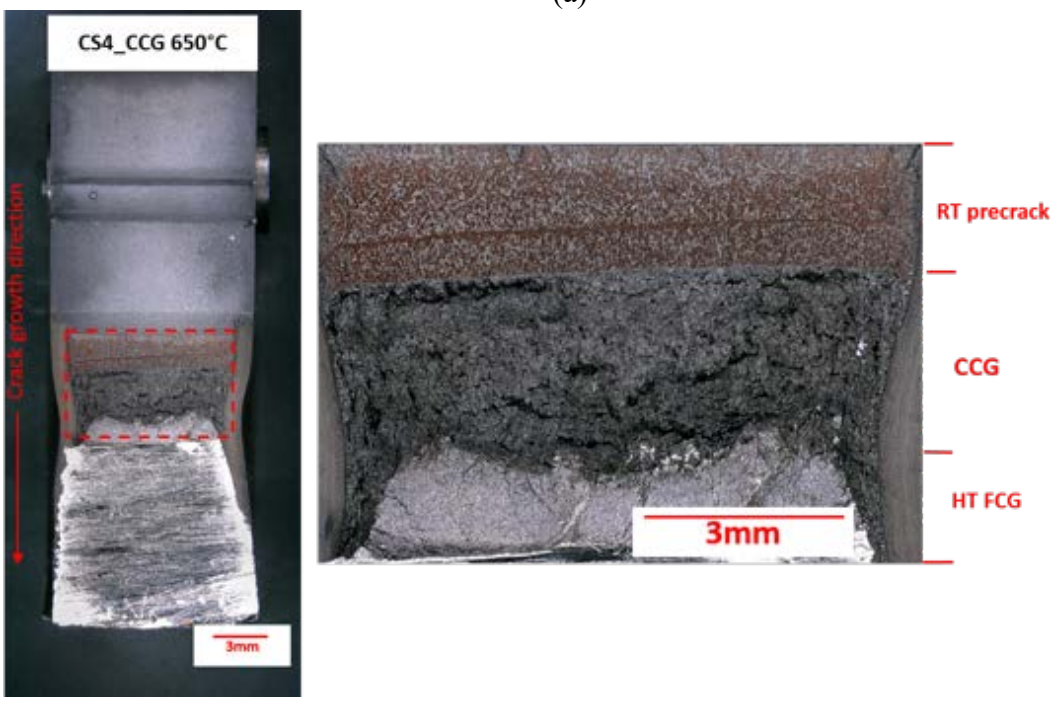

(b)

Figure 4.44 Optical fractographs for creep crack growth testpiece of the as-received Alloy 709 tested at (a) 550 (sample ID: CS1), (b), (c) 650°C (sample ID: CS4 and A1-3), (d), (e) the aged Alloy 709 tested at 650°C (sample ID: HT1 and HT2) and (f) as-received Alloy 709 at 750°C (sample ID: CS2). Continued overleaf.

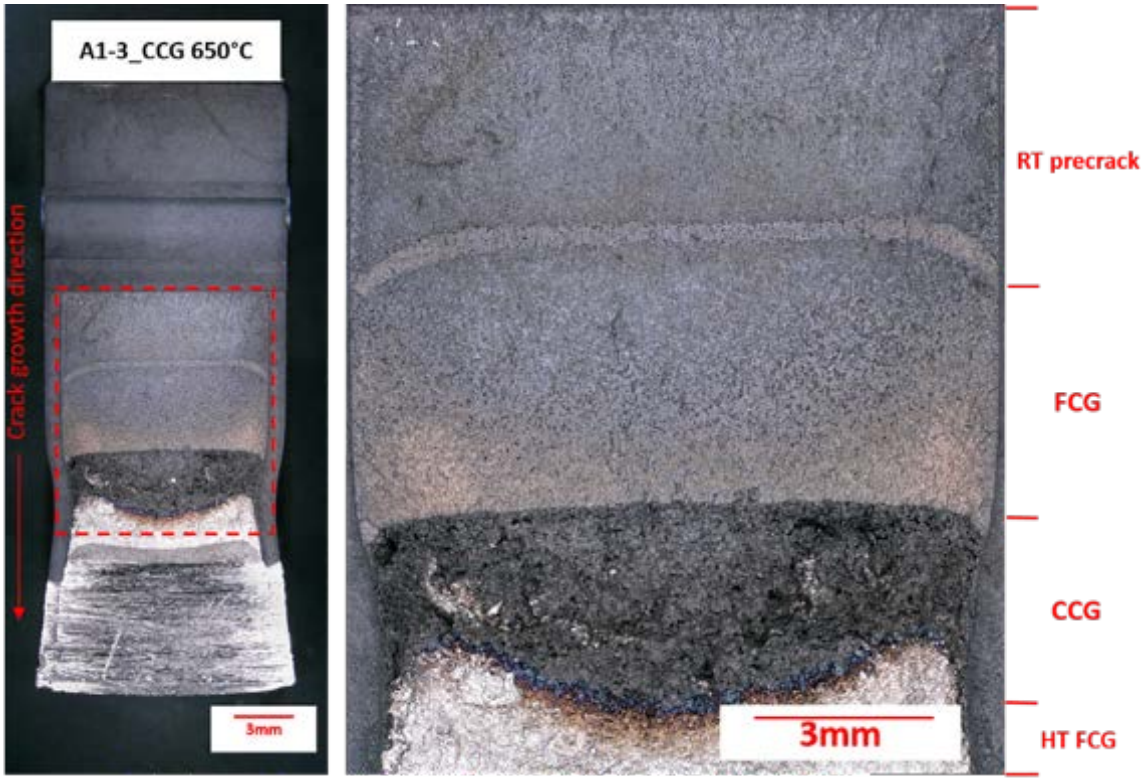

(c)

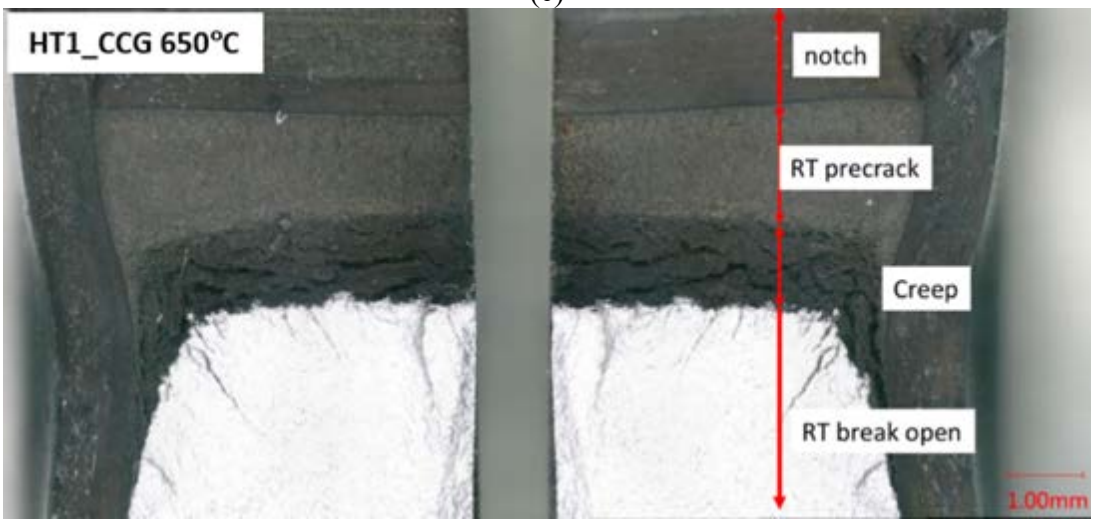

(d)

Figure 4.44 Continued. Optical fractographs for creep crack growth testpiece of the as-received Alloy 709 tested at (a) 550 (sample ID: CS1), (b), (c) 650°C (sample ID: CS4 and A1-3), (d), (e) the aged Alloy 709 tested at 650°C (sample ID: HT1 and HT2) and (f) as-received Alloy 709 at 750°C (sample ID: CS2). Continued overleaf.

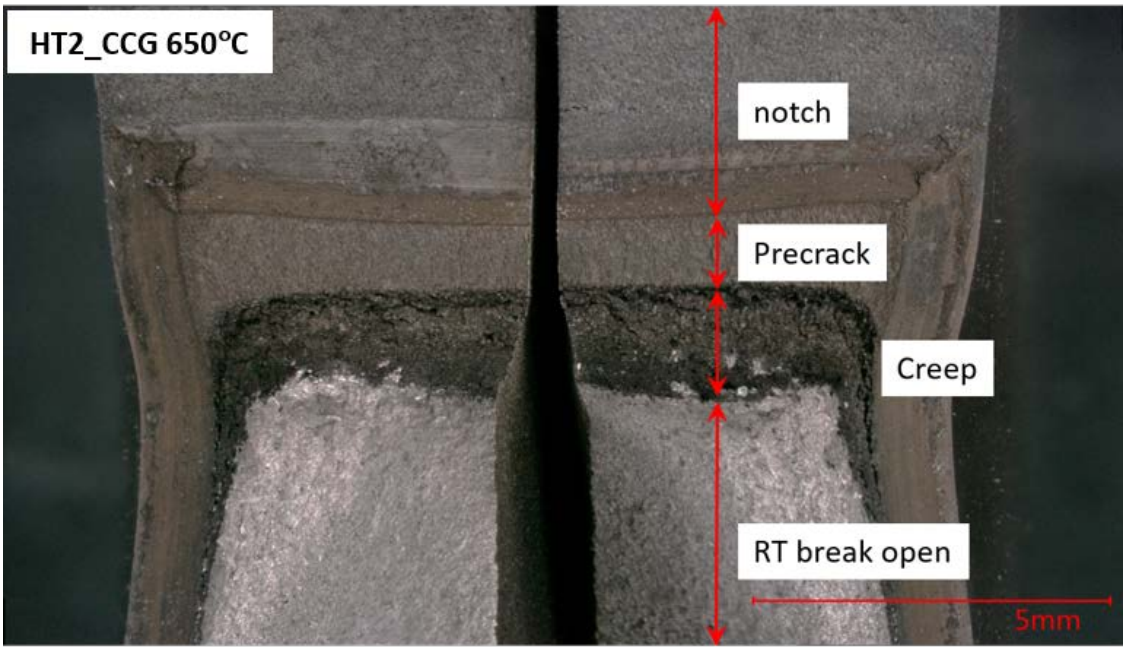

(e)

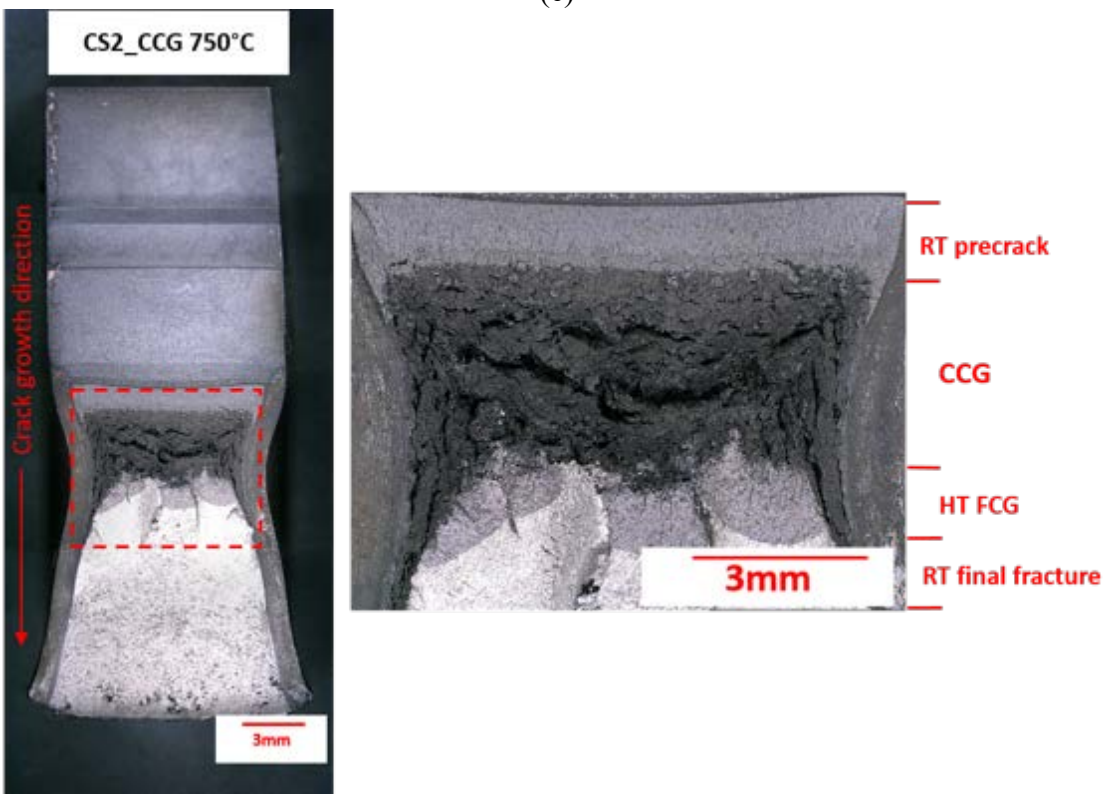

(f)

Figure 4.44 Continued. Optical fractographs for creep crack growth testpiece of the as-received Alloy 709 tested at (a) 550 (sample ID: CS1), (b), (c) 650°C (sample ID: CS4 and A1-3), (d), (e) the aged Alloy 709 tested at 650°C (sample ID: HT1 and HT2) and (f) as-received Alloy 709 at 750°C (sample ID: CS2).

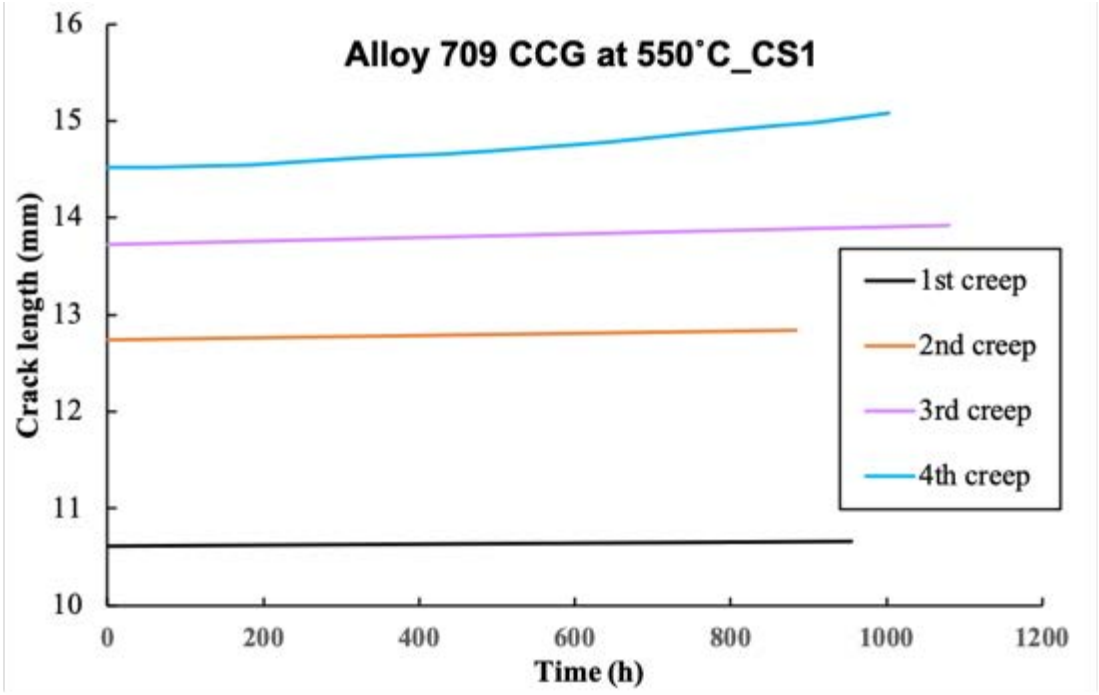

(a)

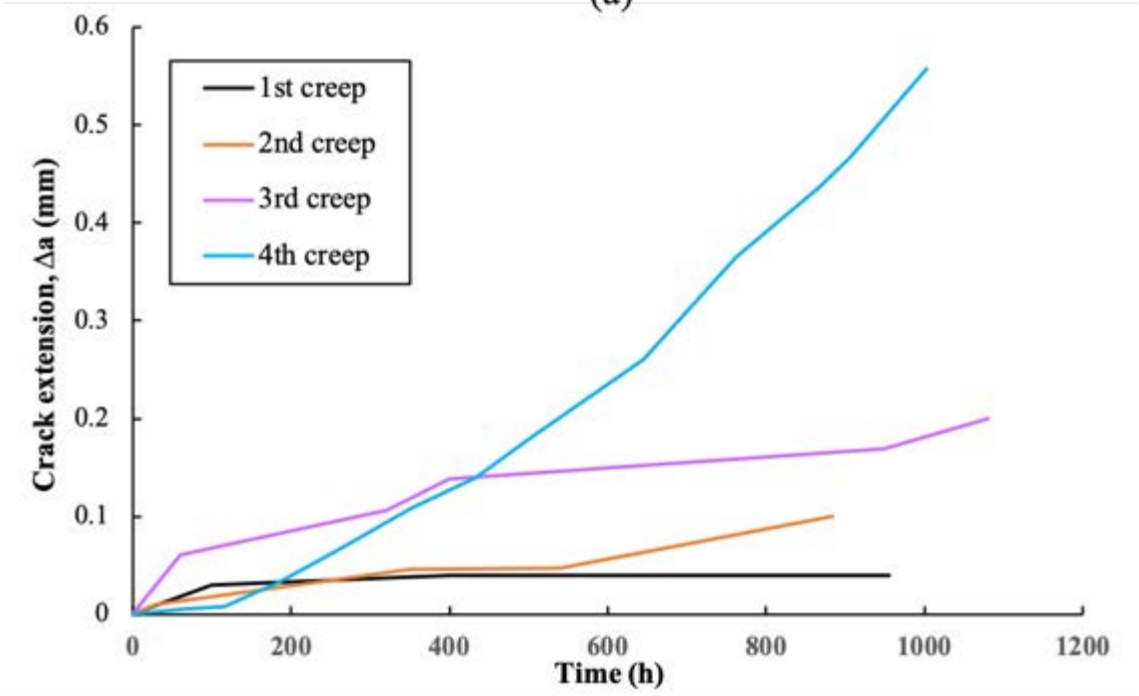

(b)

Figure 4.45 (a) creep crack length (mm), (b) crack extension, Δa (mm) (c) load-line displacement (mm), (d) load-line displacement rate (mm/h) and (e) creep crack growth rate changes with time of the as-received Alloy 709 at 550°C (sample ID: CS1). Continued overleaf.

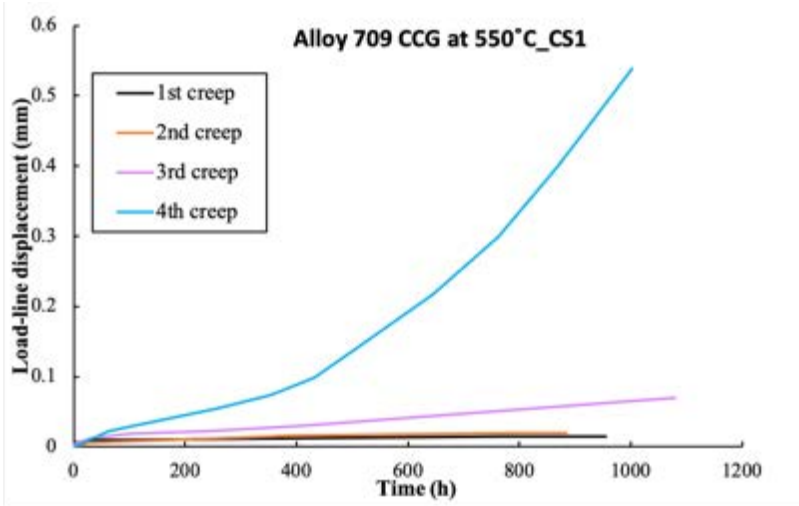

(c)

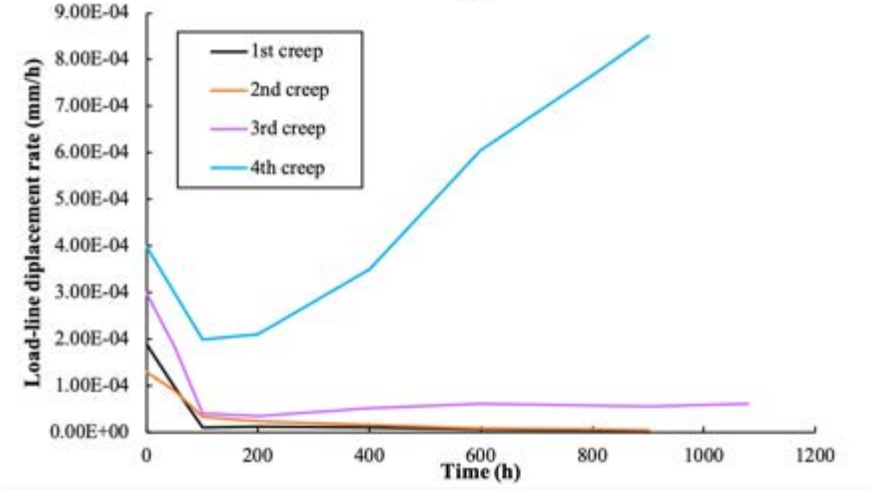

(d)

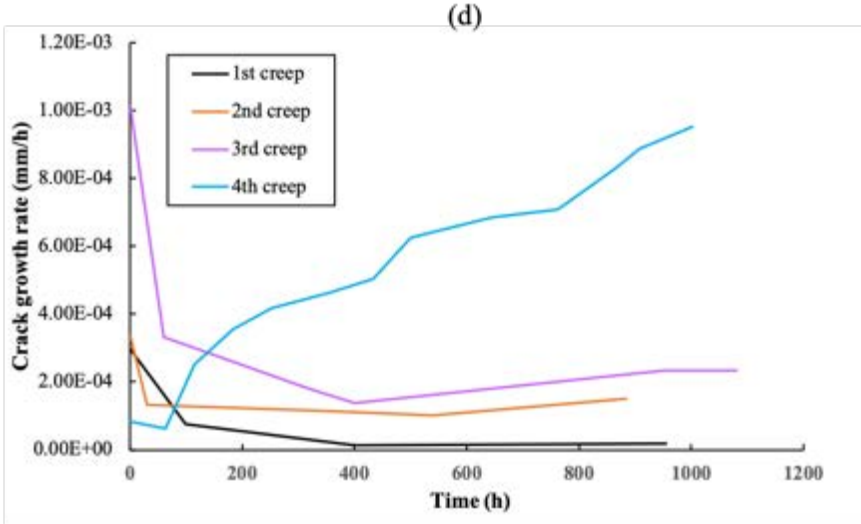

(e)

Figure 4.45 Continued. (a) creep crack length (mm), (b) crack extension, Δa (mm) (c) load-line displacement (mm), (d) load-line displacement rate (mm/h) and (e) creep crack growth rate changes with time of the as-received Alloy 709 at 550°C (sample ID: CS1).

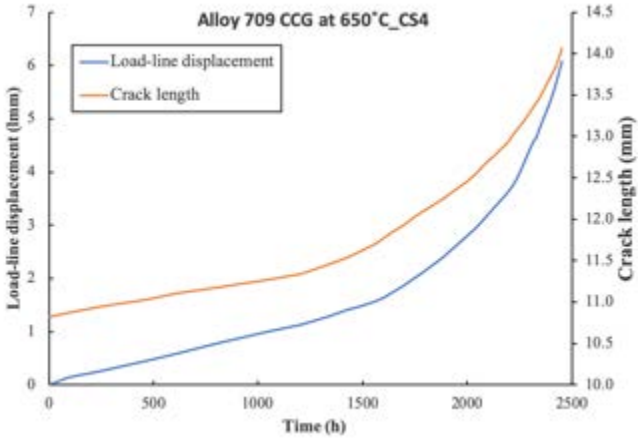

(a)

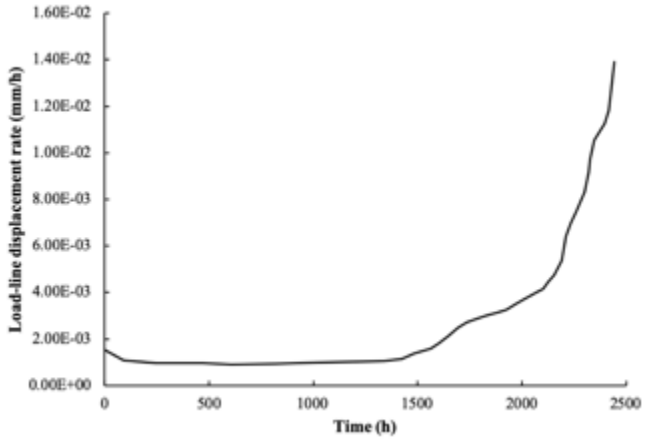

(b)

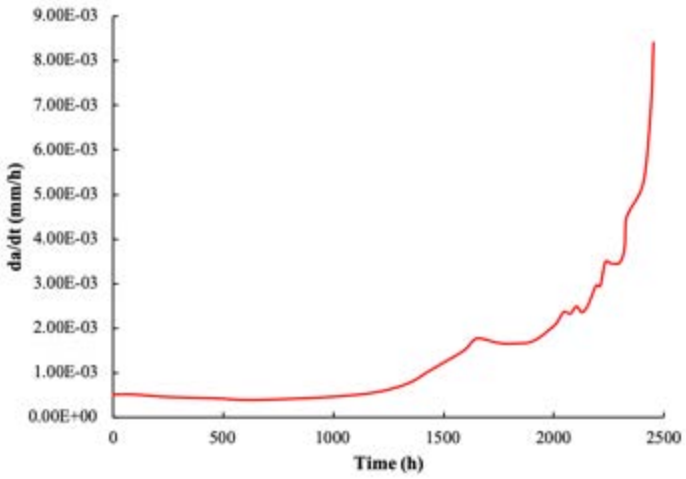

(c)

Figure 4.46 (a) creep crack length (mm) and load-line displacement (mm), (b) load-line displacement rate (mm/h) and (c) creep crack growth rate plotted against time of the as-received Alloy 709 at 650°C (sample ID: CS4).

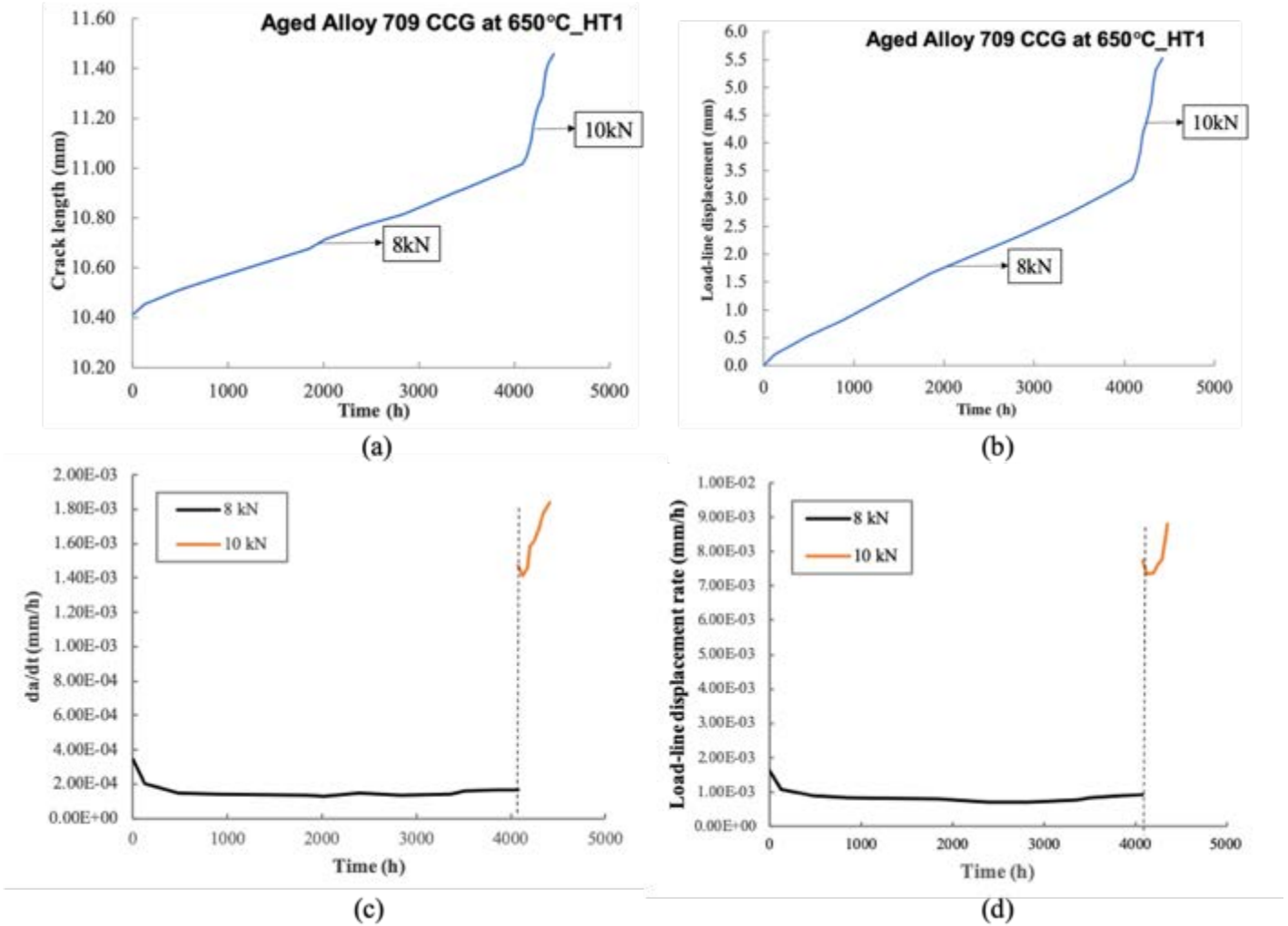

Figure 4.47 (a) creep crack length (mm), (b) load-line displacement (mm), (c) creep crack growth rate and (d) load-line displacement rate (mm/h) changes with time of the aged Alloy 709 at 650°C (sample ID: HT1).

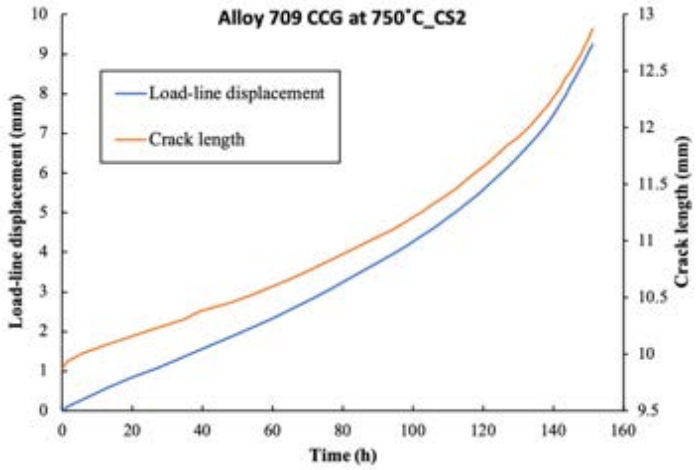

(a)

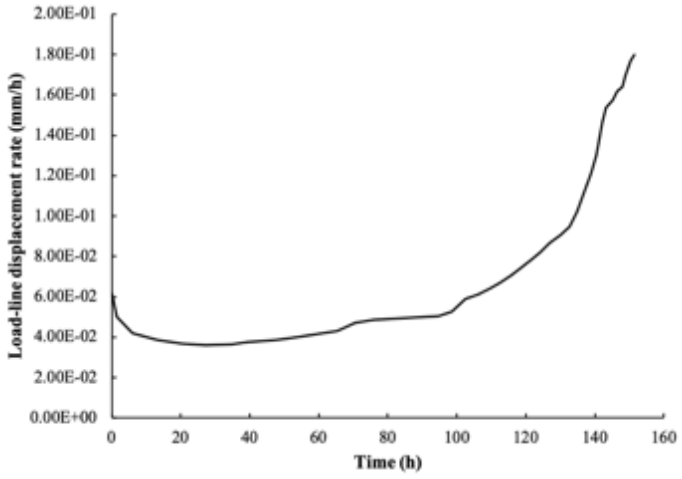

(b)

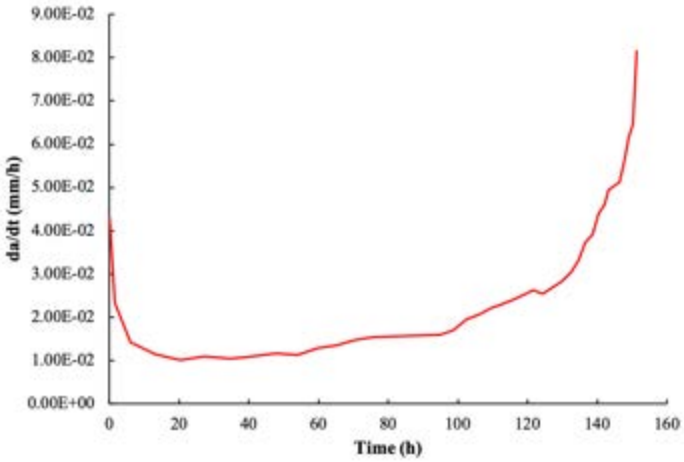

(c)

Figure 4.48 (a) creep crack length (mm) and load-line displacement (mm), (b) load-line displacement rate (mm/h) (c) creep crack growth rate plotted against time of the as-received Alloy 709 at 750°C (sample ID: CS2).

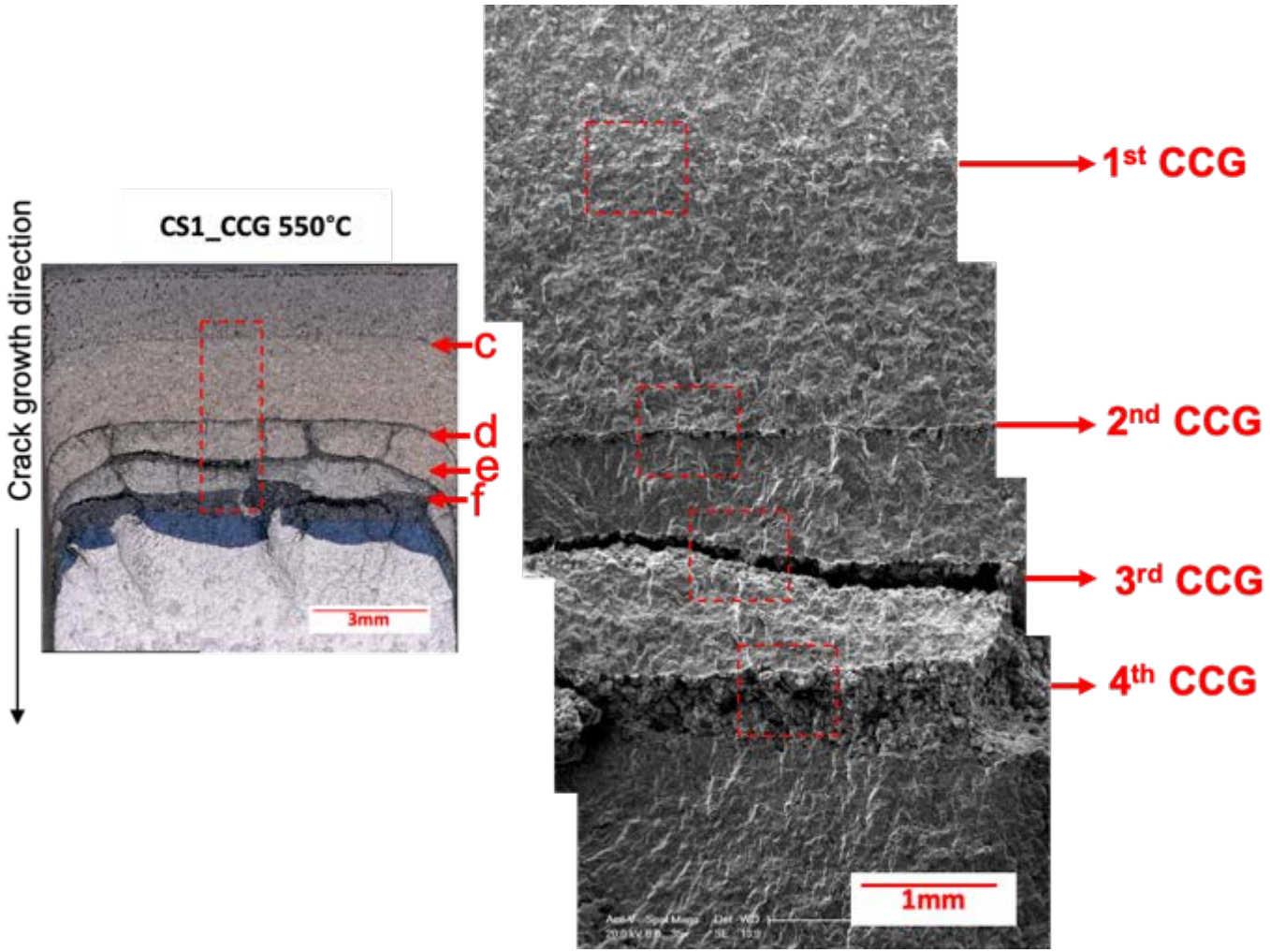

(a) (b)

Figure 4.49 (a) Optical fractography and (b) SEM fractography of the corresponding rectangle area in Figure 4.49a for the creep crack growth testpiece after testing at 550°C (sample ID: CS1).

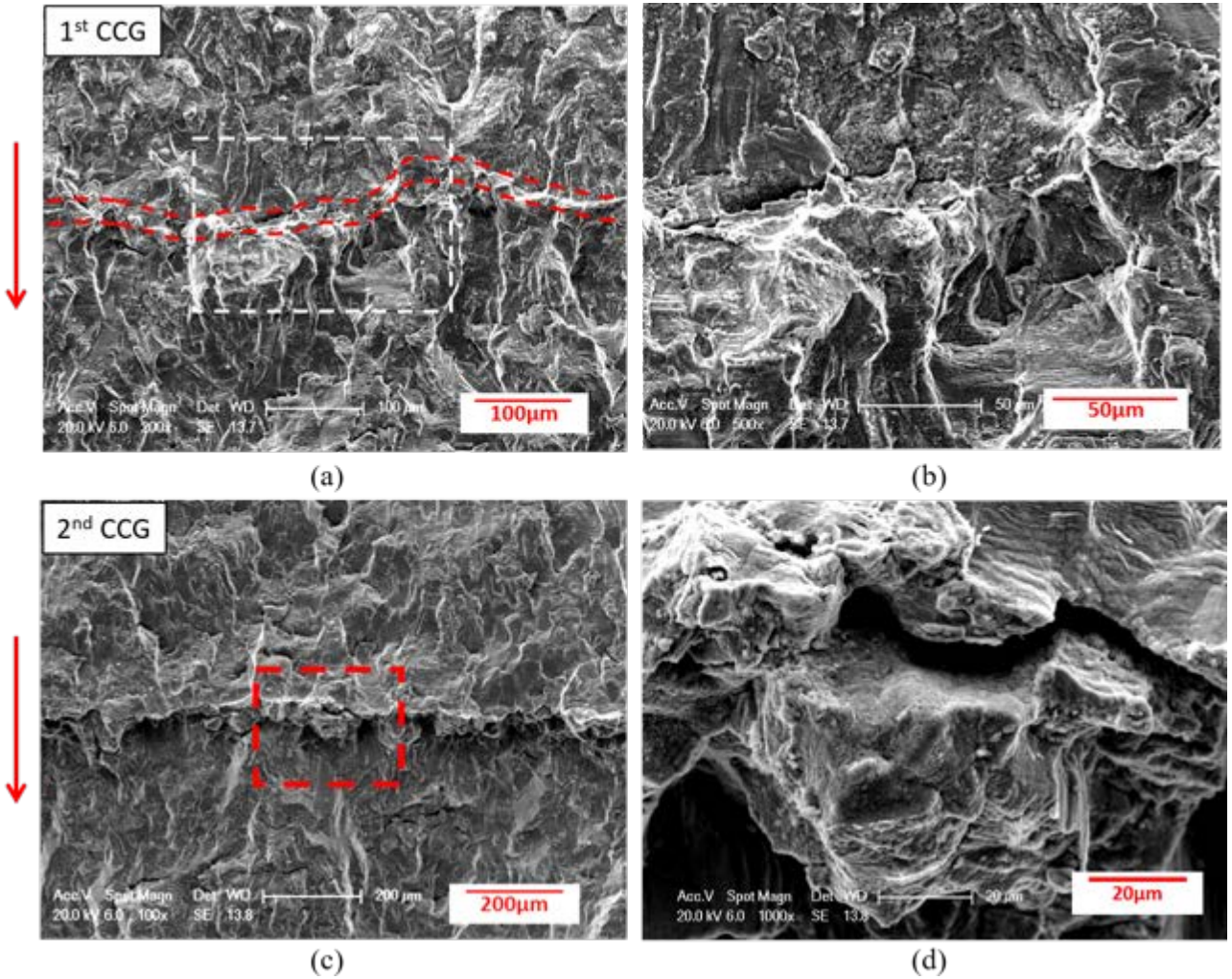

Figure 4.50 SEM fractographs of the as-received Alloy 709 creep crack growth specimen tested at 550°C (sample ID: CS1) showing the (a) first, (c) second (e) third and (g) fourth creep crack growth regions. (b), (d), (f), (h) close-up of (a), (c), (e), (g). Continued overleaf.

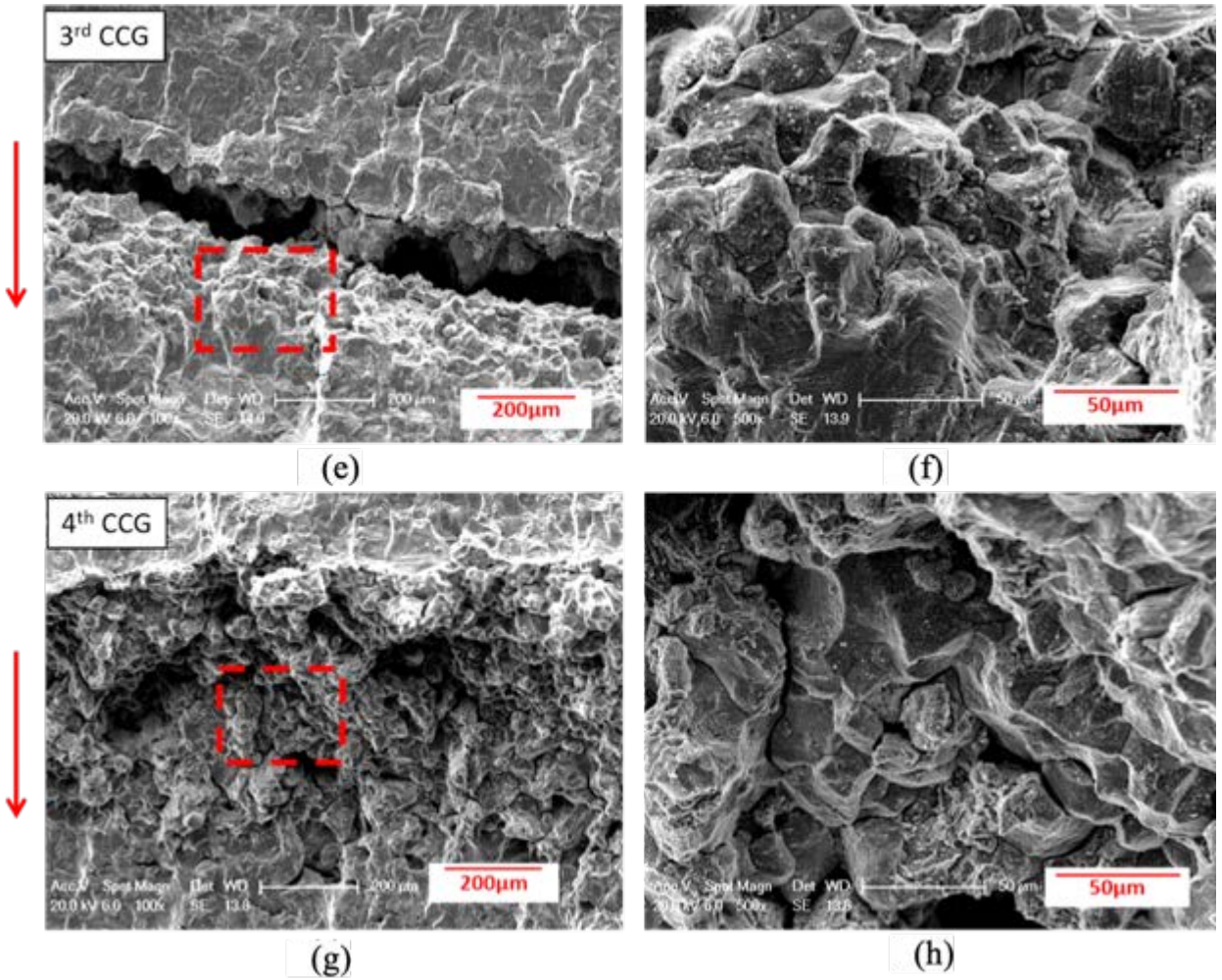

Figure 4.50 Continued. SEM fractographs of the as-received Alloy 709 creep crack growth specimen tested at 550°C (sample ID: CS1) showing the (a) first, (c) second (e) third and (g) fourth creep crack growth regions. (b), (d), (f), (h) close-up of (a), (c), (e), (g).

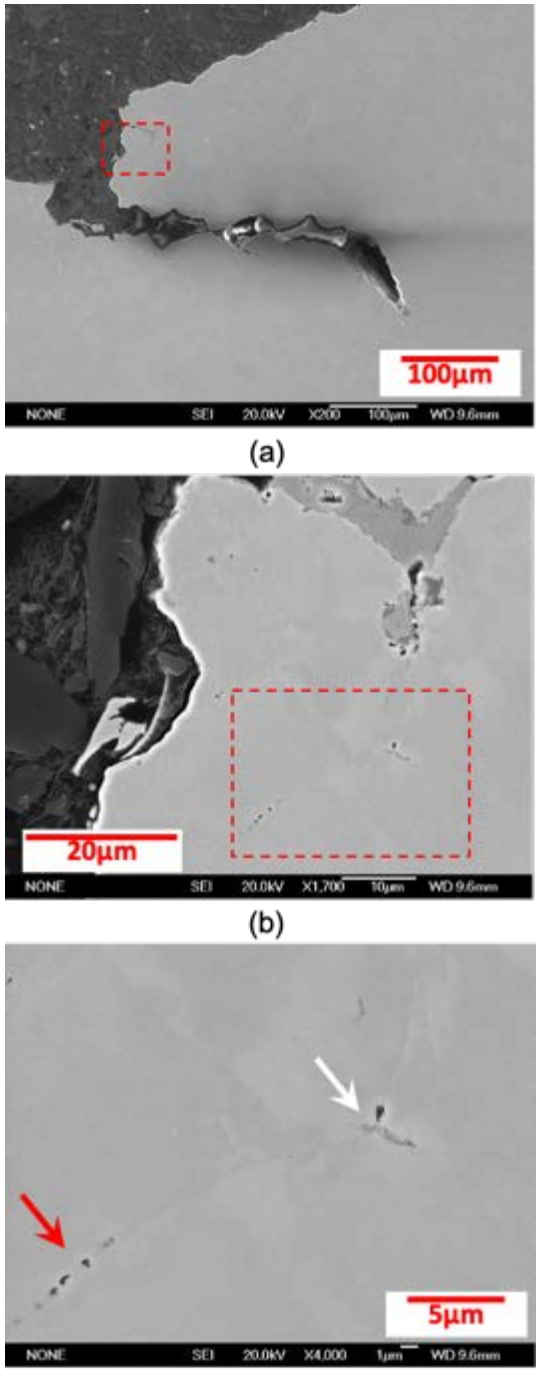

Figure 4.51 (a) SEM images taken from the 2nd CCG on longitudinal cross-sectioned creep crack growth testpiece at 550°C, (b) close-up of Figure 4.51a showing the areas near the crack surface and (c) close-up of Figure 4.51b showing the grain boundary damages associated with the linkage of grain boundary cavities (red arrow) and "wedge" cracks (white arrow).

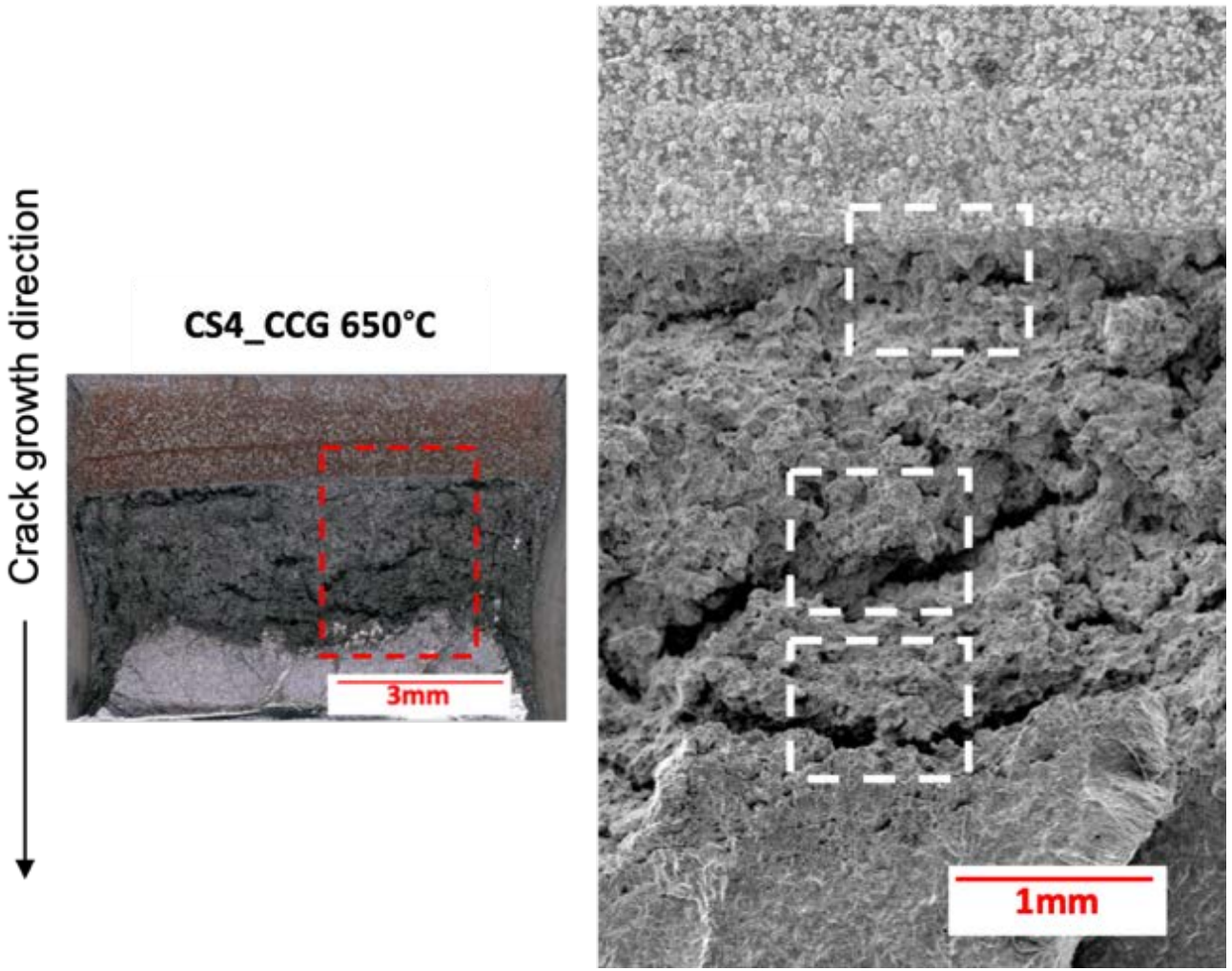

(a) (b)

Figure 4.52 (a) Optical fractography and (b) SEM fractography of the corresponding rectangle area in Figure 4.52a for the creep crack growth testpiece after testing at 650°C (sample ID: CS4).

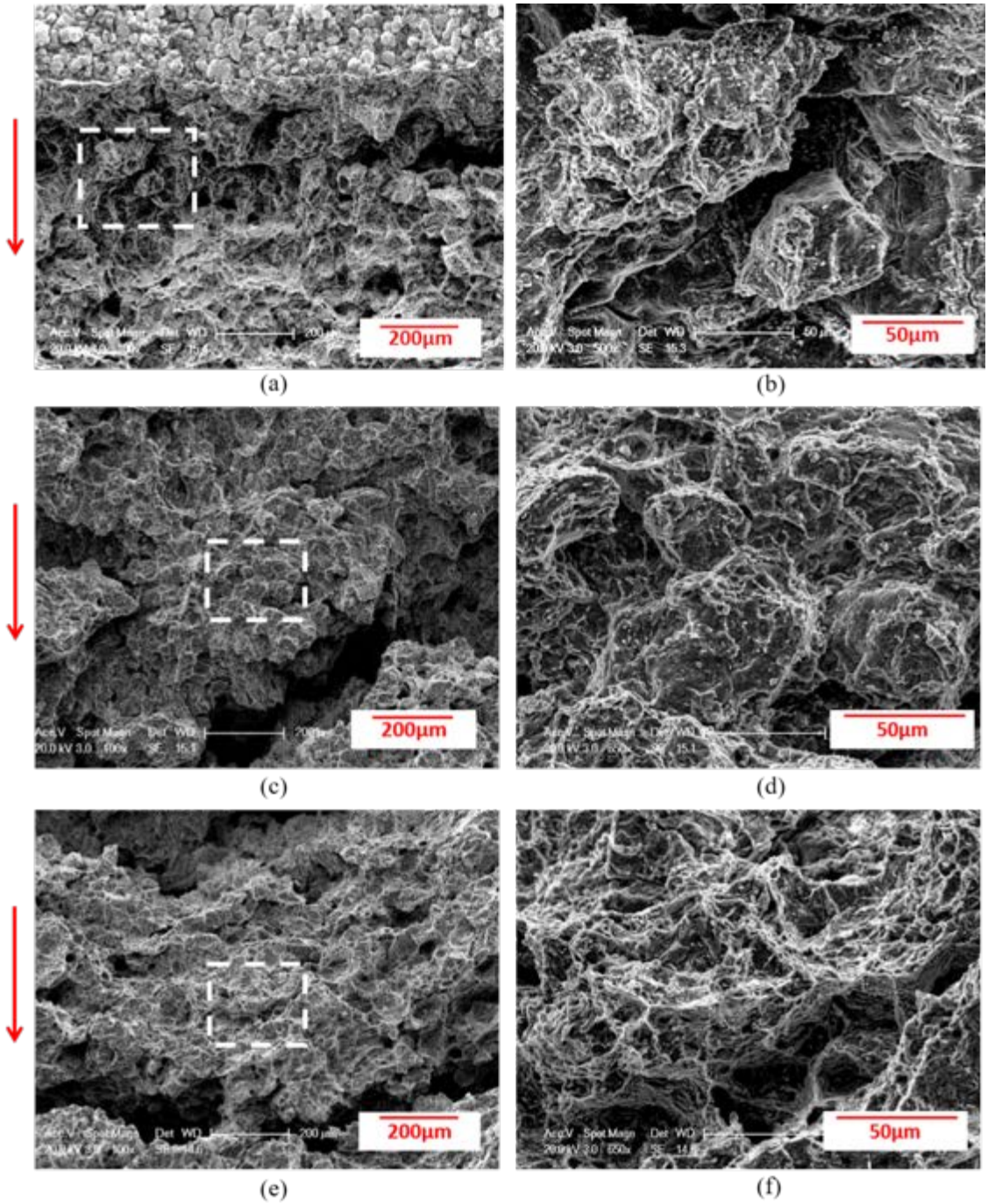

Figure 4.53 SEM fractographs of the as-received Alloy 709 creep crack growth specimen tested at 650°C (sample ID: CS4) showing (a), (c), (e) the beginning, central and final of the crack growth regions. (b), (d), (f) close-up of (a), (c), (e).

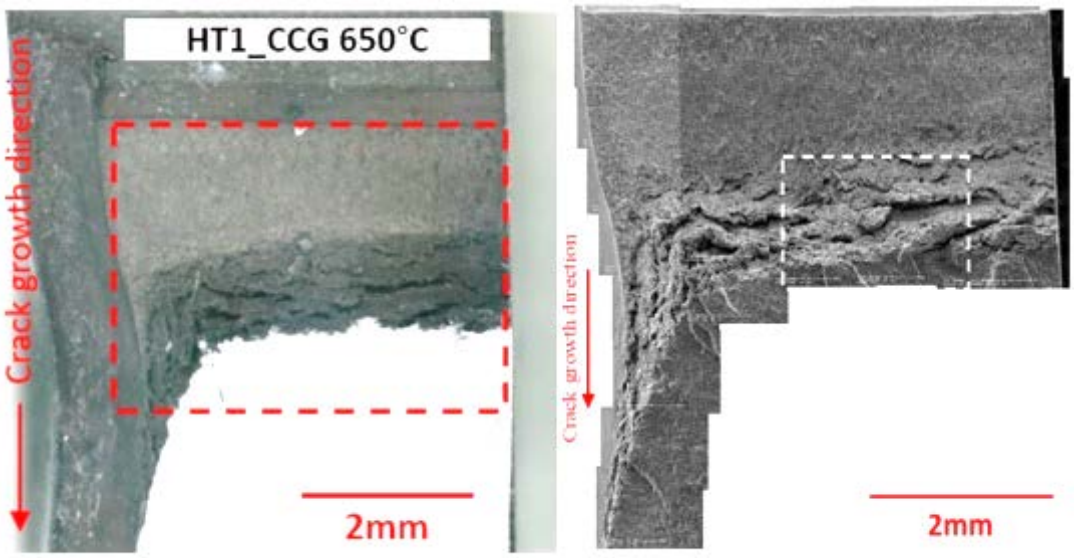

(a) (b)

Figure 4.54 (a) Optical fractography and (b) SEM fractography of the corresponding rectangle area in Figure 4.54a for the aged Alloy 709 after testing at 650°C (sample ID: HT1).

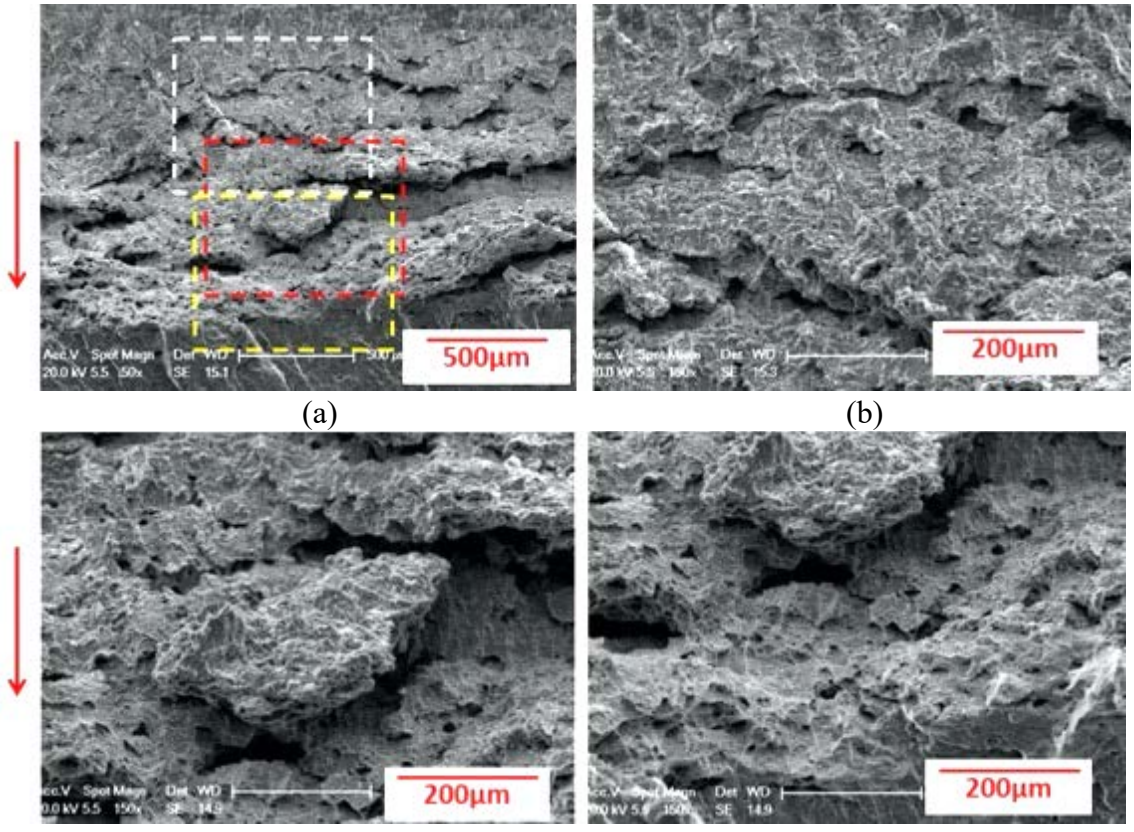

(a) (b)

(c) (d)

Figure 4.55 SEM fractographs of the aged Alloy 709 creep crack growth specimen tested at 650°C (sample ID: HT1) showing (a) the corresponding area in Figure 4.54b, (b)-(d) ductile fracture at the beginning, middle and end of the creep crack growth.

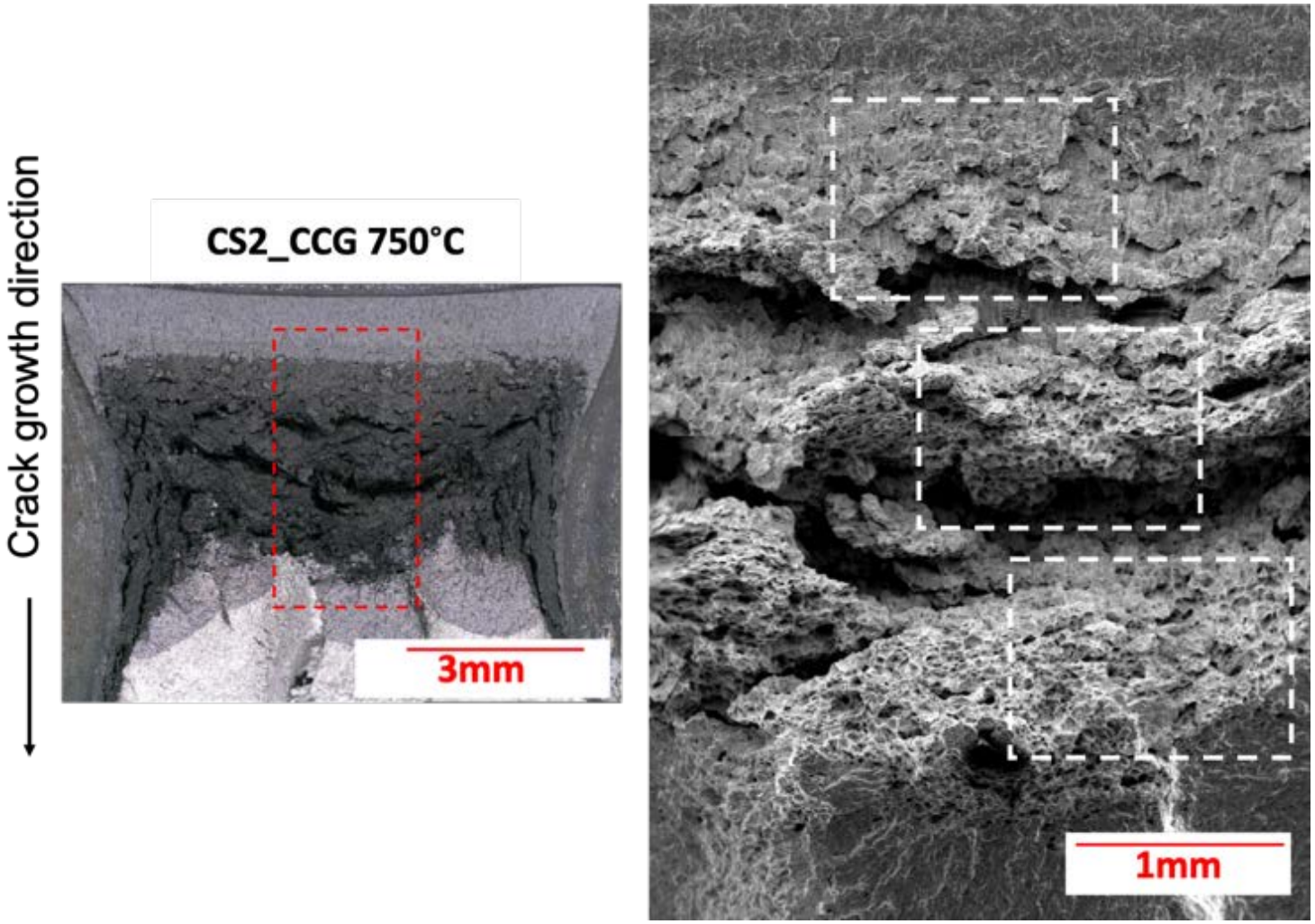

(a) (b)

Figure 4.56 (a) Optical fractography and (b) SEM fractography of the corresponding rectangle area in Figure 4.56a for the creep crack growth testpiece after testing at 750°C (sample ID: CS2).

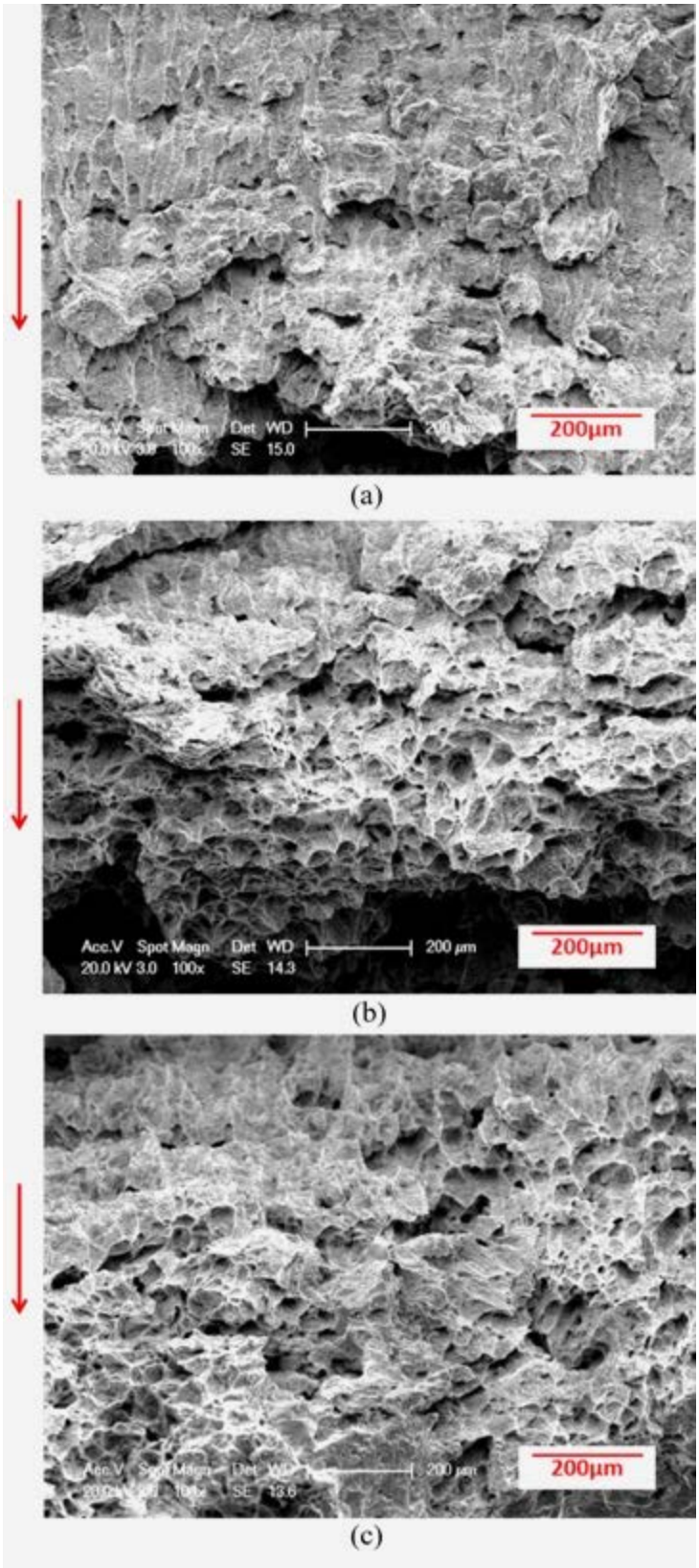

Figure 4.57 SEM fractographs of the as-received Alloy 709 creep crack growth specimen tested at 750°C (sample ID: CS2) showing (a), (b), (c) the beginning, central and final of the crack growth regions.

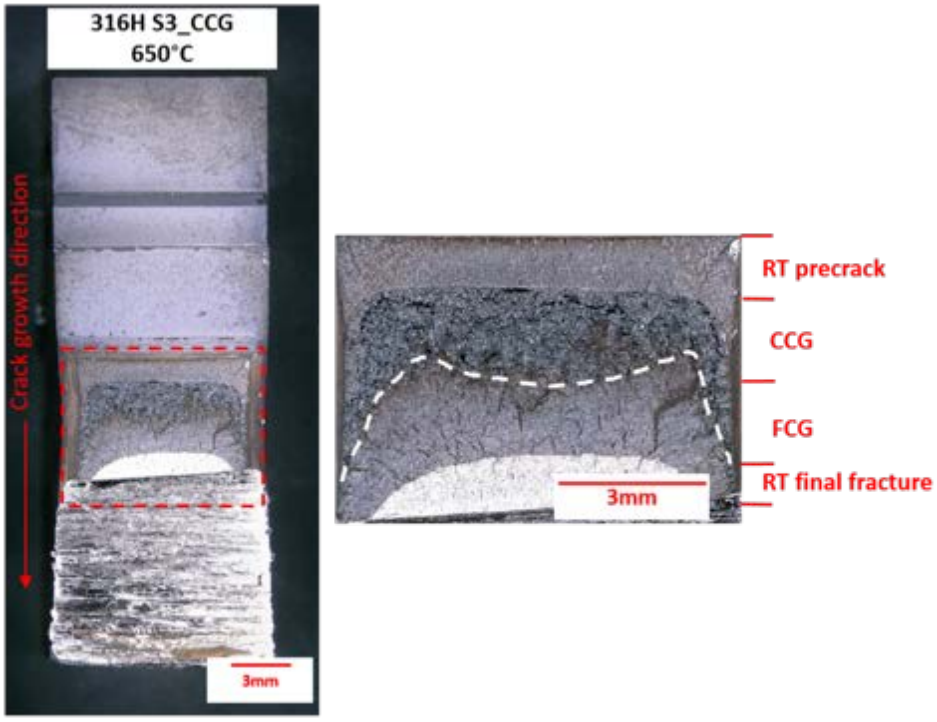

(a)

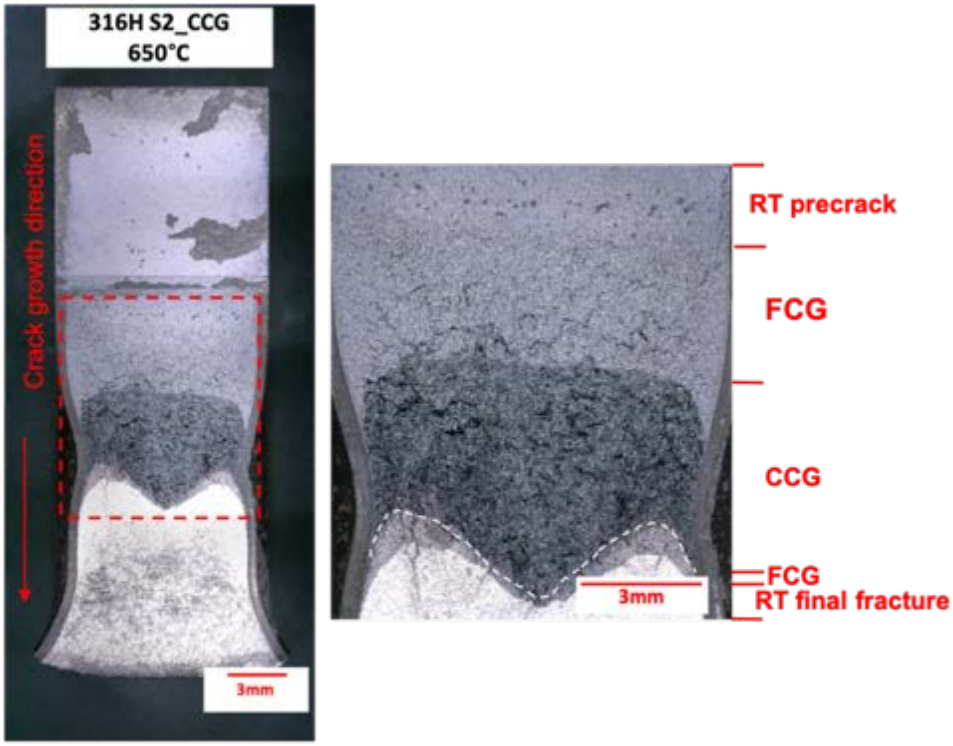

(b)

Figure 4.58 Optical fractographs for (a) the first creep crack growth testpieces of 316H tested at 650°C (sample ID: 316H S3), (b) the second creep crack growth testpieces of 316H tested at 650°C (sample ID: 316H S2). White dotted lines showing the crack front of creep crack growth behaviour.

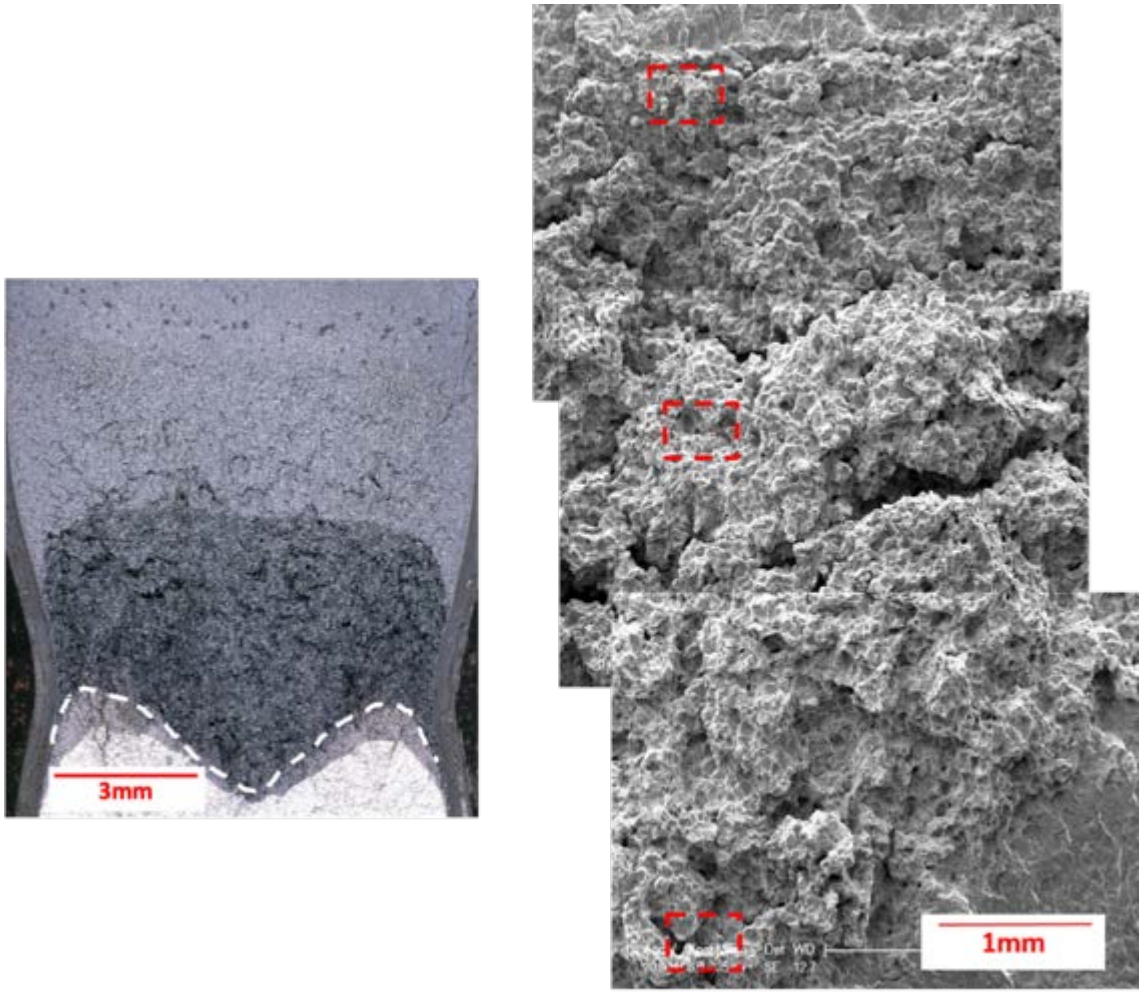

Figure 4.59 (a) Optical fractography and (b) SEM fractography of the corresponding rectangle area in Figure 4.59a for the creep crack growth testpiece of 316H after testing at 650°C (sample ID: 316H S2).

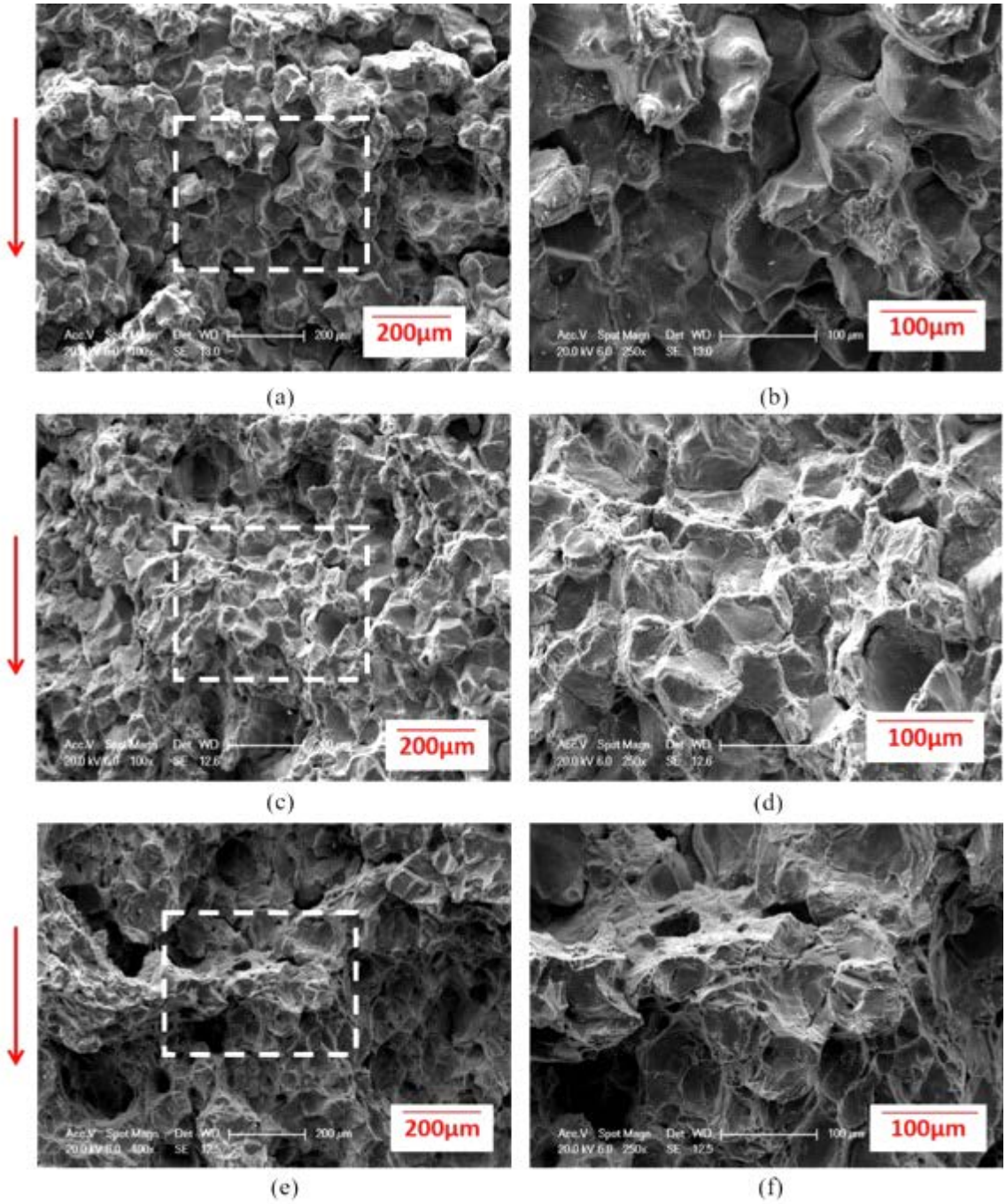

Figure 4.60 SEM fractographs of creep crack growth testpieces for 316H SS at 650°C (sample ID: 316H S2) showing (a), (c), (e) the beginning, central and final of the crack growth regions. (b), (d), (f) close-up of (a), (c), (e).

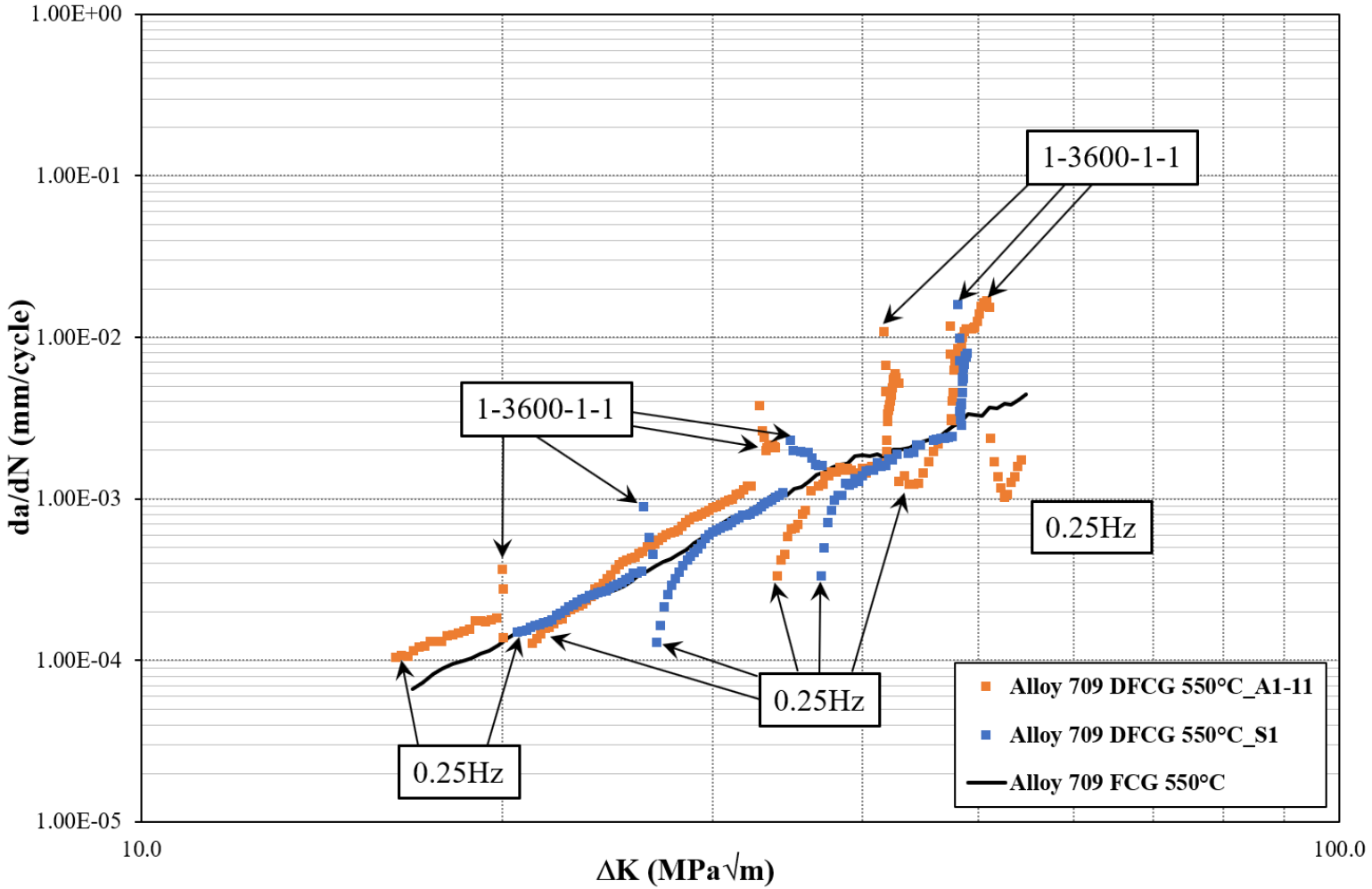

Figure 4.61 Dwell-fatigue crack growth of Alloy 709 in air at 550°C.

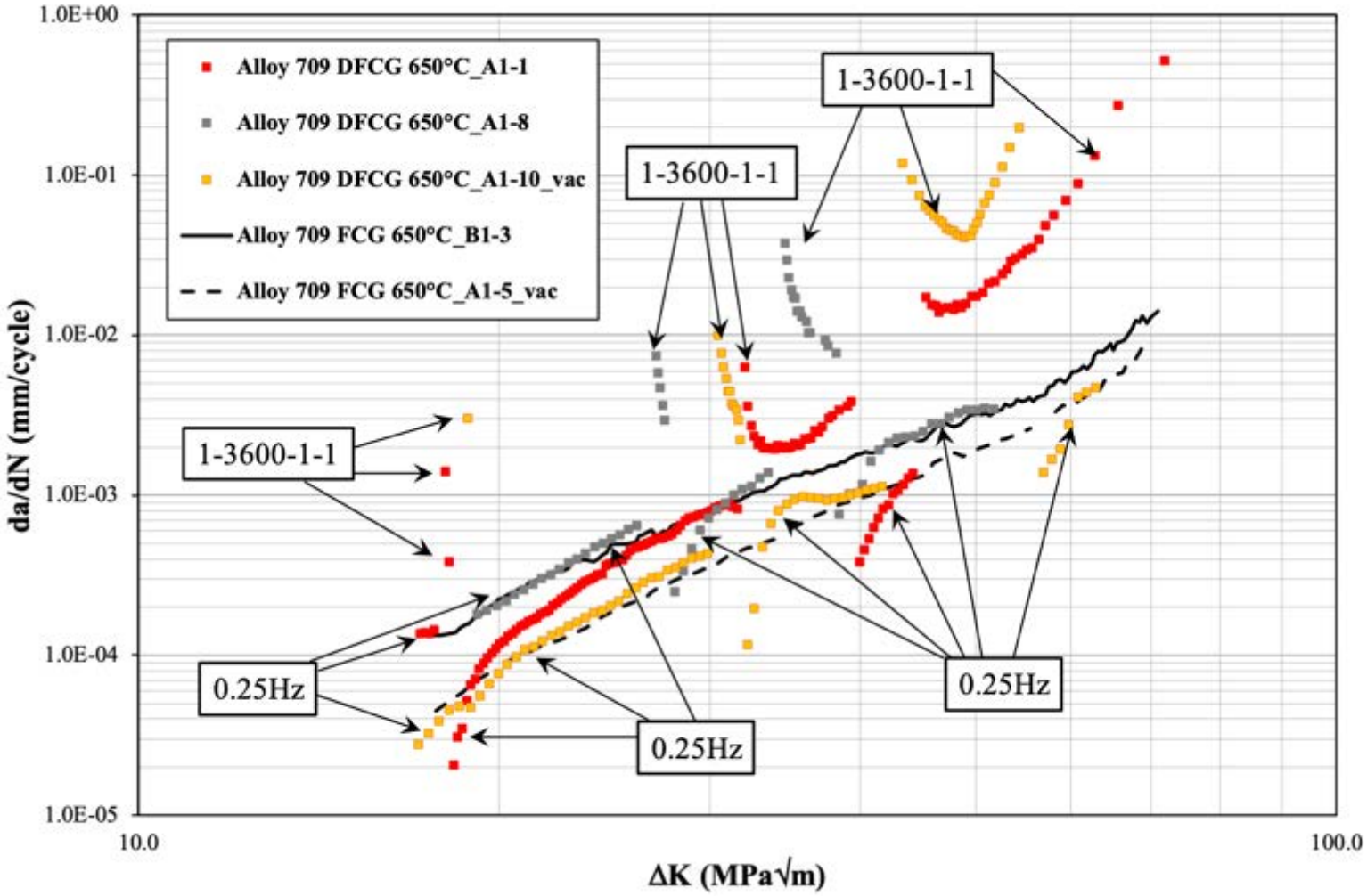

Figure 4.62 Dwell-fatigue crack growth of Alloy 709 in air at 650°C.

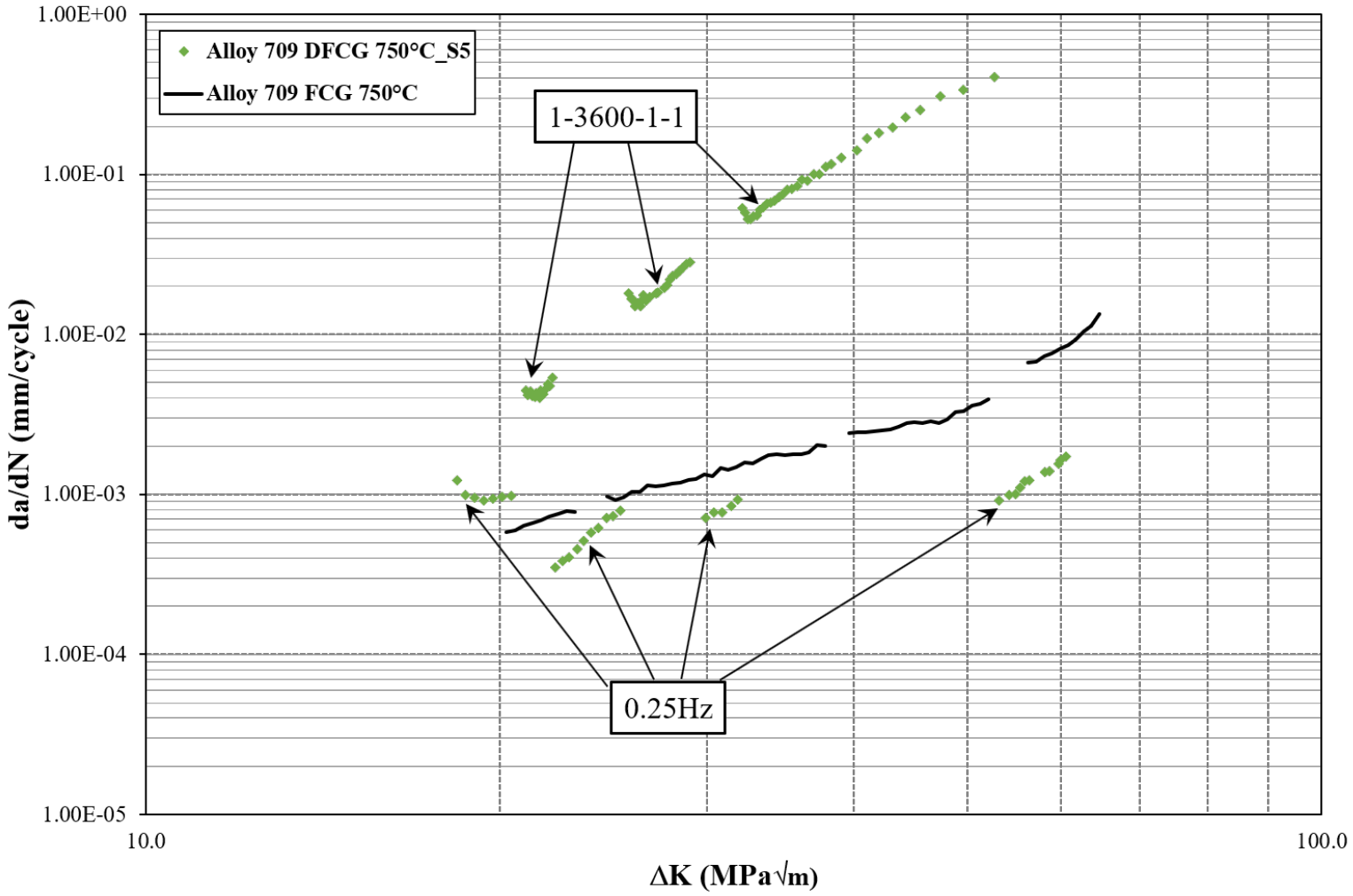

Figure 4.63 Dwell-fatigue crack growth of Alloy 709 in air at 750°C.

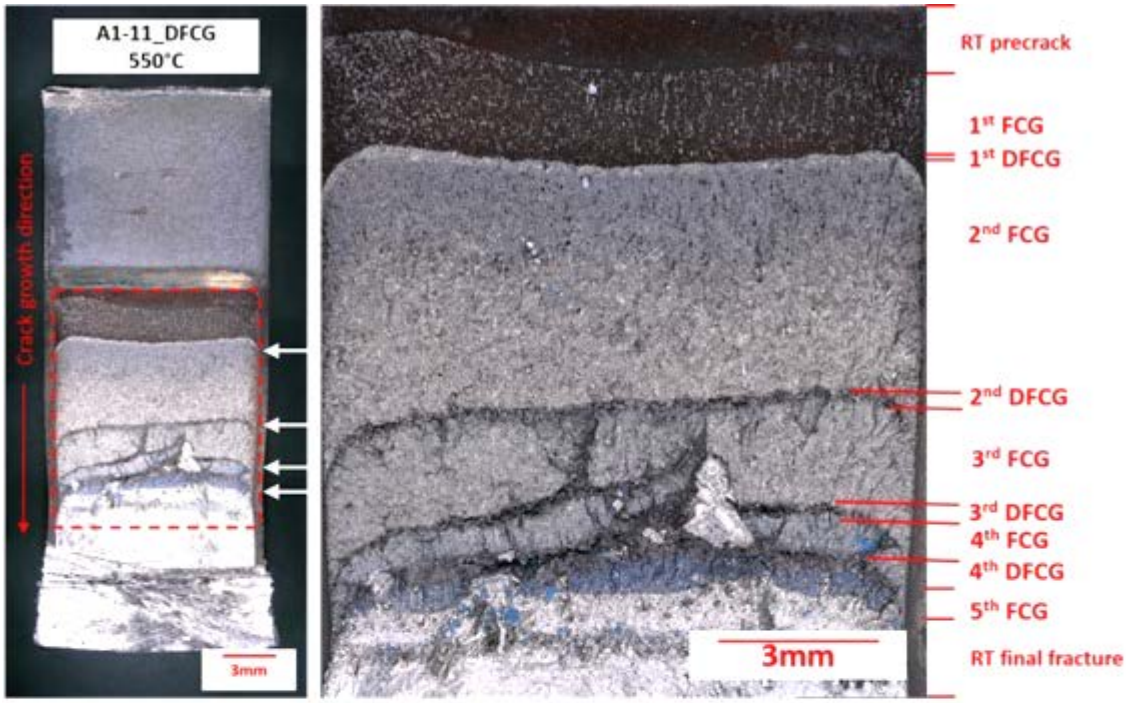

(a)

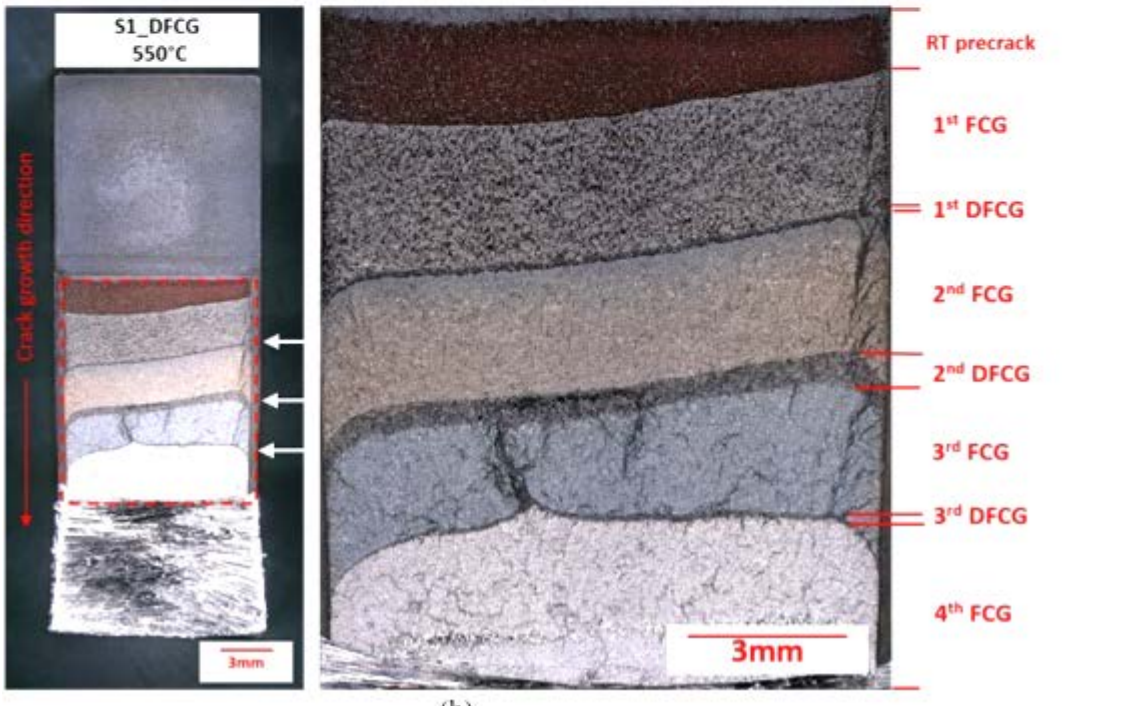

(b)

Figure 4.64 Optical micrographs of the dwell-fatigue crack growth testpieces of the as-received Alloy 709 at (a), (b) 550 (sample ID: A1-11 and S1), (c), (d) 650 (sample ID: A1-1 and A1-8) in air, (e) 650°C in vacuum (sample ID: A1-10) and (f) 750°C in air. The white arrows showing different dwell-fatigue loading segments. Continued overleaf.

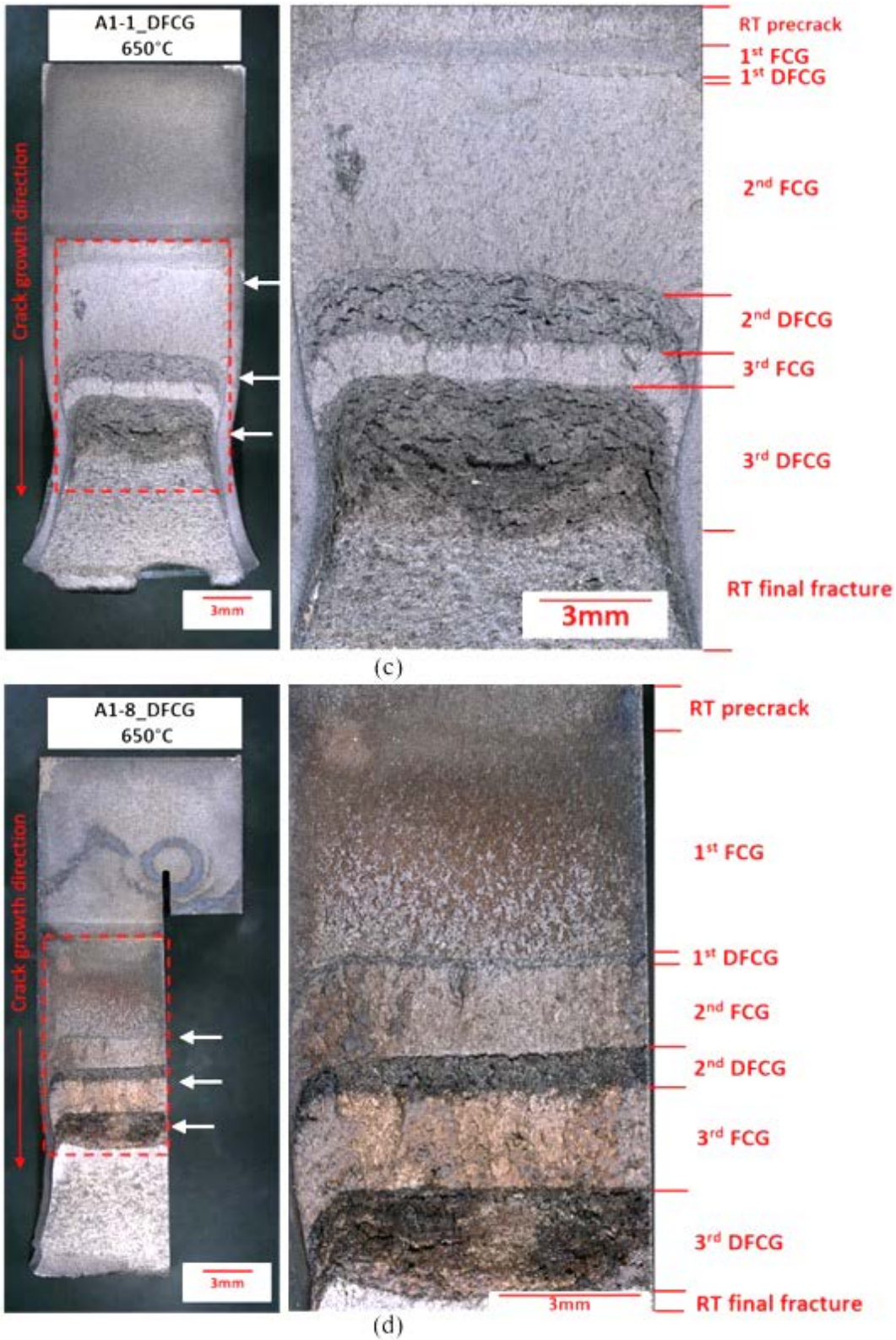

Figure 4.64 Continued. Optical micrographs of the as-received Alloy 709 CT testpiece after dwell-fatigue crack growth testing at (a), (b) 550 (sample ID: A1-11 and S1), (c), (d) 650 (sample ID: A1-1 and A1-8) in air, (e) 650°C in vacuum (sample ID: A1-10) and (f) 750°C in air. The white arrows showing different dwell-fatigue loading segments. Continued overleaf.

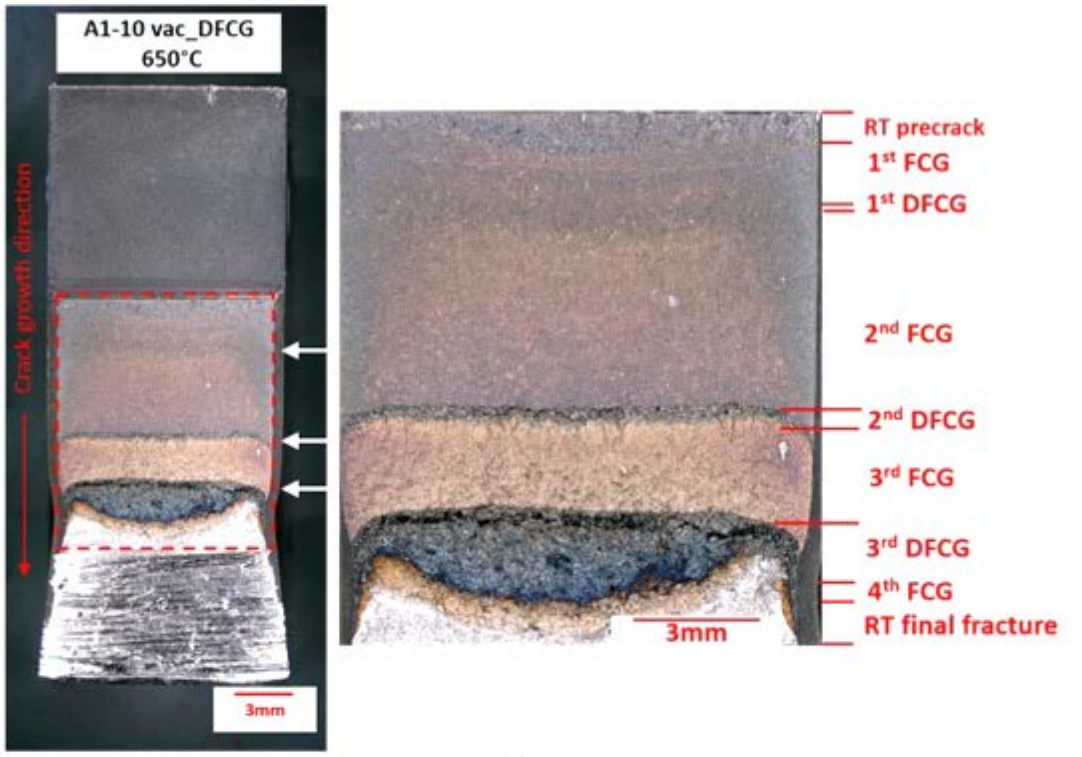

(e)

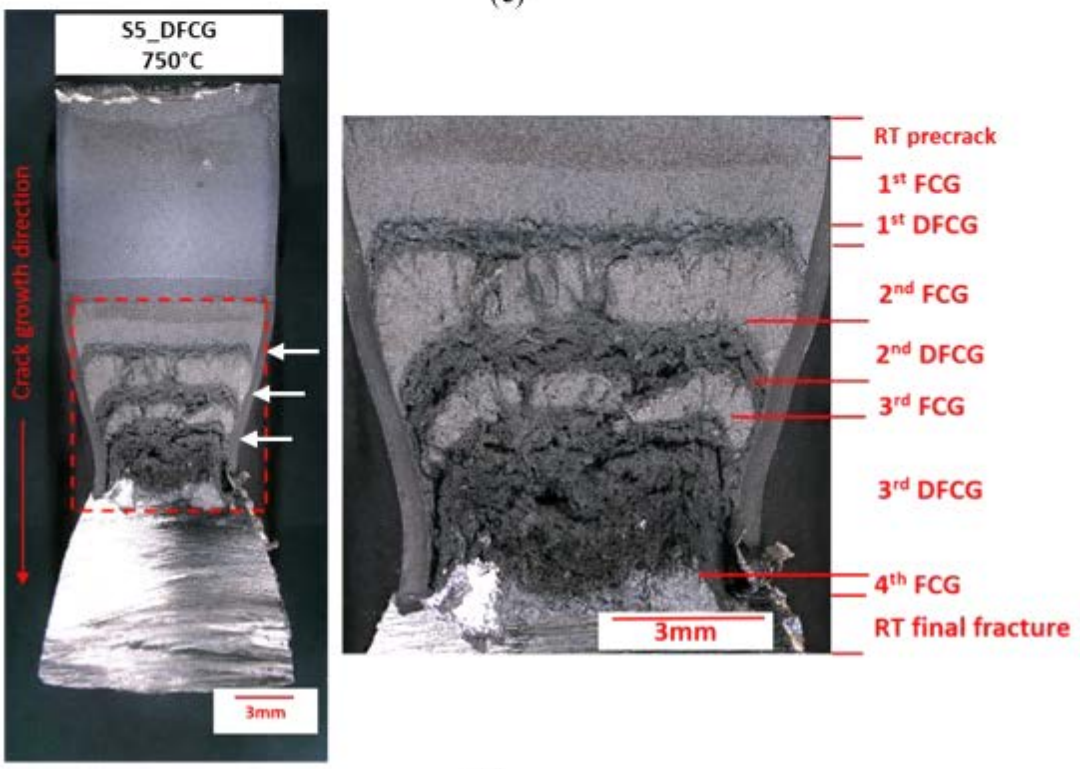

(f)

Figure 4.64 Continued. Optical micrographs of the as-received Alloy 709 CT testpiece after dwell-fatigue crack growth testing at (a), (b) 550 (sample ID: A1-11 and S1), (c), (d) 650 (sample ID: A1-1 and A1-8) in air, (e) 650°C in vacuum (sample ID: A1-10) and (f) 750°C in air. The white arrows showing different dwell-fatigue loading segments.

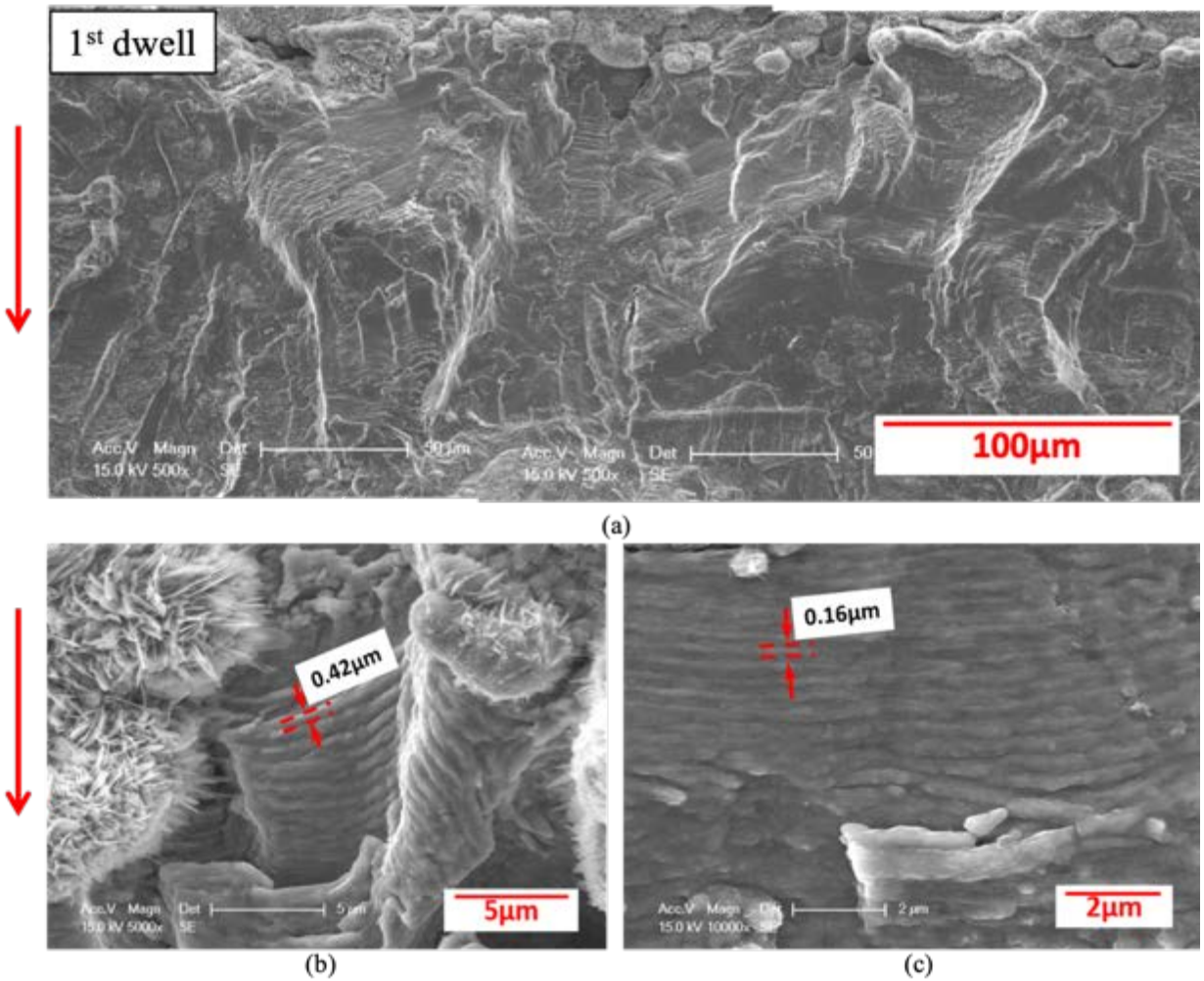

Figure 4.65 Fractographs of the as-received Alloy 709 tested under dwell fatigue loading in air at 550°C, ΔK ~20 MPa√m, (a) close-up of Figure 4.64a, (b) striations on the beginning of 1st dwell and (c) striations on the end of 1st dwell. Note: red arrows indicate the direction of crack growth, red dotted lines showing the crack front of dwell-fatigue crack growth behaviour.

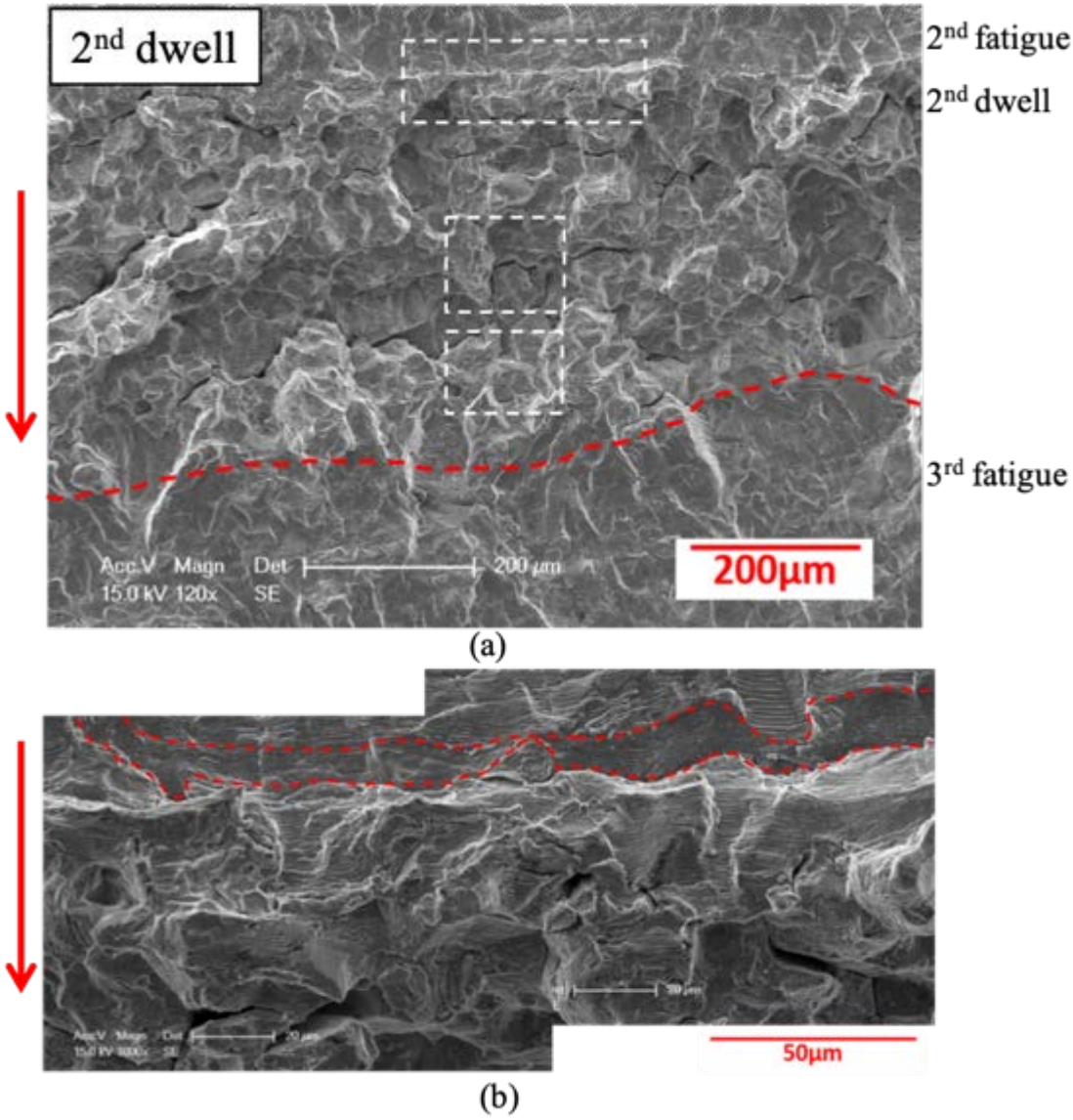

Figure 4.66 Fractographs of the as-received Alloy 709 tested under dwell fatigue loading in air at 550°C, showing (a) fractographic feature containing three bands, ΔK ~35 MPa$\sqrt{m}$, (b) predominantly transgranular failure at the beginning, (c) middle and (d) end of the 2nd dwell. Note: the area between red dotted lines in Figure 4.66b shows the stretch zone. Continued overleaf.

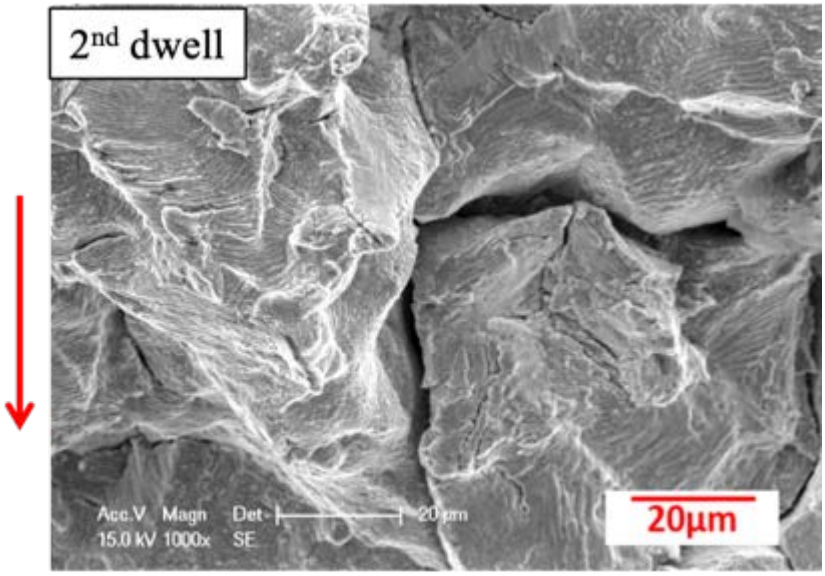

(c)

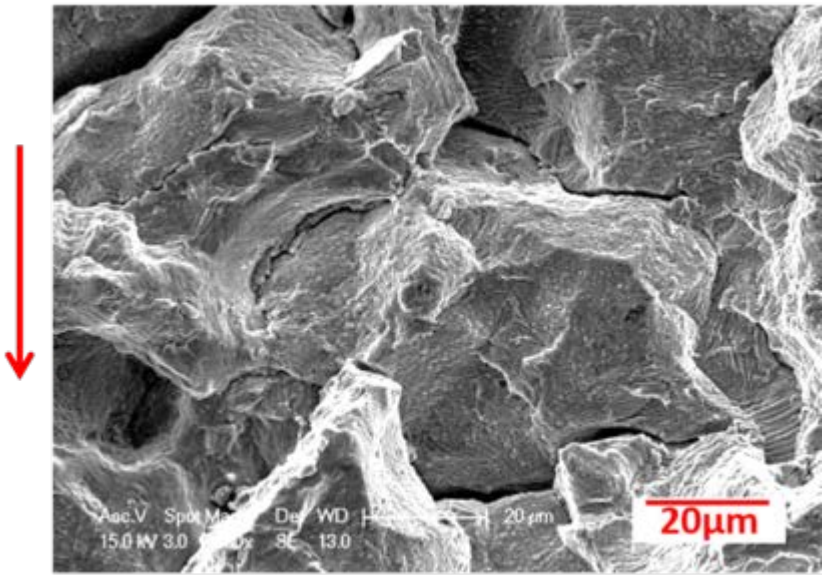

(d)

Figure 4.66 Continued. Fractographs of the as-received Alloy 709 tested under dwell fatigue loading in air at 550°C, showing (a) fractographic feature containing three bands, ΔK ~35 MPa$\sqrt{m}$, (b) predominantly transgranular failure at the beginning, (c) middle and (d) end of the 2nd dwell. Note: the area between red dotted lines in Figure 4.66b shows the stretch zone.

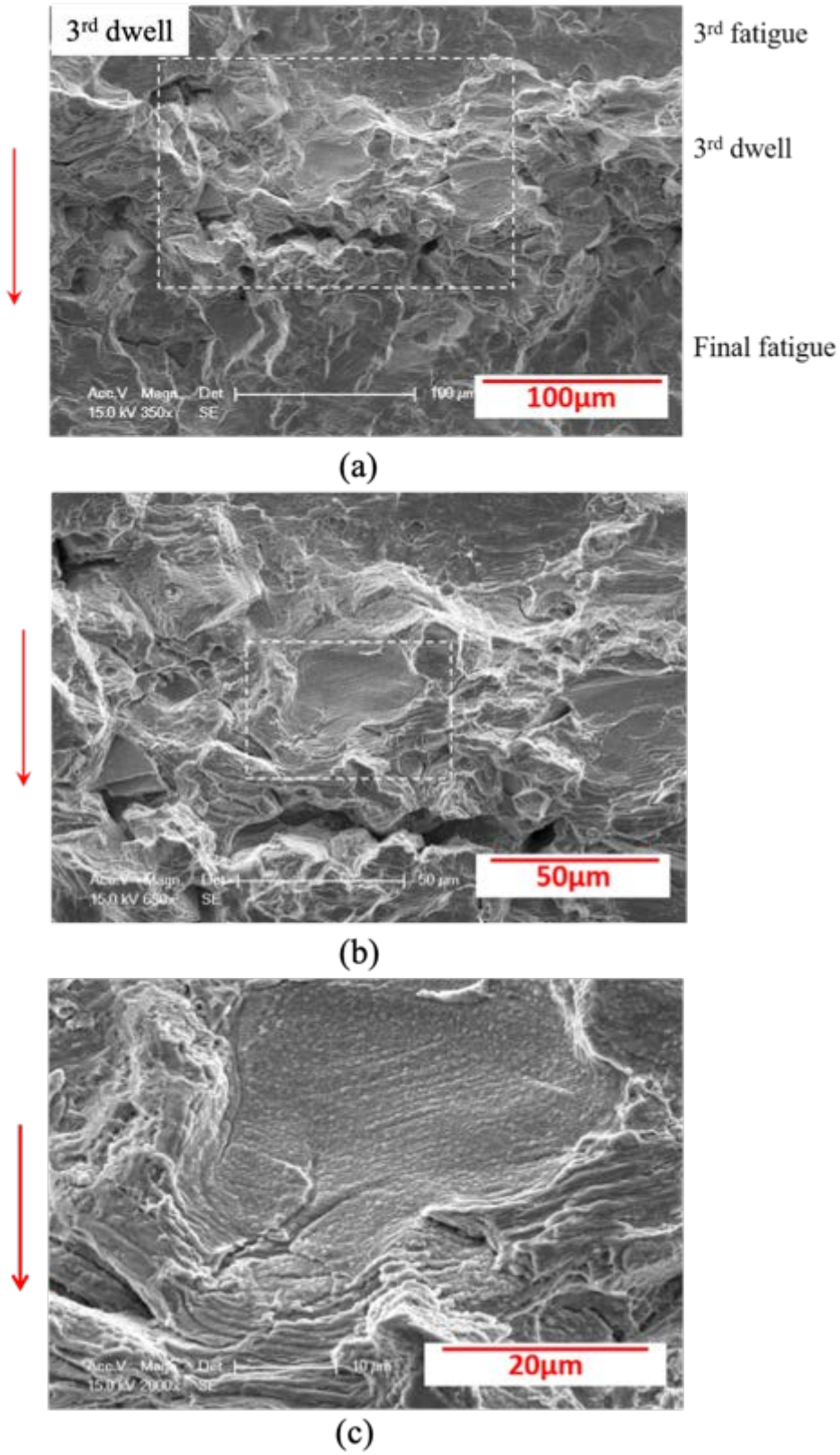

Figure 4.67 Fractographs of the as-received Alloy 709 tested under dwell fatigue loading in air at 550°C, showing (a) fractographic feature containing three bands, $\Delta K > 50$ MPa$\sqrt{m}$, (b) predominate intergranular failure in the 3rd dwell, (c) close-up of (b).

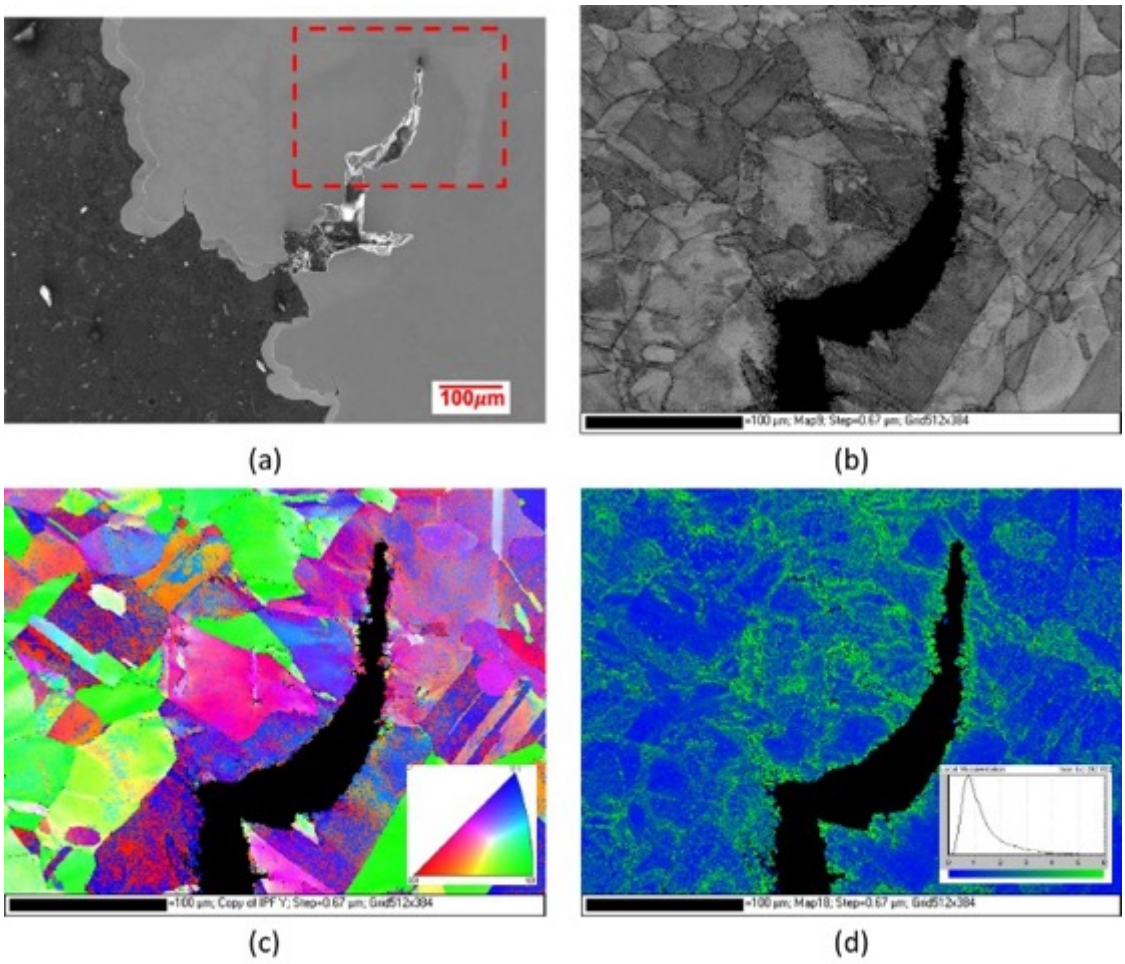

Figure 4.68 (a) BSE image and (b) EBSD band contrast map (c) crystal orientation map and (d) misorientation map taken from the second dwell region (ΔK value of ~35 MPa√m) of Alloy 709 tested at 550°C showing less obvious matrix deformation.

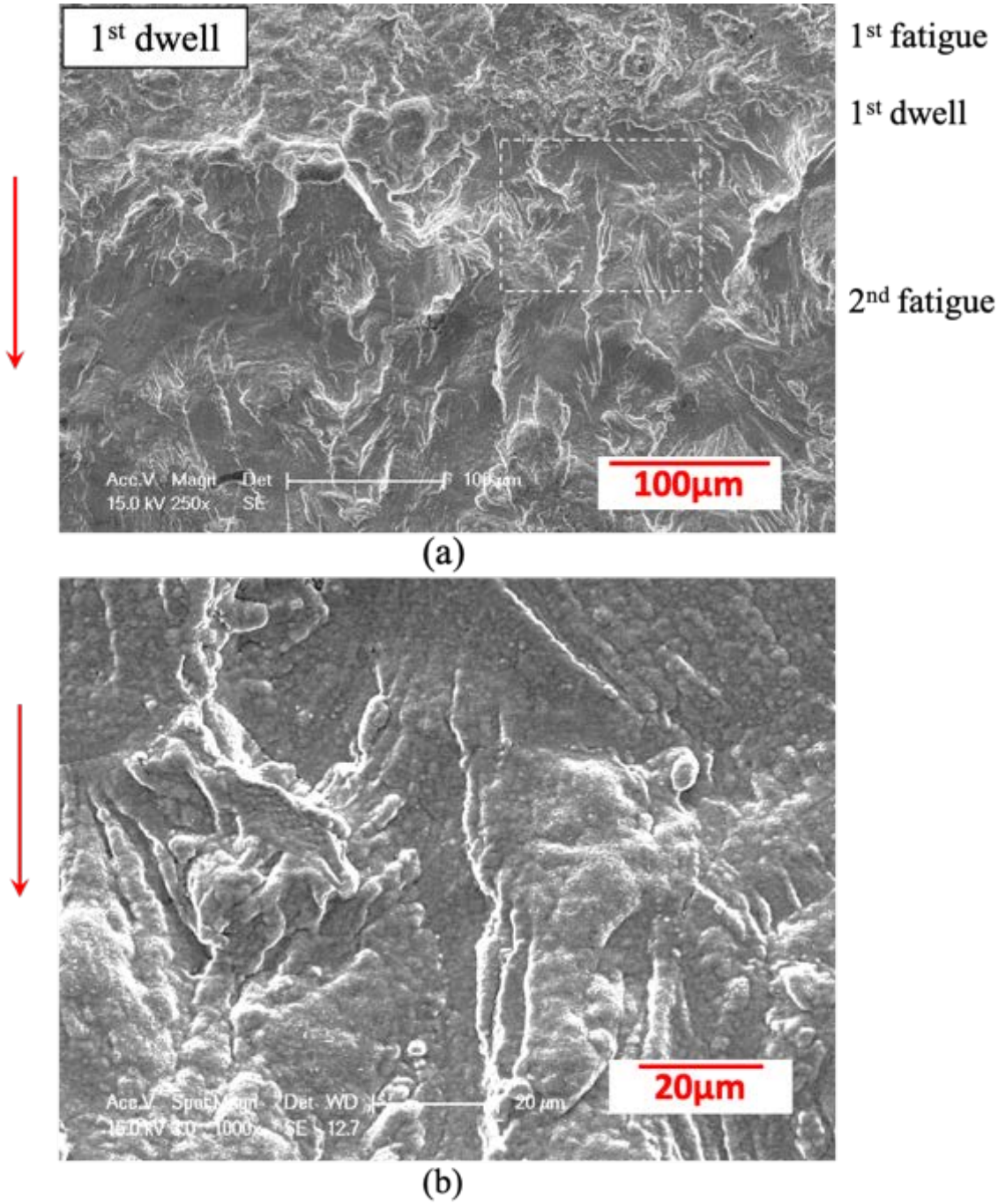

Figure 4.69 Fractographs of the as-received Alloy 709 tested under dwell fatigue loading in air at 650°C, showing (a) fractographic feature containing three bands, ΔK ~20 MPa√m, (b) predominate transgranular failure in the 1st dwell.

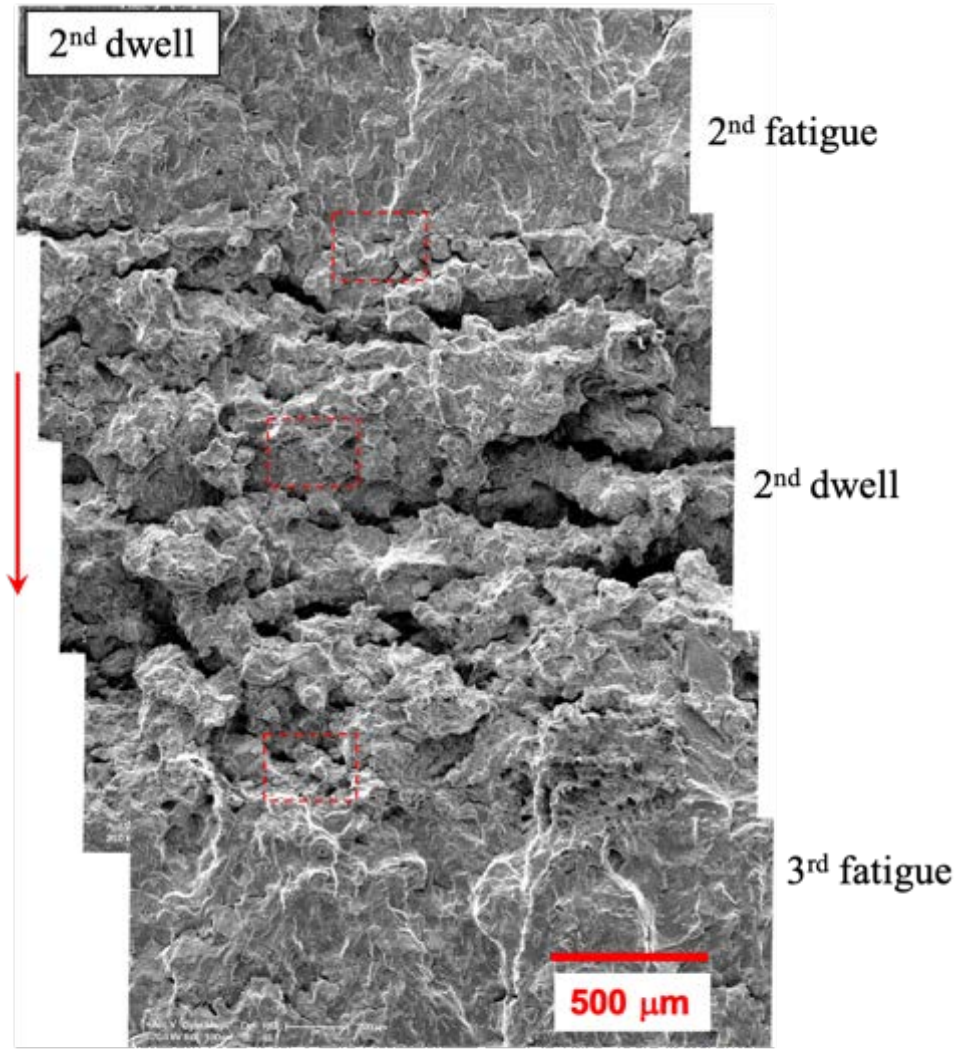

(a)

Figure 4.70 Fractographs of the as-received Alloy 709 tested under dwell fatigue loading in air at 650°C, showing (a) fractographic feature containing three bands, $\Delta K > 35$ MPa$\sqrt{m}$, (b), (d), (f) intergranular failure at the beginning, middle and end of the 2nd dwell in Figure 4.70a, (c), (e), (g) close-up of (b), (d), (f). Continued overleaf.

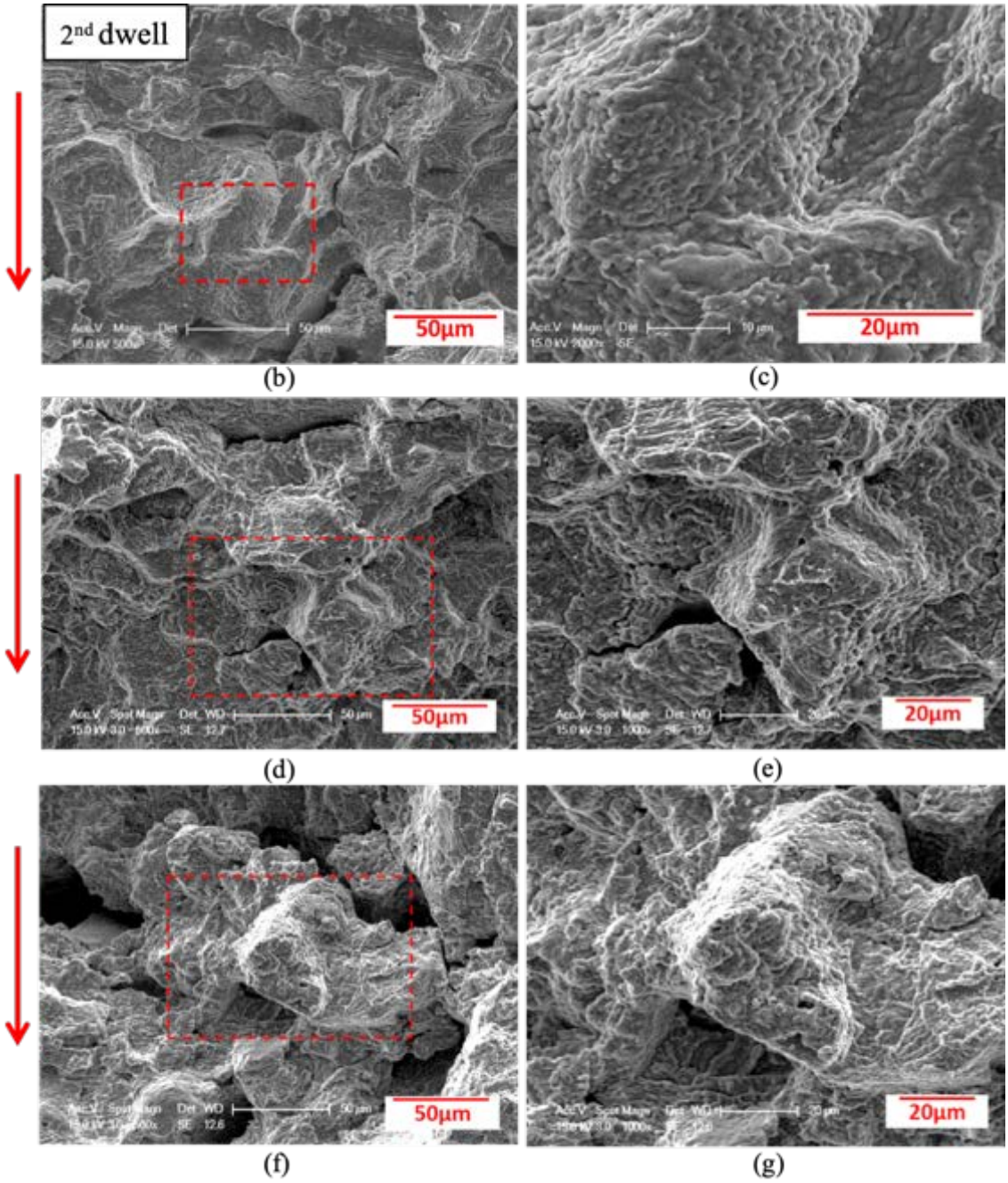

Figure 4.70 Continued. Fractographs of the as-received Alloy 709 tested under dwell fatigue loading in air at 650°C, showing (a) fractographic feature containing three bands, $\Delta K > 35$ MPa$\sqrt{m}$, (a), (c), (e) intergranular failure at the beginning, middle and end of the 2nd dwell in Figure 4.70a, (b), (d), (f) close-up of (a), (c), (e).

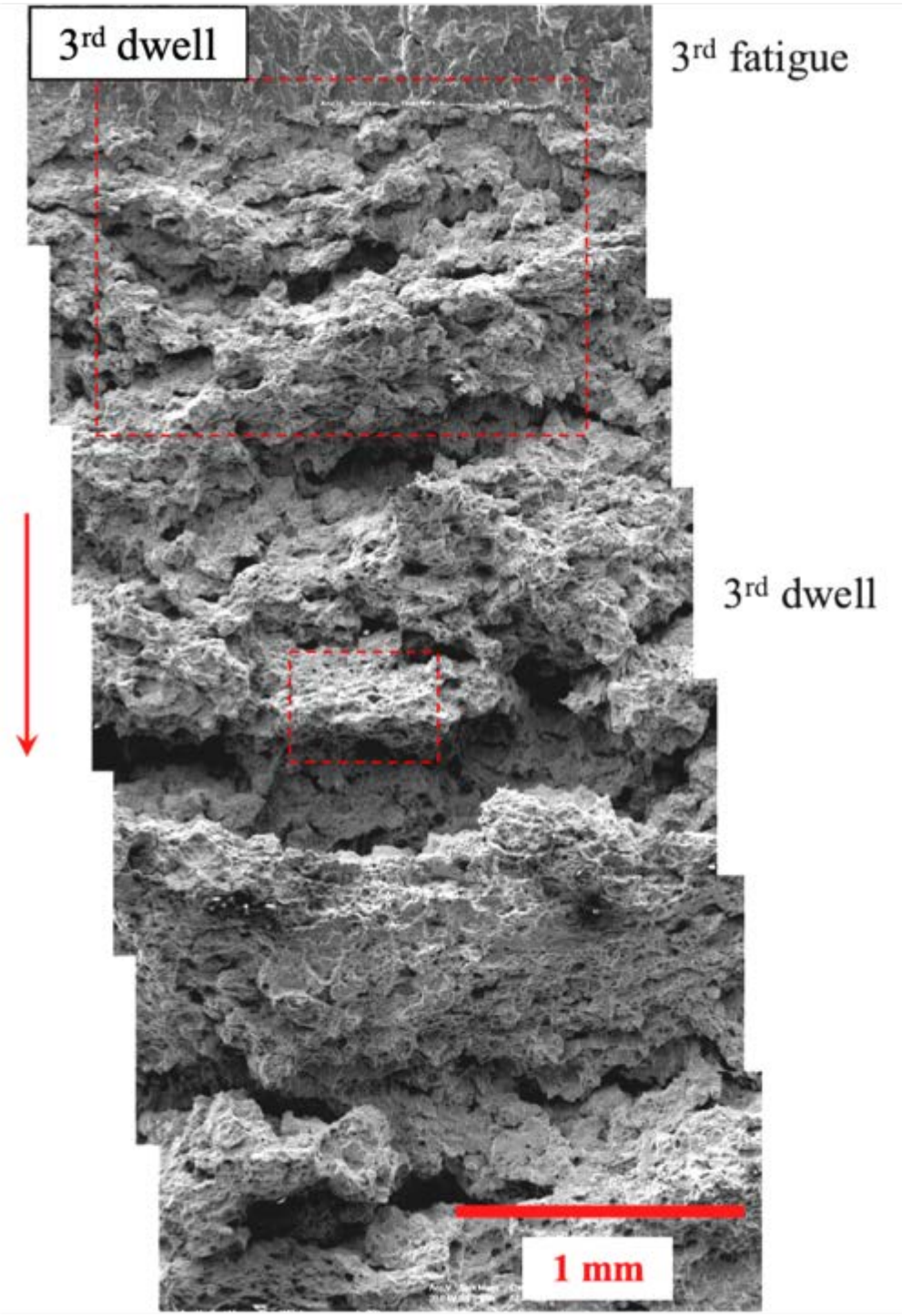

(a)

Figure 4.71 Fractographs of the as-received Alloy 709 tested under dwell fatigue loading in air at 650°C, showing (a) fractographic feature containing two bands, $\Delta K > 50$ MPa$\sqrt{m}$, (b), (d) ductile failure mode at the beginning and the middle of the 3rd dwell in Figure 4.71a, (c), (e) close-up of (b), (d). Continued overleaf.

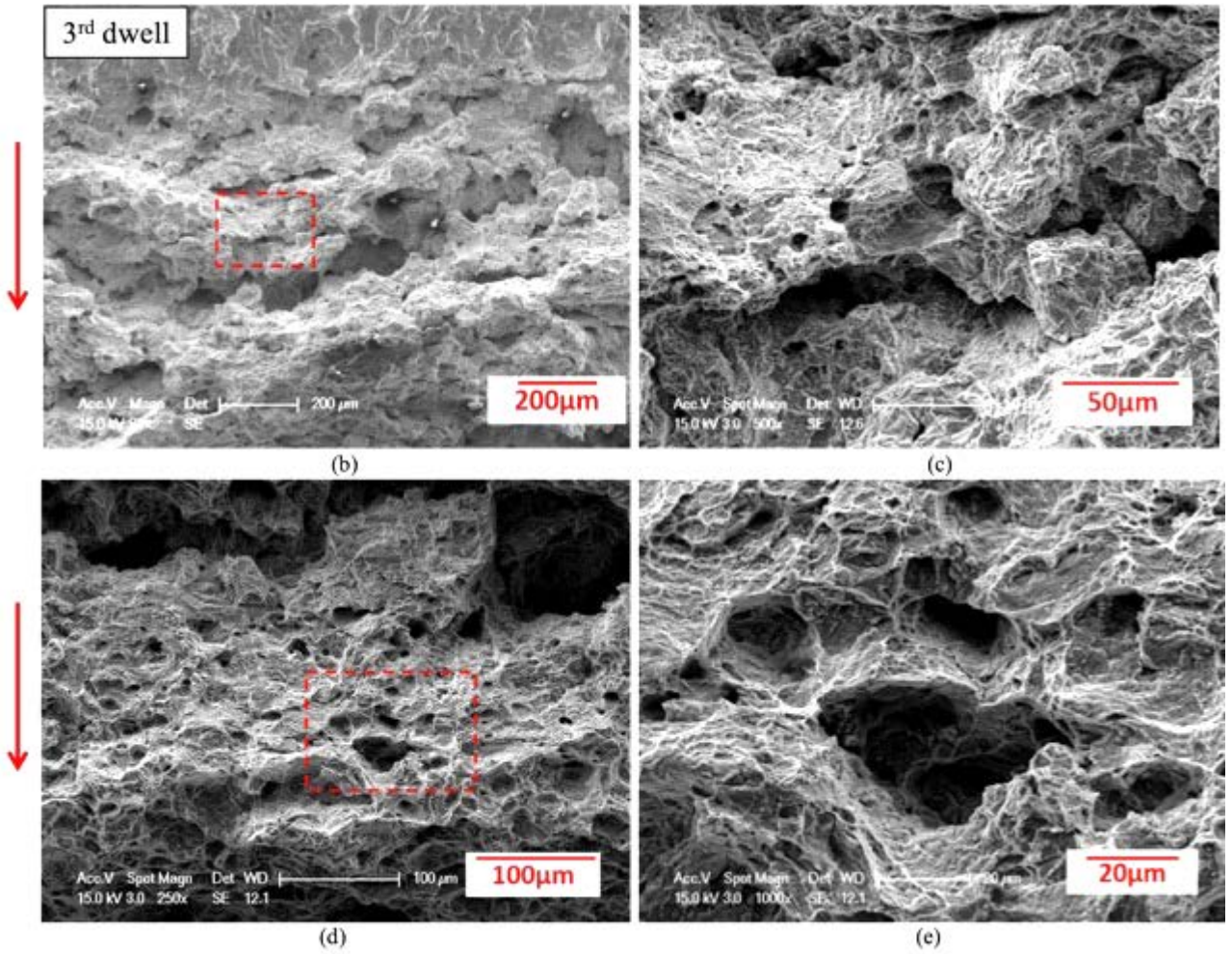

Figure 4.71 Continued. Fractographs of the as-received Alloy 709 tested under dwell fatigue loading in air at 650°C, showing (a) fractographic feature containing two bands, $\Delta K > 50$ MPa$\sqrt{m}$, (b), (d) ductile failure mode at the beginning and the middle of the 3rd dwell in Figure 4.71a, (c), (e) close-up of (b), (d).

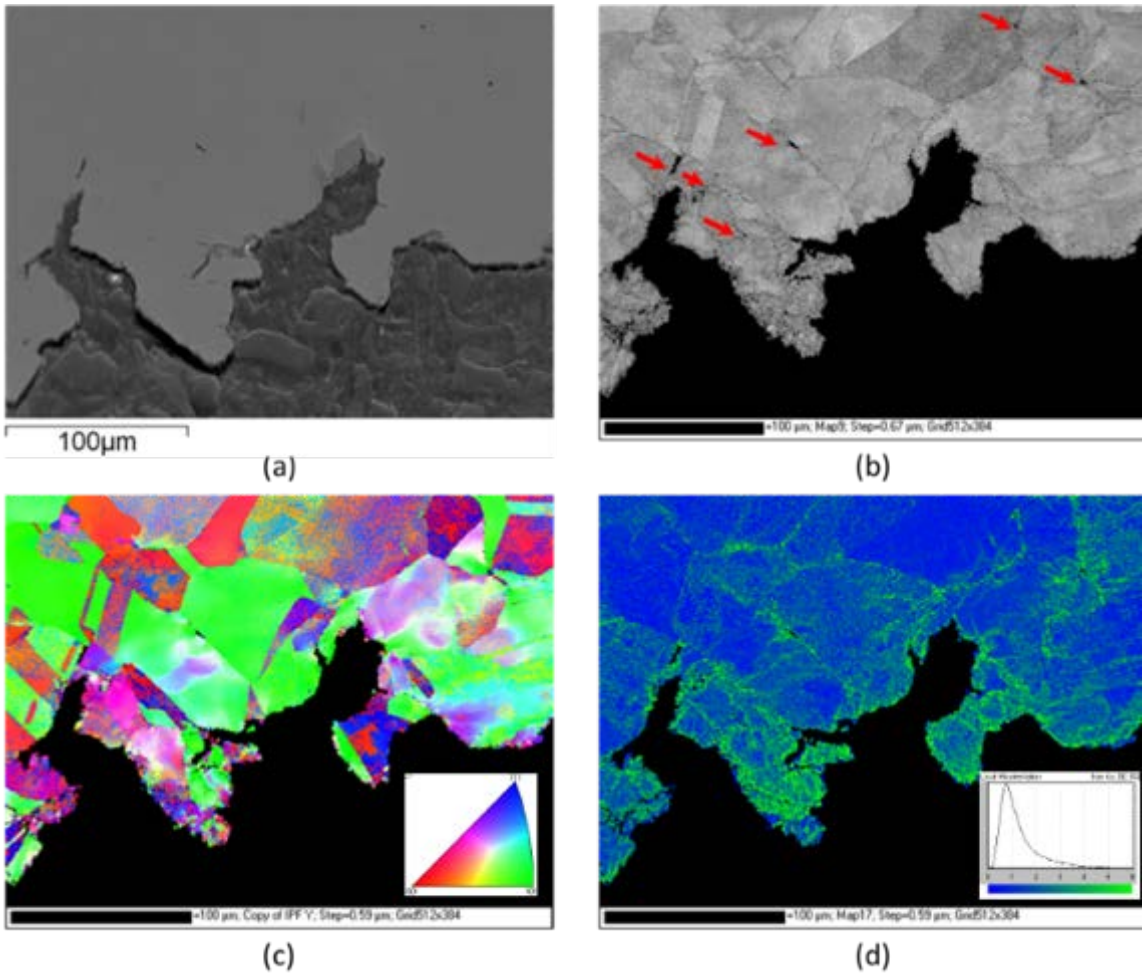

Figure 4.72 (a) BSE image and (b) EBSD band contrast map (c) crystal orientation map and (d) misorientation map for the second dwell-fatigue (ΔK ~35 MPa√m) of Alloy 709 tested at 650°C showing an intergranular crack and limited subgrain formation.

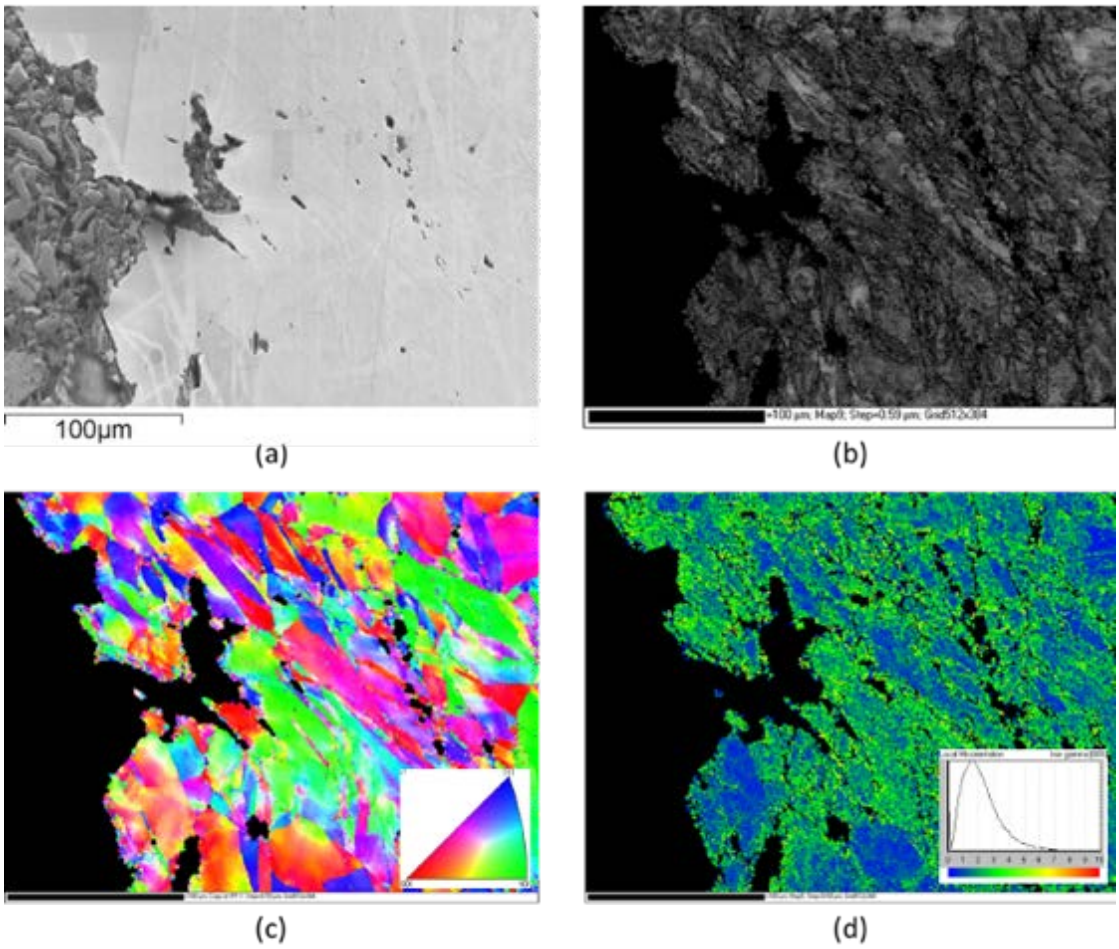

Figure 4.73 (a) BSE image and (b) EBSD band contrast map (c) crystal orientation map and (d) misorientation map for the third dwell-fatigue (ΔK ~50 MPa√m) of Alloy 709 tested at 650°C (A1-1) showing excessive matrix deformation and subgrain formation.

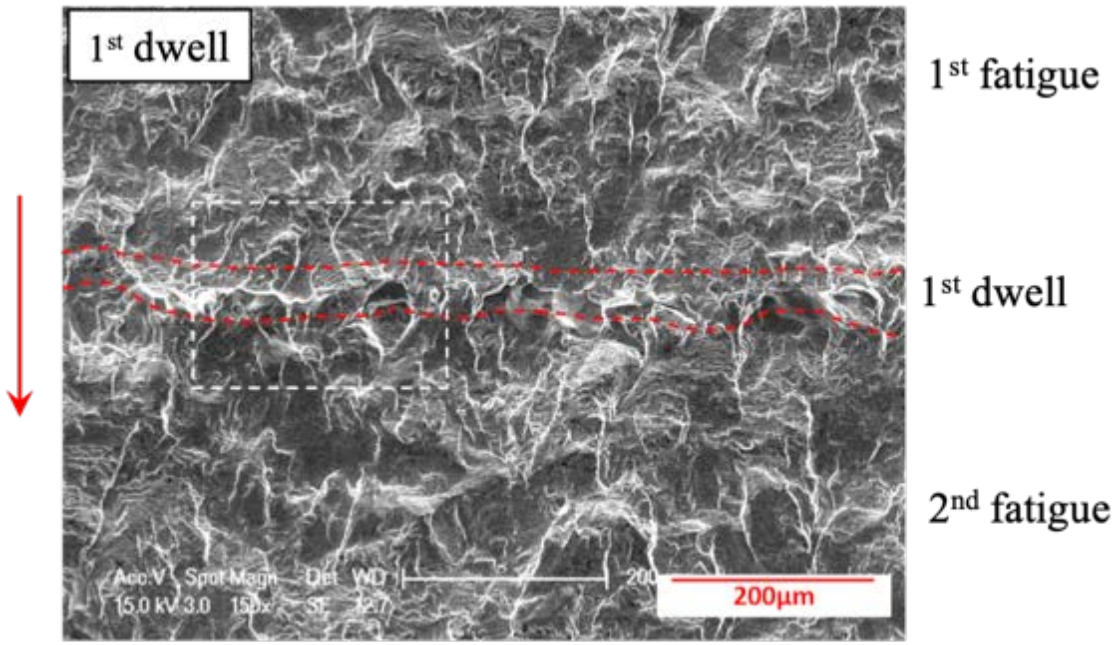

(a)

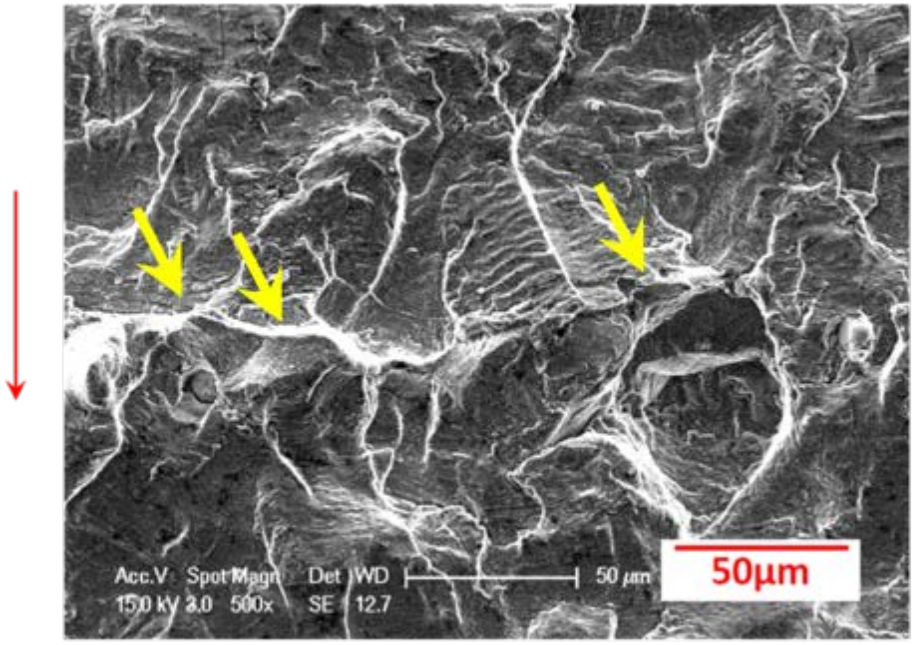

(b)

Figure 4.74 Fractographs of the as-received Alloy 709 tested under dwell fatigue loading in vacuum at 650°C, showing (a) fractographic feature containing three bands, ΔK ~20 MPa√m, (b) transgranular failure in the 1st dwell. Note: yellow arrows showing the isolated intergranular facets, red dotted lines showing the crack front of dwell-fatigue crack growth behaviour.

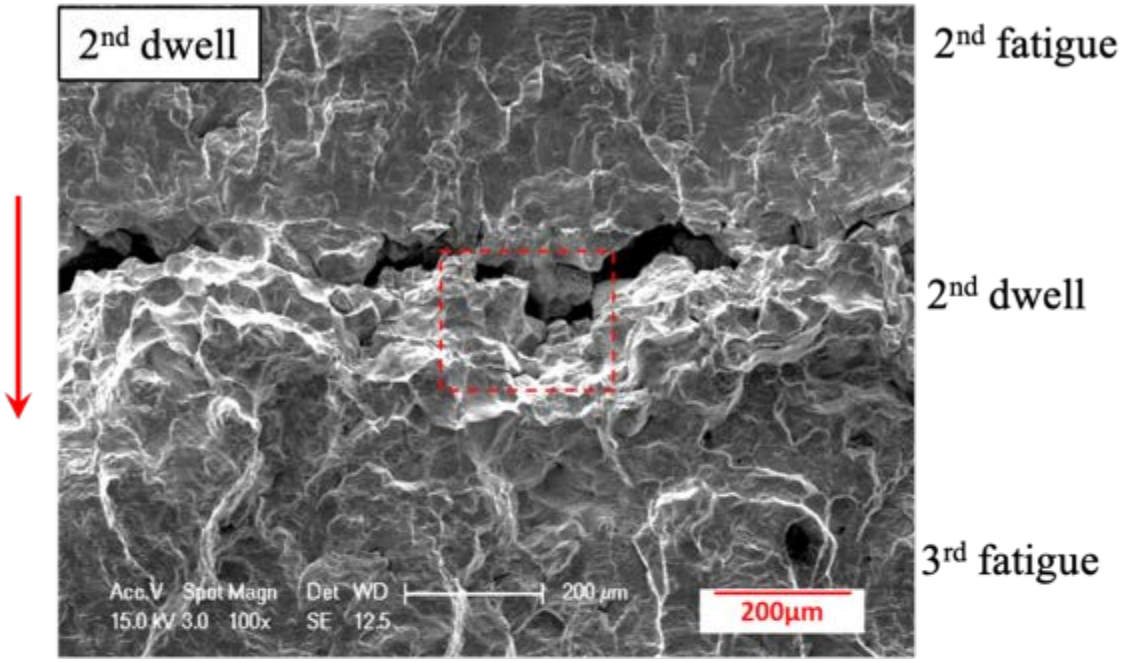

(a)

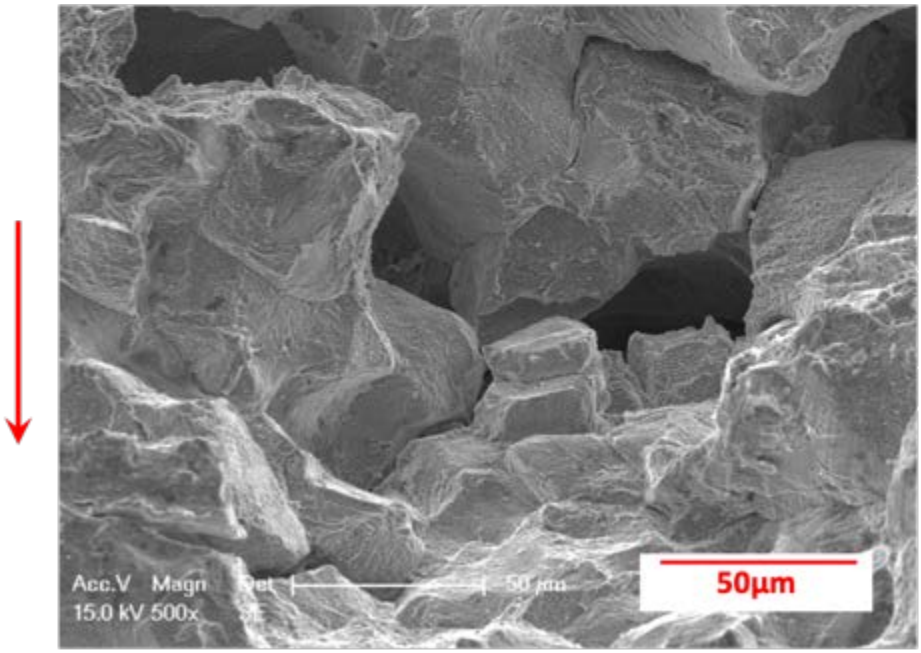

(b)

Figure 4.75 Fractographs of the as-received Alloy 709 tested under dwell fatigue loading in vacuum at 650°C, showing (a) fractographic feature containing three bands, $\Delta K > 30$ MPa$\sqrt{m}$, (b) intergranular failure in the 2nd dwell.

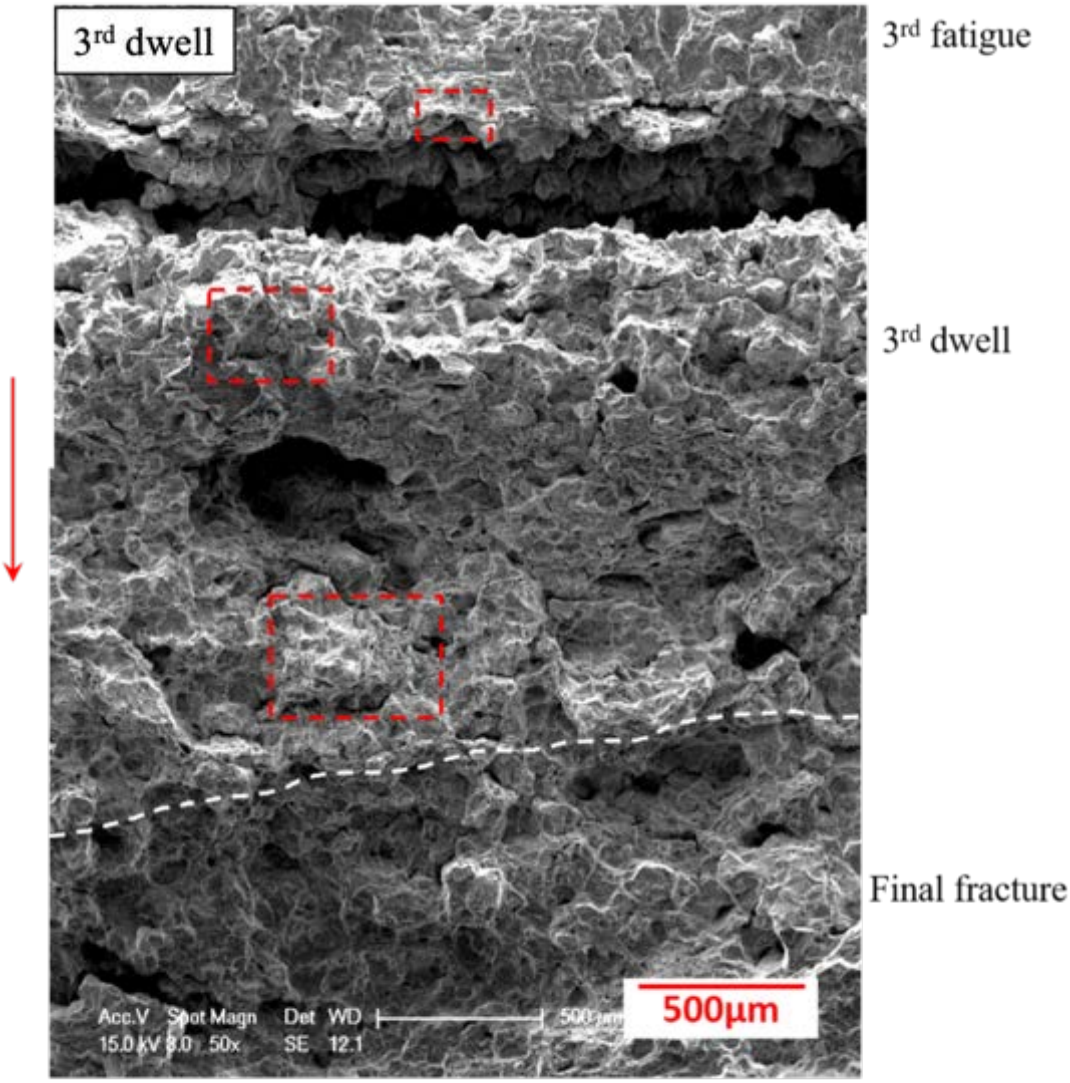

(a)

Figure 4.76 Fractographs of the as-received Alloy 709 tested under dwell fatigue loading in vacuum at 650°C, showing (a) fractographic feature containing three bands, $\Delta K > 50$ MPa$\sqrt{m}$, (b), (c) and (d) the corresponding areas at the beginning and the middle of the 3rd dwell in Figure 4.76a. Note: red arrows indicate the direction of crack growth, white dotted lines showing the crack front of dwell-fatigue crack growth behaviour. Continued overleaf.

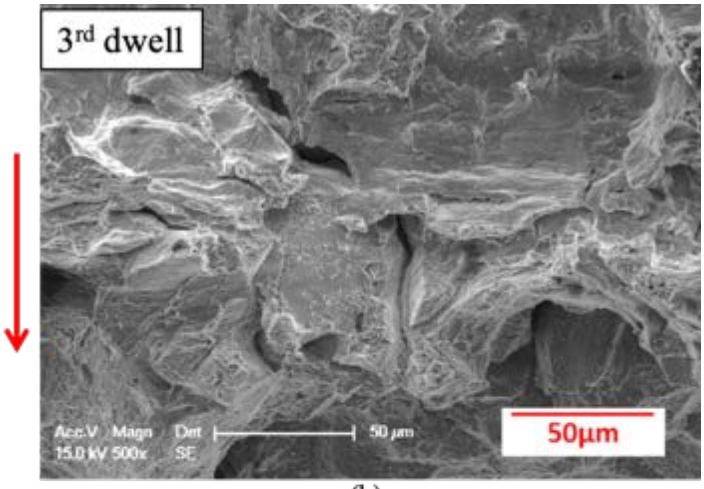

(b)

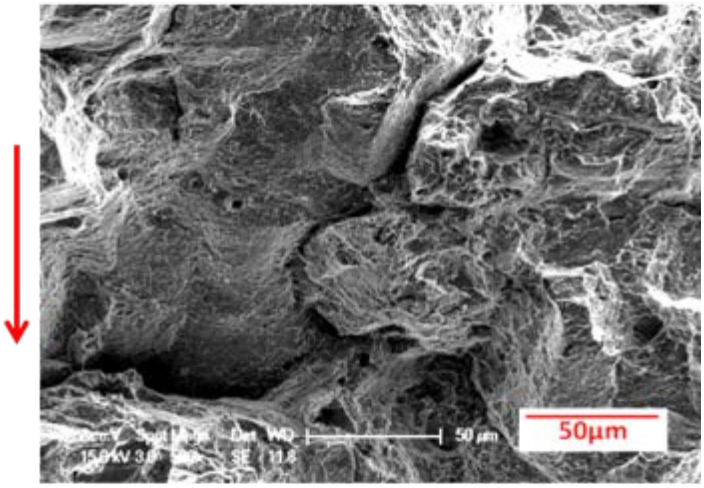

(c)

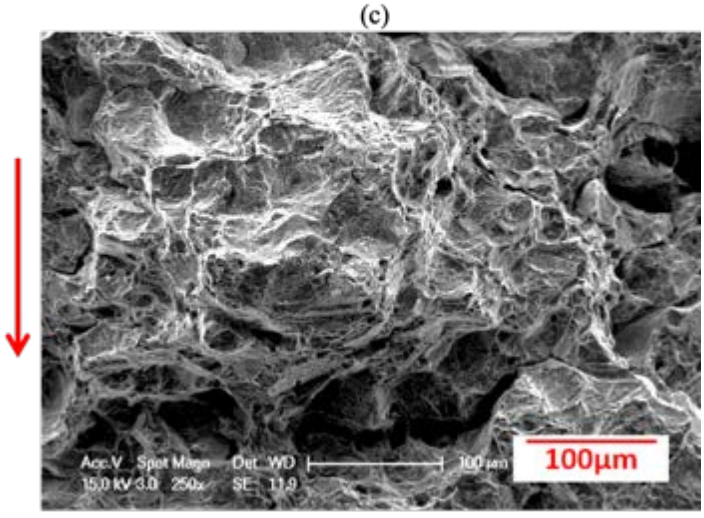

(d)

Figure 4.76 Continued. Fractographs of the as-received Alloy 709 tested under dwell fatigue loading in vacuum at 650°C, showing (a) fractographic feature containing three bands, $\Delta K > 50$ MPa$\sqrt{m}$, (b), (c) and (d) the corresponding areas at the beginning and the middle of the 3rd dwell in Figure 4.76a. Note: red arrows indicate the direction of crack growth, white dotted lines showing the crack front of dwell-fatigue crack growth behaviour.

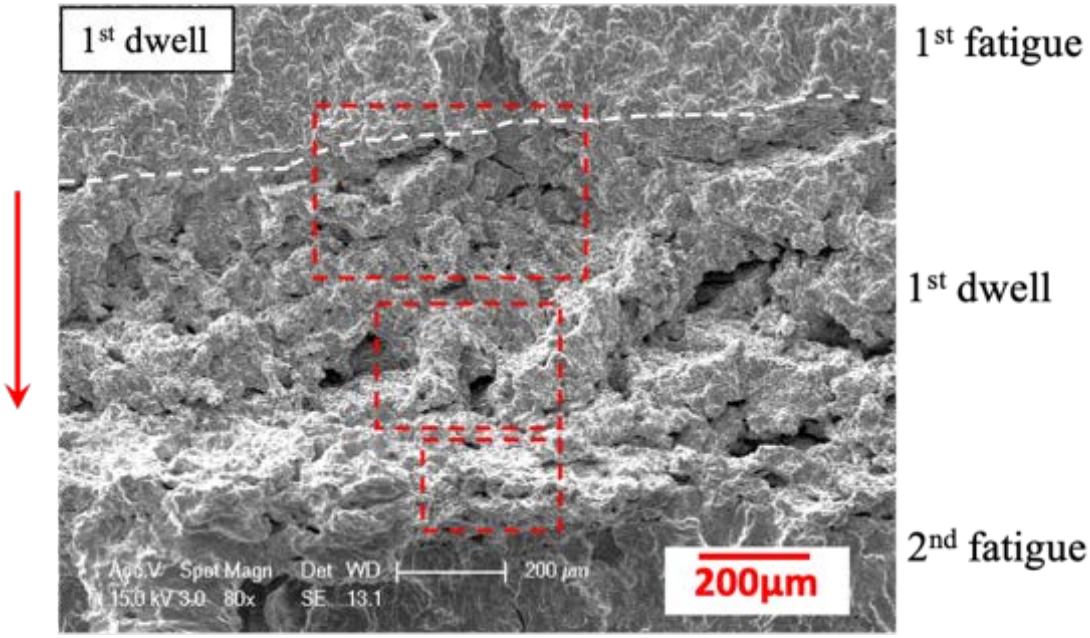

(a)

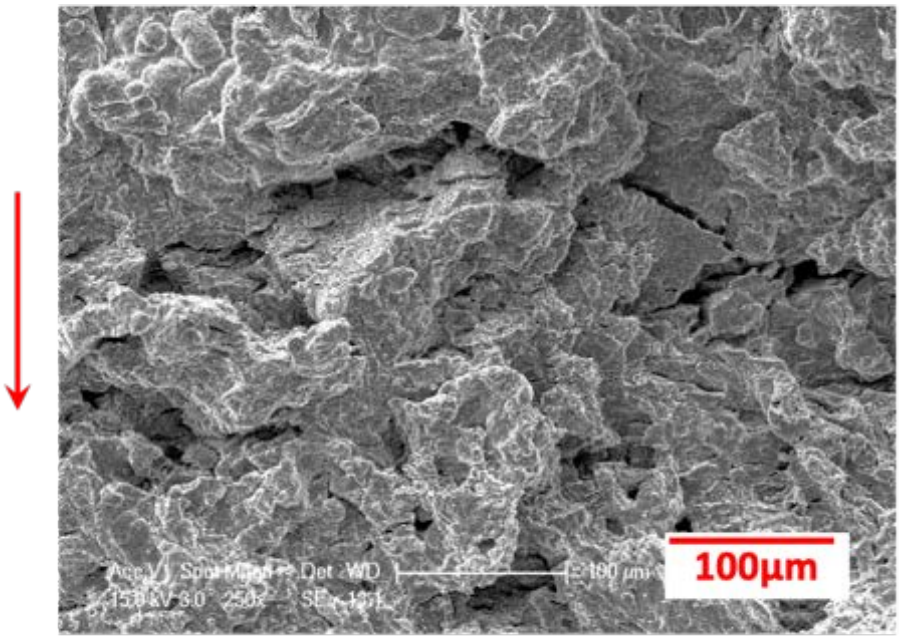

(b)

Figure 4.77 Fractographs of the as-received Alloy 709 tested under dwell fatigue loading in air at 750°C, showing (a) fractographic feature containing three bands, $\Delta K > 20$ MPa$\sqrt{m}$, (b) predominantly ductile failure at the beginning of the 1st dwell, (c), (d) ductile fracture at the middle and end of the 1st dwell in Figure 4.77a. Note: red arrows indicate the direction of crack growth, white dotted lines showing the crack front of dwell-fatigue crack growth behaviour. Continued overleaf.

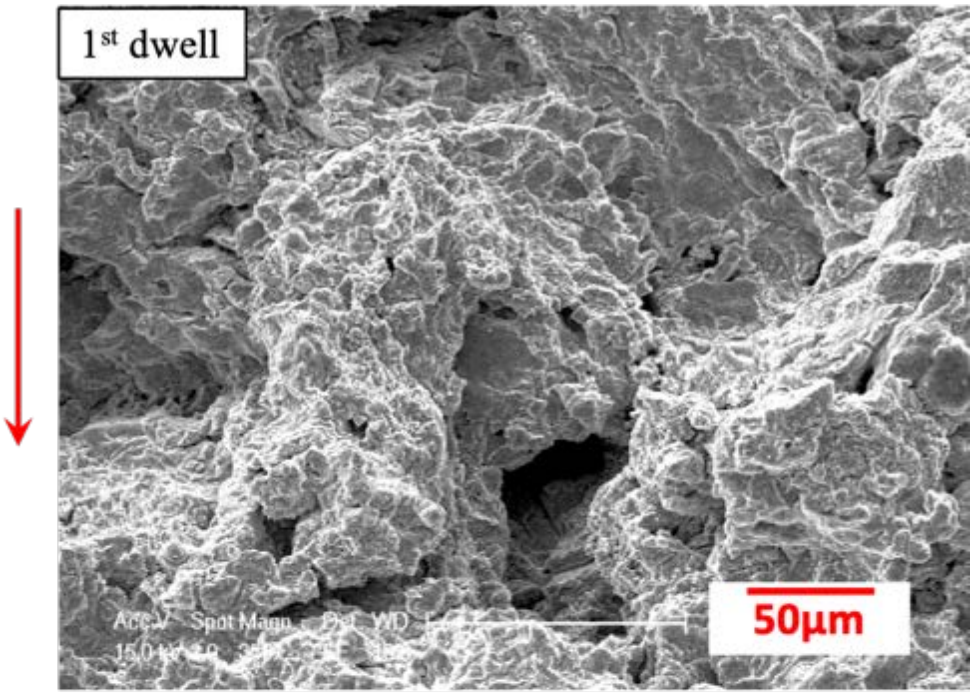

(c)

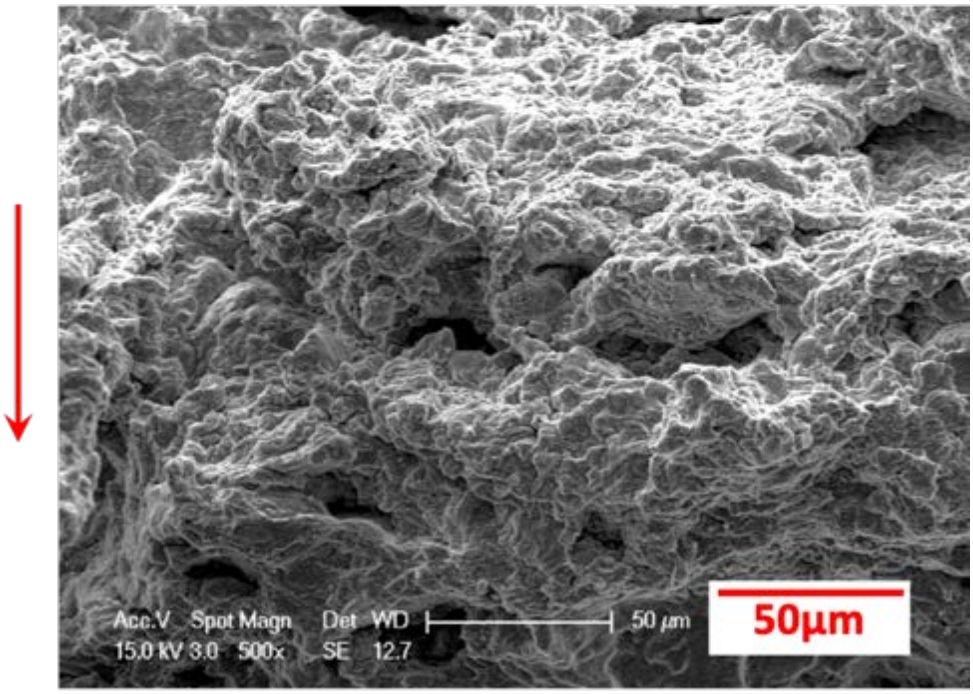

(d)

Figure 4.77 Continued. Fractographs of the as-received Alloy 709 tested under dwell fatigue loading in air at 750°C, showing (a) fractographic feature containing three bands, $\Delta K > 20$ MPa$\sqrt{m}$, (b) predominantly ductile failure at the beginning of the 1st dwell, (c), (d) ductile fracture at the middle and end of the 1st dwell in Figure 4.77a. Note: red arrows indicate the direction of crack growth, white dotted lines showing the crack front of dwell-fatigue crack growth behaviour.

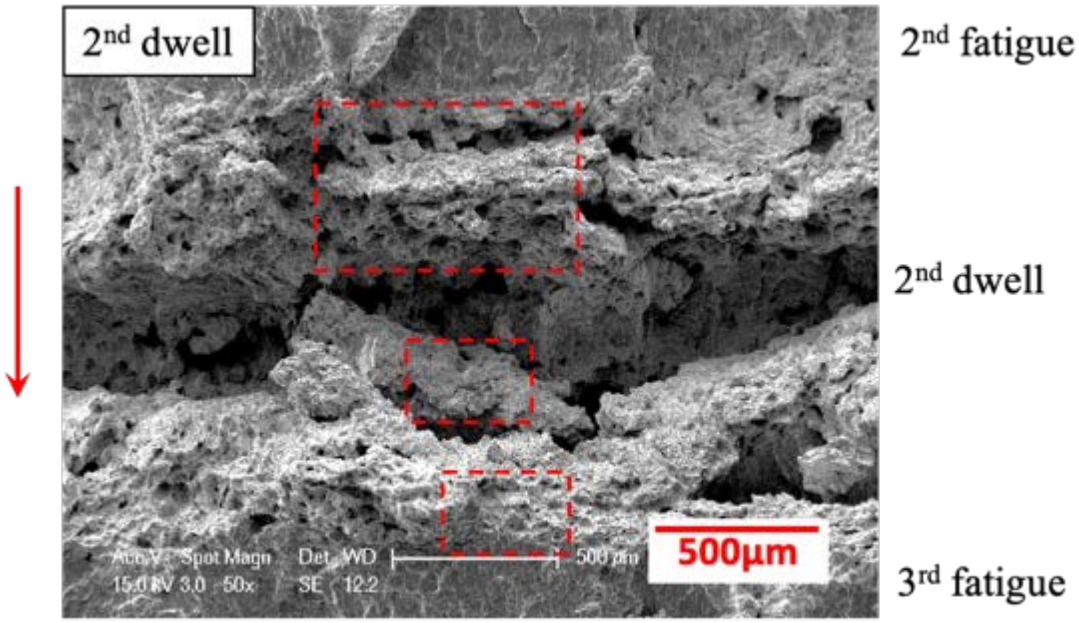

(a)

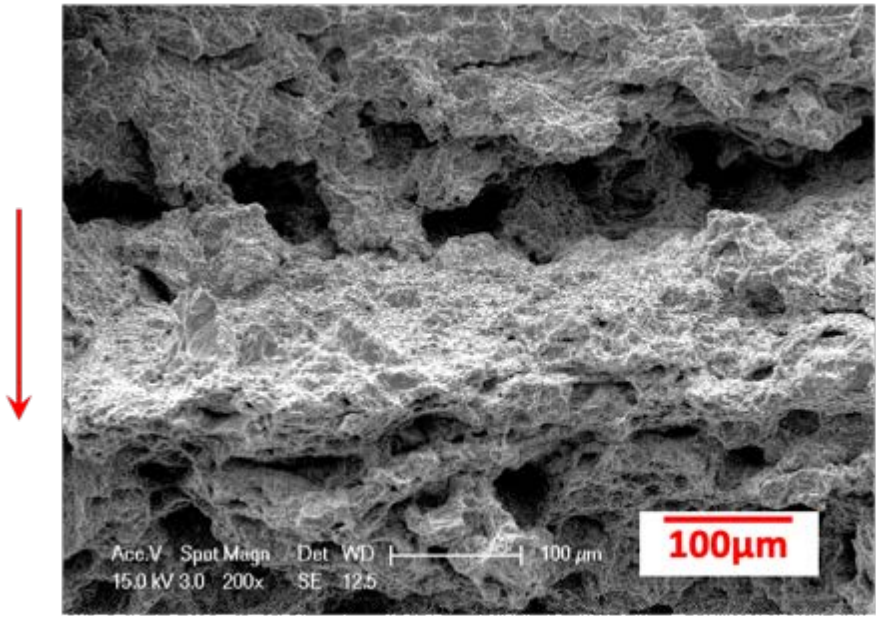

(b)

Figure 4.78 Fractographs of the as-received Alloy 709 tested under dwell fatigue loading in air at 750°C, showing (a) fractographic feature containing three bands, $\Delta K > 35$ MPa$\sqrt{m}$, (b) ductile failure mode at the beginning, of the 2nd dwell, (c), (d) ductile failure mode at the middle and end of the 2nd dwell in Figure 4.78a. Continued overleaf.

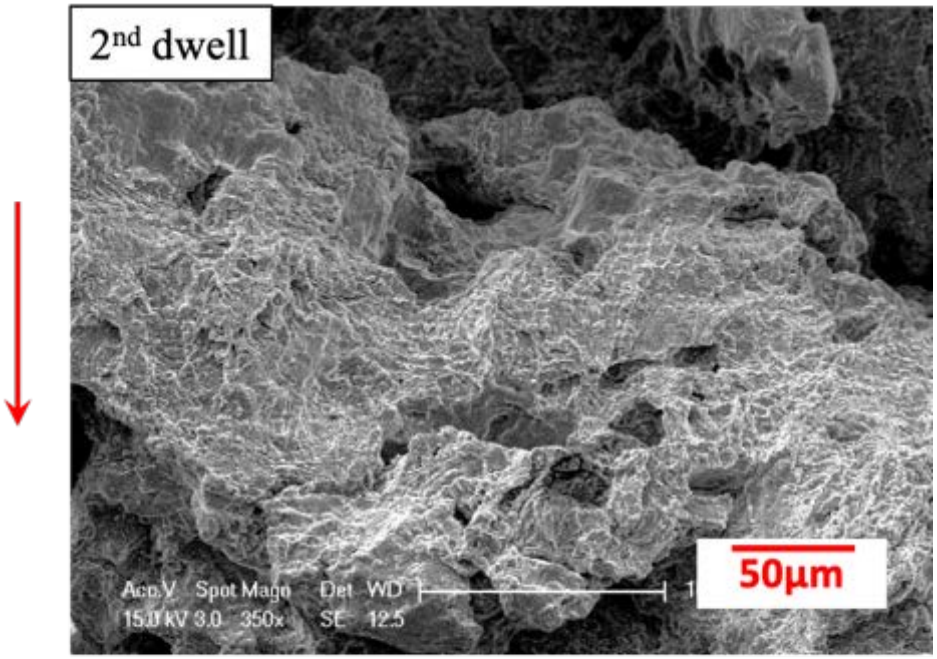

(c)

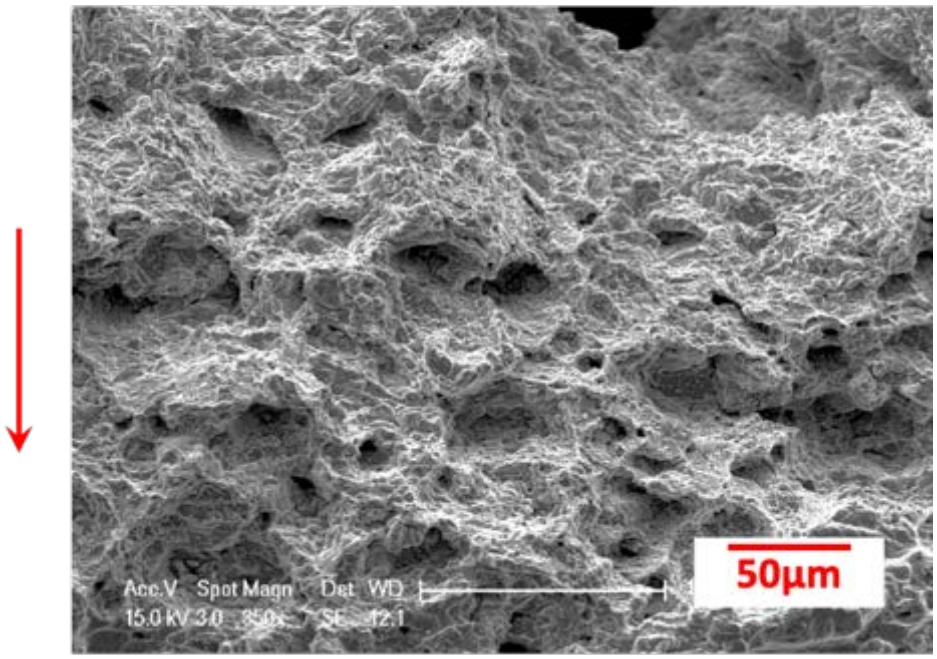

(d)

Figure 4.78 Continued. Fractographs of the as-received Alloy 709 tested under dwell fatigue loading in air at 750°C, showing (a) fractographic feature containing three bands, $\Delta K > 35$ MPa$\sqrt{m}$, (b) ductile failure mode at the beginning, of the 2nd dwell, (c), (d) ductile failure mode at the middle and end of the 2nd dwell in Figure 4.78a.

.

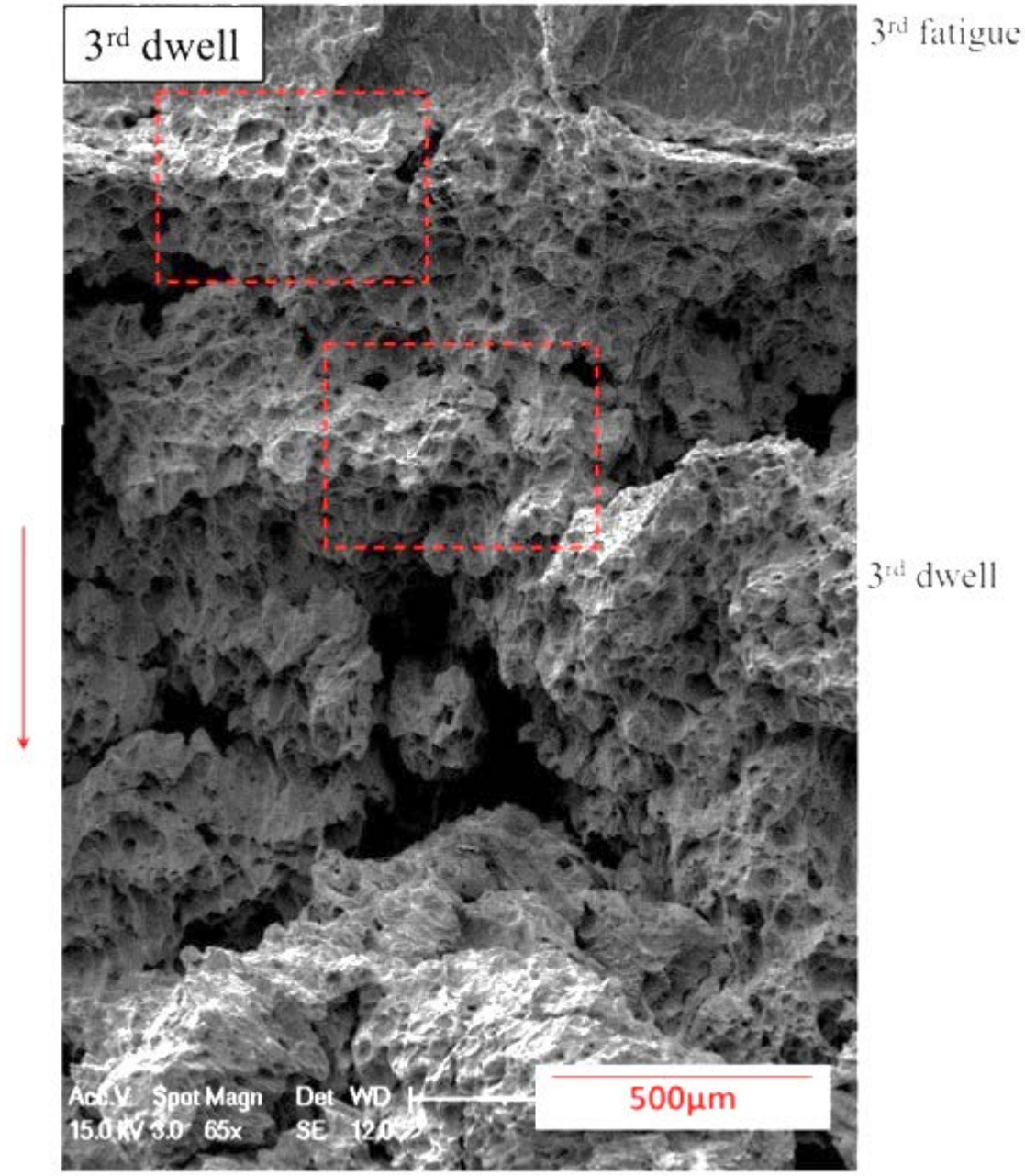

Figure 4.79 Fractographs of the as-received Alloy 709 tested under dwell fatigue loading in air at 750°C, ΔK >50 MPa√m, showing fractographic features containing two bands.

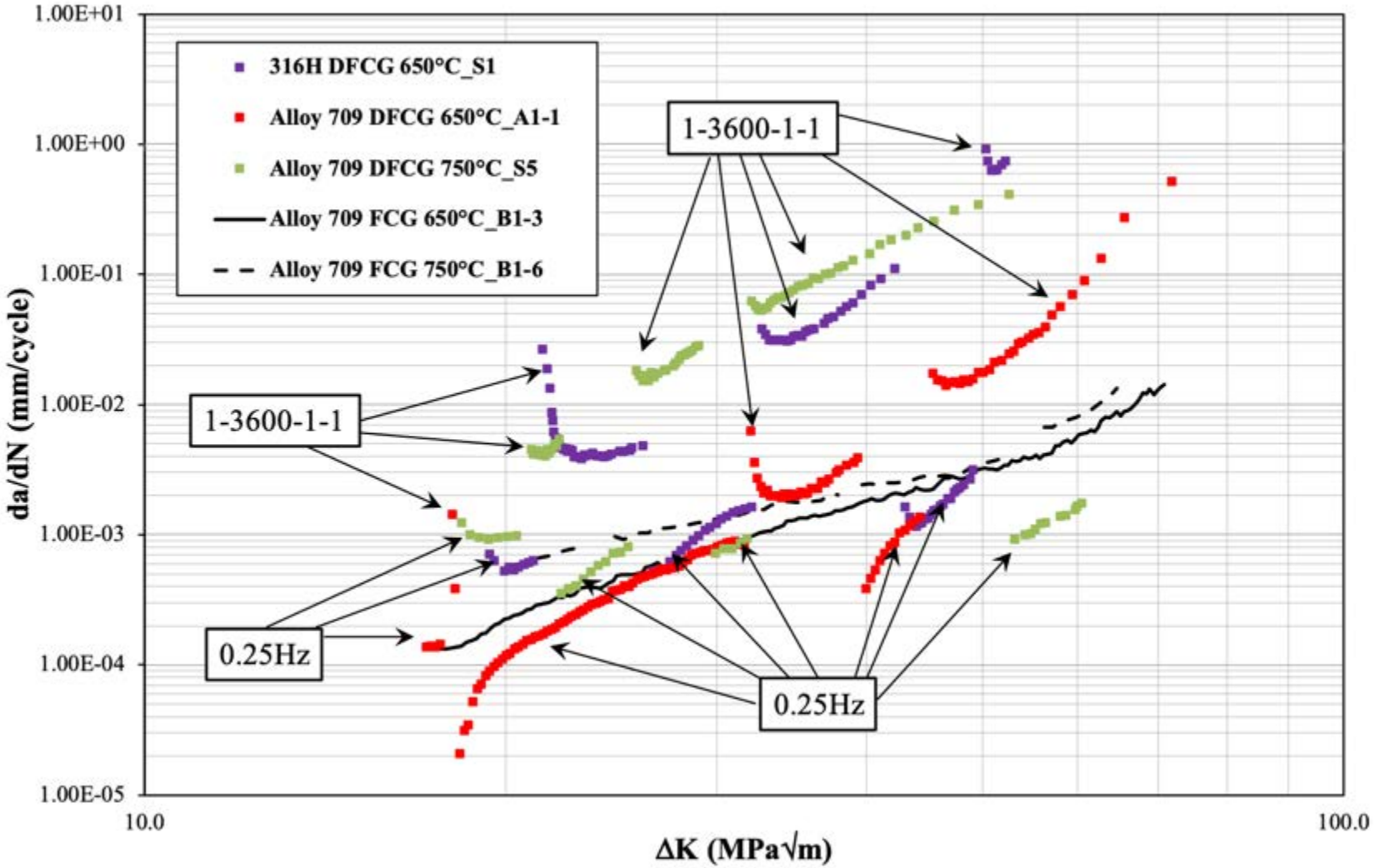

Figure 4.80 Dwell-fatigue crack growth of 316H and Alloy 709 tested in air at 650°C.

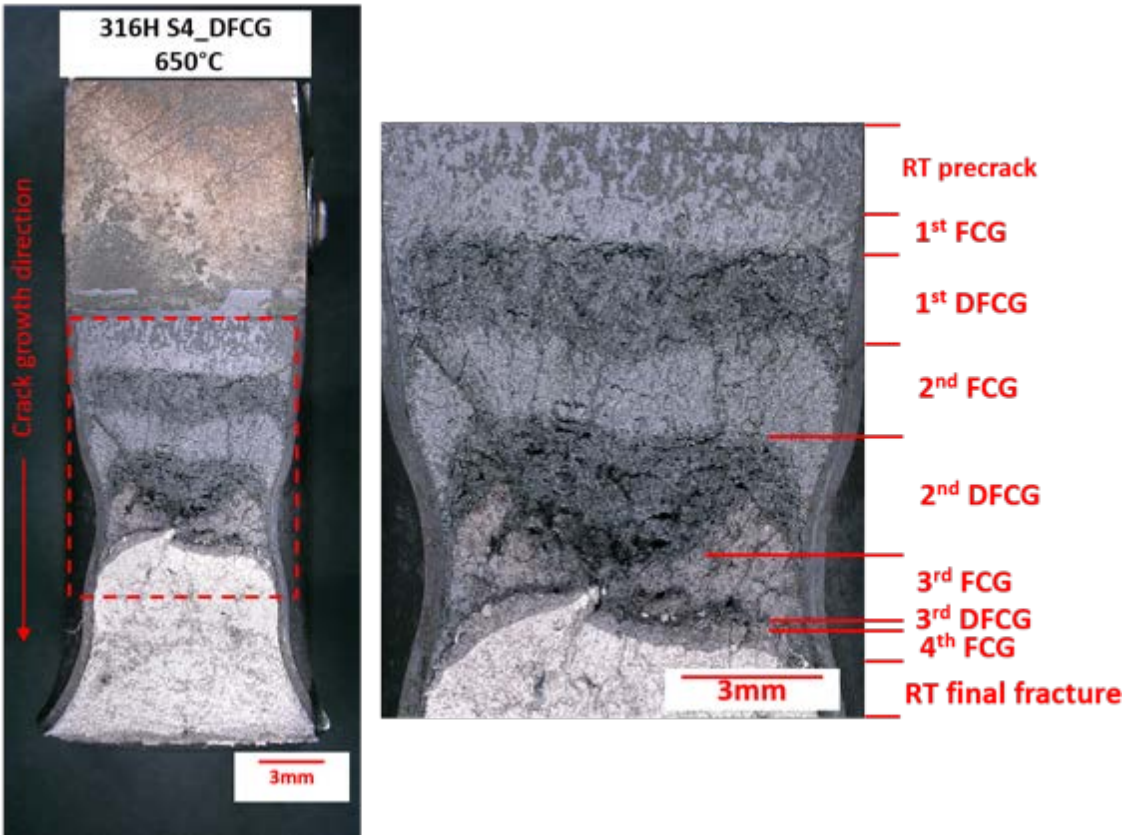

Figure 4.81 Optical fractographs of 316H CT testpiece under 1-3600-1-1 dwell-fatigue loading in air at 650°C.

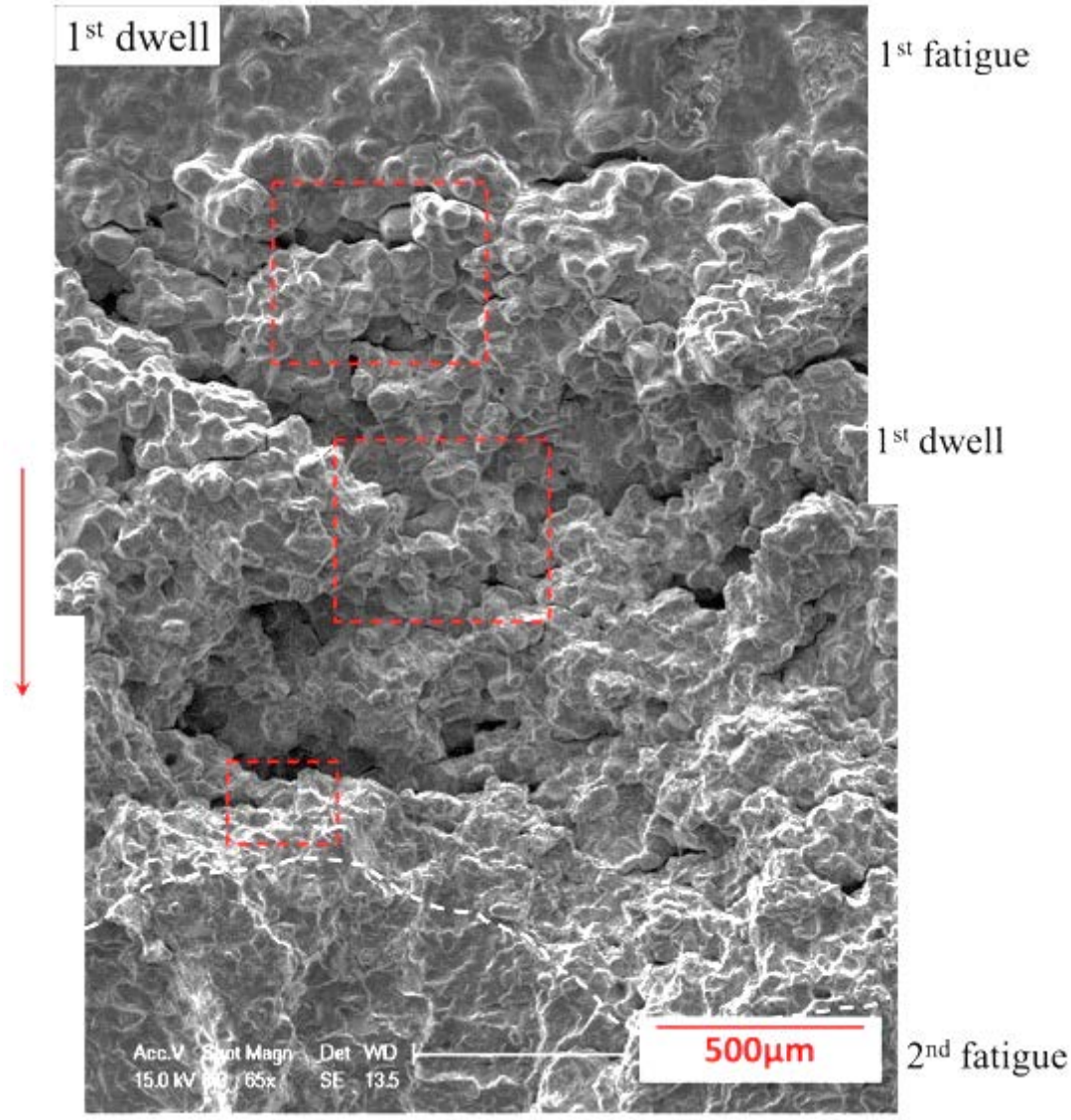

(a)

Figure 4.82 (a) Fractographs of 316H tested under 1st dwell fatigue loading in air at 650°C, showing fractographic feature containing three bands, $\Delta K > 20$ MPa$\sqrt{m}$, (b), (d), (e) intergranular failure at the beginning, middle and end of crack growth marked in Figure 4.82a, (c) close-up of (b). Note: red arrows indicate the direction of crack growth, white dotted lines showing the crack front of dwell-fatigue crack growth behaviour. Continued overleaf.

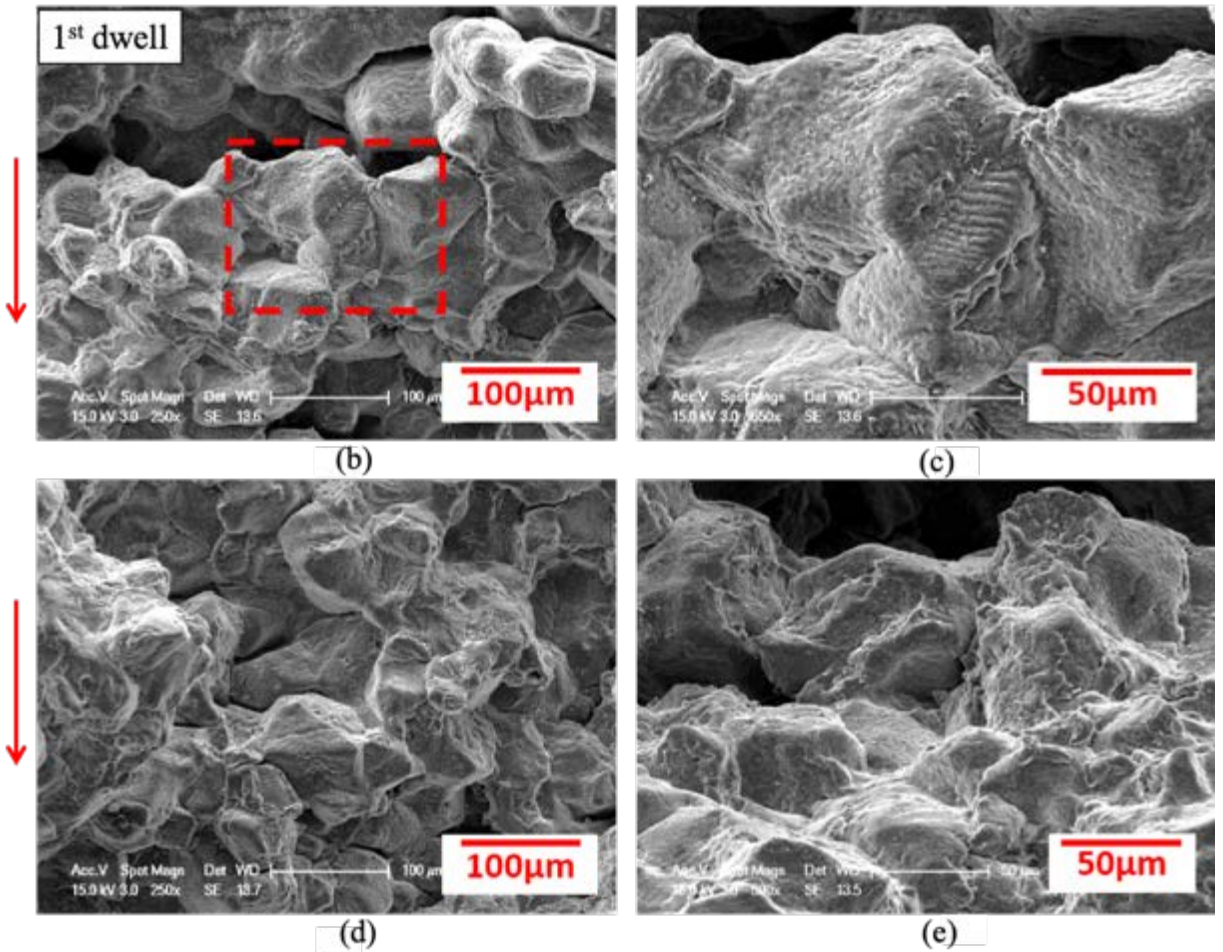

Figure 4.82 Continued. (a) Fractographs of 316H tested under 1st dwell fatigue loading in air at 650°C, showing fractographic feature containing three bands, $\Delta K > 20$ MPa$\sqrt{m}$, (b), (d), (e) intergranular failure at the beginning, middle and end of crack growth marked in Figure 4.82a, (c) close-up of (b). Note: red arrows indicate the direction of crack growth, white dotted lines showing the crack front of dwell-fatigue crack growth behaviour.

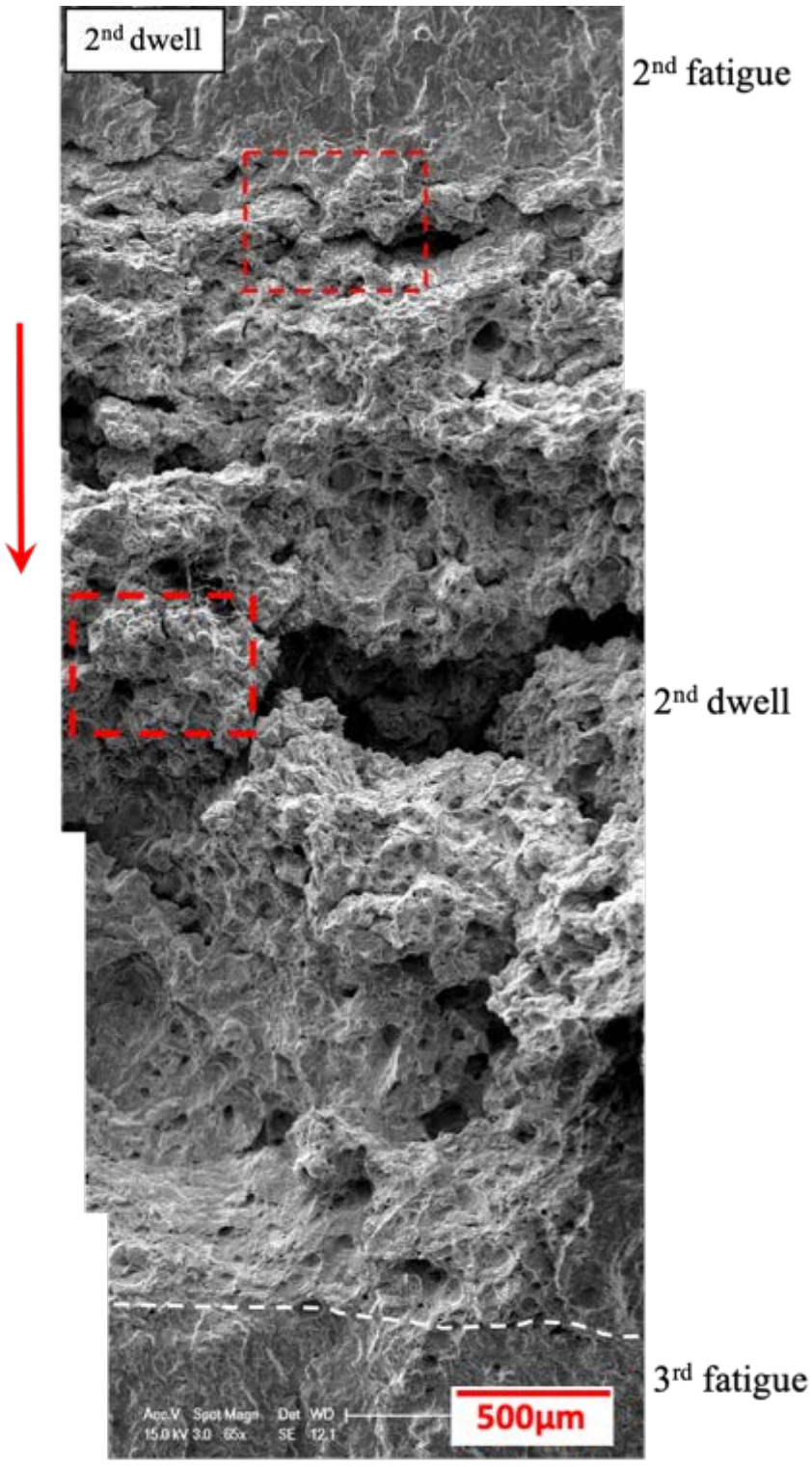

(a)

Figure 4.83 (a) Fractographs of 316H tested under 2nd dwell fatigue loading in air at 650° C, showing fractographic feature containing three bands, $\Delta K > 35$ MPa$\sqrt{m}$, (b), (c) ductile failure at beginning and middle of the 2nd dwell marked in Figure 4.83a. Note: red arrows indicate the direction of crack growth, white dotted lines showing the crack front of dwell-fatigue crack growth behaviour. Continued overleaf.

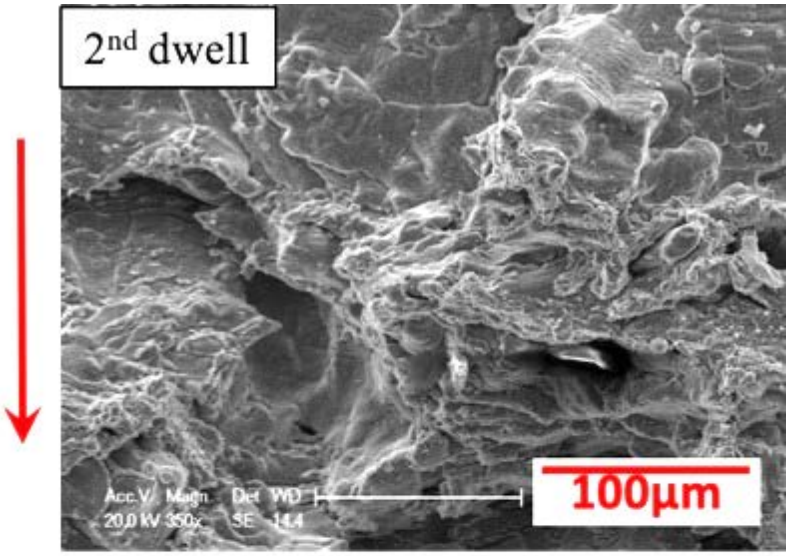

(b)

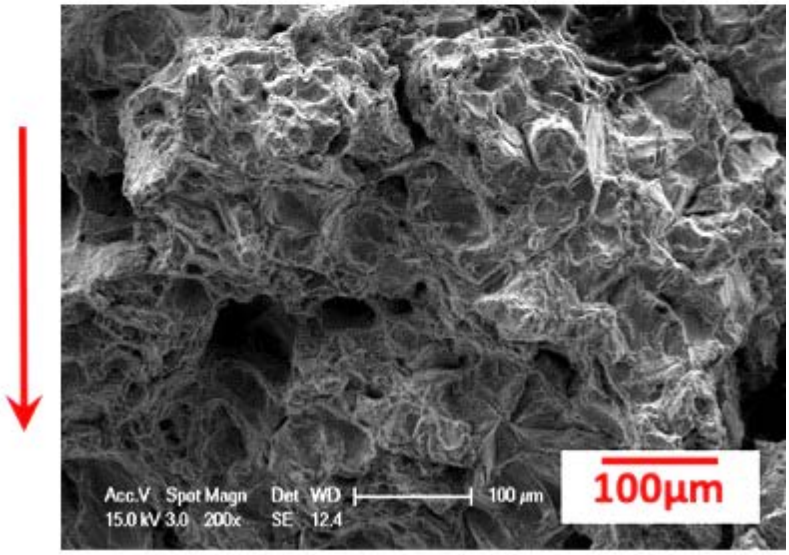

(c)

Figure 4.83 Continued. (a) Fractographs of 316H tested under 2nd dwell fatigue loading in air at 650°C, showing fractographic feature containing three bands, $\Delta K > 35$ MPa$\sqrt{m}$, (b), (c) ductile failure at beginning and middle of the 2nd dwell marked in Figure 4.83a. Note: red arrows indicate the direction of crack growth, white dotted lines showing the crack front of dwell-fatigue crack growth behaviour.

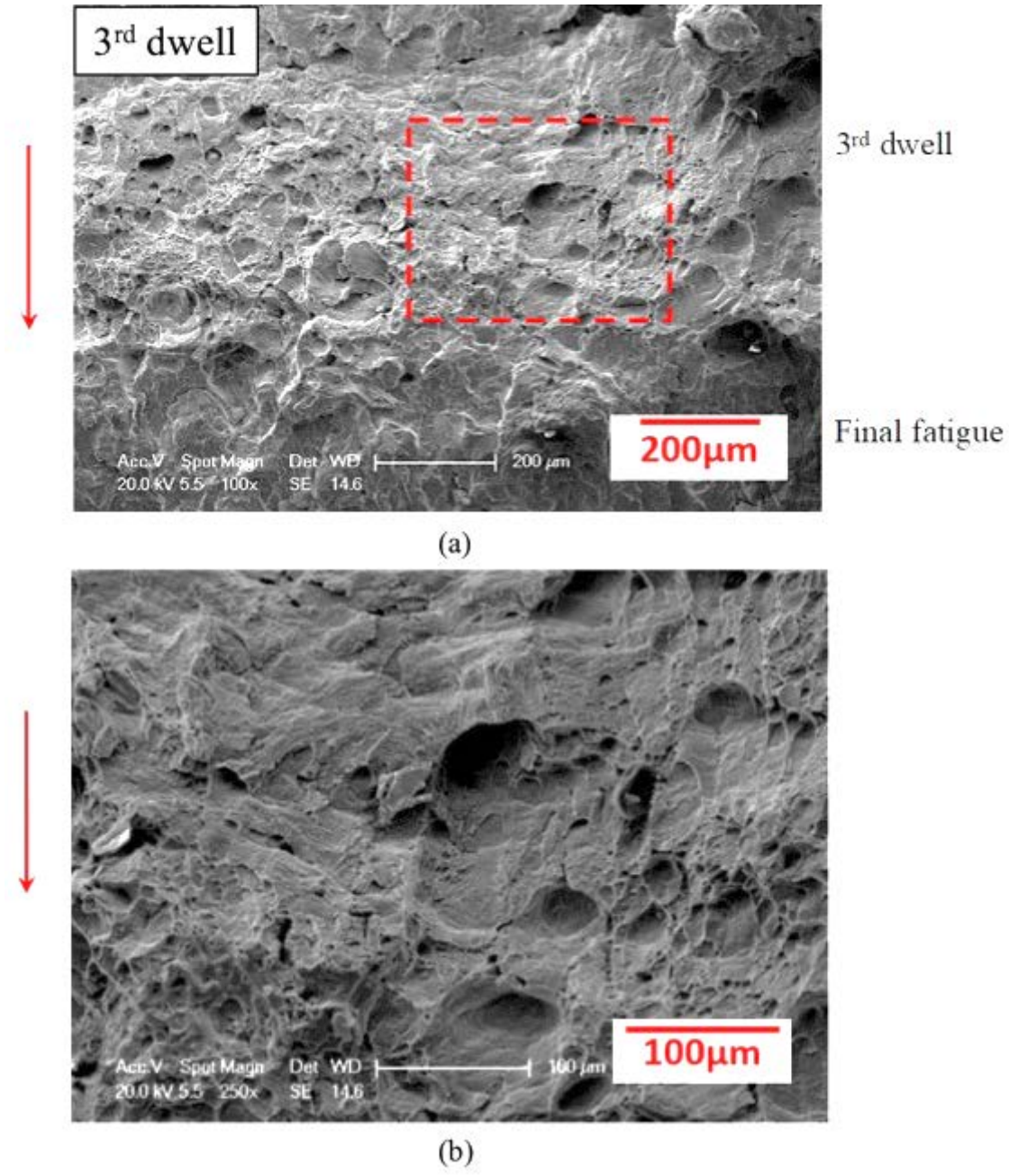

Figure 4.84 Fractographs of 316H tested under dwell fatigue loading in air at 650°C, ΔK value of >50 MPa$\sqrt{m}$, showing (a) fractographic feature containing two bands, (b) ductile failure in the 3rd dwell. Note: red arrows indicate the direction of crack growth.

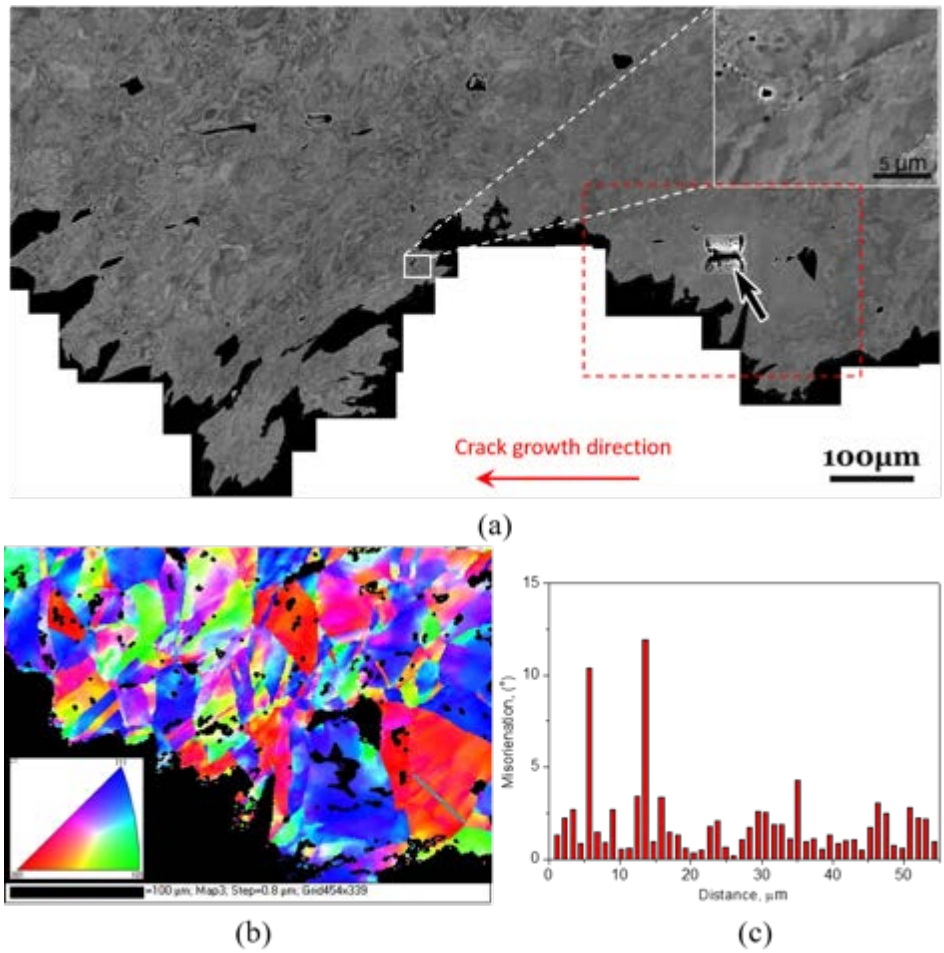

Figure 4.85 (a) BSE images for the second dwell (ΔK value of ~35 MPa√m) of 316H tested at 650°C showing some voids on grain boundary (inset) and the formation of some subgrains (inset), (b) the EBSD Inverse pole figure map for the second dwell region, (c) misorientation profile along the line in Figure 4.85b showing the existence of subgrains. Note: the arrow in Figure 4.85a shows the region where a TEM foil was extracted from.

Chapter 5

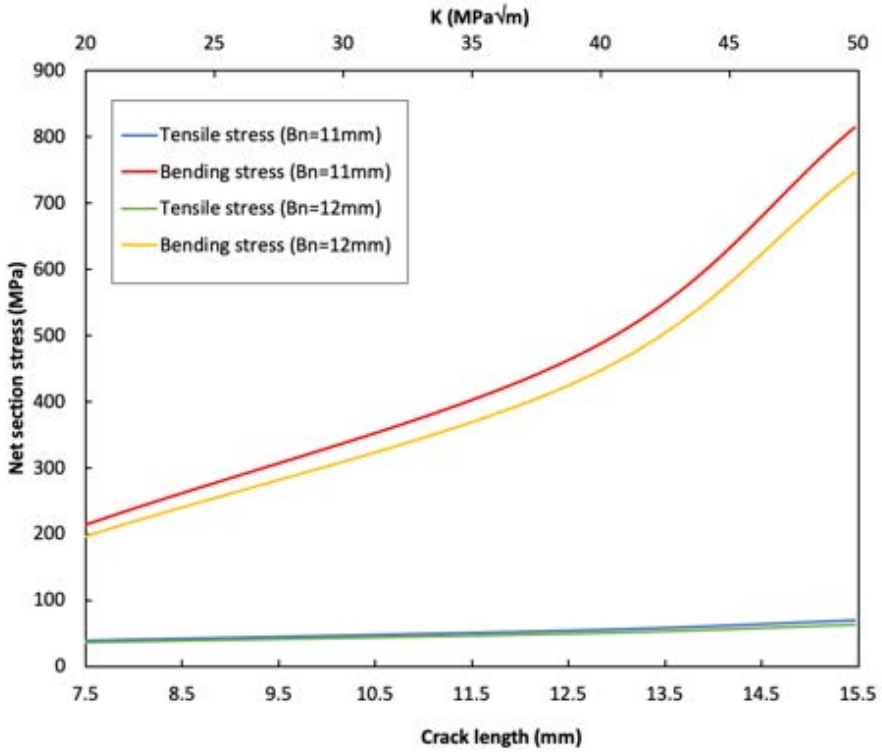

Figure 5.1 Net section stress distribution ahead of the crack tip during creep and dwell-fatigue crack growth at 550, 650 and 750°C with applied K value of 20 to 50 MPa√m and different thickness values (11 and 12 mm). Note that the tensile ($\boldsymbol{\sigma_T = \frac{P}{B_n(W-a)}}$) and bending ($\boldsymbol{\sigma_B = \frac{6P\left(a+\frac{W-a}{2}\right)}{B_n(W-a)^2}}$) stresses given are elastic stresses without considering crack tip geometry and assuming limited crack opening. σ_B is the peak bending stress located ahead of the crack tip.

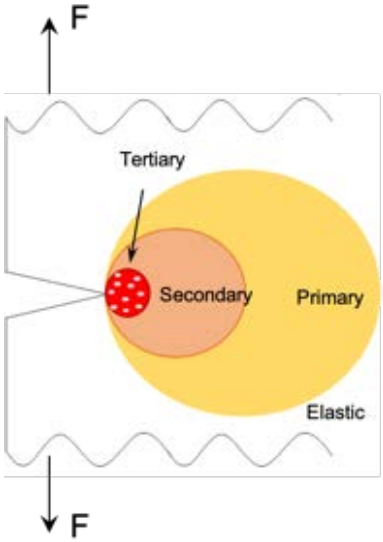

Figure 5.2 Schematic drawing of creep zone ahead of the crack tip.

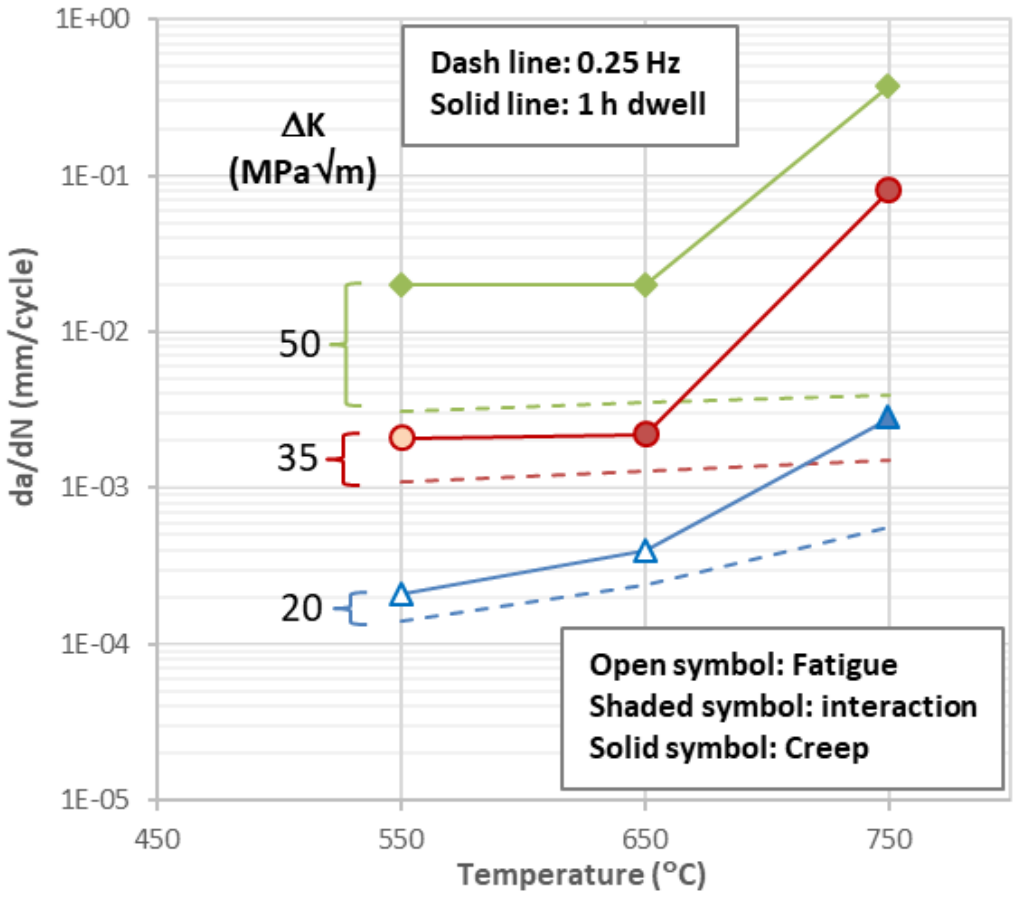

Figure 5.3 Comparison of crack growth rates between baseline fatigue and initial dwell-fatigue crack growth at 550, 650 and 750°C with applied ΔK value of 20, 35 and 50 MPa√m. Note: the different kinds of symbols showing the variation in fracture mechanisms from striated transgranular, mixed failure mode to ductile failure mode.

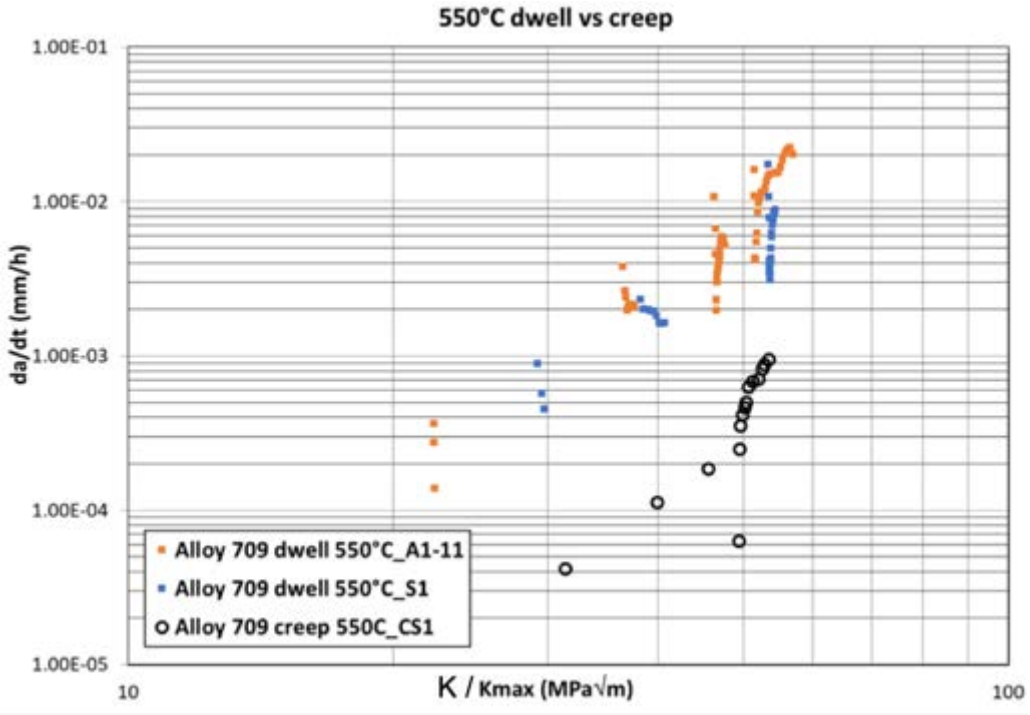

Figure 5.4 The comparison of dwell-fatigue crack growth with creep crack growth at 550°C

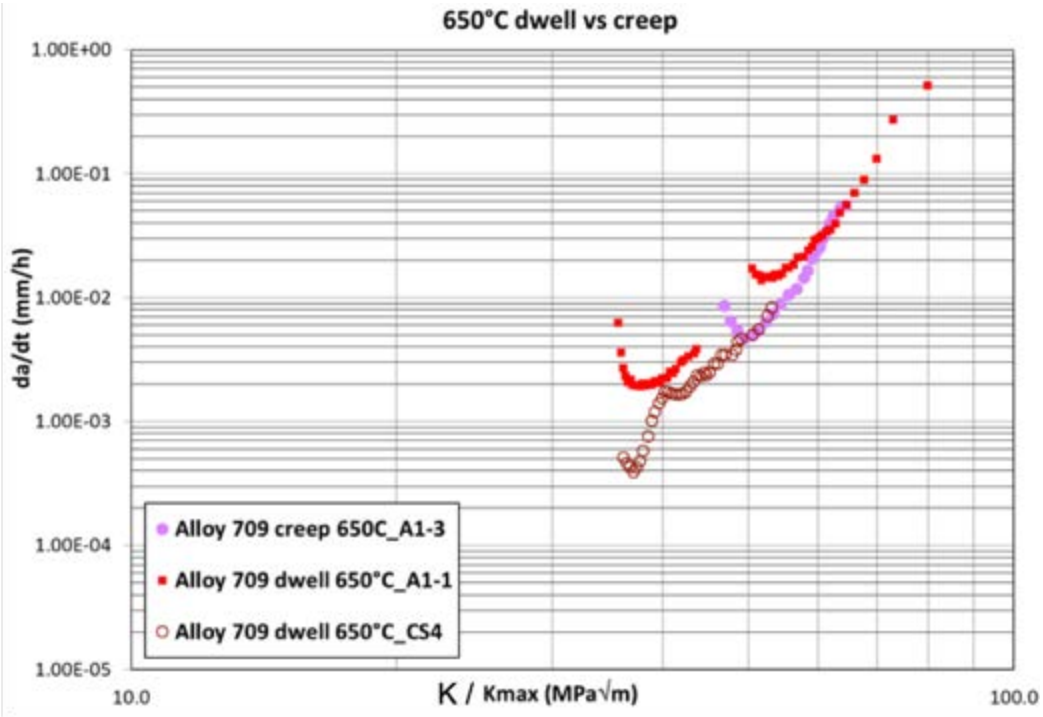

Figure 5.5 The comparison of dwell-fatigue crack growth with creep crack growth at 650°C.

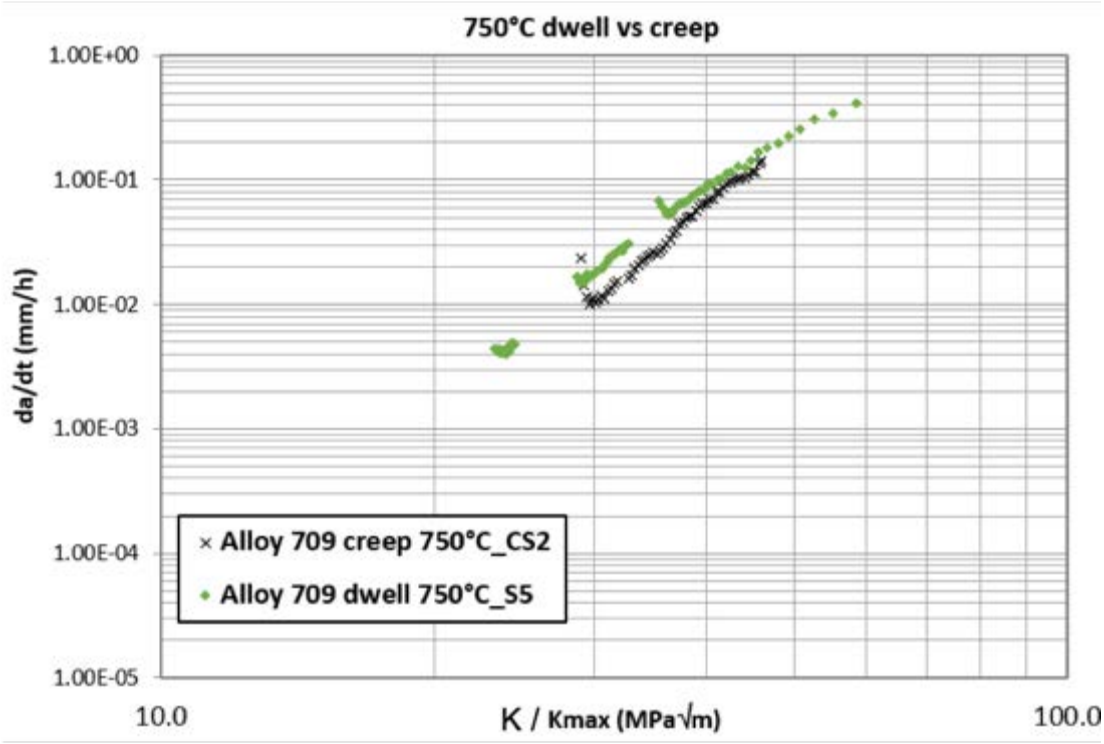

Figure 5.6 The comparison of dwell-fatigue crack growth with creep crack growth at 750°C.